High precision modelling of thermal perturbations with application to Pioneer 10 and Rosetta

Vom Fachbereich Produktionstechnik
der
UNIVERSITÄT BREMEN

zur Erlangung des Grades
Doktor-Ingenieur
genehmigte

Dissertation
von
Dipl.-Ing. Benny Rievers

Gutachter:	Prof. Dr.-Ing. Hans J. Rath Fachbereich Produktionstechnik Universität Bremen	Prof. Dr. rer. nat. Hansjörg Dittus Fachbereich Produktionstechnik Universität Bremen

Tag der mündlichen Prüfung: 13. Januar 2012

Kurzzusammenfassung in Deutscher Sprache

Das Hauptthema dieser Doktorarbeit ist die präzise numerische Bestimmung von Thermaldruck (TRP) und Solardruck (SRP) für Satelliten mit komplexer Geometrie. Für beide Effekte werden analytische Modelle entwickelt und als generischen numerischen Methoden zur Anwendung auf komplexe Modellgeometrien umgesetzt. Die Analysemethode für TRP wird zur Untersuchung des Thermaldrucks für den Pioneer 10 Satelliten für den kompletten Zeitraum seiner 30-jährigen Mission verwendet. Hierfür wird ein komplexes dreidimensionales Finite-Elemente Modell des Satelliten einschließlich detaillierter Materialmodelle sowie dem detailliertem äußerem und innerem Aufbau entwickelt. Durch die Spezifizierung von gemessenen Temperaturen, der beobachteten Trajektorie sowie detaillierten Modellen für die Wärmeabgabe der verschiedenen Komponenten, wird eine genaue Verteilung der Temperaturen auf der Oberfläche von Pioneer 10 für jeden Zeitpunkt der Mission bestimmt. Basierend auf den Ergebnissen der Temperaturberechnung wird der resultierende Thermaldruck mit Hilfe einer Raytracing-Methode unter Berücksichtigung des Strahlungsaustauschs zwischen den verschiedenen Oberfächen sowie der Mehrfachreflexion, berechnet. Der Verlauf des berechneten TRPs wird mit den von der NASA veröffentlichten Pioneer 10 Residuen verglichen, und es wird aufgezeigt, dass TRP die so genannte Pioneer Anomalie innerhalb einer Modellierungsgenauigkeit von 11.5 % vollständig erklären kann.

Durch eine Modifizierung des Algorithmus für die Bestimmung von TRP, wird ein numerisches Vefahren für die Analyse von SRP entwickelt. Beide Methoden werden für die Analyse von SRP und TRP für die Rosetta Sonde am Beispiel ausgewählter heliozentrische Freiflugphasen sowie für den ersten Erd-Flyby verwendet. Für die untersuchten Freiflugphasen ergibt sich die Höhe des TRPs im Bereich von 10 % der berechneten SRP Größenordnung, was Abweichungen der erwarteten Rosetta-Trajektorie erklärt, die von ESA/ESOC festgestellt wurden. Hierbei wurden für die Modellierung des SRPs Abweichungen im Bereich 5 % - 10 % festgestellt, welche nahezu perfekt mit der modellierten Größenordung des TRP übereinstimmen. Für den Flyby werden sowohl TRP als auch SRP als mögliche Ursachen für die beobachtete Flyby Anomalie ausgeschlossen, da beide Effekte zu einer Abbremsung von Rosetta führen, wohingegen eine anomale Beschleunigung während des Flybys beobachtet wurde.

Abstract

The main topic of this thesis is the precise numerical determination of thermal recoil pressure (TRP) and solar radiation pressure (SRP) acting on complex spacecraft bodies. Analytical models for both effects are developed and expanded into a generic numerical approach for the treatment of complex model geometries. The TRP analysis method is used for an evaluation of thermal recoils acting on the Pioneer 10 spacecraft during its 30 years mission. For this a complex three-dimensional Finite Element model of the craft with detailed material models and accurate exterior and interior geometrical configuration is developed. By specifying the available housekeeping data, the measured trajectory as well as detailed models for the heat generation of the different components, an accurate distribution of the Pioneer 10 surface temperatures can be computed for each part of the mission. Based on these surface temperature distributions, the resulting recoil is computed by means of a ray tracing method, which allows for the radiation exchange between surfaces as well as the inclusion of multiple reflections. The evolution of the computed TRP is compared to the Pioneer 10 residuals published by NASA and it is found that TRP can explain the so called Pioneer anomaly completely within a modelling accuracy of 11.5 %.

By modifying the TRP algorithm, a numerical approach for the analysis of SRP is developed. Both methods are used to analyse SRP and TRP for the Rosetta spacecraft during chosen heliocentric cruise phases as well as for the first Rosetta Earth flyby. For the cruise phases it is found that the TRP is in the order of 10 % of the SRP magnitude which explains discrepancies from the expected Rosetta trajectory found by ESA/ESOC. Here acceleration errors in the order of 5 % to 10 % of the SRP magnitude have been observed during the heliocentric cruise phases which perfectly complies to the obtained TRP magnitude. For the flyby TRP and SRP are ruled out as possible causes for the flyby anomaly due to the fact that both effects lead to a deceleration of Rosetta on its flyby trajectory and not to an anomalous increase of the velocity, as is the case for the observed anomaly.

Acknowledgements

First of all, I would like to acknowledge the support of Prof. Dr. Hans J. Rath and Prof. Dr. Hansjörg Dittus for being the referees of this thesis. In particular, I would like to thank Prof. Dr. Claus Lämmerzahl for his support throughout the years, the many fruitful discussions, the cooperative work as well as initially providing me with the interesting research topic of the Pioneer anomaly.

I would also like to acknowledge the cooperation with Prof. Dr. Jozef van der Ha and Dr. Takahiro Kato, who strongly supported my work regarding the Rosetta mission, especially during the last year. Furthermore, I would like to thank the ISSI institute for providing support for the meetings of the Pioneer collaboration as well as Dr. Slava G. Turyshev and the JPL for fruitful discussions.

Likewise, I would like to thank all my colleagues of the fundamental physics group at ZARM for their support and the good time that I had. Additionally, I would like to express my gratitude to my office colleagues, Dr. Meike List and Stefanie Bremer, for all these years of kind support. Furthermore, many thanks go to Dr. Eva Hackmann, Dennis Lorek, Benjamin Tilch and Torben Prieß, who did a remarkable job at proof-reading this thesis in a very limited time.

The financial support by the German Research Foundation DFG as well as the cluster of excellence QUEST is gratefully acknowledged.

I would like to express my deep gratitude to my family, in particular my mother Petra, for supporting me by all means throughout all these years. Finally, I would like to thank my wife Silvia for all her love and patience. Without her support, this work would not have been possible.

Bremen, August 2011 Benny Rievers

Symbols

a	Gauss integration border 1	[-]
a_i	Transformed triangle vertex point a	[-]
a_p	SRP component perpendicular to sun direction	[m/s^2]
a_s	SRP component aligned with sun direction	[m/s^2]
A	Surface area	[m^2]
$\mathbf{A}$	Quaternion rotation matrix	[-]
$A(i)$	Surface area of element i	[m^2]
$\mathbf{A}_\mathrm{y}$	Quaternion rotation matrix with axis y'	[-]
$\mathbf{A}_\mathrm{z}$	Quaternion rotation matrix with axis z	[-]
A_1	Surface of active element	[m^2]
A_2	Surface of receiving element	[m^2]
α	Coefficient of absorption	[-]
α_gap	Absorptivity of gabs between solar cells	[-]
α_mean	Mean absorptivity	[-]
α_cell	Solar cell absorptivity	[-]
α_SP	Solar panel absorptivity	[-]
b	Gauss integration border 2	[-]
b_i	Transformed triangle vertex point b	[-]
c_1, c_2, c_3	Hit detection parameters 1-3	[-]
C_i	Polynomial term for DOF constraint equation	[-]
C_0	Constant term for DOF constraint equation	[-]
$\chi_i, \chi_j, \chi_k, \chi_l$	Uniform Gauss coordinates	[-]
d_hs	Diameter of hemisphere	[m]
d_MLI	Thickness of MLI	[m]
D_i	DOF parameter for DOF constraint equation	[-]
$\mathrm{d}\Omega$	Solid angle element surface	[-]
Δv	Velocity jump during flyby	[m/s]
ΔT	Temperature gradient	[K]
e	Eccentricity	[-]
e_1, e_2, e_3	Components 1-3 of Quaternion rotation axis	[-]
$\vec{e}_\mathrm{c}(i)$	Active element centre	[-]
$\vec{e}_\mathrm{c}(j)$	Receiving element centre	[-]
$\vec{e}_{\mathrm{c},\Omega}(i, \phi, \theta)$	Solid angle element centre	[-]
$\vec{e}_\mathrm{N}(i)$	Element normal vector on element i	[-]
E	Energy	[J]
$\vec{E}$	Quaternion rotation axis	[-]
E_Heat	Heat energy	[J]
E_inc	Incoming energy	[J]
E_Ph	Photon energy	[J]
E_Volt	Electrical energy	[J]
ε	Coefficient of emission	[-]
$\varepsilon_\mathrm{l,eff}$	Effective louver emissivity	[-]
ε_γ	Specific coefficient of emission	[-]
$\varepsilon_\mathrm{mean}$	Mean coefficient of emission	[-]
ε_ss	Emissivity of second surface mirrors	[-]

ε_{b}	Emissivity of louver blades	[-]
ε^*	Effective MLI emissivity	[-]
η_{cell}	Efficiency of solar cells	[-]
η_{c}	Efficiency of louver heat conduction	[-]
η_{MLI}	MLI performance	[-]
$\vec{f}_{\mathrm{a}}$	Force resulting from absorption	[N]
f_{p}	Cell packing factor	[-]
$\vec{f}_{\mathrm{s}}$	Force resulting from specular reflection	[N]
$\vec{f}_{\mathrm{s,abs}}$	Absorption component of specular reflection force	[N]
$\vec{f}_{\mathrm{s,refl}}$	Reflection component of specular reflection force	[N]
$\vec{f}_{\mathrm{d}}$	Force resulting from diffuse reflection	[N]
$\vec{f}_{\mathrm{d,abs}}$	Absorption component of diffuse reflection force	[N]
$\vec{f}_{\mathrm{d,refl}}$	Reflection component of diffuse reflection force	[N]
F_{a}	Force component resulting from absorption	[N]
F_{r}	Force component resulting from reflection	[N]
$\vec{F}_{\mathrm{TRP}}$	Thermal recoil force	[N]
$\vec{F}_{\mathrm{TRP},\Omega,eff}$	Effective thermal recoil force component	[N]
$g(x)$	Parametric function	[-]
$\tilde{g}(\chi)$	Transformed parametric function	[-]
γ	Coefficient of reflection	[-]
γ_{d}	Coefficient of diffuse reflection	[-]
γ_{mean}	Mean reflectivity	[-]
γ_{s}	Coefficient of specular reflection	[-]
i	Active Element number	[-]
I	Intensity of radiation	[W/m^2]
I_{n}	Intensity of radiation emitted normal to source	[W/m^2]
j	Receiving Element number	[-]
k_{al}	Conductivity of solid aluminium	[W/mK]
k_{BUS}	Mean conductivity of Rosetta bus	[W/mK]
k_{cond}	Thermal conductivity	[W/mK]
k_{HGA}	Mean conductivity of Rosetta HGA	[W/mK]
k^*	Effective MLI conductivity	[W/mK]
k_{SP}	Through-thickness conductivity of solar panels	[W/mK]
κ	Orientation angle	[°]
λ	Wavelength	[m]
L	Radiance	[W/(m^{2}Sr)]
L_λ	Spectral radiance	[W/(m^{3}Sr)]
m	Spacecraft mass	[kg]
m_0	Photon rest mass	[kg]
n	Total number of elements in model	[-]
$\vec{n}_{A_1ij}$	Normal vector on active element	[-]
$\vec{n}_{A_2kl}$	Normal vector on receiving element	[-]
n_E	Total number of considered elements	[-]
$n_{\mathrm{rays},\phi}$	Number of emitted rays in ϕ-direction	[-]
$n_{\mathrm{rays},\theta}$	Number of emitted rays in θ-direction	[-]

n_{refl}	Number of considered reflections	[-]
n_{x}	Number of solar pixels in x-direction	[-]
n_{y}	Number of solar pixels in y-direction	[-]
N	Number of Photons	[-]
$N_1(i)$	Node 1 of Element i	[-]
$N_2(i)$	Node 2 of Element i	[-]
$N_3(i)$	Node 3 of Element i	[-]
$N_4(i)$	Node 4 of Element i	[-]
$\vec{N_{i,*}}$	Node in rotated coordinates	[-]
ν_{Ph}	Photon frequency	[Hz]
Ω_r	Electrical resistance	[Ω]
p	Momentum acting on the source of emission	[kgm/s]
p_{e}	Proportional factor for electrical energy	[W]
p_i,p_j,p_k,p_l	Gauss integration points	[-]
$\tilde{p}_i$, $\tilde{p}_j$, $\tilde{p}_k$, $\tilde{p}_l$	Transformed Gauss integration points	[-]
$p_{\vec{\text{HGA}}}$	HGA pointing vector	[-]
p_{Ph}	Photon momentum	[kgm/s]
$\vec{P}$	Intersection point	[-]
P_{AMD}	AMD energy	[W]
$\vec{P}_{A_1ij}$	Gauss integration point on active element	[-]
$\vec{P}_{A_2kl}$	Gauss integration point on receiving element	[-]
P_{BH}	BH energy	[W]
$P_{\text{BUS}}(i)$	Heat load on bus surface	[W]
$\vec{P}_{\text{C}}(i,j)$	Solar pixel centre position	[-]
P_{cable}	Cable loss	[W]
P_{comp}	Compartment energy	[W]
P_{CRT}	CRT energy	[W]
P_{diss}	Heat to be dissipated by RTG	[W]
P_{e}	Total emitted power	[W]
P_{el}	Electrical power	[W]
$P_{\text{el,ref}}$	Electrical reference power	[W]
P_{gen}	Heat produced by radioactive fuel	[W]
$P_{\text{HGA}}(i)$	Absorbed solar flux on HGA element i	[W]
P_{ij}	Radiation flux from element i to element j	[W]
$P_{\text{inc}}(i,j)$	Incoming radiation flux	[W]
P_{LH}	LH power	[W]
P_{MLI}	Heat transport through MLI	[W]
$P_n(z)$	Legendre Polynomial	[-]
P_{PPA}	PPA power	[W]
P_{rec}	Received Solar power	[W]
P_{SP}	Solar panel load	[W]
$\vec{P}_{\text{SRP}}$	Solar radiation pressure	[m/s^2]
$\vec{P}_{\text{SRP,res}}$	Resulting Solar radiation pressure	[m/s^2]
$\vec{P}_{\text{SRP,abs}}$	Solar radiation pressure absorption component	[m/s^2]
$\vec{P}_{\text{SRP,spe}}$	Solar radiation pressure specular reflection component	[m/s^2]

$\vec{P}_{\mathrm{SRP,dif}}$	Solar radiation pressure diffuse reflection component	[m/s^2]
$\vec{P}_{\mathrm{TRP,res}}$	Resulting Thermal recoil pressure	[m/s^2]
$\vec{P}_{\mathrm{TRP,emi}}$	Thermal recoil pressure for free emission	[m/s^2]
$\vec{P}_{\mathrm{TRP,abs}}$	Thermal recoil pressure correction for absorption	[m/s^2]
$\vec{P}_{\mathrm{TRP,ref}}$	Thermal recoil pressure correction for reflection	[m/s^2]
$\vec{P}_{\mathrm{TRP}}$	Thermal recoil pressure	[m/s^2]
P_{tot}	Total power received by unit hemisphere	[W]
$P_{\odot}(r)$	Solar flux at heliocentric distance r	[W/m^2]
$\vec{P}_{*}$	Intersection point in rotated coordinates	[-]
ϕ	Azimuth angle	[°]
ϕ_{BUS}	Bus azimuth angle	[°]
ϕ_{HGA}	HGA azimuth angle	[°]
ϕ_{l}	Louver opening angle	[°]
ϕ_1, ϕ_2	Azimuth borders of radiation hemisphere	[rad]
Φ	Quaternion rotation angle	[°]
$\Phi(x)$	Polynomial function	[-]
$\psi_1(i,j)$	Visibility angle 1	[°]
$\psi_2(i,j)$	Visibility angle 2	[°]
$\psi_3(i,j)$	Visibility angle 3	[°]
q_1	Quaternion Euler symmetric parameter 1	[-]
q_2	Quaternion Euler symmetric parameter 2	[-]
q_3	Quaternion Euler symmetric parameter 3	[-]
q_4	Quaternion Euler symmetric parameter 4	[-]
Q_{LINK33}	Heat transfer through LINK33 element	[W]
Q_{HGA}	Heat flux conducted through the HGA	[W]
r	Heliocentric distance	[AU]
$\vec{r}_{\mathrm{COM}}(i)$	Distance of surface centre to centre of mass	[m]
$\vec{r}_{ijkl}$	Distance between two Gauss integration points	[m]
$\vec{r}_{\mathrm{ref}}(i,j)$	Direction of specular reflection	[-]
r_p	Pericentre	[m]
$\vec{r}_{\mathrm{S}at}$	Satellite position in heliocentric frame	[-]
$\vec{r}_{\mathrm{SUN}}$	Sun vector	[-]
$r_{\mathrm{SUN,x}}$	X-component of Sun vector	[-]
$r_{\mathrm{SUN,y}}$	Y-component of Sun vector	[-]
$r_{\mathrm{SUN,z}}$	Z-component of Sun vector	[-]
r_{12}	Distance between active and receiving element	[m]
R	Projection point coordinate	[-]
R_{hc}	Ratio between honeycomb and solid material density	[-]
$\vec{R}(i,\phi,\theta)$	Ray direction	[-]
ρ_{Al}	Aluminium density	[kg/m^3]
ρ_{hc}	Honeycomb density	[kg/m^3]
t	Time	[s]
t_{half}	Half-time of radioactive fuel	[s]
t_{HGA}	Thickness of HGA	[m]
t_0	Reference date	[s]
θ	Elevation angle	[°]

θ_{BUS}	Bus elevation angle	[°]
θ_{HGA}	HGA elevation angle	[°]
θ_1, θ_2	Elevation borders of radiation hemisphere	[rad]
Θ_i	Orientation angle of element i	[°]
Θ_j	Orientation angle of element j	[°]
T	Surface temperature	[K]
$T(i)$	Surface temperature of element i	[K]
T_{ANA}	Analytical reference surface temperature	[K]
T_{BOT}	Bottom MLI temperature DOF	[-]
T_{e}	Exterior MLI temperature	[K]
$T_{\mathrm{E,n}}$	N-th MLI sheet temperature DOF	[-]
T_{i}	Interior MLI temperature	[K]
T_{MAX}	Maximum surface temperature	[K]
T_{MEAN}	Mean surface temperature	[K]
T_{MIN}	Minimum surface temperature	[K]
T_n	Nodal temperature DOF	[K]
T_{res}	Resulting thermal recoil torque	[Nm]
T_{TOP}	Top MLI temperature DOF	[K]
T_1	Element triangle 1	[-]
T_2	Element triangle 2	[-]
$TRP_{\perp}$	TRP aligned with normal direction	[m/s^2]
$\vec{v}(i,j)$	Middle node connection vector	[-]
$\vec{V}_{A_1 i}, \vec{V}_{A_1 j}$	Vertex vectors of active element	[-]
$\vec{V}_{A_2 k}, \vec{V}_{A_2 l}$	Vertex vectors of receiving element	[-]
$\vec{V}_1$	Vertex vector 1	[-]
$\vec{V}_2$	Vertex vector 2	[-]
$w(x)$	Weighting function	[-]
w_i, w_j, w_k, w_l	Gauss integration weights	[-]
$\tilde{w}_i$,$\tilde{w}_j$,$\tilde{w}_k$,$\tilde{w}_l$	Transformed Gauss integration weights	[-]
x_*	Rotated coordinate 1	[-]
$\vec{x}_{spe}$	Direction of specular reflection	[-]
x_{pix}	Width of individual solar pixel	[m]
x_{SUN}	Sun-spacecraft vector	[-]
x_{tot}	Width of solar pixel array	[m]
$\vec{x_0}$	Offset of solar panel frame to bus frame	[m]
x_1, x_2, x_3, x_4	Nodal coordinates for active element	[-]
x_5, x_6, x_7, x_8	Nodal coordinates for receiving element	[-]
$\xi_{i,j}$	Radiation view factor form element i to element j	[-]
ξ_{Ω}	Hemisphere method view factor ratio	[-]
y_*	Rotated coordinate 2	[-]
y_{pix}	Height of individual solar pixel	[m]
y_{tot}	Height of solar pixel array	[m]

Acronyms

AMD	Asteroid/meteoroid detector assembly
AU	Astronomical Unit
APDL	ANSYS Parametric Design Language
BH	Battery heater
BOL	Begin of Life
CEA	Control Electronics Assembly
CRT	Cosmic ray telescope
DOF	Degree of Freedom
DSU	Data Storage Unit
DTU	Digital Telemetry Unit
EOL	End of Life
ESA	European Space Agency
ESOC	European Space Operations Centre
FE	Finite Element
GEO	Geocentric orbit
GMM	Geometrical-Mathematical Model
HCF	Heliocentric coordinate frame
HGA	High Gain Antenna
ICCG	Incomplete Cholesky Conjugate Gradient
ITER	Iterative Solver option
JCG	Jacobi Conjugate Gradient
JPL	Jet Propulsion Laboratory
LEO	Low Earth orbit
LGA	Low gain antenna
LH	Propellant line heater
LISA	Laser Interferometer Space Antenna
MEX	Mars express
MICROSCOPE	Micro-Satellite a Trainee Compensee pour l'Observation du Principe d'Equivalence
MJD	Modified Julian Date
MOND	Modified Newtonian Dynamics
NASA	National Aeronautics and Space Administration
PA	Pioneer Anomaly
PCG	Preconditioned Conjugate Gradient
PCU	Power Control Unit
PPA	Plasma analyser
QMR	Quasi-Minimal Residual
RHU	Radioisotopic heater unit
RTG	Radioisotopic Thermal Generator
SHU	Shunt radiator
SRA	Stellar Reference Assembly
SRP	Solar Radiation Pressure
TASC	Toolkit for Auxiliary Science Calculations
TDB	Barycentric Dynamic Time
TRP	Thermal Recoil Pressure
VEX	Venus express

Constants

c	Speed of light	299792458 m/s
σ	Stefan-Boltzmann's constant	$5.67 \cdot 10^{-8} \mathrm{W/m^2K^4}$
h	Plancks Number	$6.62606896 \cdot 10^{-34} \mathrm{J\,s}$
$P_{\odot,1\mathrm{AU}}$	Solar constant at 1 AU	1367 $\mathrm{W/m^2}$

Own Publications

- B. Rievers, M. List, S. Bremer, C. Lämmerzahl, and H. Rath, *Thermal dissipation force modeling with preliminary results for Pioneer 10/11*, Proceedings ofthe 61th International Astronautical Congress, Glasgow, UK, 2008.

- B. Rievers, D. Bindel, B. Dachwald, E. Plescher, and H. Dittus, *The Thermal determinator satellite mission*, 7th Symposium on Small Satellites for Earth Observations, Hans-Peter Röser and Rainer Sandau, editors, page 107 - 110, Wissenschaft & Technik Verlag, Berlin, May 2009.

- B. Rievers and C. Lämmerzahl, *New precise method for accurate modeling of thermal recoil forces*, in: Relativity in Fundamental Astronomy: Dynamics, Reference Frames, Data Analysis, Sergei A. Klioner, P. Kenneth Seidelmann and Michael H. Soffel, editors, page 426 - 428, Cambridge University Press, Cambridge, 2009.

- B. Christophe, P. H. Andersen, J. D. Anderson, S. Asmar, Ph. Berio, O. Bertolami, R. Bingham, F. Bondu, Ph. Bouyer, S. Bremer, J.-M. Courty, H. Dittus, B. Foulon, P. Gil, U. Johann, J. F. Jordan, B. Kent, C. Lämmerzahl, A. Levy, G. Metris, O. Olsen, J. Paramos, J. D. Prestage, S. V. Progrebenko, E. Rasel, A. Rathke, S. Reynaud, B. Rievers, E. Samain, T. J. Sumner, S. Theil, P. Touboul, S. Turyshev, P. Vrancken, P. Wolf, and N. Yu, *Odyssey: a solar system mission*, *Exp. Astron.* 23, 529 (2009).

- B. Rievers, M. List, S. Bremer, C. Lämmerzahl, and H. Rath, *New Methods for Accurate Thermal Disturbance Force Calculation with Application to Pioneer and Flyby Anomaly*, Proceedings of the 62th International Astronautical Congress, South Korea, 2009.

- B. Rievers, C. Lämmerzahl, M. List, S. Bremer, and H. Dittus, *New powerful thermal modelling for high-precision gravity missions with application to Pioneer 10/11*, New J. Phys. 11, 113032 (24pp), 2009.

- D. Bindel, O. Khromov, M. Ovchinnikov, B. Rievers, J. Rodriguez Navarro, and A. Selivanov, *German Russian Education Satellite - Mission Outline and Objectives*, Small Satellite Missions for Earth Observation, Hans-Peter Röser and Rainer Sandau, editors, page 215 - 221, Springer, Heidelberg, February 2010.

- B. Rievers, S. Bremer, M. List, C. Lämmerzahl, and H. Dittus, *Thermal dissipation force modeling with preliminary results for Pioneer 10/11*, Acta Astronautica, Vol. 66, Issues 3-4, February-March 2010, Pages 467–476.

- B. Rievers, C. Lämmerzahl, and H. Dittus, *Modeling of Thermal Perturbations Using Raytracing Method with Preliminary Results for a test case Model of the Pioneer 10/11 Radioisotopic Thermal Generators*, Space Sci Rev 151, pp. 123-133, Springer, 2010.

- Y. Sugimoto, B. Rievers, and J. Van der Ha, *Thermal Radiation Model for the Rosetta Spacecraft*, Proceedings of the 2010 AIAA Astrodynamics Specialists Conference, Toronto, Ontario, Canada, August 2010.

- C. Braxmaier, H. Dittus, B. Foulon, E. Göklü, C. Grimani, J. Guo, S. Herrmann, C. Lämmerzahl, W. T. Ni, A. Peters, B. Rievers, É. Samain, H. Selig, D. Shaul, D. Svehla, P. Touboul, G. Wang, A. M. Wu, and A. F. Zakharov, *Astrodynamical Space Test of Relativity using Optical Devices I (ASTROD I) - A class-M fundamental physics mission proposal for Cosmic Vision 2015-2025: 2010 Update*, arXiv, gr-qc:1104.0060, 2011.

- B. Rievers and C. Lämmerzahl, *High precision thermal modeling of complex systems with application to the flyby and Pioneer anomaly*, Annalen der Physik 523, 6, Pages 439–449, 2011.

Contents

Part I

Basics of thermal perturbation analysis

Chapter 1

Introduction

This chapter gives an introduction to the topic of thermal modelling for space missions, discusses the influence of non-gravitational forces on a spacecraft's motion and reviews the main motivation and objectives for this study. The outline of the thesis is presented.

1.1 Overview

Spacecraft orbit determination and orbit propagation are central tasks for the design and the successful conduct of modern spacecraft missions. In order to realise an accurate modelling of spacecraft motion and attitude the gravitational forces as well as the non-gravitational perturbations acting on the orbit have to be assessed. In particular current and future fundamental physics space missions (such as LISA [1], LISA pathfinder [2], MICROSCOPE [3] and the upcoming Bepi Colombo mission [4]) require high modelling accuracies of these perturbations in order to achieve the scientific mission goals. One example for this are the disturbance requirements of the NASA/ESA mission LISA which is aiming at the detection of low frequency gravitational waves. The spacecraft needs to operate in drag-free mode which involves the use of proof masses as perturbation sensors. In order to fulfil the scientific requirements the total perturbations for each proof mass need to be below $3 \cdot 10^{-15}\,\mathrm{ms}^{-2}$ at 0.1 mHz [5, 6, 7]. Here the magnitude of solar radiation pressure (SRP) acting on the craft is already several magnitudes higher than the required perturbation level, which demands an accurate modelling and assessment of the effect.

Type	**Perturbation**	**Origin**
External	Solar radiation pressure	Sun
	Solar wind pressure	Sun
	Albedo	Planet
	Atmospheric drag	Planet
	Interstellar dust	Interstellar medium
	Micrometeorites	Interstellar medium
Internal	Thermal recoil pressure	Spacecraft surface
	Gas leakage	Spacecraft thrusters

Table 1.1: Main non-gravitational disturbances acting on spacecraft.

Two different classes of non-gravitational disturbances may perturb a spacecrafts motion. *External* perturbations result from environmental sources interacting with the spacecraft while *internal* perturbations originate from the spacecraft itself. Due to the fact that the influence of non-gravitational effects on the resulting orbit is several orders of magnitude weaker than the influence of the gravitational pull, external and internal disturbances are also often labelled as *small forces*. Table 1.1 gives an overview of the main internal and external disturbance effects for earthbound and interplanetary spacecraft missions.

Among those small forces, the assessment of the SRP and the thermal radiation pressure (TRP) plays a central role in the improvement of current orbit perturbation modelling capabilities. The SRP results from impacting solar photons on a spacecraft surface and is the dominating non-gravitational disturbance effect for earthbound, near-solar and solar sailing missions. The magnitude of the effect depends on the surface area exposed to the sunlight, the optical properties of the spacecraft surface, the surface shapes and on the distance to the Sun. The TRP results from the emission of photons by the spacecraft surface. Any spacecraft with electrical appliances such as computers, payloads and actuators produces waste heat that has to be emitted into the space environment in order to maintain suitable temperature ranges within the craft. Furthermore, if the satellite is exposed to the Sun, the solar flux is an additional heat load acting on the illuminated surfaces. Due to a heat balance between the energy provided by internal heat production and/or external heat sources and the emitted radiation, an equilibrium surface temperature distribution develops. The resulting emission pattern depends on the geometry and design of the craft, the surface materials and the thermal control concept (active or passive thermal control). Due to momentum conservation any radiation emitted by a source results in a recoil force opposite to the direction of emission. Thus, if the pattern of emission is not spherically symmetric a TRP acting on the source results and the spacecraft orbit and attitude will be perturbed. The magnitude of the perturbation thus depends on the internal energy dissipation of the craft, the illumination conditions, the thermal properties of the internal materials (which influence heat conduction), the optical properties of the spacecraft surface and the spacecraft shape.

While SRP is the dominating non-gravitational disturbance effect for earthbound, near-solar and solar sailing missions, TRP becomes dominant for deep space missions with large distances from the Sun. This results from the fact that SRP decreases with the inverse square of the distance to the Sun while TRP is scaled by the spacecraft surface temperatures which merely depend on the waste heat produced by the satellite hardware. An overview of the regions where TRP or SRP dominate and typical spacecraft missions operating in those regions is given in figure 1.1.

1.2 Motivation

In order to satisfy the need for the required modelling accuracy of non-gravitational perturbations, in particular SRP and TRP, new techniques allowing for an improved modelling accuracy have to be developed. The largest error sorces in existing models

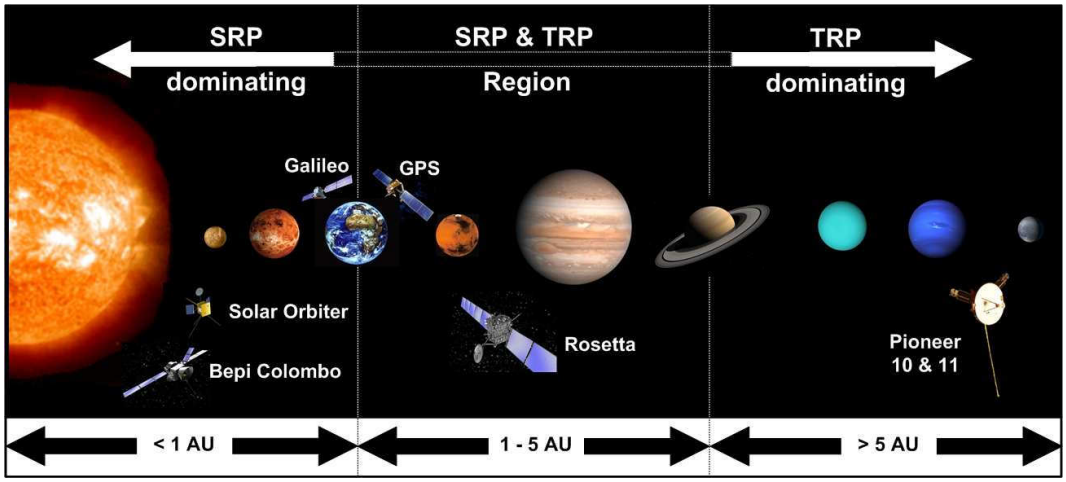

Figure 1.1: SRP and TRP regions within the solar system.

are the low level of precision of the geometrical model of the spacecraft used in the analysis and the treatment of radiation interaction between different parts of the model. The directions of reflection of incident sunlight as well as secondary reflections and radiation interchange between different satellite components are influencing the resulting magnitude of SRP and TRP as well as the direction of the resulting forces and accelerations. Therefore the resulting SRP/TRP magnitudes and directions may be erroneous if radiative heat transfer is not accounted for in the analysis. In order to develop high precision models for the assessment and evaluation of SRP and TRP the currently achievable level of accuracy of the geometric modeling has to be improved considerably.

The shortcomings of current modelling methods can be visualised by simple test case geometries. If numerical models are used, the radiation exchange between different parts of the satellite and multiple reflections are mostly disregarded. A commonly used model is the so called cannonball model [8], where the whole satellite is treated as a spherical black body. As displayed in figure 1.2 left this may lead to significant errors in the computed resulting force. Directions and magnitudes of the radiation fluxes of different components may vary and depend on the visibility of other parts of the spacecraft as well as on the optical surface parameters. Here the amount of exchange of radiation is determined by radiation view factors which have to be computed precisely for each model surface. In case of the SRP, for oblique Sun directions components may shadow other components which results in a modified magnitude of the perturbation. As seen in figure 1.2, the resulting modelling errors can be significant if shadowing is not accounted for.

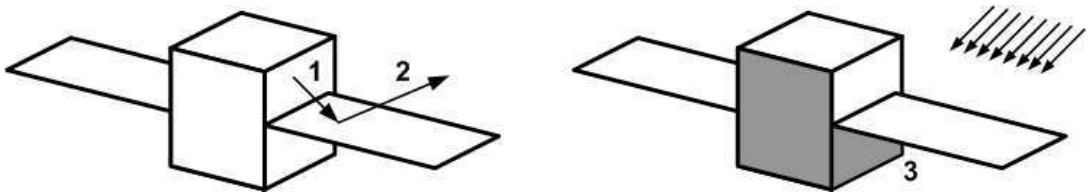

Figure 1.2: Absorption (1), reflection (2) and shadowing (3) of emitted and received radiation.

Analytical models are limited in the achievable level of geometric detail even if radiation exchange is implemented and the modelling of shadowing is a difficult task often only possible for specific attitudes and geometric configurations of the spacecraft. Therefore new improved numeric modelling methods have to be developed which enable the inclusion of the detailed spacecraft geometry into the perturbation analysis and account for radiation interchange as well as shadowing.

The realisation of such methods enables the high precision analysis of yet unresolved thermal perturbation problems. One example is the analysis of thermal recoil forces acting on the deep space probe Pioneer 10. For this spacecraft (and its twin craft Pioneer 11) a constant, still unexplained residual deceleration has been observed. Due to the small magnitude of this so called Pioneer anomaly (PA) of $8.74 \cdot 10^{-10}\,\mathrm{m/s^2}$ [9] a thorough modelling of all perturbation effects is crucial to be able to resolve the origin of the effect [9].

Many theories on the origin of the effect have been tested but up to now none has delivered an unambiguous explanation of the observed anomaly. Among other effects, the influence of the cosmological expansion of the universe on the trajectory and Doppler signal has been ruled out as a conventional physics explanation for the PA. Here it was found that the influence of the cosmological dynamics on Doppler tracking or the trajectory of planets as well as spacecraft is much smaller than any achievable measurement accuracy [10, 11]. The MOND (modified Newtonian Dynamics) theory postulated by Milgrom [12], as well as relativistic effects on the on-board clocks [13] have been considered to find an explanation for the PA. Alternative physics approaches such as antisymmetric metrics [14, 15], gravitational theories in higher dimensions [16] or modified inertia [17] have been considered as well. Although some of these theories can model the constant PA, some of the resulting modifications on larger scales are in contradiction to other observations (such as the trajectory of planets or galaxies). As a result of this, none of these proposed new theories were able to provide a convincing solution to the PA. Beneath the theoretical explanations conventional effects have as well been investigated as possible causes of the PA [18, 19]. In particular thermal effects are supposed to cause at least a considerable part of the anomaly. Estimations show that only a small fraction of asymmetry in the emission pattern could lead to an effect of the magnitude of the PA [20]. This fact demands an accurate thermal modelling and a precise determination of the resulting TRP. The results of this study will show whether such an asymmetry in the radiation pattern exists and quantify the fraction of thermal recoil in the currently unexplained residual effect.

Another, more recent example is the analysis of TRP and SRP acting on the ESA

Rosetta spacecraft [21]. Here the motivation is twofold. Firstly the current thermal perturbation models used for orbit determination by ESA/ESOC have shown an up to 10 % unexplained residual acceleration on the spacecraft. The resulting discrepancy of the observed and the modelled spacecraft orbit dictates a more detailed analysis of the thermal effects in general. Secondly the Rosetta spacecraft has, among others, shown an anomalous velocity jump during its first gravity assist manoeuvre which has become known as the flyby anomaly [22, 23]. Similar to the case of the PA, the analysis of this flyby anomaly demands a precise knowledge of conventional disturbance effects such as TRP and SRP to clarify the influence of these effects on the flyby trajectory what may lead to a better understanding of the spacecraft behaviour.

Thus the development and realisation of advanced modelling techniques will lead to a better understanding of yet unexplained observations and can support the design and planning of future space missions considerably. Only by a precise modelling of the disturbances acting on a spacecraft, the mission and data analysis can be performed at the level of precision required by modern scientific space missions.

1.3 Thesis objectives

The main goal of this thesis is the development and the validation of generic numerical modelling methods for the high precision analysis of SRP and TRP acting on spacecraft with complex shape. The methods will allow for the inclusion of the detailed spacecraft geometry, the high precision implementation of radiation exchange, the treatment of multiple reflections including different reflection models as well as the inclusion of orbit parameters and telemetry data.

The elaborated numerical TRP modelling method will be utilised for the analysis of the magnitude of thermal recoil pressure acting on the deep space probe Pioneer 10. For this the evolution of the TRP will be evaluated for the 30 years of mission time from 1972 to 2002, where the last telemetry data of Pioneer has been received. An accurate TRP analysis implies the development of a detailed Finite Element (FE) model of the Pioneer 10 spacecraft as well as a thorough thermal FE analysis with respect to the different thermal boundary conditions during the course of the mission. Furthermore the influence of varying parameters on the resulting thermal recoil will be subject of a detailed investigation. Due to the long exposure of the spacecraft to the harsh conditions within the space environment, in particular the optical properties of the exterior surfaces and the thermal properties of the thermal insulation may have degraded considerably, possibly leading to a significant influence on the resulting magnitude of the perturbation. By means of parameter analyses the sensitivity of TRP to those parameters as well as the probability of the degradation of the surfaces will be discussed. Based on the results of this analysis realistic parameter sets which lead to a TRP in the magnitude of the PA will be subject of a closer investigation. The results of the thermal analysis and the TRP computations will then be evaluated with respect to the PA.

Based on the general approach developed for the modelling of TRP, a corresponding numerical method for the modelling and the analysis of SRP acting on spacecraft

surfaces will be introduced and discussed. Both models will be utilised for the analysis of the influence of SRP and TRP on the observed trajectory of ESA's current deep space mission Rosetta. For this a detailed thermal FE analysis will be conducted for Rosetta. Based on the results of the FE analysis, TRP and SRP can be computed for different boundaries and attitudes of the spacecraft. Here chosen heliocentric cruise phases will be selected for evaluation which are suitable for a high precision calculation of non-gravitational disturbance effects. For the cruise phases SRP and TRP results will be compared to the ESA observations and improvements with respect to the currently used models will be discussed. Furthermore SRP and TRP will be analysed in proximity of Earth for the trajectory of the first Earth flyby of Rosetta. The results will be compared to the observed flyby anomaly.

1.4 Thesis outline

Chapter one gives an introduction to the topic of non-gravitational perturbation modelling and discusses the importance of precise SRP and TRP modelling for the improvement of current orbit perturbation modelling accuracy. The motivation for an improvement in modelling accuracy and the need for new modelling methods is discussed and the thesis objectives are stated. The Pioneer 10 mission and the Rosetta mission are introduced as test cases for the numerical SRP/TRP analysis methods worked out in this thesis.

Chapter two reviews the state of the art of thermal perturbation modelling. Earlier works in the field of SRP and TRP modelling are presented and the approaches are discussed with respect to the implemented level of accuracy. Previous thermal analysis of the Pioneer 10 and the Rosetta spacecraft are outlined and discussed with respect to the Pioneer and flyby anomalies.

Chapter three introduces the numerical approach for the modelling of TRP on complex spacecraft geometries. An analytical model for TRP acting on a single flat plate is developed and expanded to a numerical approach for complex spacecraft shapes. The basic equations for radiation exchange and the resulting recoil forces are stated. The procedure for TRP analysis consisting of a full thermal FE analysis of the spacecraft, the determination of the equilibrium surface temperatures and the computation of the resulting TRP by means of the analytical models are discussed in detail. Here an overview on the FE modelling approach with an FE macro language is given. Details on the implementation of the method such as the treatment of radiation view factors as well as the ray tracing approach implemented to detect radiation exchange between different surfaces in the model are given. Performance considerations for the utilised algorithms are discussed. The principles of the method as well as the computation accuracy are evaluated by a set of test cases based on simply geometries and the subsequent comparison to analytical results.

Chapter four introduces the Pioneer 10 mission design, discusses the geometrical features of the spacecraft and gives a general overview on the topic of the Pioneer anomaly. The motivation for a thermal investigation of the Pioneer 10 spacecraft with respect to the Pioneer anomaly is outlined in detail.

Chapter five describes the macro approach taken for the FE modelling of the Pioneer 10 spacecraft and discusses the individually implemented component models such as the radio isotopic thermal generators (RTG), the high gain antenna (HGA) and the spacecraft compartment. An overview on the FE macro interfaces is given and the material models, the applied boundaries and loads are reviewed in detail. The basics for the treatment of multi layer insulation (MLI) in a thermal 3D FE analysis are worked out and verified by a simplified test case.

Chapter six treats the analysis of TRP acting on the Pioneer 10 spacecraft ranging from 1972 to 2002. The critical parameters for the magnitude of the thermal recoil are identified and a parameter analysis is conducted to reveal the sensitivity of the solution to these parameters. A realistic parameter set which fits the observed anomalous acceleration effect is discussed. With this the observed unexplained residual acceleration acting on the craft can completely be reconstructed as a combined effect of the SRP and the TRP.

Chapter seven introduces a numerical approach for the modelling of SRP which is based on the developed TRP model. Here the Sun is modelled as a pixel array which interacts with the FE spacecraft model. The analytical basics and the numerical implementation are discussed in detail.

Chapter eight gives an overview of the Rosetta mission and describes the main geometrical features of the craft. Background information on the flyby anomaly as well as the motivation for an investigation of thermal perturbations acting on the Rosetta spacecraft are given.

Chapter nine describes the FE model of the Rosetta spacecraft, discusses the approach taken for the evaluation of SRP and TRP for different times in the mission and presents the models for environmental and internal boundaries/loads as well as material models.

Chapter ten discusses the evaluation of TRP and SRP acting on the Rosetta spacecraft for chosen heliocentric cruise phases. The results are compared to the ESA/ESOC observations. Results of thermal FE analysis of the craft are discussed. Furthermore, TRP and SRP are evaluated for the first Rosetta Earth flyby. The results show that SRP and TRP can not explain the observed velocity jumps.

Chapter eleven summarises the work performed in this thesis and highlights the main scientific results. An outlook for further works within the scope of the thesis topic is given and applications for the developed methods are discussed.

Chapter 2

State of the art

In this section the previous works in the field of thermal perturbation modelling for space missions are reviewed with respect to the work performed in this thesis. The Pioneer anomaly and investigations of possible thermal sources of the effect are reviewed and the importance of accurate thermal modelling for all these approaches is outlined. Furthermore thermal investigations performed for the Rosetta mission are discussed and the need for higher accuracy in thermal modelling of Rosetta, in particular for flyby trajectories is stated.

2.1 Modelling of thermal forces

The first investigations of thermal forces acting on satellite trajectories were triggered by the observation of the Yarkovsky-Effect [24, 25, 26] as an anomalous spin rate of asteroids resulting from anisotropic thermal radiation properties of the body surfaces and the high temperature gradients between the night and day sides. In the late 1980s this idea was expanded to by that time unexplainable observed drag effects in decommissioned telecommunication satellites. The significance of the modelling of these thermal recoil forces for satellites was first demonstrated by Rubincam et al. [27] in 1987 within the scope of the LAGEOS mission. Rubincam showed that the recoil forces resulting from absorbed Earth infrared radiation are big enough to perturb satellite motion considerably [28]. Slabinski et al. [29] expanded this idea in 1988 to the analysis of reaction forces resulting from the emission of energy by spacecraft surfaces. Another approach was taken by Cook et al. [30] in 1989 who approximated the spacecraft structure as a simple box-and-wing model which enabled the estimation of thermal perturbations acting on the spacecraft with inclusion of geometrical features in the analysis. One year later, in 1990, the influence of thermal thrust on node and inclination was investigated for the LAGEOS orbits by Farinella et al. [31, 32]. The importance of an accurate determination of non-gravitational forces was also stated by Klinkrad et al. who proposed the use of Monte-Carlo raytracing codes for satellite skin force analysis for the first time [33]. In 1992 Fliegel et al. [34] introduced the treatment of spacecraft surfaces as a set of sub surfaces thus enabling a higher level of geometrical detail.

The next improvement in modelling detail was realised by Vigue et al. in 1994 [35, 36] who first proposed to utilise FE techniques for the estimation of thermal perturbations. Their analysis aimed at the determination of the solar panel surface

temperatures of the GPS Block IIa satellites using solar panel geometry, material parameters and solar illumination as inputs for the calculation. Here it was argued that for the GPS satellites the solar panel surface area is large compared to the bus area. Because of this the resulting thermal force has to be dominated by the solar panels (which are always facing the sun) and the influence of the bus area is negligible. Thus the FE model could be held simple and a one-dimensional FE approach with regard to the different panel layer properties delivers a suitable heat distribution for the force calculation. Using orbit determination codes the accumulating effects of thermal perturbations were investigated and their findings showed that thermal recoils possessed a significant influence on the spacecraft orbit. A more analytical approach was taken by Sengoku et al. in 1995 [37] where models for absorption, specular and diffuse reflection of solar radiation were specified to estimate solar radiation pressure for the Ajisai satellite. Vokrouhlicky and Metris analysed Earth Albedo and Earth infrared influence on LAGEOS-type satellites in 1996 [38]. They came to the conclusion that both effects can significantly affect spacecraft orbits and have to be included in disturbance budgets. Here an analytical approach was taken which simplified Albedo models and heat conduction between the different spacecraft components.

In 2001 Duha et al. [39] presented a unified model for thermal forces resulting from sun and earth heating simultaneously for the LAGEOS satellite I. They concluded that the observed residuals acting on in the LAGEOS orbit can be explained and predicted with their thermal model. In the same scope the so called "cannonball" model was presented by Lucchesi [8] which approximated the shape of LAGEOS as a sphere for SRP analysis. Following the approach of Vigue, Ziebart et al. [40] developed a more complex modelling approach in 2001 for the assessment of solar radiation pressure in case of the GLONASS constellation. Here the solar radiation was implemented by means of a pixel array where each pixel interacts with the spacecraft body. Furthermore models for different reflection effects were included. The interaction between different spacecraft surfaces (secondary reflection) was accounted for and the spacecraft has been modelled by a set of primitive geometries (boxes, cylinders etc.). Improvements and a generalisation of the method have been presented by Ziebart in 2004 [41] and Adhia in 2005 [42]. The methods have been verified and tested by on-orbit tests [43]. However, TRP investigations were not discussed in their approaches. Recently, in the beginning of 2011, an analytical model for the assessment of SRP has been published by McMahon [44]. Here SRP is modelled by a Fourier series where a new set of coefficients has to be determined for each discrete sun direction. Due to the analytical approach the implementation of complex spacecraft geometries is somehow limited and multiple reflections are not treated.

2.2 Pioneer anomaly investigations

The PA was discovered in 1998 by the Jet Propulsion Laboratory (JPL) as a Doppler velocity shift corresponding to a constant residual acceleration of $8.74 \cdot 10^{-10}\mathrm{m/s}^2$ [9] acting on the deep space probes Pioneer 10 and 11. Remarkably both missions showed the same residual effect although their trajectory points to roughly opposite directions of the solar system plane. Since its first detection the existence of the anomaly has

been confirmed by a number of independent international teams [45, 46, 47, 48]. Besides numerous theories which suspect a not yet understood new physical cause the analysis of conventional effects has been a major focus of PA investigations. After first assessments of thermal forces acting on the Pioneer probes the JPL argued that the effective thrust should be small and that, instead of the observed constant deceleration the effect should decrease due to the radioactive decay of the RTG fuel if a thermal effect would dominate. Thus thermal effects were first ruled out as a possible explanation of the effect.

In contradiction to the JPL findings, Murphy [49] and Katz [50] already argued in 1999 that at least a fraction of the anomaly might be credited to thermal effects. Markwardt stated in his independent analysis of the Pioneer 10 Doppler data in 2002 that the acceleration is reasonably constant over the evaluation time of 7.5 years but not constant enough to rule out that it might not be connected to the radioactive decay of Plutonium on board the spacecraft [45]. Later in 2003 Scheffer supported this argument [51] with a new approach. He stated that a significant effect is possible due to the high emissive properties of the MLI and the geometry of the craft using a simple estimation method. A review of possible causes of the effect by Turyshev et al. stated in 2005 that an anisotropy of 60 W (out of a total of 2600 W at BOL) could lead to a disturbance in the observed magnitude [52]. This triggered the idea of a thermal source of the effects and several investigations since [53, 54, 55]. Furthermore the fact that the effect has shown up for both Pioneer 10 and 11 points out that the effect may be connected to the spacecraft themselves rather than the orbit. This idea is backed by the fact that the geometry of the probes is nearly identical but the orbit is different.

Olsen supported the idea of a thermal explanation and showed in 2006 that the evaluated Pioneer Doppler data set is not suitable to distinguish between a constant acceleration model and and an acceleration proportional to the radioactive decay of the RTG plutonium [46]. With this he debilitated the argument of Anderson et al. that an exponential decay should be visible in the acceleration if it would be caused by thermal effects. In 2008 Bertolami [56] showed that a thermal acceleration in the region of a third of the PA can be explained with an analytic model where the satellite surfaces are merely considered as radiation point sources. Later in 2009 Turyshev stated that a thorough investigation of the effect is only possible with sophisticated FE-models and numerical approaches [57, 58]. Despite all these efforts no final answer on the magnitude of thermal effects for Pioneer 10/11 has been presented up to now. Therefore the work performed in this thesis focuses on the accurate numerical modelling and determination of TRP acting on the Pioneer 10 spacecraft.

2.3 Rosetta thermal research and flyby anomaly analysis

Thermal investigations of the Rosetta spacecraft have been triggered by the shortcomings of current orbit determination tools and the occurrence of the so called flyby anomaly, an unexplained velocity jump during a flyby manoeuvre which has, among other missions, been observed for the first Rosetta flyby [22, 59]. Beneath numerical errors and unmodeled effects in the implemented gravity models, un- or mismodeled

surface forces are suspected to be the cause the effect. During development and mission design phase of Rosetta extensive thermal analysis and testing has been performed. In addition to these efforts approaches for the modelling of the thermal environment during the asteroid flybys have been developed to analyse the implications of the thermal environment on the science data [60]. However, the existing thermal investigations have not been expanded to the analysis of TRP which is directly connected to the thermal environment and the heat distribution inside the craft.

As a result of the detection of the flyby anomaly for a couple of different flybys, the flyby collaboration, an international team of scientists focusing on the determination of the cause of the flyby anomaly has been founded in 2008. During the first meeting of the flyby collaboration it was reported that the uncertainty of current ESA SRP models for Rosetta has been measured to be up to 10 %. Van der Ha et al. [61] presented an analytical approach for the calculation of SRP and TRP for the Rosetta flyby and concluded that SRP and TRP can not be the cause of the flyby anomaly in case of Rosetta. Here the computed forces were decelerating the spacecraft during flyby while the anomaly was observed as an increase of velocity. However the TRP was found to be approximately 10% of the computed SRP magnitude which pointed out that the errors in current ESA SRP models may be caused by an unmodeled TRP.

Motivated by this coincidence new analytical models for the evaluation of TRP and SRP have been developed [61] and tested. A complete analytical model for SRP and TRP as well as a thorough thermal analysis have been delivered and are currently under evaluation [62]. However, the influence of the high gain antenna, the radiative coupling of the surfaces and the outer structure have not been included in thermal analyses up to now and demands the development of new numerical methods which can be used as verification cases for the analytical models. This motivates the detailed numerical thermal analysis of the Rosetta spacecraft performed in this study.

Chapter 3

Thermal Recoil Pressure model

This chapter introduces an analytical model for the determination of a thermal recoil force acting on a single emitting flat two-dimensional surface. This model is the basis for the numerical computation of TRP on complex spacecraft geometries. The numerical approach which consists of a thermal FE analysis and a subsequent numerical TRP computation using a ray tracing approach is outlined in detail. The assessment of radiation interaction by means of ray tracing methods is highlighted. As verification of the method the results of chosen test cases are compared to analytical solutions. Performance and FE modelling considerations are discussed.

3.1 Introduction to TRP modelling

Any object in space which emits radiation is subject to a momentum change if the emission characteristic differs from an ideal spherical-symmetric pattern. Thus a body with a spherical shape and homogeneous surface temperatures will not experience any TRP while a body with heat gradients or a non-symmetric shape will generate a resulting TRP.

For the analysis of the TRP for a complex spacecraft structure, the surface has to be divided into a subset of flat quadrilateral surface elements, for which the resulting TRP can be computed individually by means of analytical models. Here the element resolution has to be high enough to realise a good resemblance of model and real surface shape. By allowing radiation interaction between the individual model surfaces and cumulating the individual TRP results, the total spacecraft TRP can be computed accurately depending on the quality of the surface grid. Due to the fact that TRP is governed by the spacecraft surface temperatures a steady state temperature map of the craft is needed for the TRP computation. For this the FE method provides a suitable tool to acquire the needed information based on the spacecraft geometry, the material properties and the environmental and boundary conditions. A thermal FE analysis can be used to compute different thermal surface maps for different times during a spacecraft mission which are subject to e.g. different illumination conditions or different component heat loads. As the FE model is already set up in a grid structure, the outer FE surface geometry and the respective temperature solutions can directly be used for the subsequent TRP calculation if FEs with hexagonal shapes are used for the generation of the mesh.

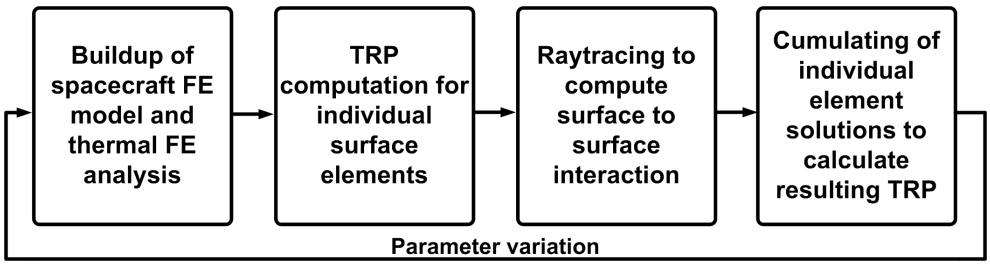

Figure 3.1: TRP computing method overview.

Figure 3.1 shows the principle processing scheme for a complete TRP analysis. In a first step a thermal FE model of the spacecraft has to be generated based on geometrical and optical parameter information. By specifying boundary conditions, loads and mesh parameters for the spacecraft state at the simulated time, an FE-solver can be used to compute the steady-state temperature solution. The results are exported and the geometrical, material and temperature data is used to compute TRP on each model surface with individual models for emission, absorption and reflection. Surface interaction (absorption of radiation by other model surfaces and multiple reflections) is accounted for by means of a ray tracing approach. The resulting individual forces directly lead to the resulting TRP for the whole craft. By means of a loop the analysis parameters can be adjusted to a new spacecraft state and the computation is repeated for a new set of boundaries. Thus TRP can be evaluated in discrete step on a complete spacecraft orbit. Details on the approaches for the generation of the FE model, the analytical TRP models and the implementation of the numerical TRP computation are given in the following subsections.

3.2 Analytical model for TRP

TRP results from a directed non-symmetric emission of energy. A suitable model for this effect is the emission of photons by a flat two-dimensional plate with surface area dA. The well known dispersion relation:

$$E = \sqrt{(m_0\, c^2)^2 + (|\vec{p}_{\mathrm{Ph}}|\, c)^2}\,, \tag{3.1}$$

yields the relation $E_{\mathrm{Ph}} = |\vec{p}_{\mathrm{Ph}}|\, c$ for photons with a zero photon rest mass ($m_0 = 0$) [63]. Here E_{Ph} is the energy carried by the photon, $|\vec{p}_{\mathrm{Ph}}|$ is the photon momentum and c is the speed of light. Using the photon model derived by Einstein, the frequency of the photon ν_{Ph} is proportional to the photons energy:

$$E_{\mathrm{Ph}} = h\, \nu_{\mathrm{Ph}}\,, \tag{3.2}$$

where h is Planck's number. Thus the photon momentum can be expressed in terms of frequency as:

$$|\vec{p}_{\mathrm{Ph}}| = \frac{h\, \nu_{\mathrm{Ph}}}{c} = \frac{h}{\lambda}\,, \tag{3.3}$$

where λ is the wavelength, at which the photon is emitted. Figure 3.2 shows the resulting change of momentum for an emission of photons (A) and an absorption of photons (B).

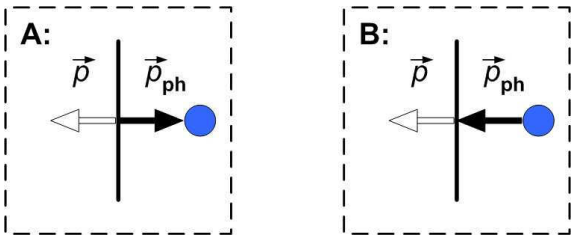

Figure 3.2: Photon and interacting surface momentum for photon emission (A) and photon absorption (B).

For photon emission the effective momentum acting on the emitting source $\vec{p}$ opposes the direction of the emitted photons momentum. In a closed system this follows directly from the postulation of the conservation of momentum. Thus the momentum of the emitted photon corresponds to the momentum loss of the emitter ($\vec{p}_{\mathrm{Ph}} + \vec{p} = 0$). In case of absorption, which will later be needed for the development of a SRP model, the directions of the photon momentum and the resulting momentum acting on the absorber are aligned. If N Photons are emitted within the time dt this leads to a source momentum derivative of:

$$\frac{d|\vec{p}|}{dt} = \frac{h\,\nu_{\mathrm{Ph}}\,dN}{c\,dt}\,, \tag{3.4}$$

which is equivalent to the force acting on the emittor directed against the moving direction of the photons. Note that $P_{\mathrm{e}} = \frac{h\,\nu\,dN}{dt}$ is the total power carried by the emitted photons. Thus the resulting force acting on the emitter can be expressed as:

$$|\vec{F}_{\mathrm{TRP}}| = \frac{d|\vec{p}|}{dt} = \frac{P_{\mathrm{e}}}{c}\,. \tag{3.5}$$

Equation (3.5) is also valid for the absorption of photons. Here the resulting momentum gained by the absorbing surface is aligned with the moving direction of the impacting photons. In case of emission this resulting force acting on the emittor is called *Thermal Recoil Force*. If the source of emission posesses a mass m, a corresponding thermal recoil pressure P_{TRP} can be defined as:

$$P_{\mathrm{TRP}} = \frac{|\vec{F}_{\mathrm{TRP}}|}{m} = \frac{P_{\mathrm{e}}}{m\,c}\,. \tag{3.6}$$

Note that for this definition the TRP obtains the unit $\mathrm{m/s^2}$ which differs from the typical definition of a pressure in units of $\mathrm{N/m^2}$. This results from the fact that it is sensible to specify orbit perturbations as specific values with respect to spaceraft dimensions. If needed, the TRP can be translated into pressure units by multiplication by the ratio of spacecraft surface area to spacecraft mass. For a complete description of P_{TRP}, the magnitude of the emitted power has to be determined. Assuming a flat, two-dimensional grey radiating surface of area A, the energy flux emitted with the emissivity ε_λ for a specific wavelength λ can be expressed in terms of the spectral radiance L_λ as [64]:

$$L_\lambda = \varepsilon_\lambda \cdot \frac{2\,h\,c^2}{\lambda^5}\,\frac{1}{e^{\frac{h\,c}{k\,\lambda\,T}} - 1}\,, \tag{3.7}$$

where h is Planck's number, c is the speed of light, k is the Boltzmann constant and T is the homogeneous surface temperature. Integration over all wavelengths of the spectrum leads to the radiance L:

$$L = \int_0^\infty L_\lambda \, d\lambda = \varepsilon \frac{\sigma}{\pi} T^4 \quad \text{with} \quad \sigma = \frac{2\,\pi^4\,k^4}{15\,h^3 c^3}\,, \tag{3.8}$$

which can be interpreted as an energy density emitted by the radiating surface. Here ε is the effective emissivity value for the respective wavelength band. The fraction of energy emitted in the direction of the elevation angle θ is defined as the intensity of radiation I and can be described with Lambert's cosine law, assuming the radiation pattern to be hemispheric:

$$I = L\,A\,\cos\theta\,. \tag{3.9}$$

By rewriting equation (3.9), the radiation intensity in a given direction specified by the elevation angle θ can be related to the intensity emitted in normal direction I_n:

$$I = I_\mathrm{n}\,\cos\theta\,. \tag{3.10}$$

The directions of emission can be characterised by discrete solid angle surface elements forming a virtual unit hemisphere above the emitting surface. These fractions of the surface of the unit hemisphere are determined by the azimuth angle ϕ and the elevation angle θ with $0 \leq \phi < 2\pi$ and $0 \leq \theta < \pi/2$. Figure 3.3 shows the definition of the solid angle elements $\mathrm{d}\Omega$ for an emitting differential surface dA with normal direction $\vec{n}$.

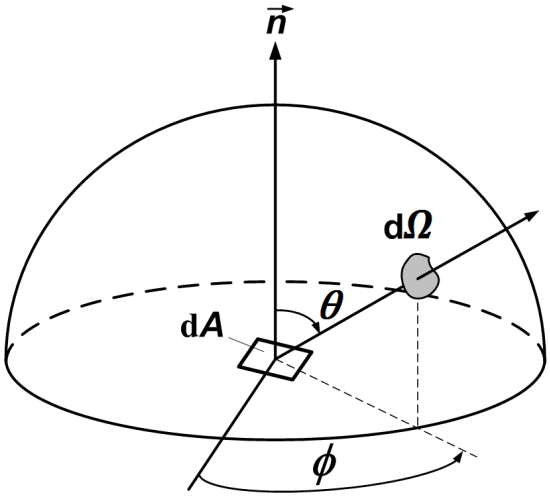

Figure 3.3: Definition of the solid angle element $d\Omega$, [64].

The total energy flux E_A emitted by dA can now be calculated by integrating the energy fluxes received by each solid angle element surface over the complete hemispherical surface:

$$E_A = \int_\Omega L\,\cos\theta\,d\Omega\,. \tag{3.11}$$

Here the solid angles can be expressed as $d\Omega = \sin\theta\,d\theta\,d\phi$, giving:

$$E_A(\phi,\theta) = \int_{\phi_1}^{\phi_2}\int_{\theta_1}^{\theta_2} L\cos\theta\,\sin\theta\;d\theta\,d\phi\,. \tag{3.12}$$

For $\phi_1 = \theta_1 = 0$, $\phi_2 = 2\pi$ and $\theta_2 = \frac{\pi}{2}$ the total energy flux P_{tot} received by the hemispherical surface evolves to

$$\begin{aligned} P_{\text{tot}} &= \int_A E_A \, dA \\ &= \int_A \int_0^{2\pi} \int_0^{\frac{\pi}{2}} \frac{\varepsilon \, \sigma \, T^4}{\pi} \cos\theta \, \sin\theta \, d\theta \, d\phi \, dA \\ &= \varepsilon \, A \, \sigma \, T^4 \,, \end{aligned} \tag{3.13}$$

which is the well known Stefan Boltzmann law for radiating grey bodies. Using equation (3.8) and equation (3.10) and the relation $P_{\text{tot}} = P_{\text{e}}$, the total emitted power P_{e} can be formulated in terms of the intensity as:

$$P_{\text{e}} = I_{\text{n}} \, \pi \,. \tag{3.14}$$

With equations (3.2) - (3.5) the the energy flux dE received by a specific solid angle element:

$$dE = L \cos\theta \, \sin\theta \; d\theta \, d\phi \, dA \,, \tag{3.15}$$

can be rewritten as a solid angle specific thermal recoil force:

$$|\vec{F}_{\text{TRP},\Omega}| = \frac{1}{c} \, dE \,, \tag{3.16}$$

for each $d\Omega$ [63]. Due to the symmetric character of the hemisphere only force components normal to the emitting surface plane will contribute to a resulting recoil. This introduces an additional $\cos\theta$ term into the force integral. As a result of the vanishing of all parallel components, the direction of the resulting force can be determined by the normal vector of the emitting surface $\vec{n}$, where $|\vec{n}| = 1$. Thus the effective thermal recoil force component resulting from emission into a specific solid angle element evolves to:

$$\vec{F}_{\text{TRP},\Omega,eff} = -\vec{n} \, \frac{1}{c} \, L \, \cos^2\theta \, \sin\theta \; d\theta \, d\phi \, dA \,, \tag{3.17}$$

where the negative sign is demanded by the balance of energy between emitted photons and emitter. Integration over the hemispheric surface with $\phi = 2\pi$ and $\theta = \frac{\pi}{2}$ leads to the total (effective) thermal recoil force $\vec{F}_{\text{TRP}}$ with:

$$\vec{F}_{\text{TRP}} = -\vec{n} \, \frac{2}{3\,c} \pi \, L \, A = -\vec{n} \, \frac{2}{3\,c} \pi \, \varepsilon \, \frac{\sigma}{\pi} \, A \, T^4 = -\vec{n} \frac{2}{3\,c} \, P_{\text{tot}} \,. \tag{3.18}$$

With this the power fraction contributing to a resulting force in normal direction of an emitting surface evolves to a ratio of $\frac{2}{3}$ of the total emitted power and the TRP can be characterised by:

$$\vec{P}_{\text{TRP}} = -\vec{n} \frac{2}{3} \frac{P_{\text{tot}}}{m \, c} \,. \tag{3.19}$$

3.3 Radiation-surface interaction

Incident radiation may interact with non-transmissive target surfaces in three distinguishable ways. The incoming radiation can A) be completely or partially absorbed, B) specularly reflected and C) diffusely reflected by the target surface $\mathrm{d}A$. Here the sum of the dimensionless coefficients of absorption α, specular reflection γ_s and diffuse reflection γ_d has to obey the relation $\alpha + \gamma_\mathrm{s} + \gamma_\mathrm{d} = 1$. In most cases the interaction is a mixture of all three effects. Figure 3.4 illustrates the physics of each interaction and the resulting differential radiation forces acting on the target surface [65].

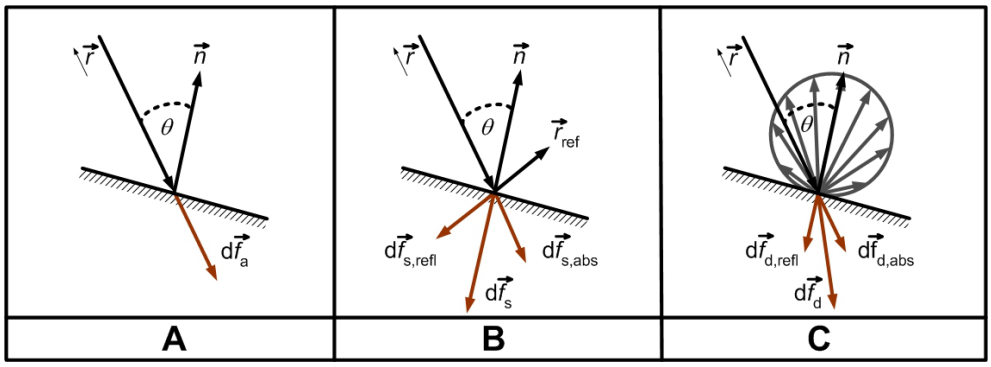

Figure 3.4: A: Absorption, B: Specular reflection, C: Diffuse Reflection.

The differential force $\mathrm{d}\,\vec{f}_\mathrm{a}$ resulting from absorption of radiation flux P_inc coming from the direction $\vec{r}$ depends on the angle of incidence θ and the coefficient of absorption α:

$$\mathrm{d}\vec{f}_\mathrm{a} = -\frac{P_\mathrm{inc}}{c}\alpha\cos\theta\,\vec{r}\,\mathrm{d}A\,. \tag{3.20}$$

The differential force resulting from specular reflection $\mathrm{d}\vec{f}_\mathrm{s}$ can be computed from the sum of the force caused by non-absorbed incoming radiation flux accounted to specular reflection $\mathrm{d}\vec{f}_\mathrm{s,abs}$ and force caused by the fraction of specularly reflected radiation $\mathrm{d}\vec{f}_\mathrm{s,refl}$:

$$\begin{aligned}\mathrm{d}\vec{f}_\mathrm{s} &= \mathrm{d}\vec{f}_\mathrm{s,abs} + \mathrm{d}\vec{f}_\mathrm{s,refl}\\ &= -\tfrac{P}{c}\gamma_\mathrm{s}\cos\theta\,\vec{r}\,\mathrm{d}A - \tfrac{P_\mathrm{inc}}{c}\gamma_\mathrm{s}\cos\theta\,(-\vec{r} + 2\,\vec{n}\,\cos\theta)\,\mathrm{d}A\\ &= -2\,\tfrac{P_\mathrm{inc}}{c}\gamma_\mathrm{s}(\cos\theta)^2\,\vec{n}\,\mathrm{d}A\,.\end{aligned} \tag{3.21}$$

Likewise the differential force resulting from the fraction of diffusely reflected radiation $\mathrm{d}\vec{f}_\mathrm{d}$ can be computed from the force caused by the sum of non-absorbed incoming radiation flux accounted to diffuse reflection $\mathrm{d}\vec{f}_\mathrm{d,abs}$ and the force caused by the fraction of diffusely reflected radiation $\mathrm{d}\vec{f}_\mathrm{d,refl}$:

$$\begin{aligned}\mathrm{d}\vec{f}_\mathrm{d} &= \mathrm{d}\vec{f}_\mathrm{d,abs} + \mathrm{d}\vec{f}_\mathrm{d,refl}\\ &= -\tfrac{P_\mathrm{inc}}{c}\gamma_\mathrm{d}\cos\theta\,\vec{r}\,\mathrm{d}A - \tfrac{2}{3}\tfrac{P_\mathrm{inc}}{c}\gamma_\mathrm{d}\cos\theta\,\vec{n}\,\mathrm{d}A\\ &= -\tfrac{P_\mathrm{inc}}{c}\gamma_\mathrm{d}\cos\theta\,(\vec{r} + \tfrac{2}{3}\,\vec{n})\,\mathrm{d}A\,.\end{aligned} \tag{3.22}$$

The resulting normal direction of the effective differential force resulting from diffusely reflected radiation is equivalent to equation (3.18). The total resulting differential force can now be computed by the sum of equations (3.20), (3.21) and (3.22):

$$\begin{aligned}\mathrm{d}\vec{f}_\mathrm{res} &= \mathrm{d}\vec{f}_\mathrm{a} + \mathrm{d}\vec{f}_\mathrm{s} + \mathrm{d}\vec{f}_\mathrm{d}\\ &= -\tfrac{P_\mathrm{inc}}{c}\left[(1-\gamma_\mathrm{s})\,\vec{r} + 2\,(\gamma_\mathrm{s}\cos\theta + \tfrac{1}{3}\gamma_\mathrm{d})\,\vec{n}\right]\cos\theta\,\mathrm{d}A\,.\end{aligned} \tag{3.23}$$

3.4 Implementation

As displayed in figure 3.5, a complete TRP analysis consists of a thermal FE analysis and a subsequent numerical TRP computation based on the FE results.

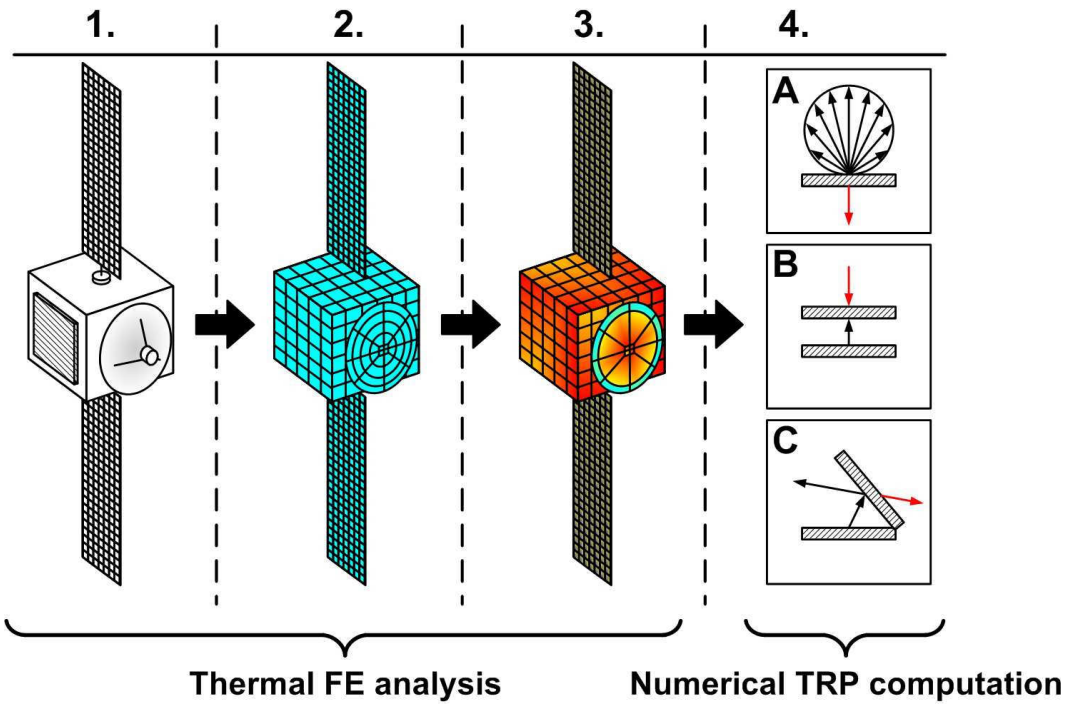

Figure 3.5: Assessment of TRP for complex model geometries. 1: Real spacecraft geometry, 2: Idealised FE model, 3: Equilibrium surface temperatures, 4A: Computation of TRP free emission components, 4B: Computation of TRP absorption components, 4C: Computation of TRP reflection components.

For a complex spacecraft geometry the surface elements do not only radiate freely into space but may also exchange radiation with other elements in the model thus causing absorption and multiple reflection effects. This has a direct influence on the magnitude and direction of the resulting TRP. In order to compute the amount of radiation which is absorbed or reflected it is necessary to check if receiving elements are visible or shadowed with respect to the emitting elements. In addition the reflected radiation may cause further reflections on other surfaces. Thus the reflected rays have to be traced in order to realise an accurate implementation of reflection.

This section focuses on the modelling of emission, absorption and reflection and the handling of a complex spacecraft models with respect to TRP computation. For the TRP analysis a spacecraft model consisting of individual quadrilateral surface elements is needed. Here each surface is specified by the position of its four edge nodes in Cartesian coordinates. Furthermore the surface material (and thus the optical properties) as well as the steady state surfaces temperatures have to be specified for each model surface. For the TRP computation the models described in section 3.3 have to be processed for each individual surface.

For each radiating surface the resulting TRP can be assessed by computing the TRP for free unblocked radiation and correcting the result by the TRP loss caused by absorption and multiple reflections as displayed in figure 3.1, 4.A-C. Due to the linearity of the problem each component can be computed by an individual model. The resulting TRP can then be computed by summing up all individual surface TRP models:

$$\vec{P}_{\mathrm{TRP,res}} = \sum_{i=1}^{n} \vec{P}_{\mathrm{TRP,emi}}(i) - \sum_{i=1}^{n} \vec{P}_{\mathrm{TRP,abs}}(i) + \sum_{i=1}^{n} \vec{P}_{\mathrm{TRP,ref}}(i)\,. \tag{3.24}$$

Here n is the total number of surface elements, $\vec{P}_{\mathrm{TRP,emi}}(i)$ is the TRP component of unblocked emission from element i, $\vec{P}_{\mathrm{TRP,abs}}(i)$ is the TRP correction resulting from absorption of radiation at element i and $\vec{P}_{\mathrm{TRP,ref}}(i)$ is the TRP correction at element i due to reflection effects. The following sections will discuss the modelling of each of the three TRP components.

Free emission component

In order to evaluate the emission component of the TRP the individual TRP contributions for each surface element have to be computed. In section 3.1 it was discussed that the recoil acts against the normal direction of the emitting element surface. Thus the surface normal vector of each surface specifies the acting direction of the resulting TRP. The element normal vector $\vec{e}_{\mathrm{N}}(i)$ with $|\vec{e}_{\mathrm{N}}(i)| = 1$ on each element surface can be computed with:

$$\vec{e}_{\mathrm{N}}(i) = \vec{V}_1(i) \times \vec{V}_2(i)\,, \tag{3.25}$$

where $\vec{V}_1$ and $\vec{V}_2$ are two linearly independent unit vertex vectors within the surface element plane. The vertexes can be acquired from the edge node coordinates $N_1(i), \cdots, N_4(i)$ where $\vec{V}_1(i) = N_4(i) - N_1(i)$ and $\vec{V}_2(i) = N_2(i) - N_1(i)$.

The TRP resulting from free emission can now be computed by modifying equation (3.19) to:

$$\vec{P}_{\mathrm{TRP,emi}}(i) = -\frac{2}{3}\frac{1}{mc}\,\varepsilon(i)\,A(i)\,\sigma\,T(i)^4\,\vec{e}_{\mathrm{N}}(i)\,. \tag{3.26}$$

Here the negative sign results from the convention that the TRP is acting against the surface normal direction. Stefan-Boltzmann's law for grey body radiation $P_{\mathrm{tot}} = \varepsilon\,\sigma\,A\,T^4$ has been used to compute the total power emitted by the surface element. The specification of the emission coefficient ε enables the modelling of different optical properties for each radiating surface in the model. The sum of all individual TRP emission components in the model gives the total TRP emission component.

Absorption component

For the modelling of absorption (and also reflection) the interaction between the different surfaces in the model has to be analysed. For this a ray tracing approach is most suitable, since the emission of specific rays will not only identify element surface pairs which may exchange radiation, but also directly implements the directions of emission

which are needed to compute the fluxes between those elements as well as the direction of reflected rays. As each surface in the model may emit radiation the interaction of each surface with any other surface in the model has to be assessed. For this the element surfaces are treated, one after another, as active elements with respect to the emission and the tracing of rays as displayed in figure 3.8 right.

When the TRP computation for the currently active element is finished the next element is set to active status and the procedure is repeated until all elements have been processed once as the active element. For better understanding the principle is visualised in figure 3.8 left. The following computational methods are described with respect to the currently active element. Consequently they have to be repeated for each element in the model. In order to implement a ray tracing approach for the determination of radiation exchange the hemispheric radiation pattern of a flat emitting surface is modelled by dividing the surface elements of a unit hemisphere above the active element into specific solid angle elements as described by figure 3.3. Here the individual solid angle elements are characterised by the angles θ and ϕ. Figure 3.6 (left) shows the resulting allocation of solid angle elements $d\,\Omega_{\phi,\theta}$ on the hemispherical surface.

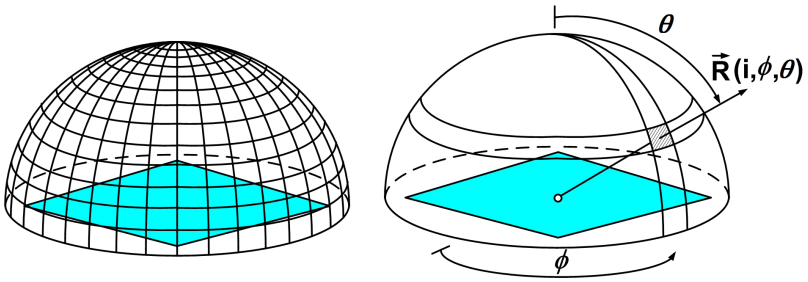

Figure 3.6: Allocation of solid angle elements and definition of ray direction $\vec{R}(i,\phi,\theta)$.

The vector from the active element centre $\vec{e}_{\mathrm{c}}(i)$ to the centre of a solid angle element on the hemisphere $\vec{e}_{\mathrm{c},\Omega}(i,\phi,\theta)$ is defined as the ray direction $\vec{R}(i,\phi,\theta)$ as displayed in figure 3.6 right:

$$\vec{R}(i,\phi,\theta) = \vec{e}_{\mathrm{c},\Omega}(i,\phi,\theta) - \vec{e}_{\mathrm{c}}(i)\,. \tag{3.27}$$

For the computation of the TRP absorption component all elements which are visible to the active element have to be detected. The visibility of any receiving element is characterised by two different requirements. An element j visible to the active element i has to be inside the hemispherical corridor above the active element. This first requirement can be formulated by the angle between the active element normal vector $\vec{e}_{\mathrm{N}}(i)$ and the centre node connection vector between the active and a receiving element $\vec{v}(i,j)$:

$$\psi_1(i,j) = \arccos\left(\frac{\vec{v}(i,j)\cdot\vec{e}_{\mathrm{N}}(i)}{|\vec{v}(i,j)|}\right) \leq \frac{\pi}{2}\,, \tag{3.28}$$

with

$$\vec{v}(i,j) = \vec{e}_{\mathrm{c}}(j) - \vec{e}_{\mathrm{c}}(i)\,,$$

where j is the index of the receiving element and i is the index of the active element.

The second requirement for visibility is that the receiving element surface has to be orientated towards the surface of the active element. As only two-dimensional elements are considered, no radiation into the rear of any element is allowed. This second criterion can be formulated as:

$$\psi_2(i,j) = \arccos\left(\vec{e}_{\mathrm{N}}(j) \cdot \vec{e}_{\mathrm{N}}(i)\right) \geq \frac{\pi}{2}\,, \tag{3.29}$$

where $\psi_2(i,j)$ is the angle between the normal vectors of receiving and active element. A receiving element is visible to the sending element if both criteria in equation (3.28) and (3.29) are met. Effectively the visibility computation enhances the performance of the absorption computation because the range of possible elements which may exchange radiation is reduced before the time-consuming ray tracing step. Now the next step in the modelling of absorption is the detection of emitted rays which hit receiving element surfaces. For a hit, the ray has to fulfil the requirement:

$$\psi_3(i,j) = \arccos\left(\frac{\vec{e}_{\mathrm{N}}(j) \cdot \vec{R}(i,\phi,\theta)}{|\vec{R}(i,\phi,\theta)|}\right) \geq \frac{\pi}{2}\,, \tag{3.30}$$

which effectively means that a receiving element has to face the plane of the receiving element surface. Radiation can only be absorbed or reflected by the receiving element if the ray hits the receiving element surface. For this the intersection point of the receiving element plane and each ray is computed using the node coordinates of the receiving element:

$$\vec{N}_1(j) + r\left(\vec{N}_2(j) - \vec{N}_1(j)\right) + s\left(\vec{N}_4(j) - \vec{N}_1(j)\right) = \vec{e}_{\mathrm{c}}(i) + t\,\vec{R}(i,\phi,\theta)\,. \tag{3.31}$$

The solution of this system for r,s and t gives the intersection point $\vec{P}$ with:

$$\vec{P} = \vec{e}_{\mathrm{c}}(i) + t\,\vec{R}(i,\phi,\theta)\,. \tag{3.32}$$

Now the coordinates of the four receiving element nodes are used to generate two adjacent triangle surfaces on the element surface. The sides of the triangles $T_1(\vec{N}_1, \vec{N}_2, \vec{N}_3)$ and $T_2(\vec{N}_1, \vec{N}_3, \vec{N}_4)$ are now considered as vertex vectors for the use of barycentric coordinates as displayed in figure 3.7.

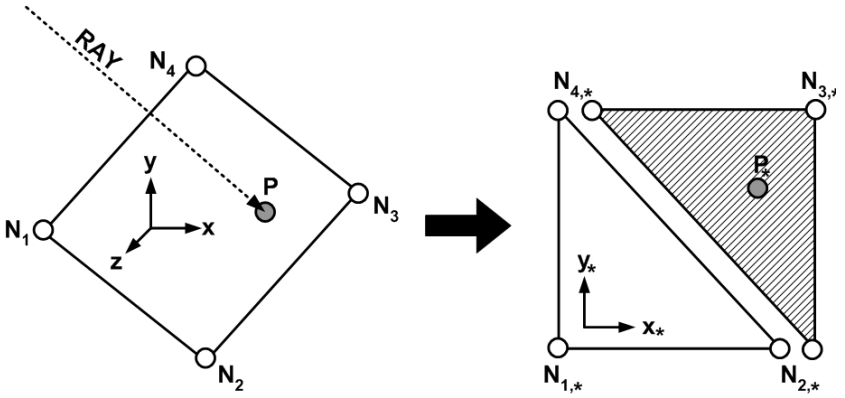

Figure 3.7: Hit detection with barycentric coordinates.

The nodal coordinates and the intersection point position have to be projected into the receiving element plane. For this the angle Φ between the global coordinate xy-plane (with normal vector $\vec{e}_{N,z}$) and the element plane as well as the rotation axis $\vec{E}$ with:

$$\begin{aligned} \Phi &= \arccos \frac{\vec{e}_{\mathrm{N}}(j)\, \vec{e}_{N,z}}{|\vec{e}_{\mathrm{N}}(j)|\, |\vec{e}_{N,z}|}\,, \\ \vec{E} &= \vec{e}_{\mathrm{N}}(j) \times \vec{e}_{N,z} = (e_1, e_2, e_3)^T\,, \end{aligned} \tag{3.33}$$

needs to be computed. The transformation into the receiving element plane is realised using the quaternion rotation matrix $\mathbf{A}$ [65] which is:

$$\mathbf{A} = \begin{pmatrix} q_1^2 - q_2^2 - q_3^2 + q_4^2 & 2(q_1q_2 + q_3q_4) & 2(q_1q_3 - q_2q_4) \\ 2(q_1q_2 - q_3q_4) & -q_1^2 + q_2^2 - q_3^2 + q_4^2 & 2(q_2q_3 + q_1q_4) \\ 2(q_1q_3 + q_2q_4) & 2(q_2q_3 - q_1q_4) & -q_1^2 - q_2^2 + q_3^2 + q_4^2 \end{pmatrix}, \tag{3.34}$$

with

$$q_1 = e_1 \sin\tfrac{\Phi}{2}\,, \quad q_2 = e_2 \sin\tfrac{\Phi}{2}\,, \quad q_3 = e_3 \sin\tfrac{\Phi}{2}\,, \quad q_4 = \cos\tfrac{\Phi}{2}\,, \tag{3.35}$$

and

$${q_1}^2 + {q_2}^2 + {q_3}^2 + {q_4}^2 = 1\,. \tag{3.36}$$

Here the vectors in the new coordinate system are given by:

$$\vec{N}_{i,*} = \mathbf{A}\, \vec{N}_i \quad \text{and} \quad \vec{P}_* = \mathbf{A}\, \vec{P}\,. \tag{3.37}$$

The element nodes and the intersection point are in the same plane and share the same z-coordinate in the new coordinate system. Therefore the dimension of the vertexes can effectively be reduced to two as seen in figure 3.7. The coordinates of the point $\vec{P}_* = \vec{P}(x, y)$ in barycentric frame [66] are defined as

$$\begin{aligned} c_1 + c_2 + c_3 &= 1\,, \\ a_1\, c_1 + a_2\, c_2 + a_3\, c_3 &= x\,, \\ b_1\, c_1 + b_2\, c_2 + b_3\, c_3 &= y\,, \end{aligned} \tag{3.38}$$

where the barycentric coordinates c_1, c_2, c_3 are the three unknowns of this system. All other values are given by the transformed triangle vertex points $\vec{N}_{i,*} = (a_i, b_i)^T$ as well as the transformed intersection point coordinate. With the solutions c_1, c_2, c_3 of the system (3.38) it can be checked whether the intersection point lies within the triangle or not. The criterion for the intersection point $\vec{P}_*$ being inside the triangle is:

$$c_1 \geq 0 \;\wedge\; c_2 \geq 0 \;\wedge\; c_3 \geq 0\,. \tag{3.39}$$

If $\vec{P}_*$ is in either one of the triangles the surface element has been hit and fluxes between the active and receiving element have to be computed. The ray and all following rays that hit the same element are deactivated thus modelling the shadowing effect of the target surface as displayed in figure 3.8 right.

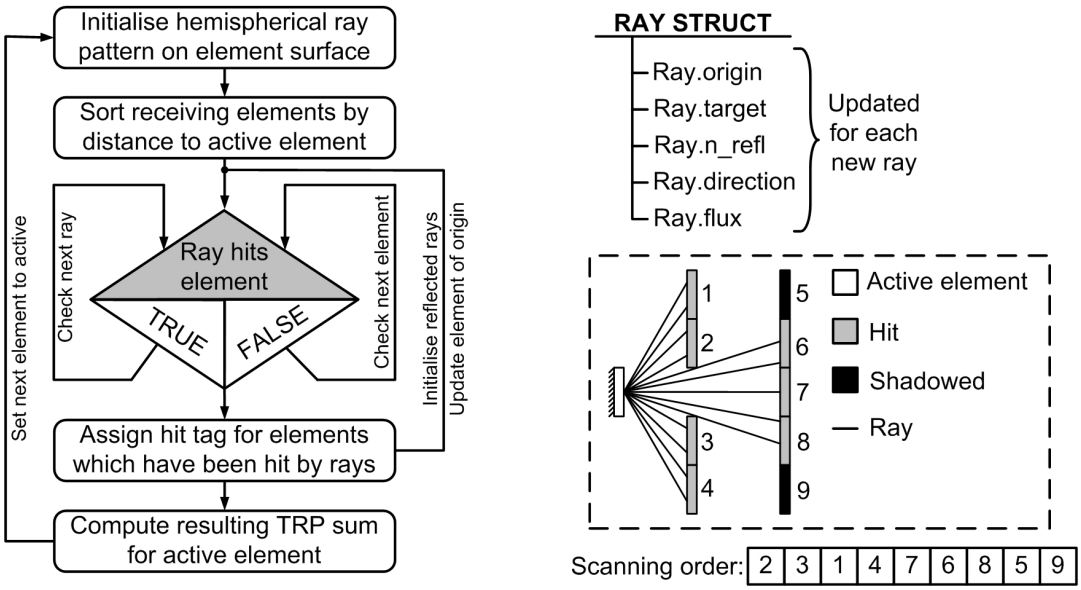

Figure 3.8: Overview of ray tracing and shadowing logic.

For all receiving elements which have been hit by any rays emerging from the active element the radiation flux between the two elements has to be computed. The flux is characterised by:

$$P_{ij} = P_{\text{tot}}\, \xi_{i,j}\,, \tag{3.40}$$

where $\xi_{i,j}$ is the so called radiation view factor (also characterised as shape or form factor) between two different elements i and j. View factors denote the fraction of radiation emerging from an active element which is received by the receiving element and ranges from zero to one. Here zero denotes that element j receives no radiation from element i while one indicates that all of the radiation emitted by element i is received by element j. Note that this would only be the case if the receiving element equals the hemispherical surface above the active element.

Figure 3.9 shows an exemplary configuration of two surface elements and the geometric information necessary to compute the view factor from surface i to surface j and vice versa.

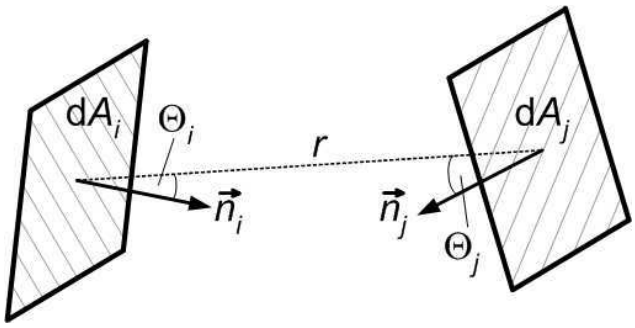

Figure 3.9: View factor between two elements.

Let Θ_i and Θ_j be the angles from the connection vector between the two element centre nodes $\vec{e}_c(i,j)$ to each element normal vector respectively (see figure 3.9) with $r = |\vec{e}_c(i,j)|$. The view factor from element i to element j is then defined as [67]:

$$\xi_{i,j} = \frac{1}{A_i \pi} \int_{A_i} \int_{A_j} \frac{\cos\Theta_i \, \cos\Theta_j}{r^2} \, dA_j \, dA_i \, . \tag{3.41}$$

The analytic solution of this integral is hard to obtain due to the dependence of both the angles and the distance on the integrands. Specific configurations such as parallel or perpendicular plates can be solved analytically but a general analytical solution is not available. In order to find a numeric approximation for the view factors, three different options are available:

- numerical integration with the Gauss method,
- numerical determination of view factor with the hemisphere method,
- simple approximation if r,Θ_i,$\Theta_j \sim$ const.

View factor determination with Gauss method

The solution of the view factor integral with numerical integration using the Gauss formalism [68] will lead to the most accurate results but also yields a high computational effort. In order to solve any function $g(x)$ it can be separated into:

$$g(x) \approx w(x)\Phi(x) \, , \tag{3.42}$$

where $w(x)$ is a weighting function and $\Phi(x)$ is a polynomial function, which can be integrated exactly. By this the integral over $g(x)$ can be approximated as the sum of the products of the solutions of the polynomial function $\Phi(x)$ at chosen integration points p_i and the individual weights w_i, where $w_i = w(x)|_{p_i}$:

$$\int_a^b g(x)dx \approx \sum_{i=1}^{n} \Phi(x = p_i) \, w_i \, , \tag{3.43}$$

where n is the number of integration points in the dimension x.

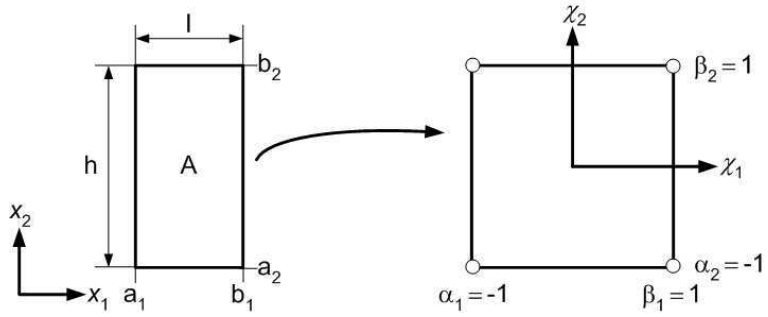

Figure 3.10: Element coordinates x_1, x_2 and uniform coordinates χ_1, χ_2.

In order to simplify the resulting polynomial functions, uniform coordinates are introduced as:

$$x \to \chi = \left(x - \frac{a+b}{2} \right) \left(\frac{2}{b-a} \right) , \tag{3.44}$$

resulting in

$$\int_a^b g(x)dx = \int_{-1}^{1} g \left(\frac{b-a}{2} \chi + \frac{a+b}{2} \right) \frac{b-a}{2} d\chi = \frac{b-a}{2} \int_{-1}^{1} \tilde{g}(\chi) d\chi \, . \tag{3.45}$$

In order to determine the view factor $\xi_{1,2}$ (given by equation (3.41)) between two surface A_1 and A_2, $g(x)$ can now be formulated as:

$$g(x_1, x_2, x_3, x_4) = \frac{1}{A_1 \pi} \frac{\cos \Theta(x_1, x_2)|_{p_i,p_j} \cos \Theta(x_3, x_4)|_{p_k,p_l}}{(r_{ijkl}(x_1, x_2, x_3, x_4))^2} \, , \tag{3.46}$$

where r_{ijkl} is the distance between the integration points and $\Theta(x_1, x_2)|_{p_i,p_j}, \Theta(x_3, x_4)|_{p_k,p_l}$ are the orientation angles at the integration points. The view factor can now be approximated to:

$$\begin{aligned} \xi_{1,2} &= \int_{a_i}^{b_i} \int_{a_j}^{b_j} \int_{a_k}^{b_k} \int_{a_l}^{b_l} g(x_1, x_2, x_3, x_4) \, dx_4 \, dx_3 \, dx_2 \, dx_1 \\ &\approx \eta_{\mathrm{T}} \sum_i \sum_j \sum_k \sum_l \left(\tilde{\Phi}(\chi_1, \chi_2, \chi_3, \chi_4)|_{\tilde{p}_i,\tilde{p}_j,\tilde{p}_k,\tilde{p}_l} \right) \tilde{w}_i \tilde{w}_j \tilde{w}_k \tilde{w}_l \, , \end{aligned} \tag{3.47}$$

where the transformation factor η_{T} is:

$$\eta_{\mathrm{T}} = \frac{(b_1 - a_1)(b_2 - a_2)(b_3 - a_3)(b_4 - a_4)}{16} \, , \tag{3.48}$$

and $\tilde{p}_i$, $\tilde{p}_j$, $\tilde{p}_k$, $\tilde{p}_l$, $\tilde{w}_i$, $\tilde{w}_j$, $\tilde{w}_k$, $\tilde{w}_l$ are the transformed integration points and weights, respectively. The function $\tilde{\Phi}(\chi_1, \chi_2, \chi_3, \chi_4)$ can now be formulated by means of the geometrical relations between two integration points on each of the surfaces as displayed in figure 3.11.

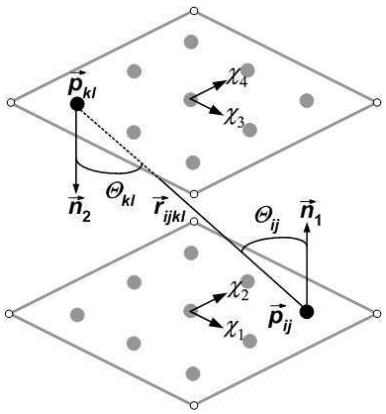

Figure 3.11: Geometrical relations between two different integration points. $\theta_{ij} = \theta(x_i, x_j)|_{p_i,p_j}$, $\theta_{ij} = \theta(x_k, x_l)|_{p_k,p_l}$.

Since A_1 and A_2 are quadrilaterals, the coordinates of any integration point on the surface can be expressed as:

$$\vec{p}_{ij} = \vec{x}_1 + \tilde{p}_i(\vec{x}_2 - \vec{x}_1) + \tilde{p}_j(\vec{x}_4 - \vec{x}_1 + \tilde{p}_i(\vec{x}_3 - \vec{x}_4 - \vec{x}_2 + \vec{x}_1))\,, \tag{3.49}$$

where $\vec{x}_1, \vec{x}_2, \vec{x}_3, \vec{x}_4$ are the four node coordinates of surface element A_1 and the integration points $\tilde{p}_i$, $\tilde{p}_j$, where $\tilde{p}_i$, $\tilde{p}_j \in [-1, \cdots, 1]$. The integration point coordinate on the second surface element $\vec{p}_{kl}$ is defined respectively for the node coordinates $\vec{x}_5, \vec{x}_6, \vec{x}_7, \vec{x}_8$ and the integration points $\tilde{p}_k$, $\tilde{p}_l$. The vertex vectors characterising the element plane can be expressed as:

$$\vec{V}_{A_1,1} = (\vec{x}_2 - \vec{x}_1) + \tilde{p}_j(\vec{x}_3 - \vec{x}_4 - \vec{x}_2 + \vec{x}_1)\,, \tag{3.50}$$

$$\vec{V}_{A_1,2} = (\vec{x}_4 - \vec{x}_1) + \tilde{p}_i(\vec{x}_3 - \vec{x}_4 - \vec{x}_2 + \vec{x}_1)\,, \tag{3.51}$$

which also allows for a sloping of the quadrilateral surfaces as displayed in figure 3.12. The vertexes of the second element plane can be computed respectively for $\tilde{p}_k, \tilde{p}_l$ and $\vec{x}_5, \vec{x}_6, \vec{x}_7, \vec{x}_8$. Note that curvatures in the element shapes (as may occur for higher order element shape functions) are not allowed in this approach.

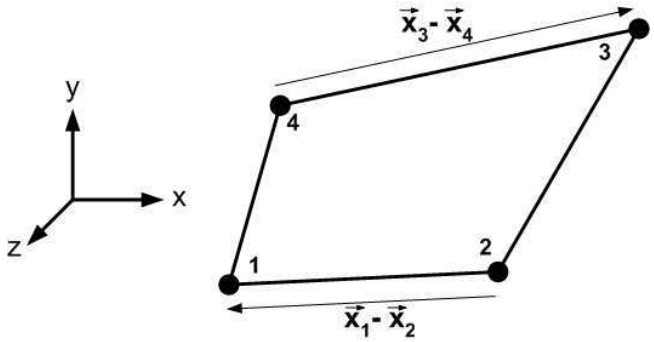

Figure 3.12: Sloped surface element.

Now the normal vector on each surface can be computed with the cross product of the two vertexes:

$$\vec{n}_{A_1} = \frac{V_{A_1,1} \times V_{A_1,2}}{|V_{A_1,1} \times V_{A_1,2}|} \quad \text{and} \quad \vec{n}_{A_2} = \frac{V_{A_2,1} \times V_{A_2,2}}{|V_{A_2,1} \times V_{A_2,2}|}\,. \tag{3.52}$$

Note that the normal vector is shared by all integration points on the same surface. The vector $\vec{r}_{ijkl}$ between two integration points $\vec{P}_{ij}$ and $\vec{P}_{kl}$ can be expressed as:

$$\vec{r}_{ijkl} = \vec{P}_{ij} - \vec{P}_{kl}\,. \tag{3.53}$$

Thus $\tilde{\Phi}(\chi_1, \chi_2, \chi_3, \chi_4)|_{\tilde{p}_i, \tilde{p}_j, \tilde{p}_k, \tilde{p}_l})$ evolves to:

$$\tilde{\Phi}(\chi_1, \chi_2, \chi_3, \chi_4)|_{\tilde{p}_i, \tilde{p}_j, \tilde{p}_k, \tilde{p}_l}) = \frac{\arccos(\vec{n}_{A_1} \cdot \vec{r}_{ijkl}) \arccos(\vec{n}_{A_2} \cdot \vec{r}_{ijkl})}{(r_{ijkl})^2}\,, \tag{3.54}$$

where $r_{ijkl} = |\vec{r}_{ijkl}|$. Following Abramowitz and Stegun [69], the weights $\tilde{w}_i$, $\tilde{w}_j$, $\tilde{w}_k$, $\tilde{w}_l$, can be characterised from the zeros of the Legendre-polynomials of degree n, where n also indicates the number of integration nodes per dimension:

$$\tilde{w}_i = \frac{b_i - a_i}{(1 - (\tilde{p}_i)^2)(P_n'(z)|_{\tilde{p}_i})^2}\,, \tag{3.55}$$

which is valid for the other weights and integration points, respectively. Here the zeros effectively equal the integration points in transformed coordinates. The Legendre polynomials P_n are defined as [69]:

$$P_n(z) = \frac{1}{2^n n!} \frac{d^n}{dz^n}((z^2-1)^n)\,. \tag{3.56}$$

This equation evolves to:

$$P_{n+1}(z) = z\,P_n(z) - \frac{1-z^2}{n+1} P_n'(z)\,, \tag{3.57}$$

and can be simplified to the Bonnet recursion equation [69]:

$$(n+1)P_{n+1}(z) = (2n+1)\,z\,P_n(z) - n\,P_{n-1}(z)\,, \tag{3.58}$$

which does not include any derivatives of P_n. By choosing suitable starting estimates ($P_0(z) = 1$ and $P_1(z) = z$), P_n and its derivatives can now be calculated for any number of integration points. The zeros can be estimated by using the Newton-Rhapson iteration method with:

$$z_{a+1} = z_a - \frac{P_n(z_a)}{P_n'(z_a)}\,. \tag{3.59}$$

The converged value of z_a equals the needed integration point $\tilde{p}_i$. By using equations (3.55) - (3.59) for each of the coordinates $\vec{x}_1$ to $\vec{x}_8$ and inserting into equation (3.47) the view factor can now be determined numerically. Here the achievable accuracy is dominated by the chosen number of integration points.

View factor determination with hemisphere method

Another numerical approach for the determination of the view factor between two surface elements is the so called hemisphere method. Here the ray tracing approach taken for the determination of radiation exchange between the model surfaces can directly be used to compute the resulting view factors. Since the ray directions are defined as the vector from active element centre to the centre of a solid angle element on the hemisphere, the surface of the solid angle element (for a unit hemisphere) can be assigned to each ray as displayed in figure 3.13.

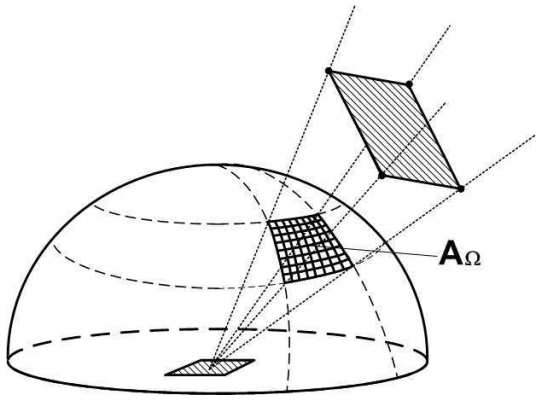

Figure 3.13: View factor determination with hemisphere method.

By scanning the rays the view factor can now be expressed as the ratio of the associated solid angle element surfaces of rays that hit the receiving element A_Ω to the total surface area of the unit hemisphere A_{tot}:

$$\xi_\Omega = \frac{A_\Omega}{A_{\text{tot}}}\,. \tag{3.60}$$

The view factor $\xi_{i,j}$ can then be approximated with ξ_Ω. Here the accuracy of the determined view factors is directly scaled with the ray resolution. Since the hit detection demands a high computational effort a trade-off between computation time and accuracy of view factor determination has to be made.

View factor determination with simple approximation

Looking at the view factor integral it can be seen that the integrand depends on the distance between the two surfaces, the relative slope between the surfaces and the surface dimensions. If the distances between the surfaces are high compared to the surface areas and the sloping, the change of the angles and the distance over the integration surface can be neglected and the view factor from element i to element j can simply be approximated to:

$$\xi_{i,j} = A_j\,\frac{\cos\Theta_i\,\cos\Theta_j}{\pi\,r^2}\,, \tag{3.61}$$

where the angles and the distance between the surface are computed with respect to the element centre nodes ($r = |\vec{e}_{\text{c}}(i,j)|$).

By computing the view factor with the methods described above, the TRP absorption component due to radiation exchange from element i to element j can now be calculated with:

$$\vec{P}_{\text{abs}}(i) = -\frac{1}{m\,c}\sum_{j}^{n}\xi_{i,j}\,P_{\text{tot}}(i)\,\vec{e}_{\text{c}}(i,j)\,, \tag{3.62}$$

which includes the reflected as well as the non-reflected part of the absorbed radiation fluxes as defined in equation (3.23).

Reflection component

The surface element receiving the radiation may reflect the incoming radiation depending on the optical properties as well as the orientation of the target surface. Here one has to distinguish between specular and diffuse radiation as described by figure 3.4. The reflected fluxes depend on the incoming radiation flux $P_{\text{inc}}(i,j)$ and the specular and diffuse coefficients of reflection $\gamma_{\text{s}}(j)$ and $\gamma_{\text{d}}(j)$. Here the optical properties yield the relation $\varepsilon + \gamma_{\text{s}}(j) + \gamma_{\text{d}}(j) = 1$, assuming a non-transmittive target material. For the specular reflection computation the direction $\vec{r}_{\text{ref}}(i,j)$ of the reflected flux $P_{\text{ref}}(i,j)$ has to be computed with respect to the incoming ray direction $\vec{r}_{\text{inc}}(i,j)$:

$$\vec{r}_{\text{ref}}(i,j) = 2\,\vec{e}_{\text{N}}(j)\big(-\vec{r}_{\text{inc}}(i,j)\,\vec{e}_{\text{N}}(j)\big) + \vec{r}_{\text{inc}}(i,j)\,, \tag{3.63}$$

where $\vec{e}_{\text{N}}$ is the normal direction of the reflecting element. The TRP reflection force contribution can then be computed for each reflecting surface element as:

$$\vec{P}_{\text{ref}}(i,j) = -\frac{1}{m\,c}\big(P_{\text{inc}}(i,j)\,\gamma_{\text{s}}(j)\,\vec{r}_{\text{ref}}(i,j) + \frac{2}{3}\,P_{\text{inc}}(i,j)\gamma_{\text{d}}(j)\vec{e}_{\text{N}}(j)\big)\,. \tag{3.64}$$

For more than one reflection, a correction of the reflection term is necessary in order to address the absorption of a reflected ray when it hits another surface element. Thus the TRP reflection component becomes:

$$\vec{P}_{\mathrm{ref}}(i,j) = P_{\mathrm{inc}}(i,j,k)\vec{r}_{\mathrm{ref}}(i,j,k) + \frac{2}{3}\sum_{k=1}^{n_{\mathrm{refl}}} P_{i,j,k}\gamma_{\mathrm{d}}(j,k)\vec{e}_{\mathrm{N}}(j,k)\,, \tag{3.65}$$

with

$$P_{\mathrm{inc}}(i,j,k) = P_{\mathrm{inc}}(i,j)\prod_{k=1}^{n_{\mathrm{refl}}}\gamma_{\mathrm{s}}(j,k)\,, \tag{3.66}$$

where n_{refl} is the total number of subsequent specular reflections considered in the model and $\vec{r}_{\mathrm{ref}}(i,j,k)$ is the direction of the ray for reflection k. Here the diffusely reflected rays are not traced further after the first reflection. The total TRP reflection component of a single element i can now be determined by the sum of the individual reflection components over all active and receiving elements:

$$\vec{P}_{\mathrm{ref}} = \sum_{i=1}^{n}\sum_{j=1}^{n}\vec{P}_{\mathrm{ref}}(i,j)\,. \tag{3.67}$$

Now the total TRP can be computed by summing up all emission, absorption and reflection components. TRP can be converted to a resulting thermal recoil force by multiplying with the spacecraft's mass. By doing this, the resulting thermal recoil force can also be converted to a resulting thermal recoil torque if the centre of mass of the spacecraft is known. Here the total thermal recoil torque T_{res} can be computed by the individual surface forces and the distances of the surface centres to the centre of mass $\vec{r}_{\mathrm{COM}}(i)$:

$$T_{\mathrm{res}} = \sum_{i}^{n}\vec{F}_{\mathrm{res}}(i)\times\vec{r}_{\mathrm{COM}}(i)\,, \tag{3.68}$$

where $\vec{r}_{\mathrm{COM}}(i)$ is the vector from the surface element centre to the spacecraft centre of mass. The resulting torque leads to a rotation of the spacecraft around its centre of mass.

3.5 Thermal FE analysis for TRP computations

As described in section 3.1 a thermal FE analysis has to be conducted as the first step in TRP assessment. This section will introduce the necessary modelling steps in order to develop a thermal FE model of a spacecraft and discuss the conversion of the results for the use in the numerical TRP computation method. The principle FE modelling approach described here is independent of the specific FE program used to model the spacecraft. However, the input models and FE analysis conducted in this thesis have been performed with the commercial FE software ANSYS and its macro design language ANSYS APDL. Thus specific steps are described which might differ from other tools.

Thermal FE analysis in ANSYS

The principle composition of a complete steady state thermal FE analysis is displayed in figure 3.14. Here the modelling work can be distinguished into six discrete modelling steps.

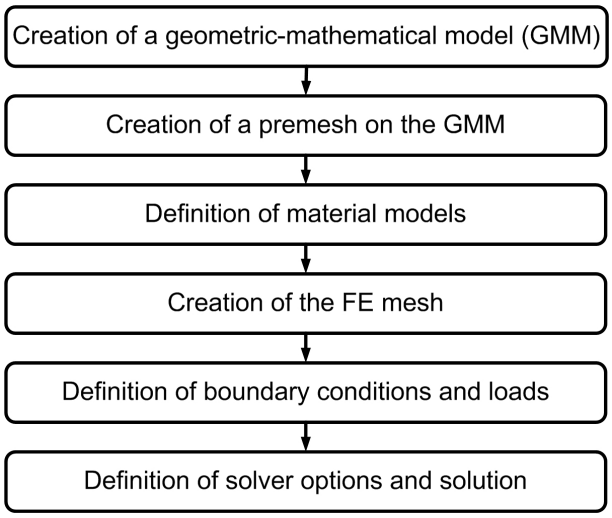

Figure 3.14: Composition of thermal FE steady state simulation.

The first modelling step is the creation of a geometric-mathematical model of the craft (GMM) which consists of individual keypoints, lines, areas and volumes. The GMM can be build up from so called primitives (spheres, tori, blocks etc.) which allow a coarse resemblance of the model to the actual structure. Two principle modelling approaches are available. In the *bottom-up* method the primitives are constructed from the level of keypoints which are then used to construct lines, areas and volumes. This approach enables the highest modelling flexibility but also involves a high modelling effort. In the *top-down* approach the volumes are constructed directly while the associated areas, lines and keypoints are generated automatically. Here the possible complexity is limited to basic shapes. After the primitives have been implemented the level of modelling detail can be increased by performing Boolean operations (such as overlapping, cutting, merging etc.). Here a trade-off between model complexity and influence of a geometrical detail to the resulting solution has to be found. Thus details which will not influence or contribute to the solution in any way are left out which reduces the work load in the meshing step considerably.

Due to the fact that the numerical method for TRP computation developed in this thesis is based on quadrilateral surface elements the GMM solids have to be meshed with hexaedrals thus implementing quadrilateral faces on each FE. For this the individual components of the GMM have to match the requirements for the so-called ANSYS mapped meshing technique [70], which uses a grid control method to ensure a good mesh quality. In order to use mapped meshing on areas, the areas have to be bordered by either three of four lines. For the meshing of volumes this criterion has to be fulfilled on each face of the volume. For complex model geometries such as complete spacecrafts the conversion of the GMM to a state where all mesh requirements

are fulfilled can be considerably work intensive. In order to illustrate this challenge the creation of the premesh of a common geometric configuration is displayed in figure 3.15.

In this example the starting primitives are a cylinder and a hexaedral plate to which the cylinder is mounted in the centre (as seen in figure 3.15 left). In order to generate the premesh each area has to be checked for the mapped mesh requirements. Here surfaces which are situated on top of other surfaces are merged into one interface surface shared by the volumes. For the given configuration the top surface of the plate is initially bordered by eight lines (note that ANSYS models circular areas with four 90°-lines) which does not allow for mapped meshing without further modifications. In order to develop a surface division which will be meshable the volumes have to be partitioned. Here a symmetric partitioning will also lead to a symmetric mesh.

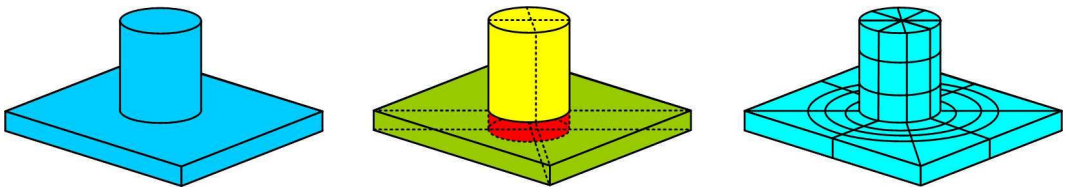

Figure 3.15: Premeshing of a cylinder on a rectangular plate.

For this the volumes are divided into equal 90°-slices. Note that the shape of the interface area has to be extruded through all volumes to which the interface belongs. This operation leads to a total of 12 volumes (4 red, 4 green, 4 yellow in figure 3.15 centre) which now all meet the requirements for mapped meshing. Now the premesh leads to a symmetric FE mesh as displayed in figure 3.15 right. This simple example shows that every detail added to the model will result in a higher complexity of the premesh. Thus the premeshing becomes the most time consuming task in high-detailed FE modelling.

Material parameters and meshing

Before applying the FE mesh to the GMM, material models which specify the physical parameters of the included materials have to be defined. For thermal analyses the thermal conductivity, the specific heat and the material density have to be specified for each new material. In case of steady state analysis only the thermal conductivity of the materials influences the resulting equilibrium temperatures because density and specific heat are associated with the internal heat energy which influence merely the time derivatives of the temperature.

The materials are then assigned to the different model volumes while the mesh is applied. The FE mesh or grid is the sum of all FEs existing in the model and corresponds to the system FE differential equations which is used to obtain the solutions. The mesh is composed by individual FEs which are defined by the locations of the FE nodes. Here the nodes possess specific degrees of freedom which are coupled by differential equations.

The element type which is used for the meshing defines the geometry of the resulting FE mesh as well as the implemented differential equations and thus the modelled physical effects. The main FE type used in this thesis is the ANSYS *SOLID 70* element which implements 3D heat conduction and can be used with hexaedral and tetraedal or prism shapes as displayed in figure 3.16. In hexaedral mode the element is defined by 8 edge nodes which corresponds to a linear element form function. Temperature and heat flux loads can be specified on the element nodes and faces. Each node possesses a single temperature degree of freedom.

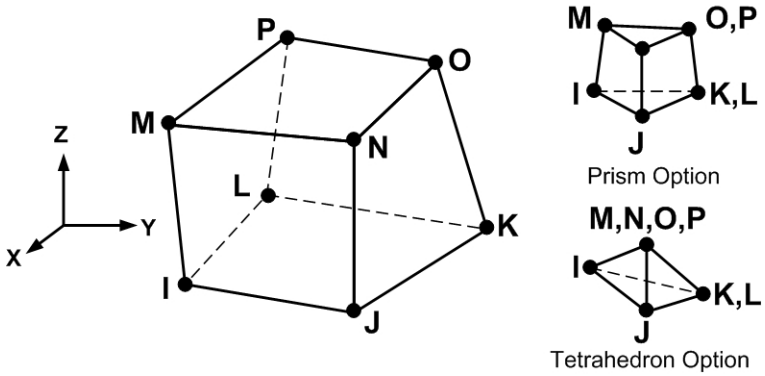

Figure 3.16: *SOLID70* element definition [70].

All volumes which have to be meshed with this element type have to fulfil the requirements for the ANSYS mapped meshing technique if the hexaedral option is used. This realises quadrilateral FE surfaces what is a requirement for the subsequent numerical TRP computation. With this *SOLID70* can be used for the generation of the 3D mesh with respect to the later use of the FE analysis results for the TRP computation. Besides the *SOLID70* FE two other ANSYS element types, *LINK 33* and *Shell 131* are used for the implementation of specific boundary conditions. Details on these two FE types will be discussed in the Pioneer FE modelling section 5.1.

In order to generate the FE mesh on the premeshed structure all volumes belonging to the same material have to be selected and meshed simultaneously. With this the material parameters of the currently selected material model are assigned to the discrete finite elements. The resulting mesh depends on the structure of the premesh, the chosen element size parameters (total size, element number per lines etc.) and the meshing order. The meshing procedure as well as the assignment of specific materials to the different components are displayed in figure 3.17.

In the displayed example a telescope opening is situated on one of the bus panel of a conventional satellite body. Due to the spherical shape of the component a radial mesh division of the volumes is necessary which is a restriction on the following meshing of the underlying surface. This results from the fact that an FE mesh is not allowed to possess singularities or discontinuities. Thus the more complex round shape of the telescope has to be meshed before the underlying surface. For this the telescope material is activated and the FEs are applied to the telescope volume. Now the bus material is activated and the bus mesh is generated. All volumes are processed one after another

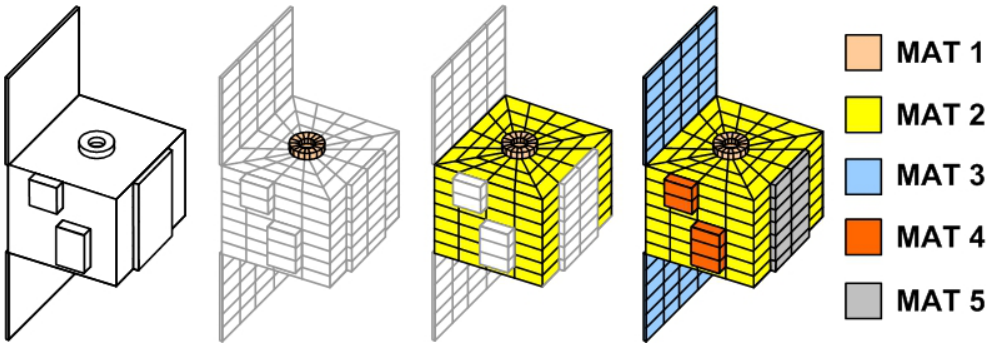

Figure 3.17: Meshing order and assignment of material properties.

according to the mesh boundaries which are defined by already existing meshes or the premesh. If a wrong meshing order is chosen mapped meshing may not be possible if already meshed volumes do not support mesh requirements of the volumes which are not yet meshed. In general the meshing order has to start at the volumes with highest complexity going to less complex volumes and from the model interior to the external volumes. Sometimes this involves the adjustment of the premesh and the element size parameters if contradicting mesh requirements exist.

Boundaries and loads

After the generation of the FE mesh, boundary conditions and loads for the FE analysis have to be be specified. Figure 3.18 shows the different possibilities for the assignment of boundary conditions in ANSYS used in this thesis.

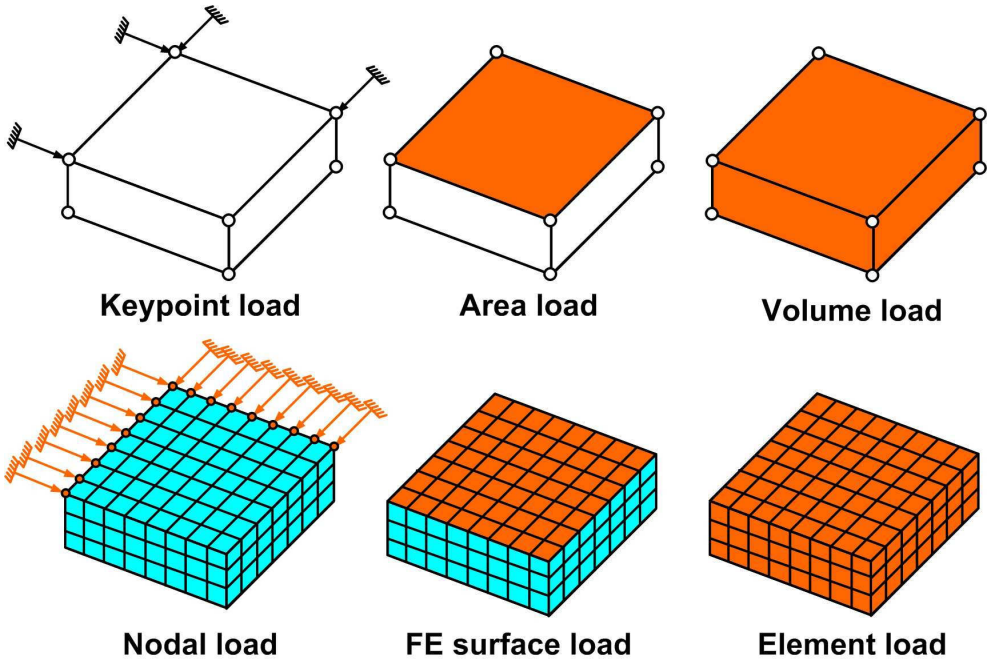

Figure 3.18: Types of loads and boundaries.

Boundaries and loads can either be specified on the GMM components or the model FEs. If the GMM is used a transformation of the boundaries to the FE model is necessary. Three different types of boundaries can be identified. Keypoints and Nodal loads directly influence the DOF at the position of the node or keypoint (e.g a fixed temperature). Surface loads (e.g. heat fluxes) are defined on the model areas or FE surfaces and are distributed by the solver between all nodes belonging to this surface. Finally volume or FE loads (such as heat generation) are distributed over all nodes belonging to the same FE or volume.

The implementation of radiation boundary conditions takes a central role for the precise computation of the steady state temperatures. In ANSYS radiation exchange can be implemented by so called enclosures which specify an environment for radiation exchange [71]. Here surfaces which belong to the same enclosure may exchange radiation, while surfaces belonging to different enclosure do not exchange radiation even though the geometric arrangement might allow for it. The ambivalent temperature of the enclosure (which is the reference temperature for outgoing radiation) can be specified by so called spacenodes which can be constrained to a fixed temperature. Thus a spacenode can be used as heat sink (e.g. at 3 K to model the space environment) and radiation exchange between space nodes and the FE surfaces belonging to the same enclosure is computed by Stefan Boltzmann's law. The definition of a single spacenode is sufficient for each enclosure. The radiation exchange among different element surfaces in the same enclosure is computed by means of view factors which are determined either with the hemisphere or hemicube method as discussed in section 3.4. The resolution for the view factor determination can be specified which influences the accuracy of radiation flux computation as well as the computational effort.

Solution

The final step in the FE analysis is the configuration of the analysis solution parameters. For thermal problems steady state and transient analysis can be conducted. In case of steady state the analysis is conducted for a single time step and iterations are performed, until the DOFs stay within a chosen convergence limit. In case of transient analysis the system of equations is solved for a specified number of time steps which may possess different boundary conditions. Here the timesteps are splitted up in sub steps for which the FE solution is calculated. Boundary conditions can be updated for the different time steps in a ramped or stepped approach.

Within single processor mode, ANSYS offers the sparse direct solution, the preconditioned Conjugate Gradient (PCG) solution, the Jacobi Conjugate Gradient (JCG) solution, the incomplete Cholesky Conjugate Gradient (ICCG) solution, the Quasi-Minimal Residual (QMR) solution and an automatic iterative solver option (ITER) as numeric solvers for the FE model [70]. Each of the solvers possess advantages and disadvantages for different FE problems. Details on this are discussed in [70]. For each of the provided solvers options, the convergence criteria as well as a memory management can be configured, thus enabling the control of solution accuracy and computational effort.

The solution itself can be performed either in the graphical user interface (GUI) or in a batch mode in background. In the batch mode the computational performance is increased in comparison to the GUI method but no visual information on the state of the solution is given. However a report log file is delivered after the analysis is finished which contains information about the iteration and convergence processes as well as error code information for unconverged or stopped analyses. After the solution has been acquired, the analysis is saved in a database file that can be loaded into the GUI to visualise the results in a post processing step.

Model export

In order to use the results of the FE analysis for the TRP computation, an interface between the FE model and the TRP algorithm has to be defined. The interface is realised as a set of text files which contain the elementary geometrical, material and temperature data of the model. Here all dimensions are given in the global Cartesian frame. The composition of the text files is displayed in table 3.1. An exemplary APDL macro file for the automatic export of the Pioneer 10 FE model is included in annexe section V.5.

Node table			Coefficient table				Temp table
$N_{1,x}$	$N_{1,y}$	$N_{1,z}$	α_1	ε_1	$\gamma_{s,1}$	$\gamma_{d,1}$	T_1
$N_{2,x}$	$N_{2,y}$	$N_{2,z}$	α_2	ε_2	$\gamma_{s,2}$	$\gamma_{d,2}$	T_2
$\vdots$	$\vdots$	$\vdots$	$\vdots$	$\vdots$	$\vdots$	$\vdots$	$\vdots$
$N_{n-1,x}$	$N_{n-1,y}$	$N_{n-1,z}$	α_{n-1}	ε_{n-1}	$\gamma_{s,n-1}$	$\gamma_{d,n-1}$	T_{n-1}
$N_{n-2,x}$	$N_{n-2,y}$	$N_{n-2,z}$	α_{n-2}	ε_{n-2}	$\gamma_{s,n-2}$	$\gamma_{d,n-2}$	T_{n-2}

Element table							
A_1	$e_{c,1,x}$	$e_{c,1,y}$	$e_{c,1,z}$	$N_{1,a}$	$N_{1,b}$	$N_{1,c}$	$N_{1,d}$
A_2	$e_{c,2,x}$	$e_{c,2,y}$	$e_{c,2,z}$	$N_{2,a}$	$N_{2,b}$	$N_{2,c}$	$N_{2,d}$
$\vdots$	$\vdots$	$\vdots$	$\vdots$	$\vdots$	$\vdots$	$\vdots$	$\vdots$
A_{n-1}	$e_{c,n-1,x}$	$e_{c,n-1,y}$	$e_{c,n-1,z}$	$N_{n-1,a}$	$N_{n-1,b}$	$N_{n-1,c}$	$N_{n-1,d}$
A_n	$e_{c,n,x}$	$e_{c,n,y}$	$e_{c,n,z}$	$N_{n,a}$	$N_{n,b}$	$N_{n,c}$	$N_{n,d}$

Table 3.1: Composition of interface text files.

The element table stores the surface area, the centre coordinate and the node numbers of each surface element. Here the line number equals the numbering of the respective surface element. The coordinates of the nodes are stored in the node table while optical coefficients and computed surface temperatures are stored for each element in the coefficient and temperature table respectively.

For the export of a model from ANSYS, an export macro has been developed which extracts the data needed to compose the text files after the FE analysis is finished. As TRP only depends on the surface conditions of the spacecraft only elements on the surface of the FE model have to be exported. For this a second mesh is overlaid in post processing on the satellite surface after the FE solution has been acquired. By choosing a 2D thermal FE with the same DOF as the underlying solid mesh the solutions computed for the solid model are inherited by the 2D mesh. The primary

model entities are deleted from the model until only the surface mesh remains. Now the text files can directly be generated by retrieving nodal and element information remaining in the model. The element temperatures can then be acquired by the simple rule:

$$T(i) = \big(T(N_1(i)) + T(N_2(i)) + T(N_3(i)) + T(N_4(i))\big)/4\,, \tag{3.69}$$

where $T(N_1(i)), \cdots, T(N_4(i))$ are the temperature DOF solutions at the edge nodes of element i. The text files can be read into the TRP algorithm to create a global data matrix which stores all relevant information needed for the TRP computation.

3.6 Numerical computation of TRP

Since the main goal of this thesis is the determination of TRP (and SRP) on spacecraft orbits, several numerical TRP computations have to be performed subsequently with changing input files based on the changing spacecraft state. For each new analysis the text files containing the model information have to be imported into the TRP algorithm. The ray resolution per element, the number of subsequent reflections considered in the analysis and the view factor option have to be specified. The resulting computed TRP has to be checked for convergence to minimise computational errors. For this subsequent TRP analysis should be performed while improving the ray resolution in each computation step. If the resulting TRP does not change (within a chosen convergence criteria) any more by an increase of ray resolution the converged TRP result has been acquired. Beneath the ray resolution the model element resolution and the chosen view factor option may additionally influence the resulting accuracy of the computed TRP. Details on the computational errors and inaccuracies resulting from these aspects are discussed in this section with respect to chosen test case geometries. Note that a detailed tutorial on the handling of the algorithms used for the analysis in included in the annexe section V.4.

Performance considerations

The computation performance of the TRP algorithm depends on the model resolution and the ray resolution that has been chosen. While model sizes under 1000 elements will lead to short computation times, even with high ray resolutions, breaking this limit will lead to exponentially growing computation times. Since the detailed Pioneer FE model possesses over 10000 surface elements and parameter analysis has to be performed, a high number of subsequent computations is necessary. Therefore ways to enhance the computation performance have to be found. Here the most time-intensive procedures in the algorithm are the detection of possible radiation exchange partner elements by means of ray tracing and the computation of view factors between those elements. One of the most important characteristics of view factors is the relation:

$$A_i\,\xi_{ij} = A_j\,\xi_{ji}\,, \tag{3.70}$$

which implies that only half of the elements of the view factor matrix have to be computed by numerical integration if the surface areas of the elements are known. A similar kind of symmetry can be used for the computation of the hit matrix. If a hit for an element has been detected the target element can also also hit the sending element. Thus the detected hit can be directly stored for sending as well as for the target element

and the element combination does not have to be considered during ray tracing when the target element becomes the active element. Due to the fact that the hit matrix has to be symmetric, the radiation fluxes can be summed over each of the symmetric hit matrix entries which effectively avoids half of the total flux computation:

$$\vec{F}_{\mathrm{abs}}(i,j) = -\frac{1}{c}\left(\xi_{ij}\, P_{\mathrm{tot}}(i)\, \vec{e}_{\mathrm{c}}(i,j) - \xi_{ji}\, P_{\mathrm{tot}}(j)\, \vec{e}_{\mathrm{c}}(i,j)\right). \tag{3.71}$$

If this option is used the reflection computation has to consider both reflected rays (sending and target element) independently.

By using all the measures described above the total computation time can be reduced by a factor of approximately five to six. For complex models such as the Pioneer FE model the resulting computation times still are in the range of a couple of days using conventional desktop computers. In particular for parameter analysis, where the computations have to be performed a large number of times such large computation times are not acceptable. A solution to this problem can be found while looking at the principles of view factors and the hit detection. View factors and also the hit matrix (which describes which elements can exchange radiation) are merely geometric information which are specific to the model composition. This means that if the model geometry (meaning nodal positions, number of elements, dimensions etc.) is not changed during a parameter analysis the view factor and hit matrices can be re-used for subsequent runs without the need to perform the ray tracing step again. In particular for Pioneer 10 which is the design case for the TRP computation, the geometry of the spacecraft does not change during the mission (no movable parts) and there is no need to change the mesh parameters for e.g. other boundary conditions. Thus the problem of large computation times can be reduced to the first run in a parameter analysis with a given model geometry. While for the Pioneer FE model the first run with complete view factor and hit computation may take up to approximately 50 hours (view factor option: 8-node Gaussian quadrature, $5 \cdot 10^5$ rays per surface element), the computation time for the following models drops to approximately 10 minutes on a conventional 4-core desktop PC.

Note that this procedure is not possible for the analysis of spacecraft with changes of geometrical configuration during the analysed time frame. Any change such as the rotation of an antenna or solar panels (with respect to the rest of the spacecraft) will result in a change in the radiation view factors thus changing the view factor matrix as well as the hit matrix. In this case, the ray tracing has to be performed for each simulated configuration.

Test cases

Before the numerical method for TRP modelling may be utilised for TRP calculations on spacecraft models with complex shape, the correct functioning and the performance of the implemented ray tracing code have to be demonstrated. For this task six test case models with different geometrical configuration as displayed in figure 3.19 have been defined. Each of these test cases is utilised for the testing of specific code characteristics as well as for the evaluation of the performance of different computational options (e.g. different methods for the determination of radiation view factors).

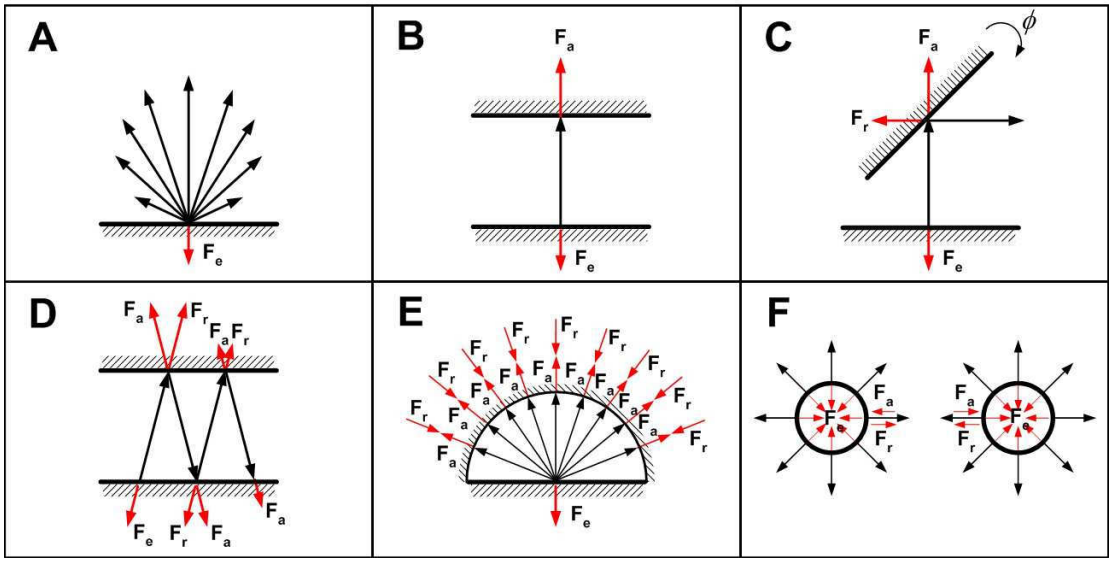

Figure 3.19: Validation test case models A - F. F_a: Recoil force component resulting from absorption, F_r: Recoil force component resulting from reflection.

The main geometrical and optical parameters considered for the six test cases are listed in table 3.2. Modifications of these default values are highlighted in the subsection discussing the respective test cases.

Property	Parameter	Value
Plate surface area	A_{test}	1 m^2
Radius of test spheres	r_{test}	1 m
Surface emissivity	ϵ_{test}	0.7
Surface reflectivity	γ_{test}	0.3
Surface temperature	T_{test}	300 K
Reference mass	m_{test}	1 kg

Table 3.2: Parameters for test cases A-F.

The TRP resulting from each test case configuration and the general character of the solution can be described analytically and compared to numerical results obtained with the ray tracing method. Thus the different sub functions for emission, absorption and reflection computation as well as general aspects on numerical accuracy, computation time, optimal ray tracing parameters and view factor determination can be evaluated. The individual test case results and their implication for the overall performance of the numerical TRP computation method are discussed in the following.

Test case A

Test case A aims at the verification of the correct computation of the TRP component resulting from free emission into the environment. For this a square flat plate with surface area A_{test}, surface emissivity ϵ_{test} and the homogeneous surface temperature T_{test} (as defined by table 3.2) is modelled while applying different element resolutions in each simulation run. Here the element resolution is defined as the total number of

equally sized surface quadrilateral FEs which together build up the complete geometric surface. The resulting FEs and the temperature solutions are then imported into the TRP algorithm and the resulting TRP is computed for each sub model configuration. For comparison, the analytical solution can be acquired by solving equation (3.26) for the default values given in table 3.2. As the resulting analytical prediction $a_{\mathrm{TRP}} = 7.149 \cdot 10^{-7}\,\mathrm{m/s^2}$ is obtained. The numerical as well as the analytical solution are displayed in figure 3.20 left. The individual numerical results obtained for different

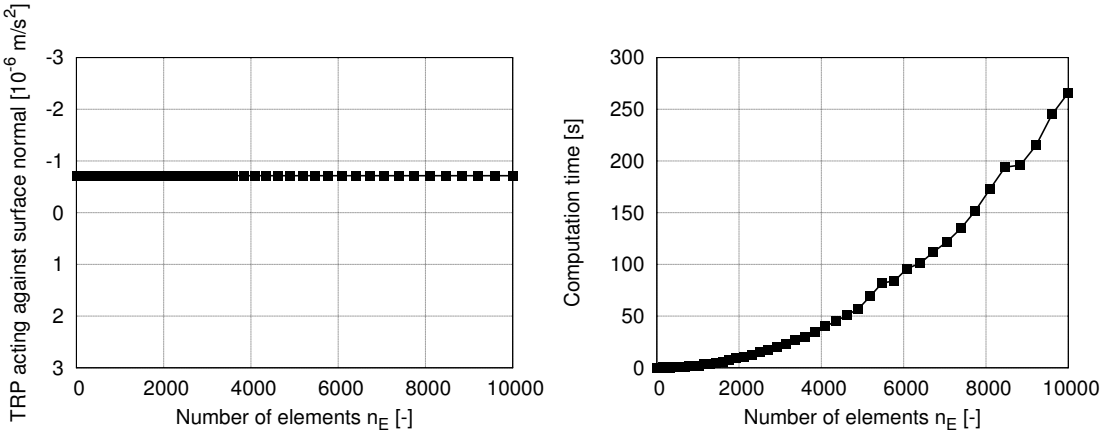

Figure 3.20: Results of test case A. Numerical results: black quads, analytical results: solid line.

element resolutions are shown as black quads while the analytical value has been plotted as a solid line. As can be seen, the number of elements does not influence the computed TRP magnitude. For all model configurations the numerical result matches the analytical result within the numerical accuracy of the used processor. This behaviour is easily understandable as the total TRP results from the sum of the individual FE TRP contributions. For a higher model element resolution the TRP has to be summed up over a higher number of elements while at the same time the TRP contribution of each individual FE, which scales by the FE surface area, decreases with the same rate. Resulting from this the sum of the individual TRP contributions stays constant for all configurations. With growing number of FEs the needed computation time grows exponentially (with slight variations that may be credited to the influence of other system processes or network activity). This behaviour is not surprising as the visibility check involves the testing of each surface pairing in the model. Thus a doubling of the number of model element will cause a an increase of computation time by factor four.

Test case B

Test case B aims at the verification of the computation of the absorption and reflection components of the TRP. This involves the checking of the view factor matrix computation, the tracing of the rays emitted by the active surface element as well as the correct computation of the reflected ray directions. Two rectangular plates facing each other are processed with different element resolutions. For the evaluation of the absorption component one of the surfaces is held at a constant temperature while the other surface is fixed to a temperature of zero Kelvin. Thus the second surface can only act as an

absorber and reflector but does not emit radiation itself. In order to evaluate the accuracy of the numerical approach for view factor determination as well as the influence of the considered emitted rays, an analytical solution for the view factor has to be found as a reference value. Figure 3.21 right shows the test case geometry in closer detail. The surfaces have the dimension $a \cdot b$ and are facing each other at the distance l. The resolution of surface elements is varying and influences the accuracy of the numerical view factor computation. In order to find an analytical solution for the resulting view

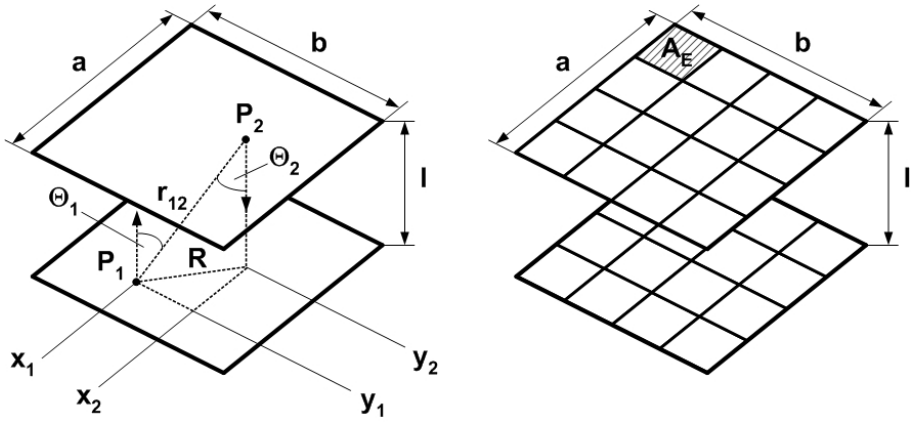

Figure 3.21: Verification test case.

factor, the view factor integral as defined by equation (3.41) has to be solved for the test case geometry. In a local Cartesian coordinate frame with axes x, y, z the surface derivatives for two surfaces with index 1 and 2 can be expressed as

$$dA_1 = dx_1\, dy_1, \quad dA_2 = dx_2\, dy_2\,. \tag{3.72}$$

Figure 3.21 right shows the geometrical arrangement of two parallel surfaces lying in the xy-plane where the z-direction points in surface normal direction. By introducing the surface points P_1 and P_2 on the surface planes with coordinates x_1, y_1 and x_2, y_2 it is possible to formulate geometrical relations between the angles Θ_1, Θ_2, the distance r_{12} and the integration variables x_1, y_1, x_2, y_2 for each possible combination of P_1 and P_2:

$$\Theta_1 = f(x_1, y_1, x_2, y_2, z_1, z_2), \tag{3.73}$$
$$\Theta_2 = f(x_1, y_1, x_2, y_2, z_1, z_2), \tag{3.74}$$
$$r_{12} = f(x_1, y_1, x_2, y_2, z_1, z_2)\,. \tag{3.75}$$

Before setting up the geometrical equations, some basic simplifications can be found. For the chosen test case configuration the distance between the two surfaces is constant, therefore $z_1 = 0$ and $z_2 = l$. Due to the fact that the plates are parallel to each other the orientation angles Θ_1 and Θ_2 have to be equal for every combination of P_1 and P_2. As the size of both surfaces is identical, a_1 furthermore equals a_2 and b_1 equals b_2:

$$a_1 = a_2 = a \quad b_1 = b_2 = b \quad . \tag{3.76}$$

For the description of angles Θ_1, Θ_2 and the distance r_{12} in terms of local coordinates the projection of point P_2 on plane 1 is considered. The distance between the projection

of P_2 and the point P_1 is defined as the distance R and can be expressed as:

$$R = \sqrt{(x_2 - x_1)^2 + (y_2 - y_1)^2}\,. \tag{3.77}$$

Now r_{12} can be formulated as

$$r_{12} = \sqrt{R^2 + l^2} \quad , \tag{3.78}$$

and the angles can be evolved to

$$\cos\Theta_1 = \cos\Theta_2 = \frac{l}{r_{12}}\,. \tag{3.79}$$

With this the view factor integral can be simplified to the form

$$\xi_{1,2} = \frac{1}{\pi ab}\int_0^a \int_0^b \int_0^a \int_0^b \frac{l^2}{((x_2 - x_1)^2 + (y_2 - y_1)^2 + l^2)^2} dx_1 dy_1 dx_2 dy_2\,. \tag{3.80}$$

By introducing the substitutions

$$X_1 = \frac{x_1}{l}\ ,\ Y_1 = \frac{y_1}{l}\ ,\ X_2 = \frac{x_2}{l}\ ,\ Y_2 = \frac{y_2}{l}\,, \tag{3.81}$$

the surface distance l can be excluded from the integral and equation (3.80) simplifies to:

$$\xi_{1,2} = \frac{1}{\pi XY}\int_0^a \int_0^b \int_0^a \int_0^b \frac{1}{(1 + (X_2 - X_1)^2 + (Y_2 - Y_1)^2)^2} dX_1 dY_1 dX_2 dY_2\,. \tag{3.82}$$

This integral for X_1, Y_1, X_2, Y_2 leads to the solution

$$\begin{aligned}\xi_{1,2} = \frac{2}{\pi XY}\Bigg[&\ln\sqrt{\frac{(1+X^2)(1+Y^2)}{1+X^2+Y^2}} + X\sqrt{1+Y^2}\arctan(\frac{X}{\sqrt{1+Y^2}}) \\ &+ Y\sqrt{1+X^2}\arctan(\frac{Y}{\sqrt{1+X^2}}) - X\arctan X - Y\arctan Y\Bigg]\,,\end{aligned} \tag{3.83}$$

where

$$X = \frac{a}{l}\,,\ Y = \frac{b}{l}\,. \tag{3.84}$$

With a normalised test case configuration of $a = b$ and $a/l = b/l = 1$ the analytical result for the view factor from surface 1 to surface 2 evolves out to a value of 0.199824. As can be seen easily the analytical solution of the integral is only feasible for specific conditions (such as parallel or perpendicular plates). Note that a general analytical solution for arbitrary plate shape and arbitrary orientation has not been found yet. As a consequence numerical methods are the only means of precise view factor implementation for complex model geometries.

In order to do a performance check of the numerical view factor computation test case B is processed with the simple view factor method, the hemisphere method and the complex Gauss integration method for different element resolutions. For the Gauss integration eight integration points have been chosen. Results for the different view factor determination methods are compared with respect to computational accuracy

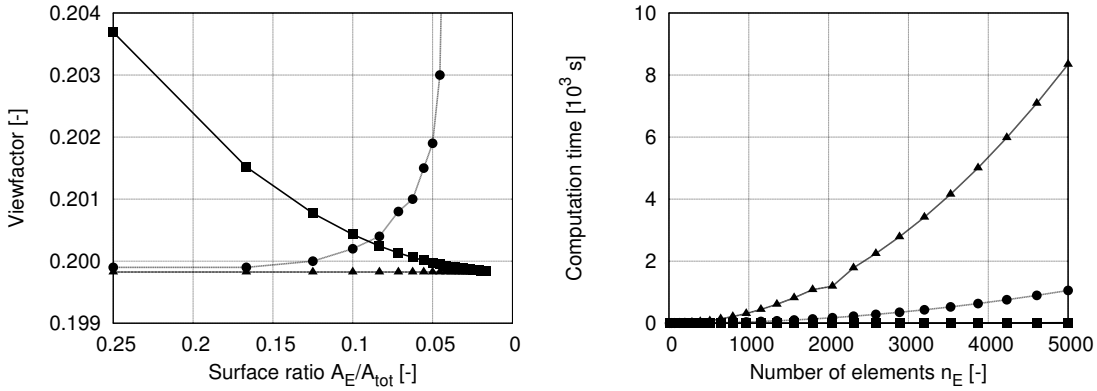

Figure 3.22: Results of numerical view factor integration, test case B. Triangles: Gauss method, circles: hemisphere method, quads: simple view factor method.

and performance. The computations have been performed for different ratios between the single FE surface area A_{E} and the total plate area A_{tot}. This value is specific to the FE mesh and can be chosen freely in conventional FE preprocessors resulting in finer or coarser meshes. Figure 3.22 shows the computed view factors for different $A_{\mathrm{E}}/A_{\mathrm{tot}}$-values. The Gauss view factor option delivers the exact analytical solution for all mesh resolutions but also leads to exponentially rising computation times for a high number of elements. The hemisphere method has been processed with a fixed hemisphere resolution of 50 x 50 elements. As can be seen the computed view factor is close to the theoretical value for small $A_{\mathrm{E}}/A_{\mathrm{tot}}$-ratios. By decreasing the surface FE size, computational errors increase and the view factor is miscomputed. This directly results from the difference in hemisphere and FE resolution. This error can be avoided by scaling the hemisphere resoultion with the FE resolution which leads to exponentially rising computation times. The simple view factor option delivers quick results but also introduces computational errors which decrease with growing $A_{\mathrm{E}}/A_{\mathrm{tot}}$-ratio. Thus a trade-off between the gain in computational speed and the reduction of integration accuracy has to be made. In general the simple view factor option can be used with negligible numerical errors if all surfaces of the model, which interchange radiation with other model parts, obey the relation:

$$A_{\mathrm{E}}/A_{\mathrm{tot}} \leq 0.03\,. \tag{3.85}$$

This effectively introduces a constraint on the resolution of the FE mesh. In other words, the simple view factor option leads to a significant numerical error if the model FE mesh is too coarse. As the view factors determines the radiation fluxes between the surfaces in the model the errors directly translate into corresponding errors in the resulting computed TRP. By comparing the different options, one finds that the Gauss integration option delivers an optimal accuracy which neither depends on the mesh resolution (as the same number of integration points are applied to each element) nor on the distribution of hemispherical surface elements. Therefore the long computation times are acceptable in order to guarantee best computational precision. The simple view factor option can be used to obtain faster results with a lower precision, however here the mesh resolution has to obey the requirement specified in equation (3.85). The

hemisphere option can in principle deliver acceptable computational precision with a lower computation time (compared to the Gauss option), however optimal values for FE mesh resolution as well as hemispherical resolution have determined by subsequent convergence calculations which intensifies the modelling workload considerably. For these reasons the Gauss view factor option will be chosen as the standard option for all TRP computations performed in this thesis.

Another constraint on the configuration of the simulation is the number of discrete rays in the ray tracing approach considered for each element. On the one hand, if the implemented number of rays is too low, surfaces which are exchanging radiation physically may not be detected which would lead to an erroneous computation of the absorption as well as the reflection components of TRP. On the other hand a too large number of considered rays per element results in large computation times and does not necessarily provide new information on the radiation fluxes in the model. Thus the challenge is to make a trade-off between the computational effort and the achievable accuracy of the hit detection. In order to evaluate this ray tracing accuracy and the computational performance, TRP simulations have been performed using test case B with a fixed model size of 800 surface elements and a varying number of rays considered for each individual FE. For the optical parameters of both surfaces as well as for the reference mass the values listed in table 3.2 are considered. With only one plate actively emitting (due to the fact that the other plate is fixed to zero Kelvin) an analytical value of the resulting TRP acting against the emitting surface normal $TRP_{\perp,\mathrm{B}}$ can be calculated to

$$TRP_{\perp,\mathrm{B}} = -\frac{1}{m\,c}(2/3\,\varepsilon_1 + \xi_{1,2} + 2/3\,\gamma_2)\,\sigma\,A_1\,T_1^4 = 4.644 \cdot 10^{-7}\mathrm{m/s^2}\,. \tag{3.86}$$

The numerical results for the TRP for different numbers of considered rays per FE as well as the analytical value are shown in figure 3.23 left.

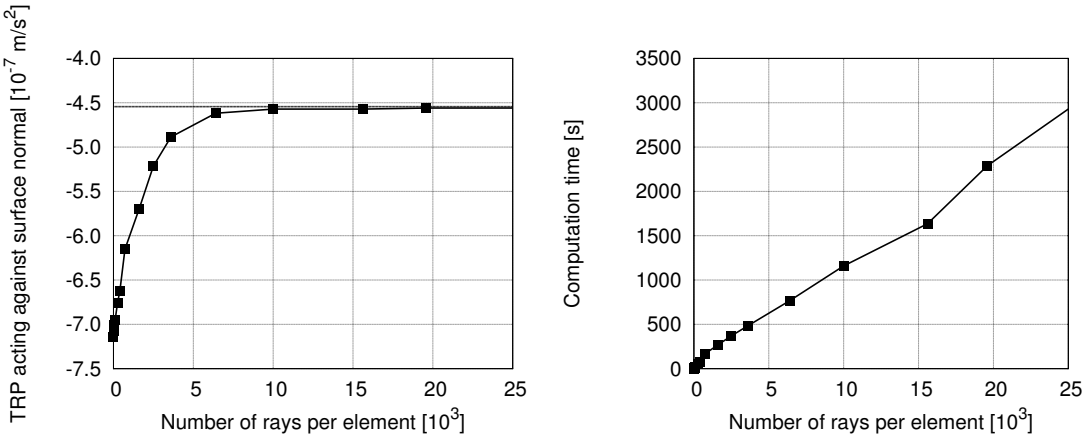

Figure 3.23: Computational accuracy vs. number of rays per element. The analytical obtained value is marked with a solid line.

By comparing the numerical results and the analytical value a huge computational error can be identified for a low number of rays while the computed TRP converges

to the analytical result for high number of rays. The reason for this behaviour can be found in the hit detection logic. If the ray number is too low not all surfaces which are physically receiving radiation from the emitting FEs are identified as receivers in the hit detection step. Effectively this leads to an underestimation of the absorption and reflection computation and thus to an erroneous TRP computation. Beneath a certain threshold value of the number of implemented rays the accuracy of the TRP computation does not increase significantly while the computation time scales linearly with the number of rays. For optimal performance, this threshold value can be found for any model by subsequently repeating TRP calculations while increasing the ray resolution. The optimal value has been found when the computed TRP converges (within a user-specified numerical accuracy). Note that the optimal value for the ray resolution strongly depends on the mesh resolution of the model. For a coarse mesh a low number of rays may be sufficient while a fine mesh requires a considerably higher number of implemented rays to yield an acceptable computational accuracy.

Test case C

Test case C aims at the verification of the implementation of specular ray deflection in the ray tracing method. For this the test case include an emitting surface with a centre distance of $l = 1$ m from a reflective plate at zero Kelvin (and thus not actively emitting itself). The reflective plate may rotate around the angle ϕ as displayed in figure 3.19. A normalised configuration of $a = b$ and $a/l = b/l = 1$ as well as optical parameters defined in table 3.2 are considered. With this the configuration of test case C is identical to test case B for the non-rotated case ($\phi = 0°$). An element resolution of 800 elements as well as the optimal ray tracing resolution identified for test case B are implemented.

The resulting TRP acting against the normal has been computed for discrete ϕ steps of 5°. The results are expressed as the components in z-direction (emitting surface normal) and in y-direction (perpendicular to z in the surface plane. The x-axis is the axis of rotation). Note that only a single reflection is considered. Figure 3.24 shows the resulting TRP components with respect to the rotation angle of the reflecting plate. The TRP component in z-direction reaches a minimum at $\phi = 0$ which effectively means that a maximum of radiation is received by the second plate and reflected back to the first plate. The corresponding y-component evolves to zero as the effective direction of the reflected rays is aligned with z. With this the TRP in z matches the analytical result for the total TRP in test case B (as computed in equation (3.86)). For a rotation of the reflecting plate the y-component of the TRP increases and a maximum evolves for a rotation angle of $\phi = 45°$. Here the reflection angle (angle between incoming and reflected radiation) is 90°. At the same time the resulting z-component of the TRP grows because a smaller fraction of the radiation received by the second plate is reflected into the direction of the first plate.

When the second plate rotates the resulting reflection gains a TRP y-component which has a maximum at 45°. Here the reflection angle (angle between incoming and reflected radiation) is 90°. At the same time the resulting z-component of the TRP grows because a smaller fraction of radiation is reflected into z. By increasing the ϕ further the y-component drops again while the z-component constantly grows until a

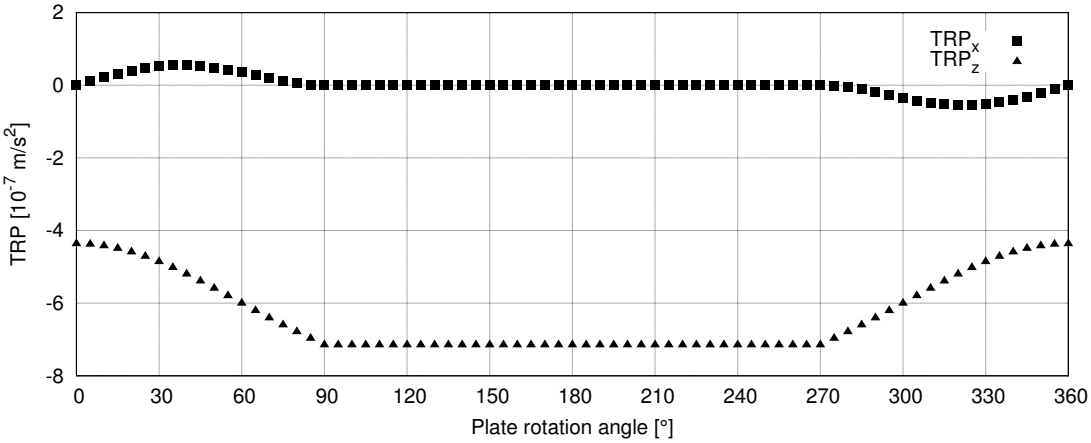

Figure 3.24: Results of test case C.

rotation angle of 90° is reached. For this configuration the second plate is not facing the first plate any more which results in a TRP only determined by free emission. Effectively within the region of rotation angles between 90° and 270° the two plates are not visible each other due to the different orientation of the surface normal vectors. Here the computed value for the z-component matches the TRP result achieved for test case A. For angles larger than 270° the plates again face each other and the y-component turns into the negative range which means that the TRP contribution now faces the opposite direction. With this the computed TRP direction follows the physical reflection law and the magnitudes of the TRP components agree to the analytical results presented in the previous test cases.

Test case D

Test case D aims at the verification of the correct implementation of the treatment of multiple reflections. For this the geometrical configuration of test case B is considered while allowing a different number of subsequent reflections. Here only specular reflections are considered. In difference to the parameters specified in table 3.2 a refection coefficient of $\gamma_\mathrm{s} = 0.8$ has been chosen to realise significant reflected radiation fluxes. The element resolution of radiating and reflecting plate is chosen to one. Effectively only two parallel FE surfaces facing each other are included in the test case model. As a result all radiation fluxes will be aligned to the normal direction of the emitting plate and multiple reflections will only change the magnitude but not the orientation of the TRP which enables an analytical description of the TRP with respect to the number of considered reflections. The analytical value for the resulting TRP aligned with surface normal direction $TRP_{\perp,\mathrm{D}}$ can be calculated with

$$TRP_{\perp,\mathrm{D}} = TRP_{\perp,\mathrm{emi}} - TRP_{\perp,\mathrm{abs}} + (-1)^n \gamma_s^{n-1} TRP_{\perp,\mathrm{abs}}\,, \tag{3.87}$$

where n is the total number of considered subsequent reflections and $TRP_{\perp,\mathrm{emi}}$ and $TRP_{\perp,\mathrm{abs}}$ denote the TRP components of free emission and absorption, respectively which are known from the results acquired for test cases A and B. For each new reflection of the radiation flux between the two surfaces a new correction of the TRP is necessary since a part of the reflected flux is absorbed and the further reflected part changes

its direction with respect to the incoming flux. Thus a resulting value of $TRP_{\mathrm{z},res} = 1.433 \cdot 10^{-7} m/s^2$ can be computed as a converged value. The numerical result for a different number of included reflections is displayed in figure 3.25 left. The converged

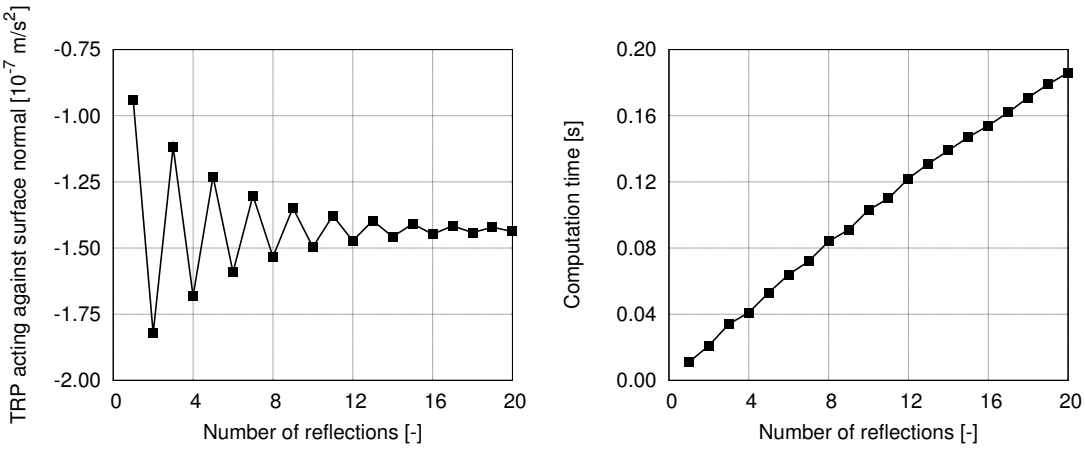

Figure 3.25: Results of test case D.

numerical results are in agreement with the analytical value and also follow equation (3.87) for the the unconverged region. For a low number of considered reflections the resulting TRP differs considerably from the converged value. For a greater number of included reflections the computed TRP fluctuates around the converged value until convergence is reached for about 20 reflections. The fluctuation directly results from the changing sign of the reflection component for each new reflection. At the same time, the magnitude of total reflected flux decreases for each new reflection as the coefficient of emission is smaller than one. Note that for a realistic spacecraft model convergence usually is reached quicker as most of the rays are not reflected a high number of times. Here the inclusion of 3-4 reflections has proven to be sufficient. Looking at the computation time needed for the different test runs (displayed in figure 3.25 right), a linear dependency of computation time to the number of considered rays can be identified. In the test case this is caused by the fact that every ray is reflected and thus the total number of processed rays is scaled by the number of considered reflections. Again, in a realistic spacecraft model not all of the emitted rays are reflected which means that the factor of computation time increase for a higher number of considered reflections will be less drastically.

Test case E

Test case E aims at the analysis of the computational errors caused by geometrical modelling inaccuracies. For this an emitting plate element is inserted into an absorbing hemisphere which itself does not emit any radiation. As the source element radiates with a hemispheric pattern of emission, under ideal conditions no radiation fluxes can escape from the enclosure and the absorption component of the TRP has to equal the emission component thus not generating a net TRP. For this the reflection coefficient of the hemisphere is set to zero, the diameter of the hemisphere is set to $d_{\mathrm{hs}} = 1$ m and for the dimensions of the plate $a = b = d_{\mathrm{hs}}$ is chosen. If the shape of the reflecting hemispherical body differs from the ideal hemisphere (as is the case for a too low number

of FEs on the hemispherical surface, as this will not model the curvature correctly) a computational shape error results. In order to quantify this error, the resulting deviation of the TRP absorption component from the TRP emission component, which is a direct measure for the shape error has been computed for different number of elements on the hemisphere. Here the TRP difference have been plotted as percentage of the PA in order to quantify the element sizes needed for the Pioneer 10 FE model which lead to acceptable shape errors. The results are plotted in figure 3.26 left.

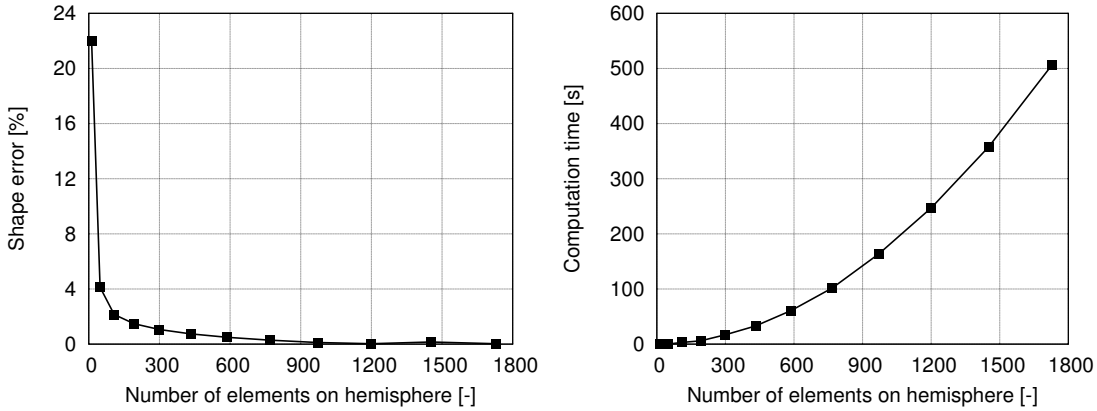

Figure 3.26: Results of test case E.

As can be seen, a low number of elements results in a high shape error because the model shape resembles the ideal hemisphere only poorly. By increasing the number of implemented elements on the hemisphere, the agreement of model shape and ideal hemisphere increases and the shape error reduces. At the same time, the computation times increases linearly with the number of elements as displayed in figure 3.26 right. Thus a trade-off between computational accuracy and computation time has to be made. An acceptable numerical error (with respect to the magnitude of the PA) can be identified for an element resolution of about 1000 elements. With the chosen geometrical test case configuration this corresponds to an element surface area of $3.14 \cdot 10^{-3}$ m^2 with an element edge length of 0.056 m for quadrilateral elements. In general for smaller radii, a higher element resolution is needed while for larger radii a lower element resolution delivers acceptable results. The optimal element resolution has to be determined by subsequently repeating TRP computations for growing element resolution until convergence is reached.

Test case F

Test case F aims at the determination of the computational error due to numerical inaccuracies. For this a symmetric model geometry consisting of two spheres with radius $r = 1$ m at the same surface temperature $T = 300$ K has been defined. The spheres are fixed (with respect to each other) at a centre distance of 5 m. (If the centres would not be fixed the TRP would have to be computed for each sphere individually as they would push each other away). TRP is expressed with respect to a system reference mass of 1 kg. The optical parameters of the sphere surfaces are taken from table 3.2 for

both spheres. By applying the same element resolution and the same meshing method on both spheres an identical FE mesh will evolve for all chosen element sizes.

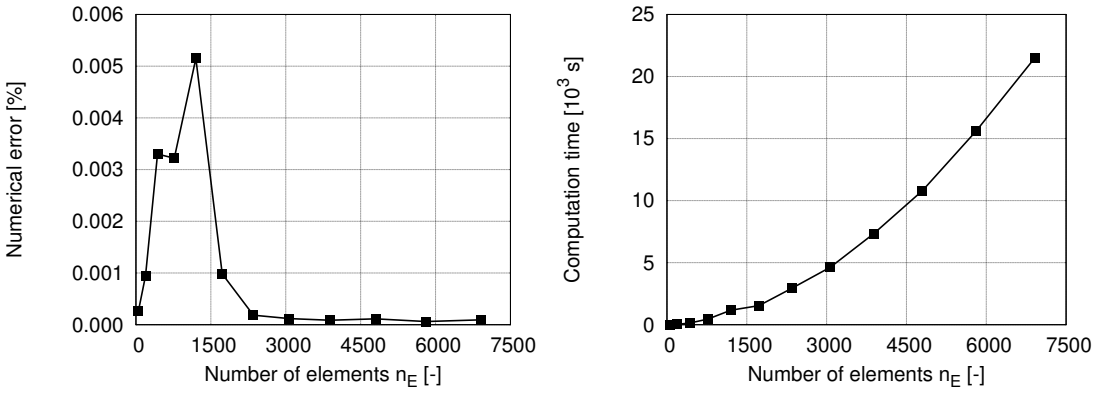

Figure 3.27: Results of test case F.

Resulting from this, all emission, absorption and reflection TRP components on the one sphere will have a respective symmetric TRP component on the other sphere effectively cancelling out all net TRP contributions. With this the total resulting TRP acting on the system has to evolve to zero in the ideal case. Realistically numerical inaccuracies in software as well as numerical limitations of the hardware delimit the total achievable numerical accuracy.

The resulting TRP acting on the system has been determined with different element resolutions. Here the numerical error is defined as the ratio of the total computed TRP magnitude to the magnitude of the PA. For the computation the optimal simulation configuration parameters (ray tracing resolution etc., as defined by test cases A - E) have been considered. In general, the needed computation times grow exponentially with the number of elements as displayed in figure 3.27 right. The obtained numerical errors are plotted in figure 3.27 left. It can be seen that a small numerical error develops for low element resolutions. This mainly results from inaccuracy introduced by the only coarse resemblance of the model surface to the realistic spherical shape. Further causes could be positioning errors which may be introduced by the import procedure. These errors possess a higher influence on the TRP for a low number of elements, since higher element resolutions lead to an averaging of such inaccuracies. Nevertheless, the maximum error is in the range of 0.005 % which shows that the numerical errors resulting from hardware and software are negligible with respect to PA investigations, if optimal values are chosen for the simulation configuration.

Part II

Thermal perturbation analysis for Pioneer 10

Chapter 4

The Pioneer 10/11 Missions

This chapter gives an overview of the main mission goals and the characteristics of the Pioneer 10 mission. An introduction to the so called Pioneer anomaly is delivered and the investigation of thermal perturbation acting on the Pioneer 10 spacecraft is motivated. The general spacecraft design as well as geometrical details are discussed.

4.1 Mission goals and trajectory

On 2nd of March 1972 Pioneer 10 was launched from Cap Canaveral and passed Jupiter in December 1973. That launch marked the first use of the Atlas-Centaur as a three-stage launch vehicle which was needed in order to gain enough speed to reach the outer parts of the solar system. Since Jupiter encounter (approximately 21 months after launch) the spacecraft has been following its hyperbolic trajectory roughly on the ecliptic plane and is now well beyond the borders of our solar system, approximately at a distance from earth of 100 AU. Thus Pioneer 10 is the most far-away man-made object to date. The twin spacecraft Pioneer 11, identical in design, was launched on the 5th of April 1973 and followed a trajectory opposite of the Pioneer 10 trajectory with a Jupiter and a Saturn encounter. The trajectories of both spacecraft are displayed in figure 4.1. As can be seen the spacecraft left the boundaries of our solar system in 1983 and 1990 respectively. One of the main goals of both missions was to perform celestial mechanics experiments which could be realised very accurately due to the spin axis stabilisation of the crafts. Being the first missions to explore the outer solar system, a variety of scientific goals were planned. As the Pioneers were the first crafts to pass the asteroid belt, the exploration of the nature of the belt was one of the dominant scientific tasks. With Jupiter and (only for Pioneer 11) Saturn encounters the environmental and atmospheric characteristics of both planets could be explored in detail. Furthermore the Pioneers were to explore the interstellar medium in the outer solar system in the regions beyond Jupiter, with emphasis on the exploration of energetic cosmic rays as well as high energy solar particles.

Originally both missions were only designed for a duration of 2 - 3 years. Due to the robust design of the crafts and the comparatively stable power source, Pioneer 10 has been functional for over 30 years which enabled a high number of additional scientific experiments. Pioneer 11 has performed an encounter with Saturn after travelling a distance of approximately 9 AU across the solar system plane which resulted in the

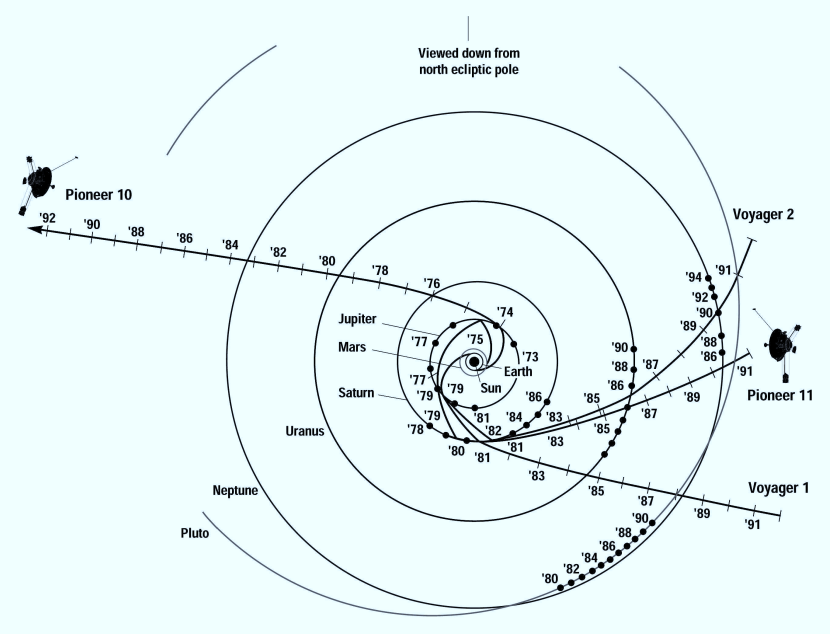

Figure 4.1: Trajectories of Pioneer 10 and 11 [52].

first close-up examination of Saturn by a space probe on the first September 1979. With this both missions were very successful both in engineering as well in scientific return. The last signal from Pioneer 10 was received on the 23rd of January 2003. At this time the craft had already reached a distance from the Earth of 82 AU. All subsequent attempts to establish a connection has failed since and it has been concluded that the total available power on the spacecraft is no longer sufficient for the transceiver to send a signal to Earth. The last contact with Pioneer 11 has been established in November 1995, however due to a technical failure in a microwave relay, the Pioneer 11 communication system could not be used in coherent mode anymore. Thus no precise Doppler data exists for Pioneer 11 after the year 1990.

4.2 The Pioneer anomaly

Due to the design of the spacecraft (spin stabilisation with minor attitude thruster control) and the implemented hardware (mode transceiver) Pioneer 10 and 11 could be used for a high number of celestial experiments. Resulting from this one of the most precise spacecraft navigation to date could be realised for both missions for a duration of approximately a decade. Due to the successful course of the mission, in 1979 the JPL proposed the extension of the mission duration to perform deep space celestial experiments. During this time the JPL analysed the existence of unmodeled accelerations in the trajectories of the both crafts. The motivation for this was the search for an undiscovered outer planet and other objects beyond Neptune. For this the Pioneer satellites were suited very well due to the high achievable acceleration sensitivity in the range of $10^{-10}\mathrm{m/s}^2$. Although no new planets were discovered the work led to the detection of a small apparently constant Doppler frequency drift to which both spacecraft were subject. While comparing the simulated orbits and the orbit reconstructed from

received Doppler data, a small constant deceleration of the craft became apparent. The resulting Pioneer 10 Doppler residuals for the mission years 1987 to 1994 are displayed in figure 4.2.

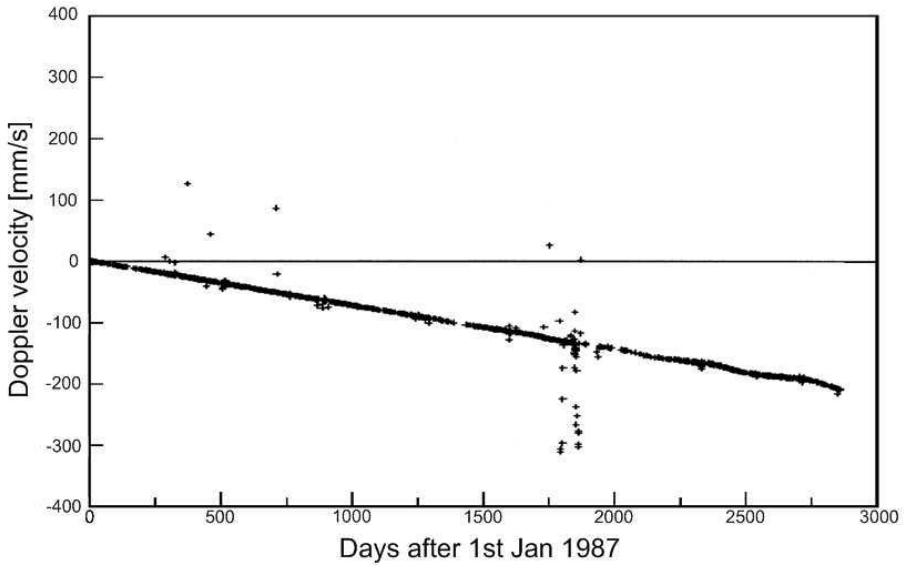

Figure 4.2: Pioneer 10 Doppler velocity residuals [9].

It is clearly visible that the resulting residual Doppler velocity decreases constantly with a mean value of $8.74 \cdot 10^{-10}\mathrm{m/s}^2$ which has become know as the Pioneer anomaly (PA). A later evaluation of Pioneer 11 Doppler data showed the same result which is remarkable due to the different orbits of both crafts. Although these findings were already published by Anderson et al. in 1998 [9], no conclusive answer to the origin of the PA has been found up to now. Many theories favour new physics such as Modified Newtonian Gravity (MOND) [12], dark matter [72] or the expansion of the universe [73] as the origin of the observed deceleration. Conventional effects have mostly been ruled out as possible sources [52]. However, the existence and resemblance of the anomaly for both crafts suggests that the effect might be connected to the geometry of the crafts.

Currently efforts for the evaluation of the complete Pioneer Doppler data (including the early mission) are undertaken by the JPL. In a recent status report it is predicted that with evaluation of the complete data set the constancy of the anomaly might change to decreasing acceleration by up to 20 % in 30 years [57].

4.3 Motivation for thermal investigations of the Pioneer spacecraft

In 2002 Anderson et al. published a detailed investigation on possible origins of the PA [18]. Here it was argued that a very small fraction of the total waste heat energy produced by the RTGs could explain the magnitude of the observed anomaly. For this the radiation pattern of Pioneer 10 and 11 would have to be such that an asymmetry arises from RTG radiation reflected off the high gain antenna rear surface. Initial es-

timations perforemd by the JPL indicated a maximum of about 2% of reflected RTG energy which would explain only half of the magnitude of the observed PA. Furthermore, the constancy of the PA seems to be in contradiction to a thermal source of the anomaly, because one would expect to see the decaying effect on the fuel sources in the Doppler residuals. This argument has been alleviated only recently by the now available analysis of the larger Doppler data set, which comes to the conclusion that the observed PA is not necessarily constant but that a decrease of the effect over the mission duration is realistic [74].

In 2007 the so called Pioneer collaboration, an international team of scientists with the goal to resolve the PA was established with support of the International Space Science Institute (ISSI). During the course of the collaborative work it became clear that the existing level of detail in the available thermal investigations of the Pioneer 10/11 spacecraft was too low to exclude thermal effects as source of the PA. All groups acknowledge that, though hard to realise, a detailed thermal model is needed to analyse the role of thermal effects in the formation of the PA [75]. In 2008 Bertolami et al. proposed an improved estimation method for thermal recoils [56]. With this he came to the conclusion that there is a significant thermal recoil acting on the Pioneer spacecraft. Still the calculations were performed without the inclusion of geometric and optical surface properties details and do not present a final value.

The intriguing fact that only 60 W of directed power emission (out of a total of 2500 W at BOL) are sufficient to explain an effect in the magnitude of the PA makes a very thorough analysis of the effect necessary. In order to realise this the accuracy of the models for the calculations of surface temperature distributions as well as the models for the resulting thermal recoils have to be improved considerably. Simple lumped mass, cannonball or box-and-wing models are not sufficient to compute a realistic surface temperature distribution on the complex structure of the Pioneer 10/11 satellites with various outer payloads, louver systems and different optical surface properties. In order to perform a sophisticated analysis of surface temperatures for the Pioneer 10/11 spacecraft a full detailed thermal FE analysis is required. Using this approach it will be possible to evaluate the influence of changing model parameters on the resulting thermal recoil. This is particularly of interest for the analysis of degradation effects which have never been included in the established estimation methods. The recoil forces have to be computed with the inclusion of a detailed geometric surface model of the spacecraft where optical surface parameters are assigned to each model component. A numerical force computation method increases the possible implemented geometric detail considerably.

In conclusion, thermal effects have not yet been analysed at the level of detail which is necessary to evaluate the influence of thermal recoils on the observed Pioneer anomaly. With a detailed thermal FE model, sophisticated surface temperature distributions can be calculated with the inclusion of sensor data and the detailed Pioneer 10/11 spacecraft geometry. Based on this the resulting recoils can be computed by using ray tracing approaches with inclusion of surface to surface interaction and multiple reflections. This approach will enable the most precise evaluation of thermal recoils for Pioneer 10/11 to date.

4.4 Spacecraft design

General design

The main geometrical features of both the Pioneer 10 and 11 spacecraft are a 2.74 m diameter High gain antenna, two hexagonal compartments for experimental payloads and satellite bus hardware (separated in a bigger main compartment and a smaller experiment section compartment) and 4 radio isotopic thermal generators (RTGs) which are mounted in pairs of two at an angle of +60 and -60 degrees from the body axis. The RTGs are connected to the main compartment with extensible booms which were deployed to a distance of 3 m from the main compartment centre after separation from the booster stage. A third boom which holds a magnetometer was deployed at a distance of 6 m to minimise magnetic influences of the craft on magnetic field measurements.

The main components of the compartment structure are the cover- and base plate, the side panels, the mounting panel dividing the compartment into equipment and experiment section and the fuel tank which is embedded into the cover plate. With exception of the mounting panel, all compartment panels consist of aluminium blank sheet mounted on an aluminium honeycomb support. The mounting panel solemnly consists of an aluminium blank sheet without any further support. All interior surfaces are painted black to realise optimum radiative heat transport within the compartments. The exterior panel surfaces are covered with Multi-layer insulation (MLI) except for parts the base plate where passive louver systems are mounted on both compartments. Here only surfaces belonging to neither louver systems nor launch adapter are covered with MLI. Figure 4.3 shows the main geometrical features of the craft.

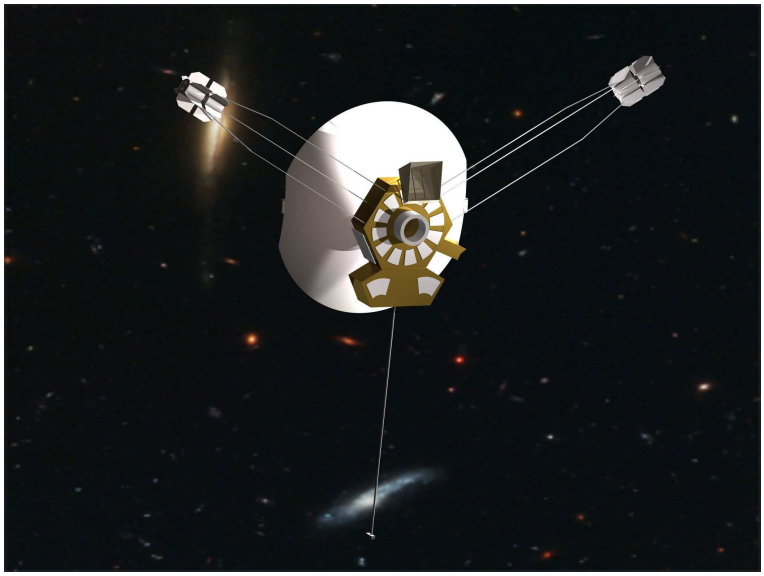

Figure 4.3: Pioneer spacecraft design.

At launch the total mass of both spacecraft was about 260 kg of which 30 kg was propellant fuel. Due to various manoeuvres and attitude corrections this mass decreased during the mission. While Pioneer 10 performed no major attitude manoeuvres, Pio-

neer 11 used extensive fuel during Jupiter encounter thus using up to 3/4 of its total propellant mass. Estimations performed by the JPL suggest an end-of-mission mass of 250 kg for Pioneer 10 and 232 kg for Pioneer 11 [16]. Pioneer 10 and 11 carried an identical set of 11 scientific experiments, Pioneer 11 had a 12th experiment. Furthermore various bus hardware for on board data handling, communication and housekeeping was mounted in the main compartment.

High gain antenna

The Pioneer 10 compartment is divided into a large central equipment section and a smaller experiment section. A high gain antenna is mounted to the compartment with fixed guiding rods. A medium gain antenna is fixed to the HGA at an angle of 5.71°. The main geometrical dimensions of compartment and antennas are displayed in figure 4.4. Thruster assemblies for craft spin-up and nutation control as well as a

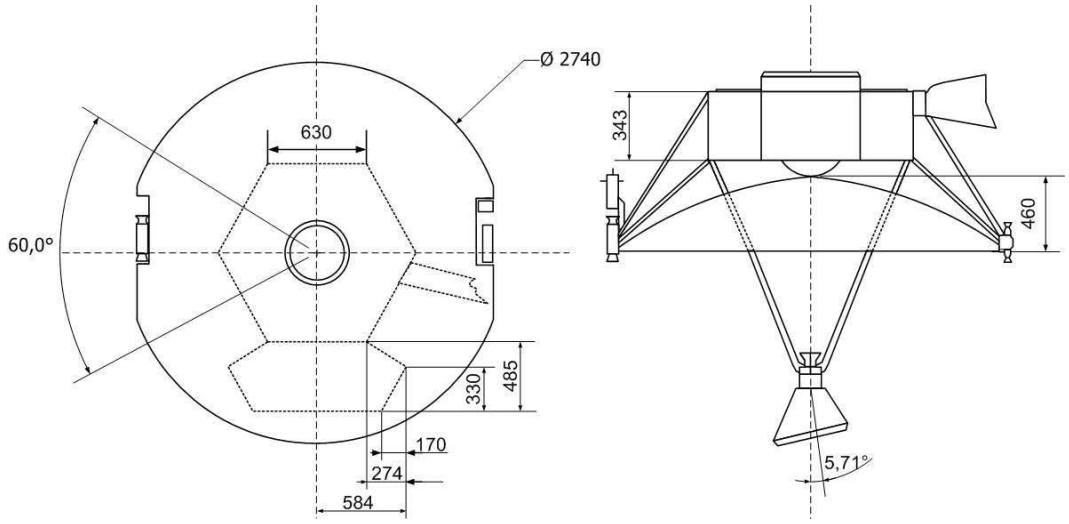

Figure 4.4: Geometry of HGA and compartment [76].

sun sensor assembly are mounted to the flat HGA sides. In order to keep the thrusters at operational temperatures, radio isotopic heater units have been attached to the thrusters.

Compartment

The Pioneer compartment composed by the large hexagonal equipment section and the smaller experiment section harbours all satellite bus hardware and most of the scientific equipment. Several openings on the side panels have been implemented for sensors of the science experiments. The position of the main internal and external payloads inside and on the compartments is shown in figure 4.5. The legend for figure 4.5 is given in table 4.1.

The outer compartment surfaces (without the louver system surfaces) are covered in Multi-layer insulation. Main outer geometrical features are a sun shield, a shunt radiator and a meteoroid detector assembly. A large magnetometer boom (not displayed) is attached to the experiment section -X panel. A fuel tank is integrated into

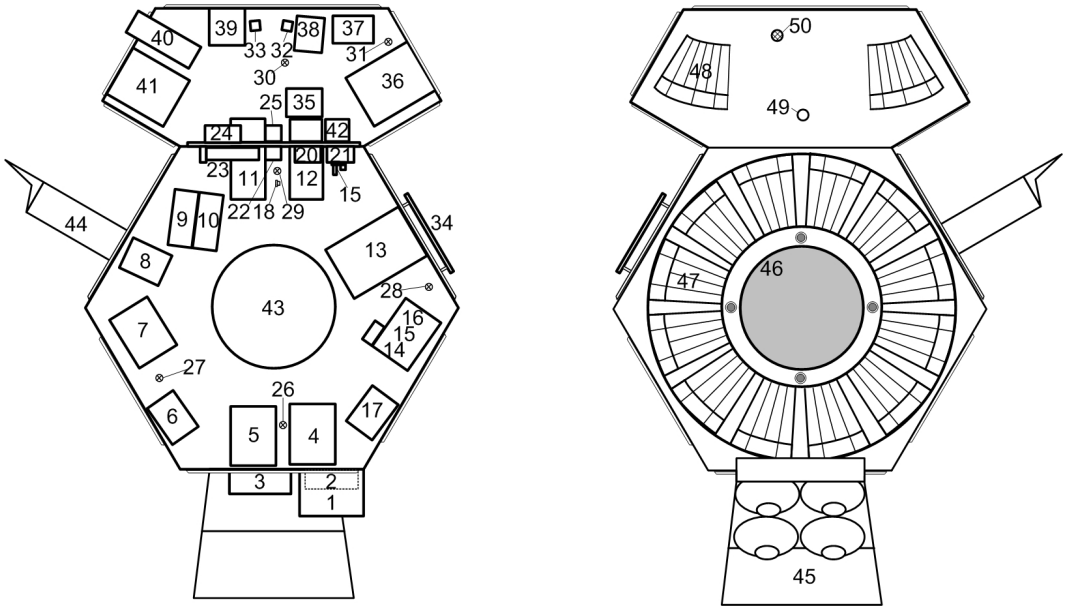

Figure 4.5: Pioneer payload and hardware configuration [76], front (left) and rear (right side).

No.	Component	No.	Component	No.	Component
1	Data storage unit (DSU)	18	Attenuator TWT No. 1	35	Magnetometer Electronics
2	Asteroid/Meteoroid Detector Electronics	19	Attenuator TWT No. 2	36	Imaging Photo-Polarimeter
3	Battery	20	Transmitter Driver No. 1	37	Geiger Tube Telescope
4	Power Control Unit (PCU)	21	Transmitter Driver No. 2	38	Ultraviolet Photometer
5	Central TRF Unit	22	Transfer Switch - receive	39	Trapped Radiation Detector
6	Inverter Assembly No.2	23	Diplexer No.2/Coupler	40	Infrared Radiometer
7	Command Distribution Unit	24	Diplexer No. 1	41	Charged Particle Instrument
8	Stellar Reference Assembly (SRA)	25	Transfer Switch - Transmit	42	Meteoroid Detector Electronics
9	Receiver No. 1	26	Thermistor No. 1	43	Propellant Tank
10	Receiver No. 2	27	Thermistor No. 2	44	Sun Shield
11	TWTA No. 1	28	Thermistor No. 3	45	Meteoroid Shield
12	TWTA No. 2	29	Thermistor No. 4	46	Launch Adapter
13	Digital Telemetry Unit (DTU)	30	Thermistor No. 5	47	Main Louver Assembly
14	Control Electronics Assembly (CEA)	31	Thermistor No. 6	48	Secondary Louver Assembly
15	Conscan Signal Processor	32	Despin Sensor No. 1	49	Low Gain Antenna
16	Digital Decoder Unit	33	Despin Sensor No. 2	50	Photometer Sensor
17	Inverter Assembly No. 1	34	Shunt Radiator Assembly		

Table 4.1: Legend for figure 4.5, definitions are derived from Pioneer Program Documentation [76].

the equipment section and protrudes into the space between compartment and HGA surface with approximately a third of its total diameter. The outer tank surface is also covered with MLI. On the compartment rear the launch adapter is centred on the equipment section ground panel. Here the adapter surfaces are bare aluminium while the equipment section surface engulfed by the launch adapter is again covered in MLI.

RTGs

As primary power source Pioneer 10 and 11 both carried 4 RTGs which provided a total thermal power of 2600 W at begin of life (BOL). The general design of the SNAP-19 RTG is displayed in figure 4.6. The outer shape is dominated by the radiation fins (e), which emit the produced waste heat into space, and the outer RTG housing (b). In the centre of each RTG a stack of 18 Plutonium (Pu-238) discs is mounted as the radioactive heat source. The fuel capsule is completely contained in a multi-layered shielding capsule (c) which is cylindrical in shape and possesses hemispheric

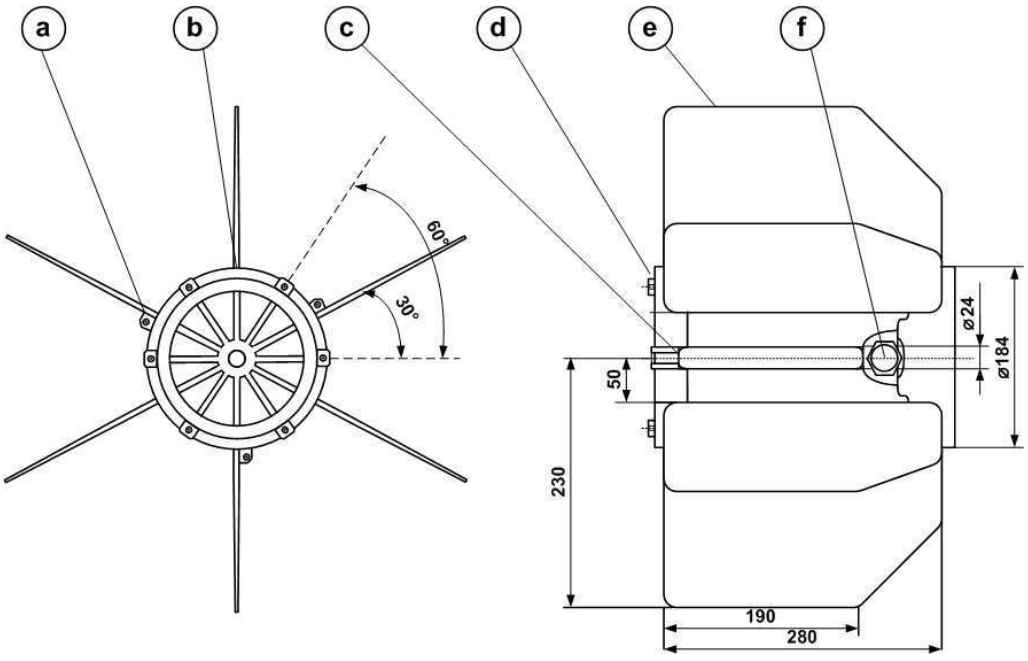

Figure 4.6: SNAP-19 RTGs front and side view [76].

end closures (d). The shielding capsule is held by two sleeve supports and two capsule support rings inside a graphite heat shield with a hexagonal cross section. The ends of the graphite shield are sealed with heat insulation disks and a graphite end plug is screwed into the heat shield on both sides. Thermoelectric converters are attached to each of the six flat sides of the heat shield. These converters consist of thermopiles which transform part of the heat energy provided by the radioactive fuel to electrical energy. The maximum fraction of converted energy is governed by the heat gradient between the hot junction (at the heat shield) and the cold junction (fin root). The generator outputs (f) are the electrical interfaces to the spacecraft. Beneath the converters heat sink bars are attached which conduct waste heat to the outer housing. Six radiation fins (e) are wielded radially to the hermetic housing and are used to dissipate the waste heat into space. For this purpose the outer fin surfaces are painted with a high emissive white coating. Wielded end covers seal the housing of each RTG at both ends. Each two RTG assemblies forming one of the RTG assemblies are mounted to each other and connected to the compartment by three guide rods.

Thermal subsystem

The thermal subsystem is designed as a completely passive system including a primary louver system, a secondary louver system, a shunt radiator and several heaters on the external surface. The primary louver system is mounted radially around the launch adapter on the rear side of the main compartment. It consists of 24 individually actuated highly reflective louver blades which are mounted on high emissive coated second surface mirrors. A bimetallic spring is thermally connected to the platform and controls the louver opening angle according to the equipment section temperature in the vicinity of the louver assembly. The main principle is shown in figure 4.7.

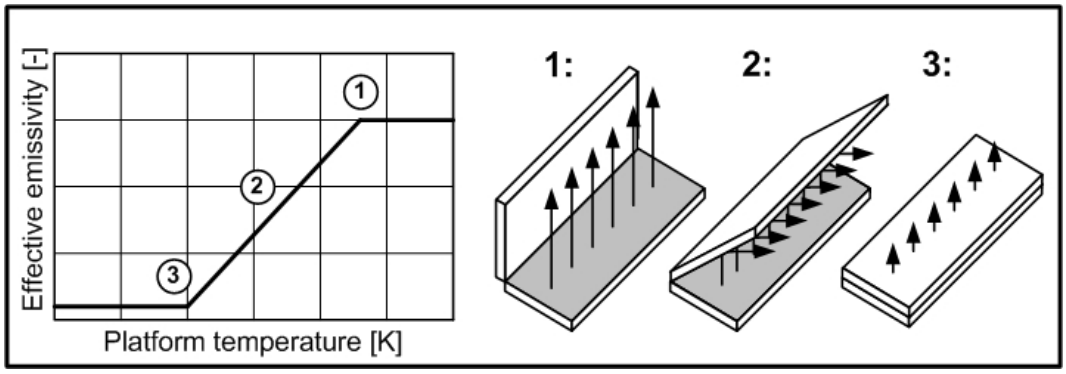

Figure 4.7: Principle of passively controlled heat rejecting louver [76]. 1: High emittance, 2: Medium emittance, 3: Low emittance.

When the platform has a high temperature the louvers are completely open and the high emissive surface can emit radiation nearly unblocked into space, for lower temperatures the louver angle decreases and partly blocks the emitted radiation thus causing a reduced effective emittance. For a completely closed louver (which corresponds to a cold platform temperature) the emittance is only characterised by the optical properties of the louver blade, emission from the second surface mirror is completely blocked. In case of Pioneer this leads to a very low effective emission coefficient of $\varepsilon_{\text{eff}} = 0.04$.

The secondary louver system with six louver/second surface mirror pairs is mounted on the experiment section in assemblies of three louvers each. In addition to the heat rejecting louver system a shunt radiator is used to dissipate a surplus of energy from the main compartment. As the fraction of electrical power provided by the RTG assemblies can not be controlled directly, the shunt radiator is used as an indirect energy control by transforming all electrical energy not needed by payloads or electrical infrastructure into heat. This heat is then dissipated into space by the shunt radiator surface. For the early mission times when a surplus of electrical energy was available the shunt radiator thus emitted a considerable amount of heat which dropped over time (governed by the rate of decrease of electrical energy) until it became negligible for the later mission times.

Chapter 5

Pioneer Finite Element model

This chapter describes the Pioneer FE model including details on model geometry, material models and boundary conditions. The APDL-approach taken for the modelling of the satellite components as well as the individual modelling steps needed to perform a steady state thermal analysis for the Pioneer 10 spacecraft are discussed in detail.

5.1 Model overview

For the computation of thermal recoil forces acting on the Pioneer 10 spacecraft the equilibrium surface temperatures have to be determined for discrete points in time during the course of the mission. Keeping in mind that the external environmental conditions such as the solar flux as well as the internal conditions (e.g. the state of the radioactive decay of the RTG fuel, the degradation of the optical properties or ageing of the electrical hardware) change during the mission, an approach where any input parameters of the model can be varied to realise parameter variations and sensitivity analysis is preferable.

In order to realise an according approach the *ANSYS Parametric Design Language* (APDL) has been selected as the main modelling tool for the generation of the Pioneer 10 thermal FE model. APDL is a macro-based method where all preprocessing is performed by means of APDL code instead of a graphical user interface. This complicates the modelling but also leads to a much greater control over the FE simulation compared to corresponding GUI methods. The coding in macros enables the complete atomisation of an FE simulation (by means of a batch run) as well as the automatised run of subsequent analysis with input parameter updates. Furthermore the individual modelling steps (as described in section 3.5) can be realised as individual sub macros which increases the overall clarity of the model considerably. The following sections will introduce the macro structure and summarise the different component models included in the Pioneer 10 FE macro.

5.2 Pioneer 10 FE macro structure

The Pioneer 10 APDL macro is composed of a set of different sub level macros which perform specific modelling tasks. Four different levels of hierarchy have been implemented:

1. The *Top level* macro controls and interfaces the complete modelling process.

2. *Task level* macros control the modelling process for one of the major Pioneer 10 components such as high gain antenna, compartments and RTGs. Furthermore macros for the control of the numerical parameters of the FE simulation (such as solver or time-stepping options) as well as post processing options are situated at this level.

3. *Modelling level* macros implement the main FE modelling steps such as the creation of GMM, mesh, material definition and boundaries.

4. *Auxiliary level* macros are used by the modelling level macros for specific operations which are used several times.

Besides the macro levels discussed above, a couple of external macros which enable the mesh control for the whole satellite model and the parameter update for subsequent simulation runs have been developed. A set of general top level help functions including coordinate system specifications and specific geometric modelling tasks is available to all levels of macros. An overview of the Pioneer 10 FE macro structure is displayed in figure 5.1.

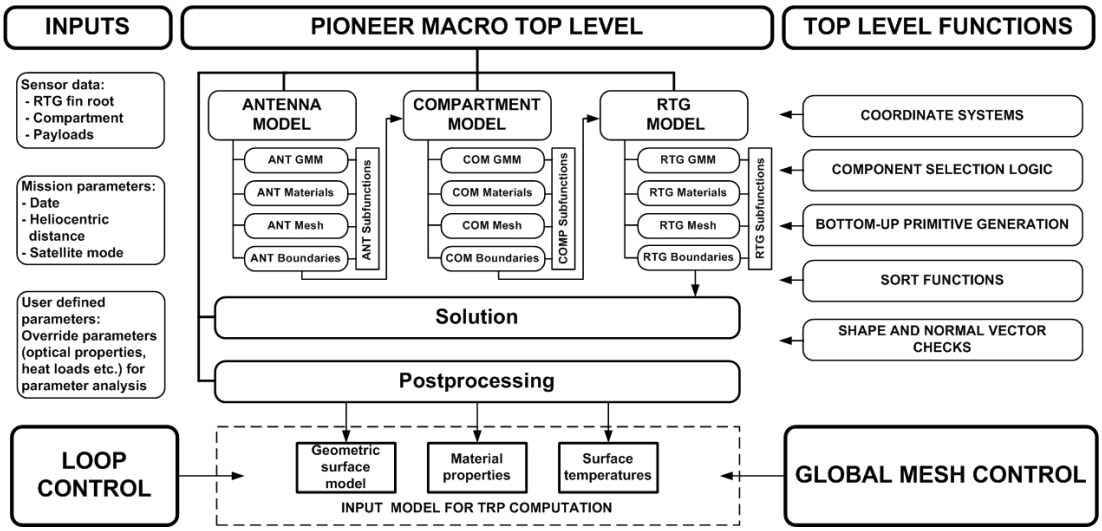

Figure 5.1: Structure of the Pioneer 10 FE APDL macro.

In order to perform a thermal FE analysis with the Pioneer 10 macro, a set of input data files and parameters have to be provided. These inputs are:

1. **Sensor data files**: The sensor data files contain the temperature sensor data on RTG fin roots as well as the six compartment sensors for the complete modelled mission part. Furthermore data files containing the available electrical energy as well as the waste heat produced by the RTGs have to be specified.

2. **Mission parameters**: Mission parameters include the date of the simulated point of time, the current heliocentric distance (for the computation of the solar flux) as well as the current satellite mode, which effects how the electrical energy is distributed over the internal payload boxes. For this the satellite modes

specified in [76] can be simulated by defining the measured temperatures directly as boundaries on the payloads. A more general approach is the calculation of the available electrical energy from compartment and RTG telemetry. This is the standard mode of operation assumed in the Pioneer 10 macro. All sensor file information will be extracted and interpolated from the sensor data files with respect to the chosen simulation date. For the simulation of a complete orbit the macro has to be processed subsequently with a changing simulation date.

3. **User defined parameters**: These parameters can override internal parameters such as optical surface properties, conductivities etc. With this a parameter analysis (e.g. the determination of the influence of surface degradation on the resulting surface temperatures) becomes feasible by repeating the simulation while changing the user-defined parameters.

As the Pioneer 10 macro composition is based on a modular approach the task level macros can also be used individually which enables the inclusion or exclusion of different satellite components into the analysis. In example the RTGs and the HGA may be included while the compartment macro is excluded from the model. This enables a closer examination of each component and the resolution of dependencies between those. Furthermore the (unblocked) contribution of each component to the resulting TRP may be resolved by this method. For the material and geometric parameter set a baseline model with default values has been defined. Each parameter can be overrode to analyse the influence of any parameter (such as reflectivity of RTG fins, HGA etc.) on the resulting surface temperatures. The outer loop control can be used to start subsequent analyses with variation of a single parameter and to store the resulting TRP input model automatically.

After the modelling of the different components has been finished, the individual meshes have been generated and all material models and boundaries have been defined, the FE system of equation is solved within the solution macro. Here all parameters concerning the numerical solution of the model can be set. The standard option is the use of the ANSYS classic sparse matrices solver and the computation of the steady state temperatures. Other options such as transient analysis or different FE solvers may be defined at this place. As the last step in the simulation the results are exported in a post processing step. Here the geometric coordinates of the FE mesh, the surface material parameters and the computed equilibrium surface temperatures are exported into a set of input text files for the following TRP computation. For subsequent simulation runs the text file names are automatically updated with a simulation counter ID to prevent overwriting and to enable a clear assignment of input parameters to the respective input model text files.

5.3 Coordinate systems

The APDL macro approach enables the definition of standard procedures by means of macros which are accessible by each part of the simulation. Thus it is sensible to define every action which is repeatedly as an APDL macro. One of the modelling steps which is performed most frequently in the Pioneer 10 FE macro is the change into different coordinate systems. These coordinate systems can be of Cartesian, cylindrical

and spherical character. In case of spherical and cylindrical systems the z-axis is the axis of symmetry while x denotes the radial direction. Figure 5.2 gives an overview of the different coordinate systemS which have been defined as individual APDL macros.

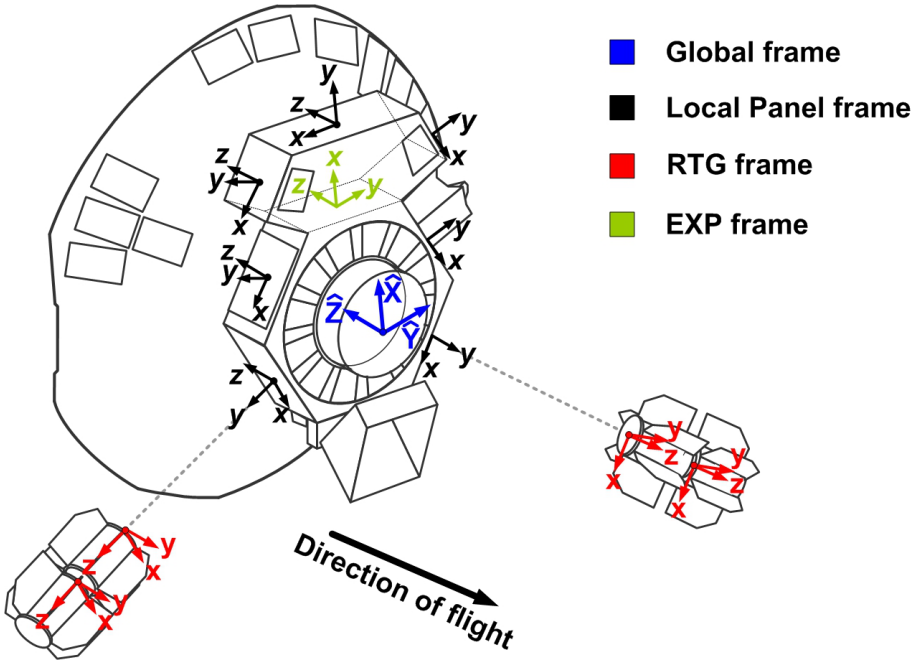

Figure 5.2: Global and local panel coordinate systems.

The most important coordinate frame is the global frame which is also used in the TRP computation step and thus also describes all computed forces and accelerations. As a convention, the global z-axis is opposing the direction of flight which means that a decelerating TRP will have a positive z-component in global coordinates. The origin of the frame is situated in the centre of the launch adapter which enables the use of symmetries, particularly for the hexagonal equipment section. Furthermore the frame is situated at the outer edge of the launch adapter ring (in z-direction). Thus all satellite model components are situate in the positive z-sector of the frame.

Besides the global frame, a number of local frames have been defined for the modelling of the individual components. The local frames for equipment section and HGA are aligned with the global frame and have an offset in global z-direction. The equipment section frame is situated at the bottom of the equipment section base plate while the HGA frame is located on the front side of the HGA. Furthermore an experiment section frame has been defined at the boundary between experiment and equipment section. A local coordinate frame is placed on the centre of each outer side panel surface of the compartment. Here the local z-axes are aligned to global z while the local y-directions are normal to the panel surfaces. The x-axEs are then perpendicular to z and y. Each individual RTG has its own coordinate frame which is defined by an offset from the associated panel in panel y-direction. Here the axis of symmetry is chosen as the local z-axis while the x-axis is aligned to the panel x-axis. The y-axis is perpendicular to x and z.

The use of local coordinate frames simplifies the modelling of individual components considerably as the models may be developed independent from each other. The complete model geometry can then be assembled in the right way by changing into the component reference frame, processing the model macro and then repeating the procedure for the next component.

5.4 Pioneer 10 component models

HGA model: Geometry

The high gain antenna is the largest single structure on board the Pioneer 10 satellite and is attached to the main compartment by a number of guiding rods. The principal shape is parabolic with a diameter of 2.76 m. At the $+Y$/-Y flanks parts of the parabolic surface have been cut out to provide mounting places for thruster assemblies as well as sun sensors. The thrusters and sensors are heated by means of radio isotopic heater units (RHUs) which also introduce heat into the main antenna shape.

HGA model: GMM, premesh and mesh

The HGA is implemented as a solid 3D FE model applying the different material properties to the individual components. Guiding rods and the attitude thrusters attached to the sides are not modelled as they do not have a large effect on the HGA surface temperatures. Due to the complicated non-symmetric shape of the HGA which results from the side cuts and the mounting places of the meteoroid detectors the generation of a FE mesh based on hexaedral FEs is particularly challenging. As preparation for the meshing three subsequent modelling steps have to be conducted:

- generation of 2D premesh with HGA and meteoroid detector shapes,
- generation of 3D HGA model and applying 2D premesh on 3D body,
- deletion of cutted parts and refurbishing of resulting premesh geometry.

The main goal for the 2D premesh is the division of the projected HGA shape into individual parts which each satisfy the requirements for mapped hexaedral meshing. Here the lines and keypoints resulting from the HGA outer border and the meteoroid detectors cannot be changed because the corresponding surfaces are needed for the definition of boundary conditions and the different optical surface properties. The distribution of meteoroid detectors on the antenna rear and the resulting flat 2D premesh is displayed in figure 5.3 left.

Now the basic parabolic volume of the antenna is generated from a spline cross-section which leads to three volumes each spanning over 120° of the antenna circle. In order to generate volumes according to the needed premesh, the 2D surfaces are extruded. The resulting volumes overlap the parabolic antenna volumes. By means of subsequent cutting of extruded volumes from HGA volumes the premesh structure displayed in figure 5.3 centre is now applied to the parabolic volumes. The resulting body has to be cutted at the sides in order to implement the real antenna structure.

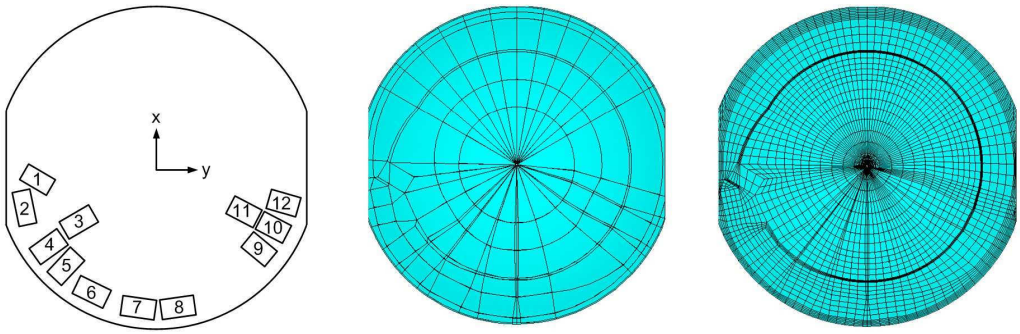

Figure 5.3: Meteoroid detector positions on HGA, HGA premesh and resulting mesh.

These cuts demand further restructuring of the 3D premesh as new volumes result from the cutting operation which do not support mapped hexaedral meshing due to additional lines and areas resulting from the cutting. For this keypoint positions in the vicinity of the cuts have been rearranged. The resulting volumes meet the requirements for mapped meshing and a FE mesh with hexaedral elements as displayed in figure 5.3 right can be generated.

HGA model: material models

The HGA consists of aluminium 6061 which is coated with white paint on the front side and left bare on the rear. The meteoroid detectors also consist of the same aluminium alloy but possess different optical surface properties due to a different surface finish. The definition of the material models used in the HGA model is listed in table 5.1.

Model	Component	Material	k_{cond}[W/mK]	α	ε	γ_s	γ_d
MAT 1	HGA front	Al 6061 white	230	0.21	0.84	0.16	0.01
MAT 2	HGA rear	Al 6061 bare	230	0.17	0.04	0.96	0.00
MAT 3	Meteoroid detectors	Al 6061	230	0.36	0.09	0.81	0.00

Table 5.1: Material models used for HGA.

The material parameters are assigned to the respective HGA components during meshing. For this the components are meshed one after another while the respective material model is activated to apply the parameters defined in the model directly to the finite elements.

HGA model: boundaries

The HGA can exchange radiation with the main compartment and the RTGs. RHUs for the heating of the thruster assemblies are situated at each side of the antenna and introduce a small amount of waste heat in the early mission. Depending on the heliocentric distance of the craft, solar radiation is absorbed by the HGA front, which leads to a heating of the material. Figure 3.18 shows an overview of the boundaries that have to be implemented. For radiation modelling the ANSYS radiosity method has been used and radiation has been specified on each outer FE surface. Here the values for emissivity is acquired from the respective material model. All surfaces radiate into the global radiation enclosure which allows for free radiation (into space) and

blocked radiation (interaction with other model surfaces in the same enclosure). The RHU heating is implemented by means of a surface flux applied to the outer sides of the HGA in the vicinity of the thruster assembly positions.

For the modelling of absorbed solar radiation the curvature of the HGA has to be taken into account, since the actual surface orientation defines the total amount of absorbed solar energy. The absorbed energy for an individual surface element on the HGA front can be expressed with:

$$P_{\mathrm{HGA}}(i) = P_{\odot}(r)\,\alpha_{\mathrm{HGA}}(i)\,\cos\theta(i)\,A_i\,, \tag{5.1}$$

where $P_{\odot}(r) = P_{\odot,1AU}/r^2$ and $\theta(i) = \arccos(\vec{n}(i)\cdot\vec{r}_{SUN})$. Here r is the heliocentric distance in units of AU, A_i is the surface of HGA element i, $P_{\odot,1AU} = 1367\mathrm{W/m}^2$, $\theta(i)$ is the sun orientation angle of element i, α_{HGA} is the solar absorptivity of the HGA, $\vec{n}(i)$ is the normal on each individual surface element and $\vec{r}_{SUN}$ is the sun direction in the HGA frame. In this model it is assumed that sun-spacecraft vector is close to the flight direction which is a valid assumption particularly in the later mission phases with large distances to Earth and Sun. The heliocentric distance of the spacecraft has been extracted from available trajectory data provided by the NASA Helioweb service[1] as displayed in figure 5.4 right. Here the actual heliocentric distance used for the determination of the boundary conditions is interpolated from the trajectory data (which has been generated with 1-day resolution) for each simulated mission date.

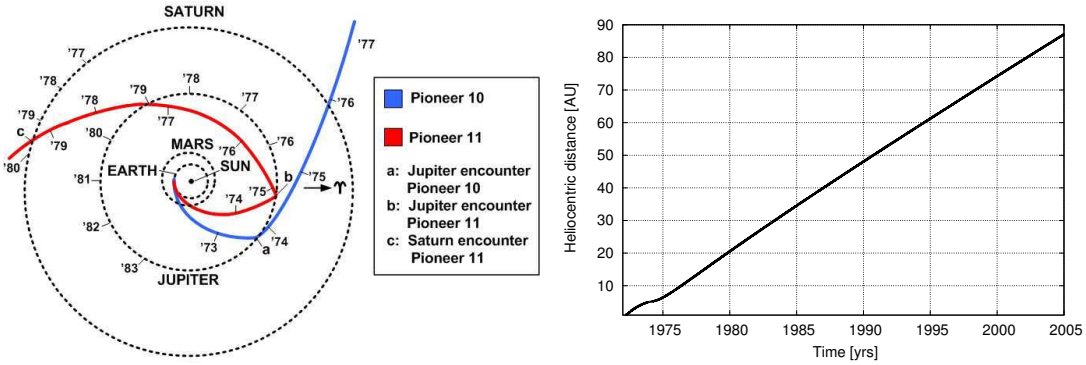

Figure 5.4: Pioneer 10/11 trajectories on solar system plane (left) and Pioneer 10 heliocentric distance vs. mission time (right).

Note that Pioneer 10 and 11 have a different trajectory which means that if TRP is simulated for Pioneer 11, the dynamics of the HGA heat load boundary will develop differently due to the different course of the heliocentric distance.

RTG model: geometry

The four Pioneer 10 RTGs have a symmetric shape and are placed in assemblies of two facing RTGs at ± 60° angles from the compartment as measured from global x-axis. The guiding rods which attach the RTGs to the main satellite body as well as the outer

[1] http://cohoweb.gsfc.nasa.gov/helios/

electrical harness are not included in the model due to their negligible contribution on the overall TRP[1].

RTG model: GMM, premesh and mesh

The complex interior structure of the RTG has been idealised to reduce the modelling effort considerably. The model consist of a single heat capsule volume with shielding layers, a surrounding heat sink bar, an outer housing, the radiation fins and end covers at both ends of the individual RTG. With this the complex structures of the electrical converters as well as the inner mounting of the fuel capsule is simplified in the model. For the creation of the model volumes the symmetry of the RTG can be utilised to reduce the overall modelling effort. The main modelling steps are displayed in figure 5.5.

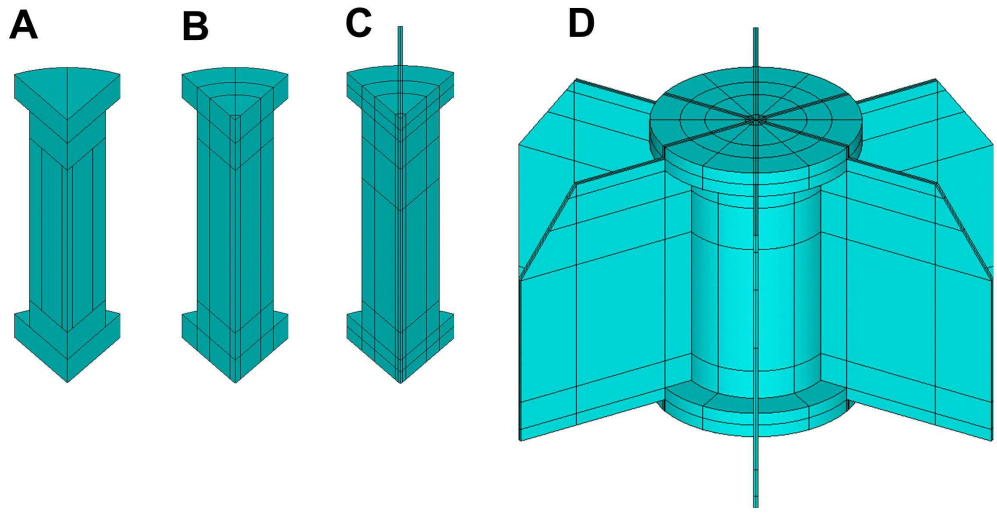

Figure 5.5: Single RTG modelling steps: A: 60° RTG slice, B: Premesh, C: Premesh with fins, D: Complete RTG volume obtained by rotation.

At first a 60° slice of the RTG including the heat capsule volume, the shielding layers, the heat sink, the radiation fins and the end closures is modelled from geometric primitives. Due to the complex shape of the RTG this step involves extensive Boolean operations (such as cutting, gluing and overlapping) in order to create a premesh structure which meets the requirements for hexaedral mapped meshing. The resulting bodies are copied around the RTG z-axis with an angular rate of 60°, which results into a full RTG model.

This RTG model can now be meshed by using the mapped meshing technique, since all of its individual parts automatically fulfil all mapped meshing requirements. Now the RTG volumes are copied and mirrored in order to create the second RTG in the assembly, as displayed in figure 5.6 A. As the last step a connection closure is inserted between the two RTGs and the different model volumes are merged. The closure has to

[1]This only refers to the direct emission, the influence of the cable losses for the total available electrical energy is included in the model.

share the FE distribution on the adjacent end closure to enable the mapped meshing of the complete assembly. The resulting FE mesh of the Pioneer 10 RTG is displayed in figure 5.6 C.

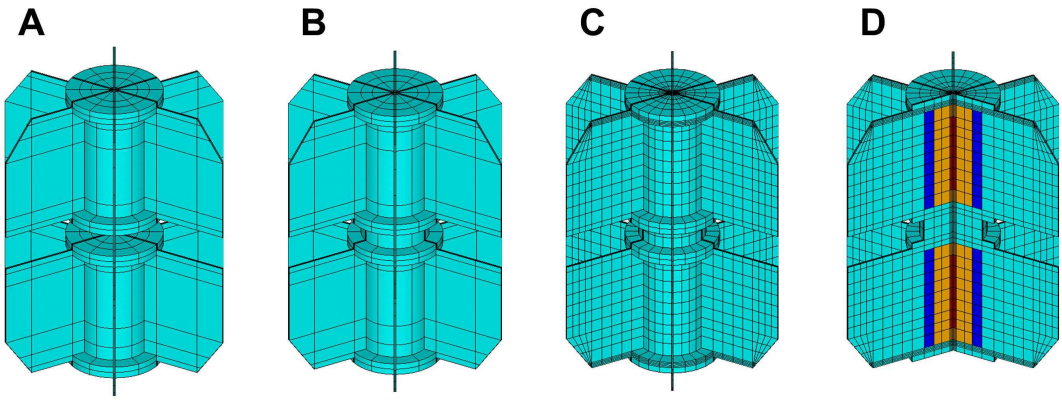

Figure 5.6: Modelling of RTG assembly and resulting FE mesh: A: Set of two RTG volumes, B: RTG assembly with connecting volume, C: RTG assembly FE mesh, D: Cut view with different materials.

The mesh evolves with a symmetric structure and has been generated by using the ANSYS mapped meshing technique, resulting into a pure hexaedral FE mesh. With this the quadrilateral surface element requirement resulting from the later use of the surface model in the force computation algorithm is met.

RTG model: material models

The RTG model inherits four different material models as displayed in figure 5.6 D. For the interior RTG core, consisting of radioactive fuel and shielding layers, a homogeneous set of material parameters has been used as a simplified model (shown in red). The shielding containment for the fuel capsule consists of graphite (shown in orange). Aluminium heat sink bars (shown in blue) are attached to the sides of the containment which also represent the thermal converter electrics in the model. For all other parts of the RTG (housing, closures and radiation fins) the thermal material properties of HM 21A-T8 magnesium alloy are considered. The corresponding material models are listed in table 5.2. Note that for the interior model parts no optical properties have been specified, since within the RTG body, the heat transfer is governed by heat conduction.

Model	Component	Material	k_{cond}[W/mK]	α	ε	γ_s	γ_d
MAT 4	RTG fuel/shielding	Pt 238 isotope	6.3	n.a.	n.a.	n.a.	n.a.
MAT 5	RTG containment	Graphite	60	n.a.	n.a.	n.a.	n.a.
MAT 6	RTG heat sink bars	Aluminium	230	n.a.	n.a.	n.a.	n.a.
MAT 7	RTG housing	HM 21A	138.07	0.20	0.82	0.18	0.01

Table 5.2: Material models used for HGA.

RTG model: boundaries

For the RTG model three different boundaries have been defined:

- heat load on the fuel capsule volumes,
- sensor boundary at the fin roots,
- radiative properties of the outer RTG surface.

The heat load that has to be assigned to the RTG fuel capsule is the total thermal waste energy which is emitted by the radiation fins which directly follows from conservation of energy. Note that this heat energy P_{diss} is the total heat produced by the radioactive fuel P_{gen} subtracted by the fraction of energy converted to usable electrical energy P_{el}:

$$P_{\text{gen}} = P_{\text{diss}} + P_{\text{el}} \,. \tag{5.2}$$

For the computation of P_{diss} two slightly different models have been implemented. The first model is based on JPL evaluations of the Pioneer fin root sensor data [77]. Here the temperature at the fin roots is modelled by:

$$T^4 = T_0^4 \cdot 2^{-(t-t_0)/t_{\text{half}}} \,, \tag{5.3}$$

where the reference date t_0 is defined as midnight, 1st of January, 1973. The half-time of the radioactive fuel can be extracted from the sensor readings as $t_{\text{half}} = 87.73 \pm 5.45\,\text{yrs}$, where the worst case variation of the half-time is a direct result of the telemetry quantisation error caused by the 6-bit resolution of the available temperature sensors. A detailed model for the computation of this value is included in the annexe section V.2. Since the total heat power has to be proportional to the temperature, the heat power at any point in the mission can be modelled by:

$$P = P_0 \cdot 2^{-(t-t_0)/t_{\text{half}}} \,, \tag{5.4}$$

where $P_0 = 2440\,\text{W}$ is the dissipated heat at the reference date. A slightly varied model has been proposed by Lou Scheffer [51]. Here equation (5.4) is used with a mean half-time of 88 years and a reference year of 1972. The heat powers obtained by this model are close to the JPL model and stay within the designated JPL error margin.

The second major boundary for the RTG model is given by the fin root temperature sensors which are placed at each RTG fin root and deliver direct temperature measurements throughout the whole mission. The available data is displayed in figure 5.7 for the four RTG sensors. The temperature data is stored in a database and read into the model where the model boundary temperatures are extracted from the data by linear interpolation corresponding to the actual simulated mission date. For the definition of the boundary all nodes sharing the circumcircle from RTG centre to the fin root sensor position are selected and assigned to the measured temperature value. Thus the resulting temperature pattern is constrained by the measured temperature data which leads to a realistic temperature distribution on the outer RTG surface.

Finally all outer RTG surfaces may exchange radiation with the environment and the rest of the spacecraft. For this the radiosity method discussed in section 3.4 is used

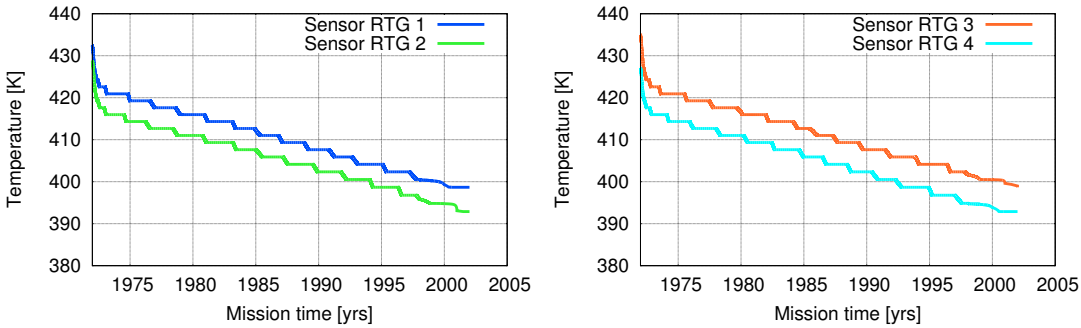

Figure 5.7: RTG fin root temperature data

to specify the radiation properties on the outer FE faces. Here a spacenode temperature of 3 K and a hemisphere resolution of 200 has been implemented. The outer RTG surfaces share the same global radiation enclosure with HGA and compartment to enable the exchange of radiation between all parts of the model.

Compartment model: geometry

The compartment is divided into the hexagonal equipment section and the smaller experiment section which are separated by a centre mounting panel. Internal payloads are mounted to the side, base and centre panels which result in a thermal interface. Except for the louver system all external surfaces are covered in MLI which also implies that the dominant fraction of waste heat energy produced within the compartment will be dissipated by the louver system. The main louver system is oriented radially around the launch adapter which is situated in the centre of the equipment section ground panel. A secondary smaller louver system is situated on the ground panel of the experiment section. Due to the complex structure of the compartment the model is divided into individual models for compartment structure, payloads, MLI and louver system which will be described in the following.

Compartment model: GMM, premesh and mesh

The first step in the compartment modelling is the creation of the equipment section base plate with the louver system oriented around the equipment section centre (step A in figure 5.8). Due to the requirements of the mapped meshing technique a premesh as displayed in figure 5.8 B has to be generated. The radial resolution of individual surface on the base plate is determined by the position of the louvers as well as the desire for a uniform mesh. Here an angular resolution of 5° has been chosen which also fits the geometry of the louver system (which covers 20° with a distance of 10° between the individual louver assemblies). Furthermore the radial symmetric cross-section of the launch adapter is added to the base plate. The next step is the creation of the experiment section base plate. Here the basic geometry is realised by direct keypoint definition by coordinates and evolution into a primitive volume (bottom-up modelling). The resulting body is premeshed corresponding to the premesh on the equipment section as well as the mapped meshing requirements (step C in figure 5.8).

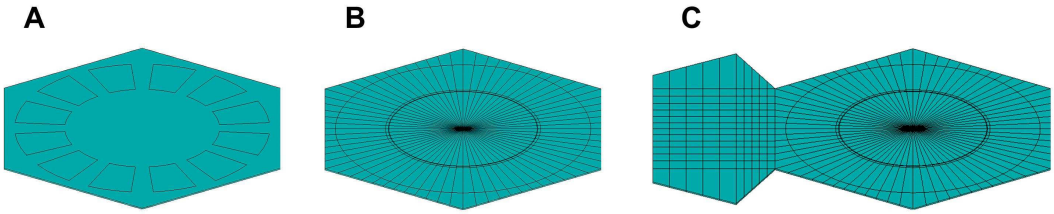

Figure 5.8: Equipment section and experiment section base plate modelling.

The launch adapter is added to the model by extrusion of the already existing launch adapter cross-section. An additional radial division of sub surfaces is added to realise uniform premesh surfaces (step A in figure 5.9). The cross-sectional areas of the side panels and the interior panel between experiment and equipment section are constructed at the base plate boundaries. Now the side panels are extruded from the resulting boundary volumes (step B in figure 5.9) and the base plate geometry is copied with the panel height as offset in order to generate the cover plate (step C in figure 5.9). All overlapping volumes are merged as preparation for the meshing. Note that the panel volumes denote the position of the cover aluminium layers while the underlying honeycomb core is modelled as part of the MLI model.

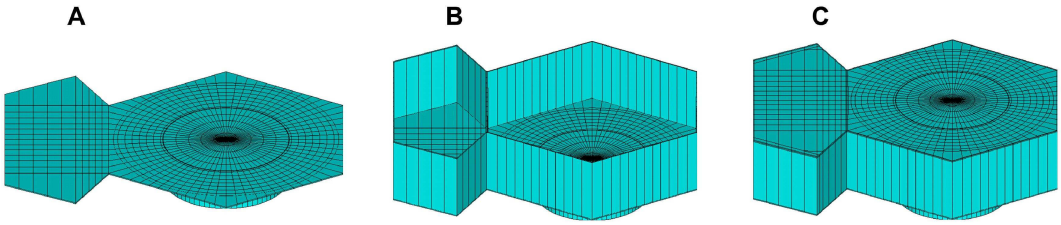

Figure 5.9: Equipment and experiment section side/top panel and launch adapter modelling.

The payload box models interior and exterior to the compartment are shown in figure 5.10 B. In order to avoid a coupling of the geometric boundaries of payloads and compartment volumes (which would complicate the premeshing considerably) all payloads are modelled with a fixed small offset to the base and side panels.

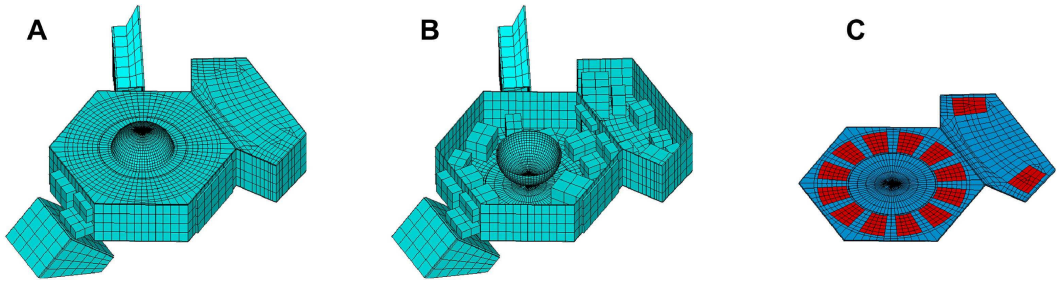

Figure 5.10: Compartment FE mesh, interior and exterior payload models and louver system.

The thermal coupling is then realised by means of 2D thermal conductors as described in the boundary section. The resulting compartment FE model is displayed in figure 5.10 A. Here the FE resolution can be chosen freely as all volumes in the model fulfil the requirements for mapped meshing. As can be seen, the base plate geometry has been modified further to include the geometry of the secondary louver system on the experiment section base plate. The structure of the needed premesh has been generated by bottom-up modelling as well as by modifying existing keypoint locations. For meshing reasons the resulting premesh is also applied to the cover plate. The resulting louver system mesh is displayed in figure 5.10 C (marked in red).

The free outer faces of the two compartments are mainly (excluding louver systems and launch adapter) wrapped in MLI. Three different kinds of MLI were used on Pioneer 10 and 11. On the side panels to which the RTG booms are mounted a 22 layered aluminised Kapton MLI has been used with an interior layer thickness of 1/4 mil[1] and 2 mil face sheets. The other side panels and the front panels are covered in a 22 layered Mylar MLI with the same geometrical composition. Finally the free faces of the compartment aft side are covered in Kapton MLI, also sharing the same geometrical configuration. Note that an additional layer is added to the internal MLI side of all MLI covering the compartment. This inner sheet models the characteristics of the reduced thermal conductivity due to the panel aluminium honeycomb cores. Figure 5.11 shows the composition of the MLI blankets and the material properties of the different materials. Due to the spacing of the individual MLI layer heat transfer by heat radiation plays an important role in the functionality of the insulation. The different layers emit radiation to neighbouring layers which partly absorb and partly reflect radiation back. Thus an effective emissivity insulating effect of each individual layer has to be taken into account in order to model the resulting total heat flux from the compartment interior to the outer MLI layer.

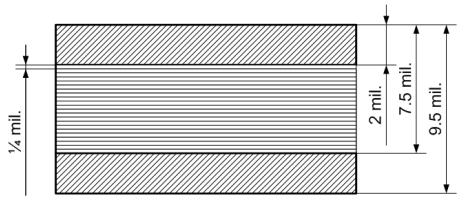

MLI material	α	ε^*	ε	γ
Alumin. Kapton	0.40	0.02	0.70	0.30
Mylar	0.17	0.02	0.70	0.30
Kapton	0.40	0.02	0.70	0.30

Figure 5.11: Composition and material properties of the MLIs implemented in the Pioneer 10 FE model with absorptivity α, effectivy emissivity ε^*, surface emissivity ε and reflectivity γ.

Assessment of MLI thermal properties

For the implementation of the MLI models into the Pioneer FE compartment model, an effective thermal conductivity for the MLI material has to be specified. For this the concept of the effective emissivity ε^* (in difference to the optical emissivity ε) has to be clarified. While the optical emissivity is a real physical property specifying the emitted heat flux following Stefan-Boltzmann's law, the effective emissivity is a technical measure, characterising the heat flux going through an MLI by means of the

[1] 1 mil $= 2.54 \cdot 10^{-5}$ m

hot (interior) and cold (exterior) temperatures T_i and T_e:

$$\varepsilon^* = \frac{P_\mathrm{MLI}}{A\sigma(T_\mathrm{i}^4 - T_\mathrm{e}^4)}\,. \tag{5.5}$$

With this the effective emissivity is an ideal index for the quality of an MLI as T_i and T_e can be measured in a simple experiment with defined geometry and a specified heat load. Due to conservation of energy the heat transported through the MLI P_MLI has to equal the power emitted by the MLI surface into free space P_e. With Stefan-Boltzmann's law for free body emission this leads to:

$$\sigma A T_\mathrm{e}^4 \varepsilon = \varepsilon^* A\sigma(T_\mathrm{i}^4 - T_\mathrm{e}^4)\,. \tag{5.6}$$

Now the temperature on the exterior of the MLI can be expressed in terms of the effective emissivity, the optical emissivity and the temperature on the interior:

$$T_\mathrm{e} = \sqrt[4]{\frac{T_\mathrm{i}^4}{\frac{\varepsilon}{\varepsilon^*} + 1}}\,. \tag{5.7}$$

This relation can now be used to approximate an exterior temperature based on the measured temperatures inside the compartment and the material properties of the compartment MLI as specified in table 5.11. The resulting values for T_e within the measured temperature range of the internal temperature sensor data is plotted in figure 5.12 left. It can be seen that for fixed MLI material parameters the exterior temperature increases linearly with the interior temperatures. The ratio $\eta_\mathrm{MLI} = (\frac{\varepsilon}{\varepsilon^*} + 1)^{(-1/4)}$

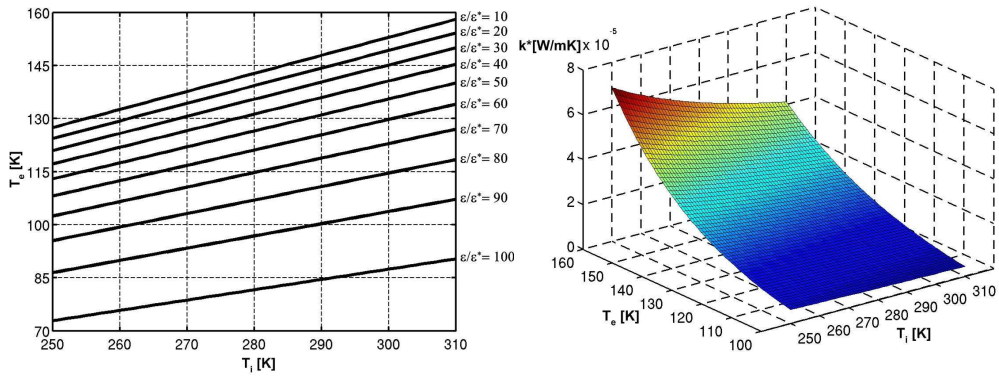

Figure 5.12: Exterior temperature vs. interior temperature for different $\frac{\varepsilon}{\varepsilon^*}$ (left) and resulting values for k^* vs. T_i and T_e.

defines the slope of the resulting graph and can be used as a performance criteria for MLI insulation quality. With this equation (5.7) can be simplified to:

$$T_\mathrm{e} = \eta_\mathrm{MLI}\, T_\mathrm{i}\,. \tag{5.8}$$

Using Fourier's law for heat conduction an effective value for the MLI conductivity k^* can now be computed by:

$$k^* = \frac{P_\mathrm{MLI}\, d_\mathrm{MLI}}{A\,(T_\mathrm{i} - T_\mathrm{e})} = \frac{\sigma\, T_\mathrm{e}^4\, \varepsilon\, d_\mathrm{MLI}}{T_\mathrm{i} - T_\mathrm{e}}\,, \tag{5.9}$$

where d_{MLI} is the total thickness of the MLI. The resulting k^* values for different combinations of T_{i} and T_{e} are plotted in figure 5.12 right. It can be seen that a high temperature gradient between interior and exterior temperature corresponds to a low k^* values while high k^* values indicate poor MLI insulation quality thus causing a lower temperature gradient. The k^* value for the Pioneer MLI can now be approximated based housekeeping data using the equations above. For conditions at the design case a mean value for the compartment temperature of $T_{MEAN} = 280\,\mathrm{K}$ can be determined using the only the data of the six compartment sensors as a simple fit for mission starting conditions. With the given η_{MLI} a corresponding outer temperature of $T_{\mathrm{e}} = 115\,\mathrm{K}$ can be derived. This gradient corresponds to an effective conductivity of $k^* = 1.0 \cdot 10^{-5}\,\mathrm{W/mK}$.

Thin walled multi layer structures have to be modelled as 2D shell elements with a virtual thickness (thickness implemented by additional DOFs at each node) rather than modelling a 3D solid. This approach saves computing time and avoids the problem of a violation of the element shape factor criterion. Furthermore, having an underlying 3D solid mesh the shell mesh can easily be applied to the solid faces without having to modify the geometrical model further.

ANSYS delivers two different kinds of shell elements, which can be used for MLI modelling: *Shell131* (4-node) and *Shell132* (8-node). In total both element types offer a maximum of up to 32 implemented temperature degrees of freedom for each modelled node. This enables the modelling of 31 layers for linear and 15 layers for quadratic thermal gradients. Both elements include in-plane and through-thickness heat conduction. The influence of the layer thicknesses is modelled by the differential equation of heat conduction between two adjacent nodes. Boundaries, dimensions and different materials can be defined for each layer for the corresponding boundary nodes which are placed on the edges in the mid-thickness of the shell element as displayed in figure 5.13.

Furthermore heat fluxes can be specified on the element surfaces and edges while radiation effects may only be modelled on the top and bottom face. Each individual layer has three DOFs: temperature at the top, temperature at the bottom and temperature in the layer centre. For more than one layer in the shell the DOF (in this case the temperature) on the contact regions are shared (displayed in figure 5.13 right). This explains the 31/15 layer boundary for linear/quadratic shell elements with a maximum number of 32 DOFs.

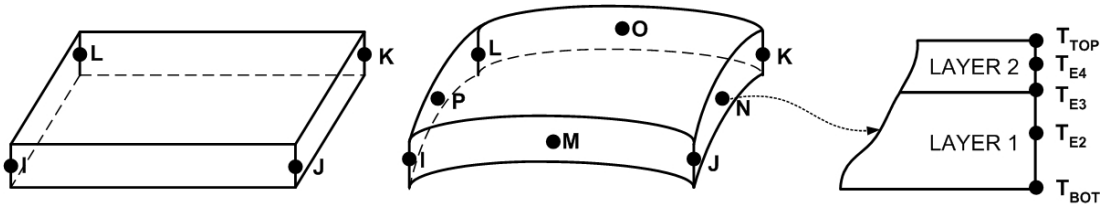

Figure 5.13: Definition of Shell 131 and 132 Element, $T_{\mathrm{E,n}}$ = nth MLI sheet temperature DOF, T_{BOT} = bottom MLI temperature DOF, T_{TOP} = top MLI temperature DOF [70].

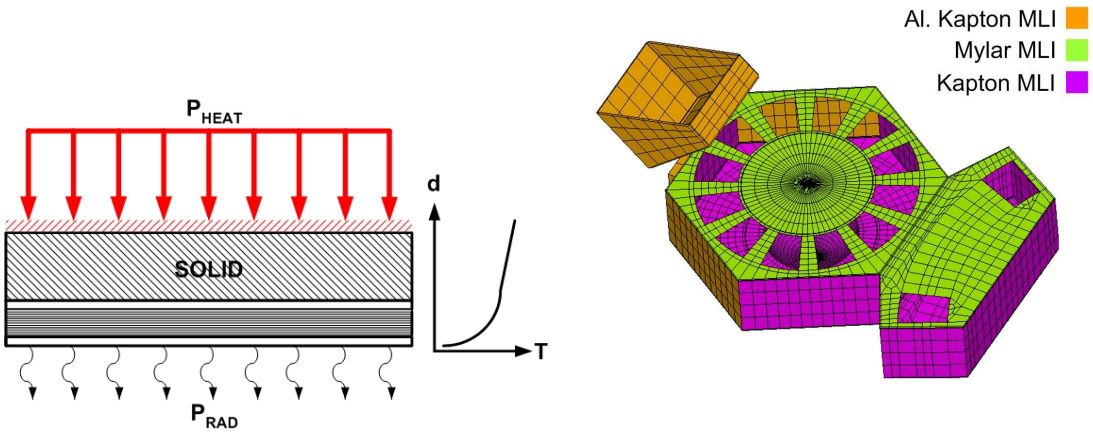

Figure 5.14: Modelled Heat transfer through MLI (left), Modelled MLI faces (right).

In order to connect the MLI model to the underlying solid mesh, the T_{BOT} DOF of the MLI shell has to be connected with the temperature DOF of the nodes at the solid face T_n. For this a DOF-constraint polynomial equation of the form:

$$C_0 = \sum_{i}^{n} D_i \cdot C_i \,, \tag{5.10}$$

can be defined for each nodal pair at the boundary of MLI and panel wall. Here C_0 is a constant, D_i are the degrees of freedom and C_i are the polynomial coefficients. With $D_1 = T_n$, $D_2 = T_{\mathrm{BOT}}$, $C_0 = 0$, $C_1 = 1$ and C_2 = -1 the equation yields:

$$T_n = T_{\mathrm{BOT}} \,. \tag{5.11}$$

Thus the temperature DOFs at the boundary of MLI and panel are properly constrained and heat conduction from the panel into the MLI is implemented. For the modelling of the Pioneer MLI three Material models resembling the three different kinds of insulation have been defined. For the mesh generation the shell elements are applied to the outer faces of the main and experiment compartment solid model. With this the geometry of the solid faces can be used for the shell mesh thus creating a geometrical interface between the inner shell layer and the solid face. This also leads to a coupling of the degrees of freedom at the boundary, in this case the temperature of the solid nodes and the temperatures of the bottom layer. The MLI Shell models are implemented corresponding to the MLI material parameters with 22 interior and top/bottom sheets as displayed in figure 5.11. For this a section with 24 data sets resembling the individual layers is defined with the ANSYS secdata command and assigned to the shell element. Using the radiation models described in section 3.4, outgoing radiation is specified on the outer shell faces (The nodes with the DOF TTOP). As displayed in figure 5.14 left, a heat transfer between the conducting solid elements and the radiating outer layer of the shell elements results.

Figure 5.14 right shows the resulting implemented Shell FE model. Here the aluminised Kapton MLI is displayed in yellow, the Kapton MLI faces are marked in blue and the Mylar blankets are shown in red. In order to visualise the thermal characteristics of the MLI modelling approach a thermal test case using a cubic satellite bus with

two internal payloads has been defined. Here the outer surfaces of the bus are covered in a 24 sheet Pioneer Kapton MLI (as specified in the last subsection) which has been thermally connected to the bus faces. For the bus panels a thickness of 1 mm and a conductivity of 300 W/mK has been assumed. As boundaries a fixed payload temperature of 300 K and outgoing radiation on the external MLI faces has been specified. The resulting temperatures on the bus panel and within different MLI sheets are displayed in figure 5.15.

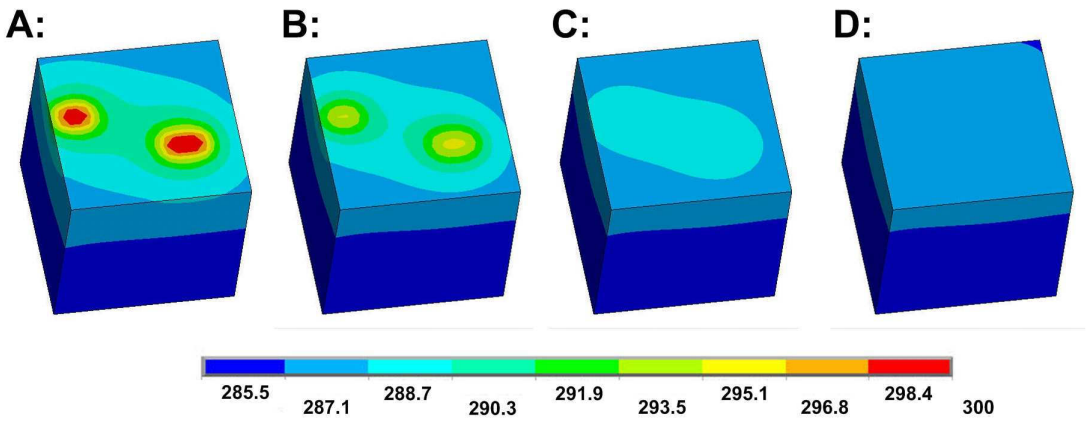

Figure 5.15: MLI test case result. A: Panel temperature (beneath the MLI sheets), B: bottom MLI sheet temperature, C: centre MLI sheet temperature, D: outer MLI sheet temperature, all temperature values are given in Kelvin.

The mounting positions of the payloads can clearly be identified as a temperature peak on the bus panel. Here a high thermal gradient is visible between the payload positions and the outer panel regions. Looking at the temperatures in the bottom MLI sheet, the insulating effect of the MLI becomes visible. It can be seen that the thermal gradient within the panel plane reduces already significantly after the first MLI sheet. For every additionally MLI sheet included in the analysis, the resulting temperature profile smooths out more and the maximum outer temperatures decrease. For the centre panel sheet (after 12 MLI sheets), only a small temperature difference remains, which becomes completely negligible at the top MLI sheet (after heat transport through a total of 23 MLI sheets). This shows the strong insulating effect of the MLI and the resulting homogeneous character of the temperature distribution for external MLI surfaces.

Compartment model: material models

The major components of the compartment model consisting of different materials are the housing (base plates, side panels, interior mountig panel and cover panels), payload boxes, MLI covering the compartment and external payloads and the louver system (consisting of second surface mirrors and louver blades). The material models used for the meshing of the different components are listed in table 5.3.

Model	Component	Material	k_{cond}[W/mK]	α	ε	γ_s	γ_d
MAT 8	Housings	Aluminium	169	0.86	0.86	0.07	0.07
MAT 9	Mirrors	SSM	60	0.07	0.82	0.09	0.09
MAT 10	Louver blades	Bare Al 6061	230	0.17	0.04	0.96	0.00
MAT 11	MLI 1	Alum. Kapton	10^{-5}	0.40	0.70	0.15	0.15
MAT 12	MLI 2	Kapton	10^{-5}	0.40	0.70	0.15	0.15
MAT 13	MLI 3	Alum. Mylar	10^{-5}	0.17	0.70	0.15	0.15
MAT 14	Honeycomb	Aluminium	0.0114	n.a	n.a	n.a	n.a

Table 5.3: Material models used for HGA. Optical properties for MAT 8 are valid for the compartment interior, MLI emissivities are the outer emissivities, the MLI conductivities have been computed from the effective emissivity value. The conductivity given for the aluminium honeycomb core is the through-thickness conductivity.

Compartment model: boundaries

The main boundaries for the compartment are

- direct temperature measurements for different places on the base plate inside the compartment,
- the electrical power available to the inner and outer payloads as well as the power dissipated over the shunt radiator,
- the radiative properties of the compartment and payload surfaces.

Six temperature sensors are mounted on different places on the compartment base plates as displayed in figure 5.16. In case of Pioneer 10 for each sensor temperature measurements are available from 1972 up to 2002. The data sets have been preprocessed, translated into ASCII-code and made available by the JPL who are in possession of magnetic storage media to where the original Pioneer telemetry has been archived. Due to data corruption, the chosen scale (Fahrenheit) and the digital character (discrete temperature steps) of the data, extensive preprocessing has to be performed before sensor data can be extracted for use as boundary conditions in the Pioneer thermal FE macro. The composition of the ASCII data files is shown in figure 5.16 right.

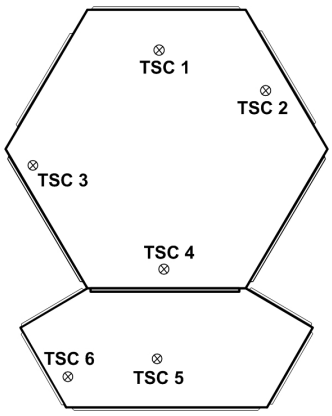

Column	Included Data	Example
1	Day in text	Mon
2	Month in text	Jun
3	Time [hrs:min:sec]	19:00:00
4	Day [-]	12
5	Year [yrs]	1972
6	$T_{\text{RTG 1}}$ [F]	312.23
7	$T_{\text{RTG 2}}$ [F]	315.13
8	$T_{\text{RTG 3}}$ [F]	311.54
9	$T_{\text{RTG 4}}$ [F]	313.71
10	$T_{\text{comp 1}}$ [F]	100.01
11	$T_{\text{comp 2}}$ [F]	100.01
12	$T_{\text{comp 3}}$ [F]	100.01
13	$T_{\text{comp 4}}$ [F]	100.01
14	$T_{\text{comp 5}}$ [F]	100.01
15	$T_{\text{comp 6}}$ [F]	100.01

Figure 5.16: Compartment sensor places (left) and structure of the Pioneer 10 RTG and compartment housekeeping data files provided by the JPL (right) [76].

The Pioneer 10 housekeeping data files contain approximately 100000 individual measurements ranging from 1972 to mid 2002 for each sensor. Due to limitations of conventional tools such as Microsoft Excel this implies the development of a dedicated data evaluation algorithm. The first step is the import of the ASCII-files and the extraction of all text parameter information. The first five parameters are used to generate a floating time code which can be assigned to the sensor measurements. The data of each sensor is extracted from the ASCII files and converted to a data file which contain time stamp and measurement data for each sensor individually. Due to data loss and artifacts, several voids are present in the data sets. Therefore the data evaluation algorithm identifies the voids and fills the void places with zero values. The resulting preprocessed raw sensor data is shown in figure 5.17. Note that the axis labels are contained in the figure caption.

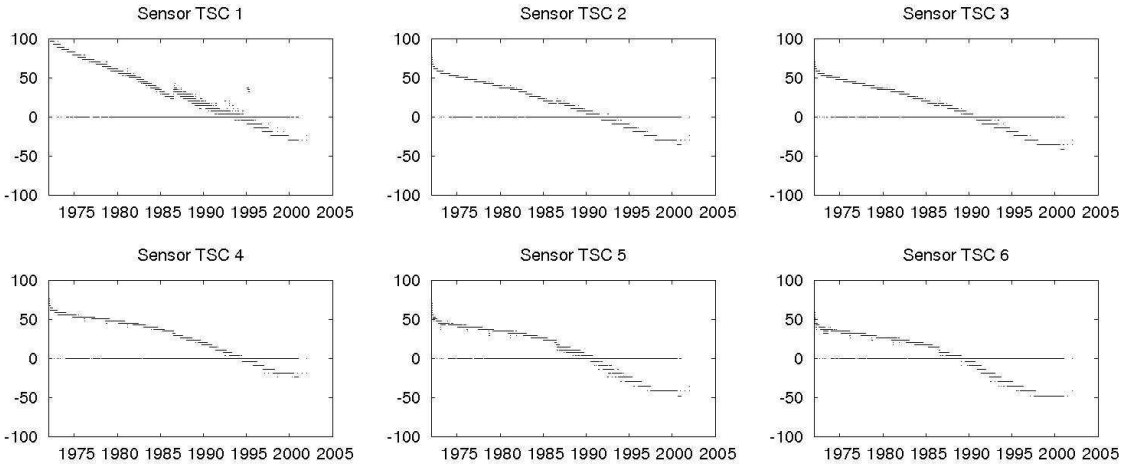

Figure 5.17: TSC 1-6 converted sensor data with zero void values. Y-axis: temperatures in Fahrenheit, x-axis: mission date [yrs].

The data is imported into a numeric data array with the type 13 x n, where n is the total number of measurements per sensor. After this the zero values in the data matrix are replaced with averaged values obtained from the nearest non-zero values in the sensor data set. Now a floating average filter is used to process the data. For this a buffer size of 2500 data points has shown good performance. The resulting filtered sensor data is plotted in figure 5.18. Note that the axis labels are contained in the figure caption.

Now the filtered sensor data is used to create input loads for the FE model. The sensor data at specific intervals (e.g. each year) is exported into a look-up table which is then used as input for the FE model boundary step. Here the temperatures for each sensor are applied as a boundary on the temperature DOF to a corresponding node on the interior face of the base plate. With this the thermal FE solution is fitted to the boundary values. Thus a realistic temperature distribution based on housekeeping data can be simulated for each point of the mission.

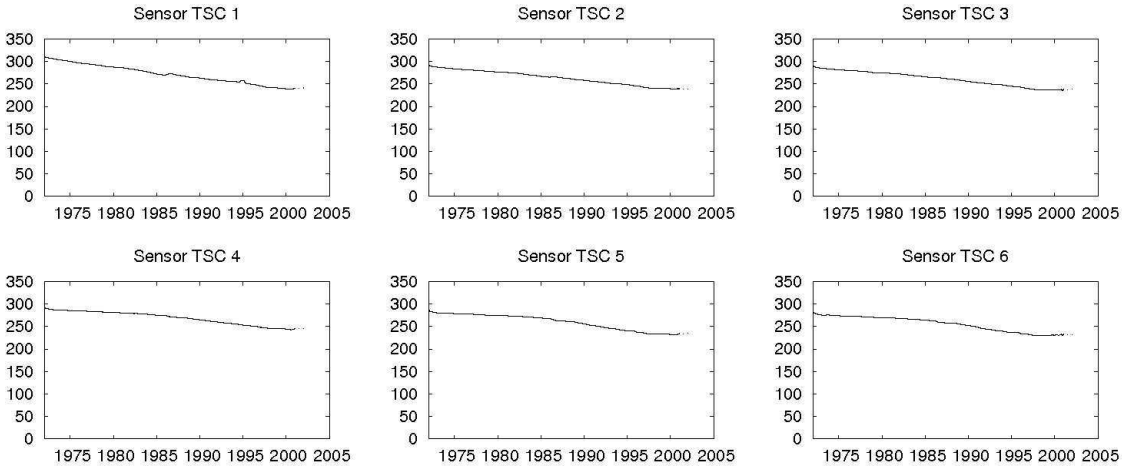

Figure 5.18: TSC 1-6 filtered continuous sensor data, y-axis: temperatures in Kelvin, x-axis: mission date in years.

For the implementation of the waste heat produced by the electrical consumers, either the amount of available electrical power provided by the RTGs or the payload temperatures have to be modelled as boundaries for the FE solution. Due to both radioactive decay and ageing of the hardware itself the conversion rate and the total amount of electrical power drops during the mission. For the payloads no actual temperature measurements are available. Measurements for test scenarios have been taken using engineering models in ground tests. The resulting measured temperatures are listed in the annexe in table V.1. However, these temperatures are only valid for specific satellite states and can not be used for a complete analysis of the TRP in the course of the mission.

Two modelling approaches for the total electrical power available for the internal payloads can be found in the literature. L. Scheffer [51] proposes to model the total amount of available electrical power for the compartment by:

$$P_{\mathrm{el}}(d) = P_{\mathrm{el,ref}} + p_{\mathrm{e}}\,(1998.5 - d)\,, \tag{5.12}$$

where

$$P_{\mathrm{el,ref}} = 68\,\mathrm{W} \;\text{ and }\; p_{\mathrm{e}} = 2.6\,\mathrm{W}\,, \tag{5.13}$$

which results from the observed RTG temperatures and assumptions of the conversion rate between electrical and thermal power which are derived from the technical parameters of the RTGs. However, a more accurate approach based on the engineering housekeeping data is proposed by Toth and Turyshev [77].

As defined by the Pioneer 10 telemetry concept voltage and current sensor data has been transmitted from the spacecraft to earth in an hourly resolution. This data can now be used to compute the amount of power used by the payloads within the compartment very precisely. Table 5.4 lists the sensor channels used in this approach and their respective content.

Word	$C_{110}, C_{125}, C_{131}, C_{113}$	$C_{127}, C_{105}, C_{114}, C_{123}$	C_{108}	C_{124}
Data	RTG 1-4 voltage	RTG 1-4 current	$P_{\mathrm{PA}} + P_{\mathrm{CRT}}$ digit	P_{AMD} digit

Table 5.4: Explanation of telemetry words used for the determination of compartment power [77].

By using the RTG telemetry the total electrical power produced by the RTG assembly can be computed with:

$$P_{\mathrm{el}} = \sum_{n=1}^{4} U_n \, I_n = C_{110} \, C_{127} + C_{125} \, C_{105} + C_{131} \, C_{114} + C_{113} \, C_{123} \, . \tag{5.14}$$

The power used within the compartment results from the total electrical power reduces by all losses and all electrical consumptions external to the compartment:

$$P_{\mathrm{comp}} = P_{\mathrm{el}} - P_{\mathrm{cable}} - P_{\mathrm{PPA}} - P_{\mathrm{HGA}} - P_{\mathrm{CRT}} - P_{\mathrm{AMD}} - P_{\mathrm{LH}} - P_{\mathrm{BH}} \, , \tag{5.15}$$

where P_{cable} is the cable loss, P_{PPA} is the power of the plasma analyser, P_{HGA} is the transmitted power by the HGA, P_{CRT} is the power of the cosmic ray telescope, P_{AMD} is the power of the asteroid/meteoroid detector assembly and P_{BH} and P_{LH} are the powers used for battery and propellant line heating respectively. The cable loss can be computed with the known cable resistance (0.017 Ω_r for the inner RTGs and 0.021 Ω_r for the outer RTGs) and the RTG current measurements:

$$P_{cable} = \sum_{n=1}^{4} R_n I_n^2 = 0.0017(C_{114}^2 + C_{123}^2) + 0.021(C_{127} + C_{105}) \, . \tag{5.16}$$

The nominal powers of the plasma analyser, the cosmic ray telescope and the asteroid/meteoroid detector assembly are given in table 5.5. They are applied according to the respective on/off bits delivered in the telemetry data. For the transmitted HGA power a mean value of 6 W is taken into account.

Component	Nominal power [W]	On/Off Bit
PPA	4.2	C_{108}, bit 2
CRT	2.2	C_{108}, bit 6
AMD	2.0	C_{124}, bit 5

Table 5.5: Nominal power values for chosen components. PAL: Plasma analyser, CRT: Cosmic ray telescope, AMD: Asteroid/meteoroid detector assembly.

The heaters are powered with a nominal power of 2 W each. As can be seen in mission logs, the battery heater has been commanded off on the 12th may 1993. The individual powers of the components and the resulting available power for the compartment are displayed in figure 5.19.

For the modelling of the compartment boundaries, the available electrical power is now distributed evenly between the payload boxes thus leading to payload boundary temperatures which will drop with mission duration according to the electrical sensor measurements. The resulting heat distribution will give a good model for the change of the power that has to be dissipated but is not completely realistic as in reality each

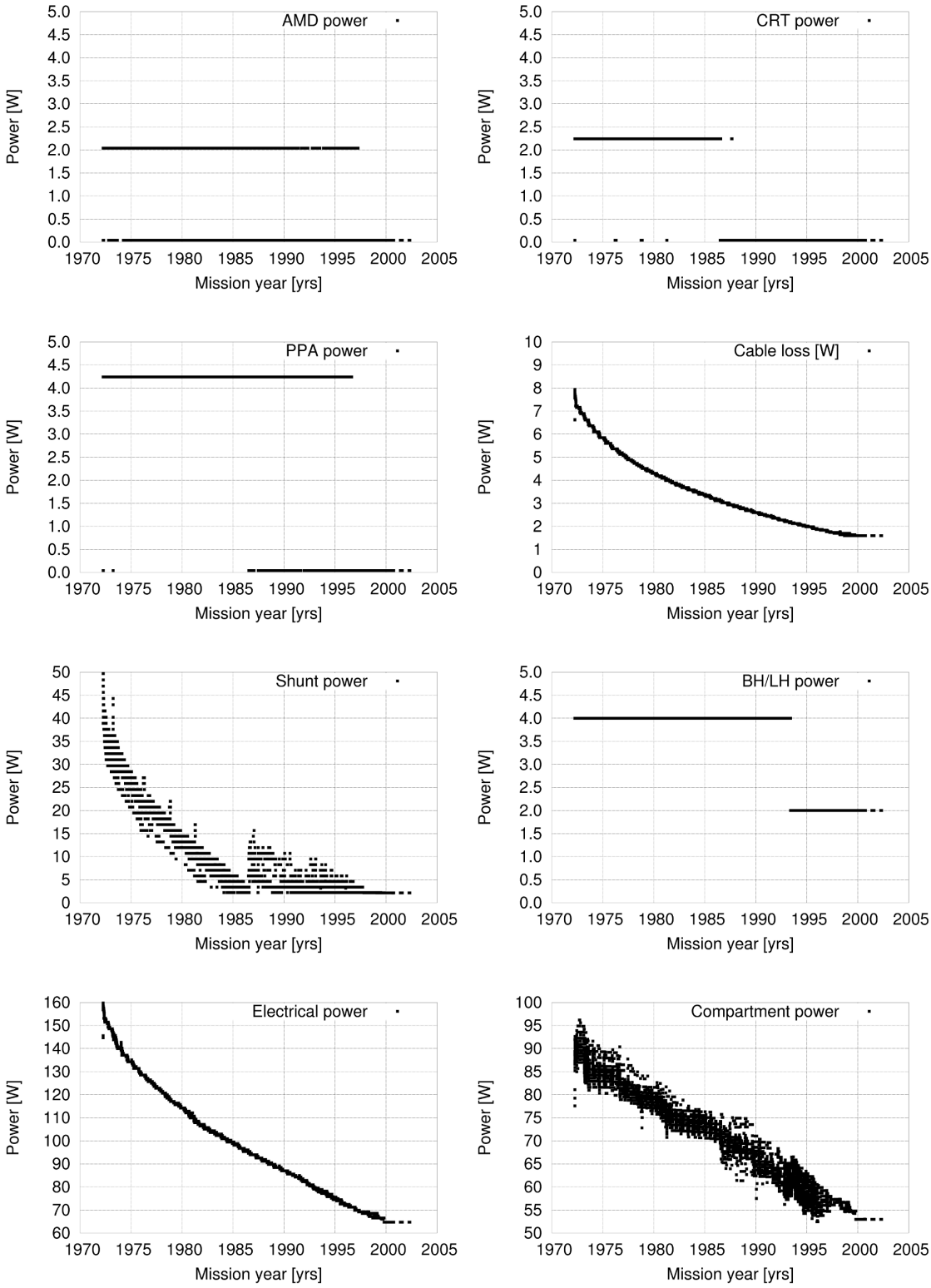

Figure 5.19: Overview on electrical power consumption and losses. AMD: asteroid/meteroid detector assembly, CRT: cosmic ray telescope, PPA: plasma analyser, SHU: shunt radiator, BH: battery heater, LH: propellant line heater.

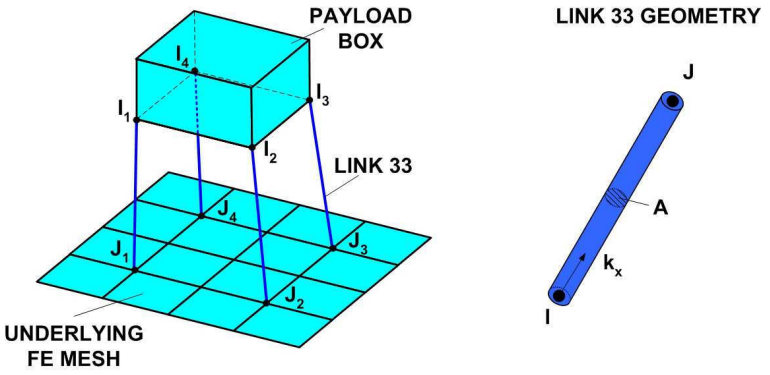

Figure 5.20: Modelling of Payload/Compartment thermal interface with LINK 33 element.

payload needs a fixed amount of power to be operated. However, due to the highly insulated main compartment, the heat exchange inside the compartment and the implementation of the compartment sensor data as temperature boundaries the influence of a difference from the modelled payload temperatures to a realistic temperature distribution will not have a strong effect on the resulting TRP. In order to test the validity of this approach and to determine the influence of variations from a realistic temperature pattern the ground measurements given in the annexe in table V.1 can be used as validation cases.

As the FE modelling approach taken in this study is based on quadrilateral elements a single mesh shared by compartment panels and payloads would be too complex and probably not feasible without the insertion of tetrahedral elements. Therefore the payload boxes are moved by a small constant offset in normal direction to their respective mounting panel. In order to model the thermal interface between payloads and compartment the mounting is realised with thermal 2 D link elements which implement node-to-node thermal conduction. Here the edge nodes of the payloads boxes are connected with the nearest nodes on the mounting panel. The material properties and an effective cross-sectional area for the link element can be specified. Effectively this models the mounting screws which connect the payloads to the panels. The geometry of the LINK33 element which has been used to model the thermal interface between the payload boxes and the compartment is plotted in figure 5.20. A link element is created from each Payload box edge $I_1 - I_4$ to the respective closest node on the compartment panel mesh $J_1 - J_4$. For the implementation of heat conduction between payload and compartment the conductivity along the link element k_x is specified. The cross-sectional area A and the size of the link element l and the temperature difference between the two nodes ΔT_{IJ} define the total heat transport rate:

$$Q_{\text{LINK33}} = \frac{A}{l} k_x \Delta T_{IJ} \,. \tag{5.17}$$

Radiative properties have been defined on the external surfaces of MLI and louver assemblies as well on the interior faces and the payloads. For the modelling of internal radiation exchange an interior radiation enclosure has been defined, all outer faces share the global radiation enclosure of RTG and HGA. All properties have been assigned by using the radiosity option and the optical parameters specified in table 5.3. For MLI

the radiation has been specified as boundary for the external DOF.

For the modelling of the radiative properties of the louver assembly no distinction between louver blades and underlying second surface mirrors has been made. This results from the fact that for the greater part of the simulated mission times the louvers are supposed to be completely closed. Thus the outer emissivity of the louver assembly equals the emissivity of the louver blade in standard mode. For earlier mission times and failure scenarios the influence of incompletely closed louvers can be simulated by computing an effective emissivity $\varepsilon_{\mathrm{l,eff}}$ scaled by the louver opening angle ϕ_{l}:

$$\varepsilon_{\mathrm{l,eff}} = \eta_{\mathrm{c}}(\cos(\phi_{\mathrm{l}})(\varepsilon_{\mathrm{ss}} - \varepsilon_{\mathrm{b}}) + \varepsilon_{\mathrm{b}})\,, \tag{5.18}$$

where $\varepsilon_{\mathrm{ss}}$ and ε_{b} are the emissivities of second surface mirror and louver blades, respectively. The efficiency factor η_c is a measure for the effective heat transfer between louver blade and second surface mirror. When the louvers are completely closed heat is transported between mirror and blade volumes by conduction and heat radiation. As the surfaces are not perfectly even, a small heat resistance scaled with the surface roughness results. On earthbound applications the needed corrections usually are negligible because heat can be transported over the gaps by heat convection. In vacuum however, due to the absence of convection, the effective heat fluxes may considerably influence the quality of the thermal contact in the interface which depends on the contact pressure, the surface roughness and the surface micro hardness. Another factor of influence for the efficiency factor is the geometrical composition of the louver blades. The blades are composed of an aluminium honeycomb core with a top and bottom aluminium face sheet. Due to the small thermal cross-section, the core may act as another heat resistor for the heat flux to the louver blade surface. Thus a correction of the effective emissivity may be introduced to model the realistic heat distribution over the louver blade. However, due to the fact that the effective heat resitance of the louver system is lower than that of the MLI, the correction of the heat flux by the effects described above are negligible with respect to TRP computations as the louver temperatures will evolve close to the internal compartment temperatures regardless of small variations in the conductive model properties of the louver system.

Chapter 6

Pioneer thermal recoil analysis

This chapter discusses the Pioneer 10 thermal analysis results as well as the constitutive analysis of the evolution of the TRP acting on the spacecraft for the duration of 1972 - 2002. The computed TRP is compared to the detected unexplained Doppler residuals and evaluated with respect to the PA. A parameter variation is performed to quantify computational errors inflicted by uncertainties in the considered boundaries, sensor data and material parameters.

6.1 Procedure for Pioneer 10 TRP determination

The main goal of the thermal FE analysis performed with the Pioneer 10 FE macro is the determination of the equilibrium temperatures on the external spacecraft surfaces and the subsequent computation of the resulting TRP evolution for the complete mission time, where telemetry and housekeeping data are available. Furthermore, the influence of different input parameters (such as the change of optical properties due to surface degradation or possible variations in the heat loads) will be analysed in order to detect the dominant parameters as well as to quantify the modelling errors introduced by uncertainties of the input parameters. For this a baseline configuration model with default values for the chosen material, the geometrical and the environmental parameters has been defined. This model, introduced in the next section, will be the reference case for the computation of the time-development of the TRP acting on the Pioneer spacecraft as well as the starting configuration for any Pioneer 10 parameter analysis conducted in this thesis. The procedure for analysing TRP on the complete orbit (thus analysing the time-evolution of TRP), or performing another parameter analysis is displayed in figure 6.1.

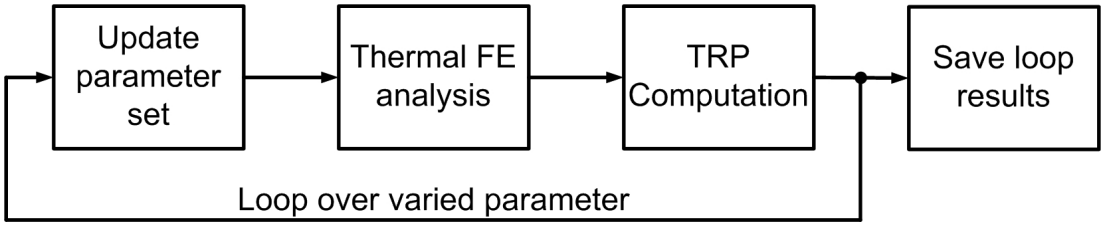

Figure 6.1: Procedure for the performed Pioneer 10 parameter analyses.

In order to analyse the change of the TRP with varying input parameters, subsequent FE analyses and numerical TRP computations have to be performed. The assessment of the time-development of TRP takes a special role in this respect, because the simulated time influences a high number of different model input parameters and boundaries. These time-dependent parameters are:

- payload electrical energy for the specified date,
- shunt heat load for the specified date,
- compartment sensor temperatures for the specified date,
- solar heat load (determined by the time-depending heliocentric distance),
- RTG fin root temperature data as well as RTG heat energy for the specified date,
- change of optical properties if degradation is accounted for.

For the computation of TRP at different mission times all parameters in the list above have to be updated for each simulated point in time, while all other parameters are kept at the baseline values. The orbit can then be modelled by processing the FE model as well as the TRP computation for different (equidistant) points during the mission. The results will then show the dependence of the TRP on the mission time. The same procedure can be used to determine the influence of any other parameter in the model on the resulting TRP. Thus, for example the influence of RTG emissivity on the resulting TRP (for a fixed point in time) may be examined.

In the APDL macro approach taken for the development of the Pioneer 10 FE model, the update of input parameters and the conduct of subsequent simulation runs is realized by means of a top level macro which controls all other FE macro levels. The top level macro includes a loop control where the parameter which has to be varied are updated by a user defined stepping for each loop. Therefore the resolution of the analysis (e.g. the duration between two simulated points in time) can be determined by the number of simulation loops and the chosen parameter stepping.

After the update of the input paramters, the FE simulation is started and the results are automatically saved with a run identifier, typically including the value of the varied parameter for which the result was obtained. By defining subsequent or nested loops, complex parameter analysis runs can be configured. All parameters, which are updated during an analysis, have to be passed through all sub functions of the macro. For this a maximum of 99 input arguments can be defined in ANSYS for each macro level.

The import of the FE results into the raytracer and the composition of subsequent TRP analysis runs based on the surface temperature distributions obtained for the thermal FE anaylsis with parameter variation is explained in detail in the annexe in section V.4. An exemplary APDL macro for the automatic export and the automatic labeling of the resulting output files with run identifiers is provided in the annexe in section V.5.

6.2 Baseline configuration

The geometrical configuration of the Pioneer 10 FE baseline model as well as a view of the real spacecraft geometry[1] is displayed in figure 6.2.

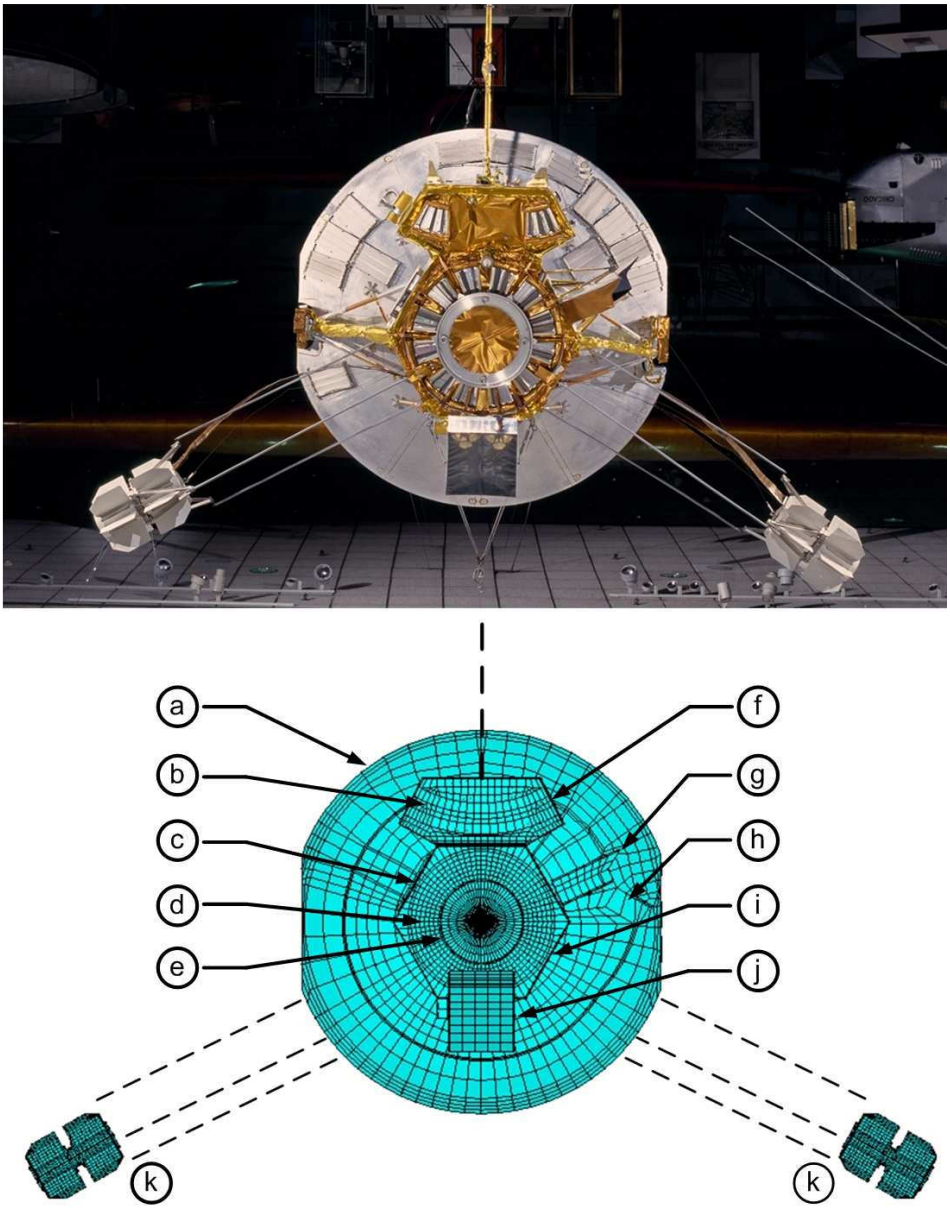

Figure 6.2: Comparison of the Pioneer 10 baseline FE model with real spacecraft geometry.

As can be seen the model includes HGA (a), RTGs (k), experiment section (f) and equipment section (i) as well as outer payloads (g, j) and shunt (c). The main and secondary louver system (b, d) and the launch adapter (e) are implemented on the equipment section base plate. Inside the compartment the different payload boxes as well as the centre mounting panel are included in the model as shown in figure 5.10. The

[1]Picture by Smithsonian National Air and Space Museum, Washington, DC, url: http://www.nasm.si.edu, accessed on 08/08/2011.

RTG guiding rods (displayed with dashed lines), the magnetometer boom, the thruster assemblies and openings for some of the internal payloads have not been included as their contribution to TRP is negligible. The optical and the thermal properties assumed for the different components are summarised in tables 5.1, 5.2, 5.3 and 5.11.

6.3 Thermal FE analysis

For each parameter set a resulting thermal map of the spacecraft has been computed with the Pioneer 10 FE model. Due to the high amount of data and different solutions the results in this section are presented for a specific point of time (01.01.1990) in the mission and the baseline model parameters. Qualitative differences for other mission times or other parameter configurations are discussed. Figure 6.3 shows the surface temperatures on the HGA front for conditions in 1972 (left) and 1990 (right).

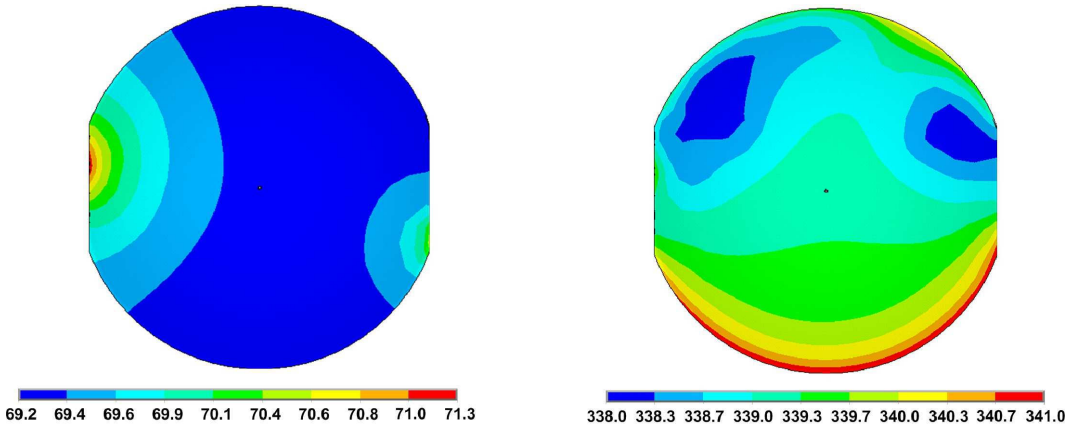

Figure 6.3: Temperature on HGA front in 1990 (left) and 1972 (right). Temperatures are given in Kelvin.

For 1972 the resulting temperatures on the HGA are quite high with a considerable uniform thermal gradient. Here the dominating factor for the magnitude of the temperatures is solar illumination of the front side of the HGA. The temperature distribution is highly asymmetric and different regions of thermal properties can clearly be identified. The coldest temperatures comply to the places where the HGA meteoroid detectors are placed on the HGA rear. Here the meteoroid detectors possess a much higher thermal emissivity compared to the highly reflective HGA rear surfaces and thus emit most of the heat on the rear side. Consequently the resulting temperatures are lower at these places. In addition it is clearly visible that the lower part of the antenna has a slightly higher temperature than the upper part. This directly results from the configuration of the main compartment below the HGA. Here the experiment section attached to the equipment section is reflecting part of the HGA radiation back to the lower HGA half which results in higher temperatures. For 1972 the temperature distribution shows different characteristics. Due to the large heliocentric distance solar illumination does not heat the HGA significantly, main heating is conducted by the HGA RHUs as well

as heating by radiation emitted from the component housing. In general the heat distribution is more uniform and the places of the modelled RHUs are clearly visible by slightly larger surface temperatures.

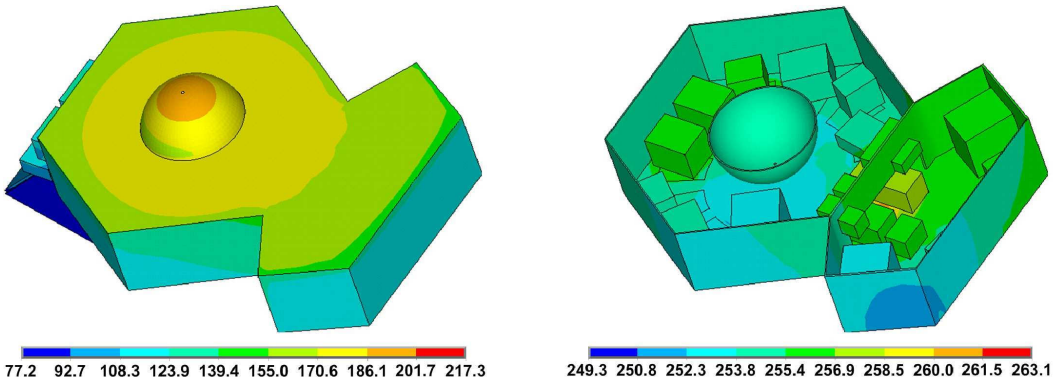

Figure 6.4: Temperature distribution on external MLI sheets (left) and interior compartment and payload surfaces (right) for conditions in 1990. Temperatures are given in Kelvin.

Figure 6.4 shows the equilibrium surface temperatures on the external MLI sheets (compartment top) as well as the interior compartment and panel temperatures for 1990. The temperatures on the MLI are considerably lower than the internal temperatures which can be credited to the good insulation properties of the MLI. A temperature gradient with a maximum at the fuel tank position is clearly visible. This is mainly caused by the close proximity to the HGA which leads to a higher fraction of heat radiation reflected back to the MLI thus leading to a higher temperature in this region. In general the temperatures of the MLI on the compartment top are higher than those at the side panels and the base panels which can also be credited to the insulating effect of the HGA.

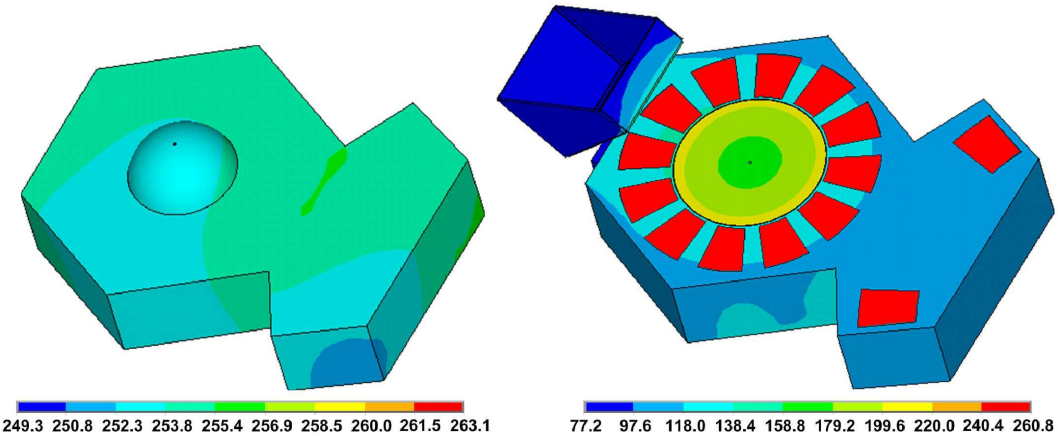

Figure 6.5: Temperature distribution on compartment cover panel and louver system / MLI on base panel (right) for conditions in 1990. Temperatures are given in Kelvin.

Figure 6.5 shows the temperatures on the compartment top panel below the MLI (left) and the base panel MLI with louvers (right). The temperatures on the top panel are fairly uniform with a maximum gradient of 6 K which can be credited to the good isolating properties of the MLI. The temperatures on the external MLI sheet at the base panel are also fairly uniform and considerably lower than on the top panel side because here the emission of heat is unobstructed by other satellite components which leads to a higher effective radiation flux.

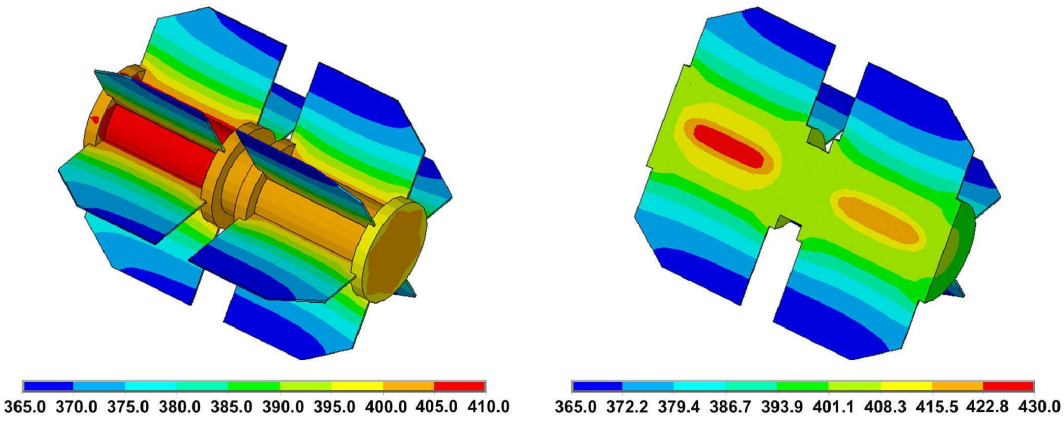

Figure 6.6: Temperature distribution on RTG housing (left) and interior RTG temperatures (right) for conditions in 1990. Temperatures are given in Kelvin.

The temperatures on the RTG external surfaces and the RTG interior are displayed in figure 6.6 left and figure 6.6 right, respectively. The highest temperatures are situated within the radioactive plutonium fuel capsules which inhibit the waste heat load. The surrounding housing has a lower, uniform temperature distribution with slightly decreasing temperatures in outward direction. The fins finally have a high temperature gradient from the fin root to the fin tips where the lowest temperatures are reached at the fin tips.

6.4 Computation of TRP on the Pioneer 10 orbit

One of the main scientific goals of this thesis is the analysis of TRP acting on the Pioneer 10 during the 30 years of mission time where flight telemetry is available. In order to achieve this goal, subsequent thermal FE analysis and numerical TRP calculations have been performed using the Pioneer 10 FE macro described in section 5.1 and the ray tracing algorithm introduced in section 3.4. The computations have been performed with a time resolution of 1 year between the simulated times, input parameters and boundaries have been updated to the values valid for the simulated times. For the computation of the resulting TRP accelerations acting on the craft a constant reference mass of 250 kg has been considered. The residual accelerations found by the JPL for Pioneer 10/11 are displayed in figure 6.7. Here the JPL residuals have been obtained for evaluating different ranges of available Doppler datA for both Pioneer 10 and 11. It can be seen that particularly for earlier mission times, errors bars in the resulting residuals are quite high. The general characteristics of the plot are an increase

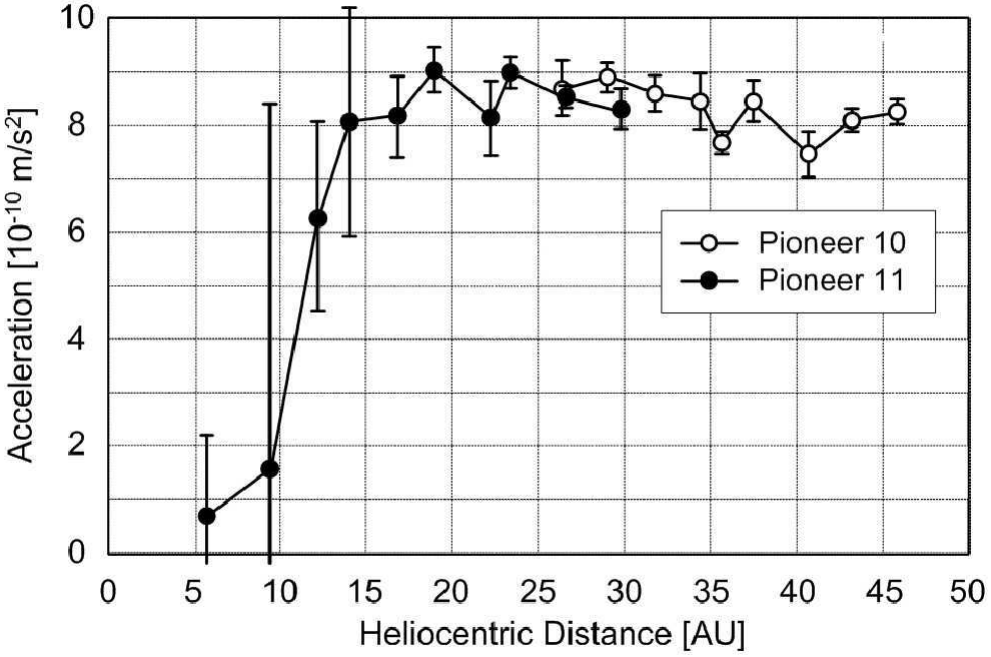

Figure 6.7: JPL Pioneer 10 acceleration residuals [18].

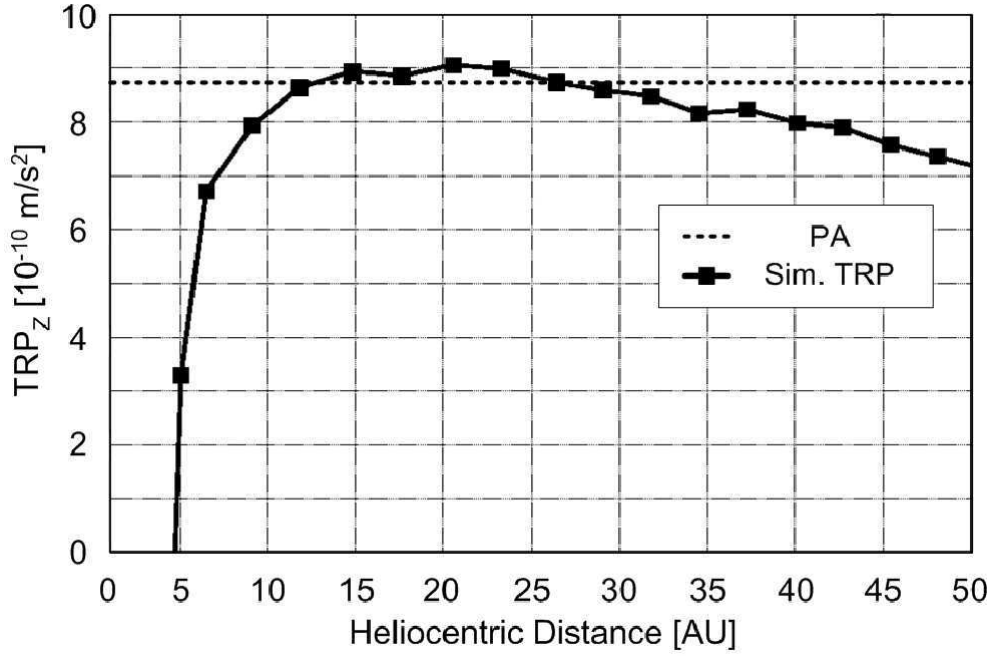

Figure 6.8: Computed TRP acting on Pioneer 10 [55].

of acceleration from close to zero at about 5 AU to a peak value at 20 AU. After this the acceleration stays in approximately the same range, although the error bars also allow to interpret a small linear decrease of TRP acceleration. The range from 15 AU - 45 AU has been used to obtain the published constant result for the Pioneer anomaly of $a_{\mathrm{Pio}} = 8.7410^{-10}\mathrm{m/s}^2$. Note that while the presented residuals have been acquired

for Pioneer 11 in the early mission range and for Pioneer 10 in the later mission times, Pioneer 10 should show corresponding results for the early mission as the spacecraft configuration is nearly identical and the trajectory does not differ drastically[1].

Figure 6.8 shows the computed TRP acceleration aligned with global z-direction vs. heliocentric distance for the range of 1 AU - 50 AU to allow for a direct comparison with the evaluated JPL residuals. Here the discrete points in time for which TRP has been computed with the raytracing and thermal FE modelling method are marked with black quads. The heliocentric distances have been acquired from the available Pioneer 10 trajectory according to the simulated mission dates as described in section 5.1. For comparison the constant value of the PA as defined by the JPL is marked with a dashed line.

In general, the computed TRP matches the JPL residuals very closely and shows the same characteristic time evolution. TRP acceleration (aligned with global z-direction) starts in the negative range for 1 AU and increases with growing heliocentric distance until it changes its sign in the region of 5 AU. It reaches a peak value at about 20 AU and decreases with a linear rate for larger heliocentric distances. With this the computed TRP results stay within the uncertainties of the JPL residuals. Note that due to the fact that the first data points given in the residuals acceleration have been evaluated for Pioneer 11, in this range a larger deviation of the computed results seems reasonable since the trajectories of Pioneer 10 and 11 are slightly different.

The significant match of computed TRP and JPL residuals leads to the conclusion that the observed anomaly is caused by an unmodeled thermal recoil pressure. All characteristics of the residuals can be explained by different TRP effects. In the early mission, where the spacecraft is still close to the sun (between 1 AU - 5 AU) the HGA gets heated by direct solar illumination as displayed in figure 6.9 right. Here higher temperatures are displayed in red/orange and lower temperatures are displayed in blue. Due to the considerable difference of HGA front and rear optical emissivities the major part of the heat energy introduced by solar illumination is emitted by the HGA front which leads to an effective TRP (not to be mixed with SRP, which is a different physical effect). The resulting contribution to the global TRP acts into flight direction and thus causes an acceleration of the craft. For small heliocentric distances this is the dominating thermal effect which explains that by global coordinate convention the resulting total TRP is in the negative range. Due to the dependency of the solar flux on the square root of the distance to the sun the resulting temperature of the HGA decreases in the course of the mission. This implies that the contribution of the HGA to the TRP also decreases with growing heliocentric distance and other thermal effects become dominant. Thus the TRP reaches the positive range (which implies a deceleration of the craft) at a heliocentric distance of about 5 AU.

The resulting TRP for distances larger than 5 AU is governed by two different effects. The first larger fraction of the total TRP is caused by the emission of waste heat

[1]While Pioneer 10 only had a Jupiter flyby in 1973 after 1.5 years of mission, Pioneer 11 had an additional Saturn flyby after 6 years of operation. With this the flight velocity and the heliocentric distance varies slightly wit respect to Pioneer 10.

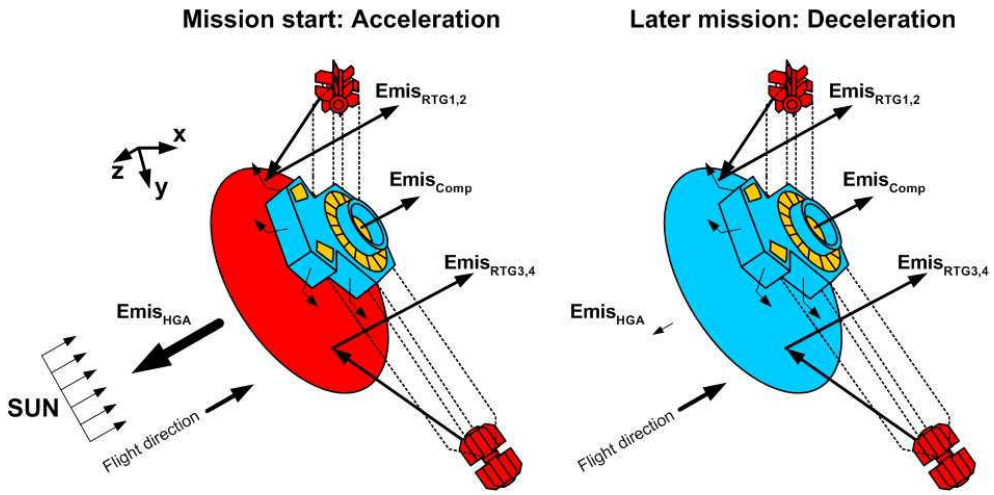

Figure 6.9: Explanation for characteristic development of effective TRP direction. Red: high temperatures, orange: medium temperatures, blue: low temperatures.

from the RTG fins. Due to the geometric arrangement of RTGs, HGA and compartment a small fraction of the heat energy emitted by the RTGs is blocked by the highly reflective HGA rear surface and reflected into flight direction. The exact magnitude of the resulting TRP depends on the RTG surface temperatures as well as the radiation view factors which are computed accurately by 8-node Gauss integration over all RTG/HGA surface pairs. The resulting recoil acts against flight direction and thus causes a deceleration of the craft in the range of 80 % of the PA at 25 AU. The effect is scaled by the mission time and subject to a small linear decrease which can be credited to the decreasing RTG fin root temperatures and the decreasing heat energy in the course of the mission.

The second dominant effect is the emission of waste heat produced within the compartment. Due to the good isolation properties of the MLI as well as internal heat radiation waste heat is distributed almost homogeneously inside the compartment. This heat energy is now dissipated over the MLI, the louver system and the shunt radiator. Due to the symmetry of the compartment and the attitude of the global coordinate system, the heat which is emitted by the side panel surfaces as well as the shunt radiator waste heat do not contribute to a TRP aligned with flight direction. The temperatures on the MLI front and rear faces are comparatively low which reduces the radiated heat flux. Furthermore radiation of the MLI front is mainly blocked by the HGA which results in multiple reflections between MLI and HGA surfaces. Effectively the thrust resulting from front MLI emission is mostly balanced by the emission of the MLI on the rear side of the compartment. This leaves the louver system as well as the MLI parts inside the launch adapter as only contributors for TRP. Here the louver system delivers the dominating fraction of compartment emission contributing to TRP which is caused by the much higher surface temperatures of the louver system and the dependence of the resulting heat flux to the fourth power of the temperature. Nevertheless the MLI inside the launch adapter contributes a small amount of emission to the resulting TRP. In combination both effects lead to an effective TRP of about 20 % PA at 25 AU directed against direction of flight which results from the geometric arrangement

of the components. As it is the case for the RTG contribution the magnitude of the effect scales with mission time which reflects the dependence on the available electrical energy as well as the compartment temperature sensor data.

In total the emission of waste heat from RTG, Louver system and partially the MLI leads to an effective TRP acting against flight direction in the magnitude of the PA at 25 AU which slowly decreases due to generally decreasing temperatures and available powers. Such a decrease in the evaluated residuals is expected by the JPL as result of the ongoing evaluation of the full Doppler data set [57]. Both the matching magnitude of the computed effect as well as the resembling characteristics of the JPL residuals and the computed results indicate that accurate modelling of TRP is the solution to the Pioneer anomaly.

6.5 Parameter variation and error analysis

In order to obtain error estimate for the TRP solution the method used for the computation of TRP for different mission times is now used to determine the influence of different parameters on the resulting TRP. Here those parameters which influence the components which dominate the magnitude of the TRP are analysed. All computations are performed using a baseline model for boundary conditions in 1990 where the single parameter to be evaluated is varied.

The ranges of variations of the different input parameter are based on various assumptions. For the optical properties of the various surfaces BOL and EOL values are known from pre-mission testing. However, due to the unknown actual state of surface degradation, a variation in the range of 10 % seems reasonable in order to perform a conservative error estimation. For heat loads extracted from sensor data (e.g. the compartment electrical power) the maximum variations are taken as worst case values for the error assessment. Here a worst case variation of 10 W can be identified for the compartment electrical energy. The specification of a worst case variation in RTG waste heat is challenging since no direct measurements exists. However, the RTG power model proposed by the JPL reflects the actual RTG behaviour quite accurately. Thus the RTG waste heat can be computed by subtracting the converted electrical energy (which is known from telemetry data) from the predicted total energy. Thus a maximum model error of 10 W (per RTG) can be evaluated.

Parameter	Varied range	Effect on TRP
RTG emissivity	0.70 - 0.90	± 1.50 %
Antenna rear emissivity	0.03 - 0.05	± 1.00 %
Louver effective emissivity	0.03 - 0.05	± 1.50 %
MLI emissivity	0.60 - 0.8	± 0.03 %
Compartment power	± 10 W	± 1.00 %
Total RTG waste heat	± 40 W	± 1.50 %

Table 6.1: Errors determined with variation of optical properties and heat loads.

Table 6.1 lists the model parameters which have been varied as well as the considered parameter ranges and the resulting influence on the resulting total TRP. As can

be seen, the TRP solution is considerably stable to variations of the input parameters which mainly results from the fact that the thermal FE solution uses the measured temperature data as boundary conditions. By this the range of possible solutions is already highly constrained which reduces the magnitude of influence of other model parameters. If, for example, a surface emissivity is varied while keeping the heat load on the surface as well as the temperature boundaries at specific places constant, the result is a variation of the temperature distribution but not a drastic change of the total emitted heat flux since the total radiated power stays constant.

Besides the influence of parameter variations additional errors might be inflicted by numerical inaccuracies in the FE solution, the ray tracing process as well as inaccuracies in the sensor readings which have been used as temperature boundaries. Inaccuracies in the FE solution are below 1 %, which has been realised through extensive global and local mesh refinement. The accuracy of the TRP computation has been demonstrated with the test cases described in section 3.6 and can be estimated to a maximum error of about 0.5 %. This low value has been realised by implementing a large number of rays per element (500000) as well as numerical integration of the radiation view factors by means of Gauss quadrature with 8 integration points per dimension. The temperature sensor readings aboard the Pioneer 10 spacecraft have a digital resolution of 6 bit which translates to a temperature inaccuracy of ± 1.44 F. The resulting worst case inaccuracy of the boundary temperature can directly be computed to ± 1.7 K. In the late stage of the mission this inaccuracy leads to a TRP variation of about 3 %. As the compartment model uses the same type of temperature sensors a corresponding error on the TRP of about 1.5 % has to be added. Note that this error is much lower for the early and intermediate mission periods, resulting from the higher mean temperature in the compartment.

In a coarse worst case scenario (where all individual errors are simply summarised) the total error in the TRP calculation evolves to about $\pm 11.5\%$. With this value the presented TRP solution is considerably robust with respect to the different error sources discussed above. Further smaller variation may result from unknown effects such as non-documented differences in the geometry of flight and engineering model or the exact characteristics of the degradation of the surface materials. For Pioneer 10, most of the degradation is supposed to have occurred during Jupiter flyby. Thus it would be reasonable to assume non-degraded optical properties before the Jupiter encounter and EOL values afterwards. However, due to the sensor temperature constraints and the small range of possible variations in the optical parameters, the computed TRP characteristics will practically not change for such a degradation profile.

Part III

Thermal perturbation analysis for Rosetta

Chapter 7

Solar radiation pressure (SRP) model

This chapter introduces a numerical method for the determination of SRP acting on a spacecraft with complex shapes. An analytical model for simple geometries is presented and the expansion into a numerical method for complex models is discussed.

7.1 Introduction to SRP modelling

Since SRP is also caused by the interaction of radiation with target surfaces the analytical models derived for the determination of the TRP can also be used for the determination of SRP. The main difference is that the source of radiation is not the model surface itself, but the Sun which can be considered as an external radiation source. Therefore a corresponding numerical method for the calculation of SRP can be developed based on the numerical methods developed for the TRP computation (described in section 3.4). The modelling approach for SRP analysis is based on a GMM of the spacecraft including geometry and optical surface properties where the spacecraft surface is represented by a set of quadrilateral FE surfaces. In difference to the TRP algorithm no surface temperature distribution of the spacecraft and thus no thermal FE analysis is necessary for the computation of the SRP as the effect only depends on the spacecraft shape and the state of illumination by the Sun.

In this approach the Sun is modelled as a high resolution pixel array from which individual parallel solar ray vectors originate. In a ray tracing process the interaction of the solar ray vectors with the spacecraft surfaces as well as shadowing aspects are assessed. The SRP is calculated on each individual model surface. By summing up all individual surface drags, the resulting SRP can be computed. The algorithm for the numerical computation of the SRP is realised as a set of c-functions which import text files containing GMM info in order to calculate the forces. The geometric modelling is performed with an FE preprocessor as explained in section 3.4. The individual modelling steps are discussed in the following.

7.2 Analytical model for solar radiation pressure

SRP results from a momentum exchange with photons impacting on a spacecraft's surface. The resulting change in the spacecraft's momentum can be described by equation (3.5), as introduced in section 3.2. Here the solar energy received by the spacecraft and the orientation of the spacecraft surfaces to the Sun determine the magnitude and the orientation of the resulting SRP.

Assuming a flat quadrilateral surface in space, the received solar energy at the heliocentric distance r can be expressed as:

$$P_{\mathrm{rec}}(r) = A\, P_{\odot}(r) \cos\kappa_{\mathrm{abs}}\,, \tag{7.1}$$

where A is the element surface area, $P_{\odot}(r)$ is the solar flux at the heliocentric distance r and κ_{abs} is the orientation angle of the plate with respect to the Sun. Here the solar flux can be related to the known solar flux at earth distance with $P_{\odot}(r) = \frac{P_{\odot,1AU}}{r^2}$ where r is measured in units of AU.

Resulting from the model for radiation-surface interaction evolved in section 3.3, the SRP magnitude for a single flat surface exposed to the Sun can now be written as:

$$\vec{P}_{\mathrm{SRP}} = -\frac{P_{\mathrm{rec}}(r)}{m\,c}\left[(1-\gamma_{\mathrm{s}})\,\vec{r}_{\mathrm{SUN}} + 2\,(\gamma_{\mathrm{s}}\cos\kappa_{\mathrm{abs}} + \frac{1}{3}\gamma_{\mathrm{d}})\,\vec{n}\right], \tag{7.2}$$

allowing for diffuse and specular reflection of the received sunlight. Here the acting direction of the resulting SRP is characterised by the normalized Sun vector $\vec{r}_{\mathrm{SUN}}$ and the normal direction $\vec{n}$ of the respective surface.

7.3 Solar pixel array model

The first step in the numerical modelling of SRP is the generation of a solar plane which is perpendicular to the Sun direction as displayed in figure 7.1 left. For this the normalized Sun-spacecraft vector in the satellite frame $\vec{r}_{\mathrm{SUN}}$ can be computed from the satellite quaternions q_1, q_2, q_3, q_4 and the known satellite position $\vec{r}_{\mathrm{Sat}}$ in the heliocentric frame:

$$\vec{r}_{\mathrm{SUN}} = \begin{pmatrix} r_{\mathrm{SUN,x}} \\ r_{\mathrm{SUN,y}} \\ r_{\mathrm{SUN,z}} \end{pmatrix} = -\mathbf{A}\frac{\vec{r}_{\mathrm{Sat}}}{|\vec{r}_{\mathrm{Sat}}|}\,, \tag{7.3}$$

where the quaternion rotation matrix $\mathbf{A}$ is characterised by equation (3.34). For a tracked spacecraft orbit the needed information can directly be acquired from attitude and ephemeris data. Now azimuth and elevation angle in the satellite frame can be characterised by:

$$\theta = \arctan\frac{r_{\mathrm{SUN,z}}}{r_{\mathrm{SUN,x}}}, \qquad \phi = \arctan\frac{r_{\mathrm{SUN,y}}}{r_{\mathrm{SUN,x}}}\,, \tag{7.4}$$

where $r_{\mathrm{SUN,x}}, r_{\mathrm{SUN,y}}$ and $r_{\mathrm{SUN,z}}$ are the three components of the Sun-spacecraft vector. For the creation of the solar plane a first vertex vector $\vec{V}_1$ can be computed by rotating

a virtual xy-plane around the z-axis by azimuth ϕ. The resulting vector is then rotated around the virtual direction y' by an angle of $\theta_{V1} = \theta - \frac{\pi}{2}$. This can be expressed as:

$$\vec{V}_1 = \mathbf{A}'_{\mathbf{y}}\,\mathbf{A}_{\mathbf{z}} \begin{pmatrix} 1 \\ 0 \\ 0 \end{pmatrix} , \tag{7.5}$$

where $\mathbf{A}'_{\mathbf{y}}$ and $\mathbf{A}_{\mathbf{z}}$ are the quaternion rotation matrices for a rotation around y' and z respectively.

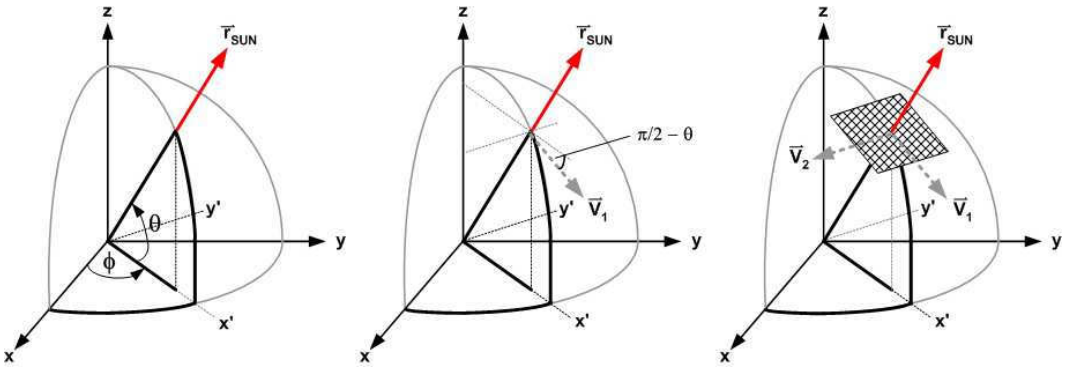

Figure 7.1: Computation of vertex vectors for solar pixel array.

The second vertex vector $\vec{V}_2$ can be computed from the vector product of $\vec{r}_{\mathrm{SUN}}$ and $\vec{V}_1$. Now the vertexes are used for the generation of a solar plane perpendicular to the Sun-spacecraft vector where the plane centre is determined by the intersection of the plane and the vector from the satellite centre to the Sun $\vec{r}_{\mathrm{SUN}}$. For the resulting plane a total size has to be be specified. The projection of the plane onto the spacecraft has to fully engulf the surface model. For the preparation of the ray tracing (which is used for the detection of shadowed elements and the calculation of reflections) the solar pixel plane is partitioned into individual solar pixels. Here the pixel resolution determines the accuracy of absorption and reflection implementation.

The actual size of the individual solar pixels x_{pix} and y_{pix} is determined by the total number of lateral and longitudinal pixels n_{x} and n_{y} and the specified total dimensions of the array x_{tot} and y_{tot}:

$$x_{\mathrm{pix}} = \frac{x_{\mathrm{tot}}}{n_{\mathrm{x}}} \;\text{ and }\; y_{\mathrm{pix}} = \frac{y_{\mathrm{tot}}}{n_{\mathrm{y}}} . \tag{7.6}$$

Now the centre position of each pixel within the array can be expressed as:

$$\vec{P}_{\mathrm{C}}(i,j) = \big((i-0.5)\cdot x_{\mathrm{pix}} - \frac{x_{\mathrm{tot}}}{2}\big)\cdot\vec{V}_1 + \big((j-0.5)\cdot y_{\mathrm{pix}} - \frac{y_{\mathrm{tot}}}{2}\big)\cdot\vec{V}_2 - d\cdot\vec{x}_{\mathrm{SUN}} , \tag{7.7}$$

where d is the modelling distance of the array surface to the spacecraft model and i and j denote the position of the pixel in the array as displayed in figure 7.2 left for the specific pixel (7,7).

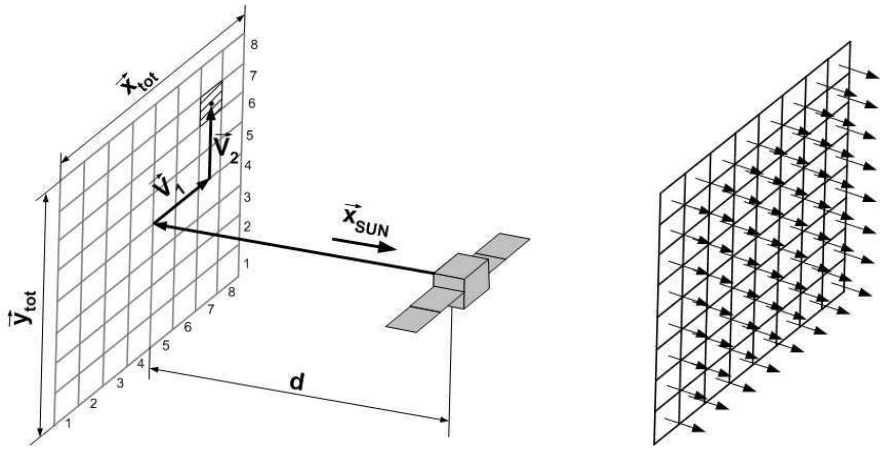

Figure 7.2: Computation of individual pixel centre (left) and composition of complete solar pixel array (right) with $\vec{x}_{\mathrm{SUN}} = -\vec{r}_{\mathrm{SUN}}$.

Originating at each pixel's centre, ray vectors pointing in the direction of $-\vec{r}_{\mathrm{SUN}}$ are initialised as displayed in figure 7.2 right. Each ray is scanned for intersections with the model surface elements in order to detect illuminated and shadowed surfaces. For this the surface elements are sorted by distance from the current pixel centre and the hit evaluation (determined by a ray intersecting a surface element) is performed for the nearest elements first. If a hit is detected the respective ray is not traced further thus no other elements can be hit by the same ray. For each hit diffusely and specularly reflected rays are initialised as discussed in section. A received energy $P(i)$ can be computed for each target surface intersected by a ray based on the mean solar flux $P_{\odot}(r)$ at the distance r, the surface of the target element $A(i)$ and the surface normal direction $\vec{n}(i)$:

$$P_{\mathrm{rec}}(i) = P_{\odot}(r)\, A(i)\, \vec{r}_{\mathrm{SUN}} \cdot \vec{n}(i)\,. \tag{7.8}$$

Note that in this case the orientation vector is given by $\kappa_{\mathrm{abs}} = \arccos(\vec{r}_{\mathrm{SUN}} \cdot \vec{n}(i))$. Following the approach taken for the modelling of the TRP the SRP component resulting from absorption can be computed with:

$$\vec{P}_{\mathrm{SRP,abs}}(i) = -\vec{r}_{\mathrm{SUN}}\, \frac{\alpha\, P_{\mathrm{rec}}(i)}{m\, c}\,. \tag{7.9}$$

For specular reflection the resulting SRP component can be expressed as:

$$\vec{P}_{\mathrm{SRP,spe}}(i) = -\vec{r}_{\mathrm{SUN}}\, \frac{\gamma_{\mathrm{s}}\, P_{\mathrm{rec}}(i)}{m\, c} + \vec{x}_{\mathrm{spe}}\, \frac{\gamma_{\mathrm{s}}\, P_{\mathrm{rec}}(i)}{m\, c}\,, \tag{7.10}$$

where $\vec{x}_{\mathrm{spe}}$ is the direction of specular reflection as modelled in section 3.3. Finally the SRP component resulting from diffuse reflection can be computed for each surface element by:

$$\vec{P}_{\mathrm{SRP,dif}}(i) = -\vec{r}_{\mathrm{SUN}} \frac{\gamma_{\mathrm{d}}\, P_{\mathrm{rec}}(i)}{m\, c} - \frac{2}{3}\, \vec{n}(i)\, \frac{\gamma_{\mathrm{d}}\, P_{\mathrm{rec}}(i)}{m\, c}\,. \tag{7.11}$$

The resulting SRP can be calculated by the sum of all absorption and specular and diffuse reflection components of all individual surface elements:

$$\vec{P}_{\mathrm{SRP,res}} = \sum_{i}^{n}(\vec{P}_{\mathrm{SRP,abs}}(i)) + \sum_{i}^{n}(\vec{P}_{\mathrm{SRP,spe}}(i)) + \sum_{i}^{n}(\vec{P}_{\mathrm{SRP,dif}}(i))\,. \tag{7.12}$$

In this approach the resulting TRP vector and the individual surface TRP vectors are given in the spacecraft frame. The detection of radiation exchange between the different model surfaces is implemented with the ray tracing approach described in section 3.4. Note that for multiple reflections the reflection contribution caused by a reflected ray which is absorbed again has to be subtracted from $\vec{P}_{\mathrm{SRP,spe}}(i)$. As for the TRP method, the SRP can be converted to a solar radiation force. If these forces are determined for each of the model surfaces and the centre of mass of the spacecraft is known a resulting solar radiation torque can be determined.

Chapter 8

The Rosetta Mission

This chapter gives an overview on the main characteristics of the Rosetta mission as well as the geometrical features of the spacecraft. The flyby anomaly is introduced and the motivation for SRP and TRP analysis for the Rosetta spacecraft is discussed.

8.1 Mission goals and trajectory

The international Rosetta mission is a cooperation between ESA, NASA and the national European space agencies. The main scientific mission goal is the investigation of the solar system origin by examining the properties of cometary nuclei [78]. For this purpose Rosetta will rendezvous with comet 67P/Churyumov-Gerasimenko in 2014 where its lander payload Philae will land on the comet surface to study the physical and chemical structure of the body [79]. Other scientific goals are the examination of the evolution of the coma during the comets approach to the Sun, the interaction of solar winds with the satellite and a study of the two asteroids 2867 Steins and 21 Lutetia which have already been passed on the way to the comet as displayed in figure 8.1. In total Rosetta includes a set of 25 individual science experiments to be conducted in the various stages of the mission. In order to save fuel and to perform scientific experiments the satellite conducts a series of gravity assist manoeuvres, which partly have been tracked. Here the flybys of Earth are particularly interesting due to the observation of an anomalous increase of the spacecrafts velocity during the first flyby. This so called flyby anomaly has been also been observed for other spacecraft and will be discussed in section 8.2 in more detail. In the times without manoeuvres the satellite performs so called cruise phases where attitude control is reduced to a minimum. This creates ideal conditions for an observation of non-gravitational forces acting on the spacecraft.

Currently Rosetta is on its approach to Churyumov-Gerasimenko and has been put to deep space hibernation mode to ensure a minimum of energy consumption and hardware degradation. It will be put back to full operation in 2014 shortly before the final approach to the comet.

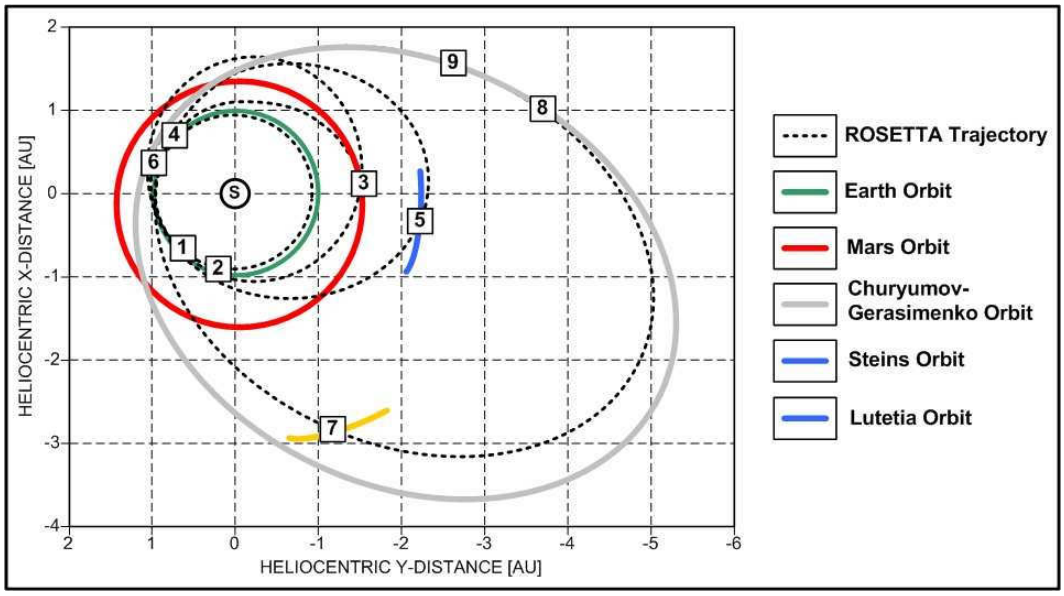

Figure 8.1: Rosetta Trajectory in heliocentric frame, 1: Start of Rosetta on 2004/03/02, 2: 1st Earth flyby on 2005/03/04, 3: Mars flyby on 2007/02/25, 4: 2nd Earth flyby on 2007/11/13, 5: Asteroid Steins flyby on 2008/09/05, 6: 3rd Earth flyby on 2009/11/13, 7: Lutetia flyby on 2010/07/10 8: Rendezvous with Churyumov-Gerasimenko on 2014/05/22, 9: Touchdown of Philae on 2014/11/10 [80].

8.2 The flyby anomaly

The flyby technique has been used several times and is a common manoeuvre for the acceleration of spacecraft without the need for additional fuel. By choosing a hyperbolic flight approach a spacecraft is accelerated by the gravitational pull of a planets gravitational field and leaves the planet with a higher (heliocentric) velocity. In particular, this technique is used for deep space missions where high velocities are needed to reach the destinations within considerable time frames. Up to now there have been eight flybys around the earth. Also other planets have been used, e.g. Jupiter and Saturn for the deep space probes Pioneer 10 and 11. From all these flybys only the Earth-flybys have been tracked with high accuracy (flybys at earth can be tracked and ranged with very high precision, e.g. 10^{-6} m/s). For four of the Earth-flybys an anomalous change of the velocity has been observed (see table 8.1) which has not been understood using current orbit determination codes. The anomaly has been obtained from Doppler and ranging data of the Deep Space Network (DSN) at the JPL. It results from all used ODPs.

Mission	Agency	Year	Pericentre r_p [km]	Eccentricity e	Δv [mm/s]
Galileo	NASA	Dec 1990	959.9	2.47	3.92 ± 0.3
Galileo	NASA	Dec 1992	303.1	2.32	-4.6 ± 1
NEAR	NASA	Jan 1998	538.8	1.81	13.46 ± 0.01
Cassini	NASA	Aug 1999	1173	5.8	-2 ± 1
Rosetta	ESA	Mar 2005	1954	1.327	2 ± 0.03
Messenger	private	Aug 2005	2347	1.3	0.02 ± 0.01

Table 8.1: Observed anomalous velocity increases Δv for Earth flybys [22].

The first indication for a flyby anomaly came up with the precise observation and tracking of the Galileo spacecraft on December 8, 1990 [81]. Despite intensive studies of the tracking data by the Galileo work group no plausible explanation could be found for this phenomenon. The next flyby of Galileo on December 8, 1992 had a too low perigee (300 km) so that the atmospheric disturbances covered any anomalous behaviour of the flyby completely [81]. However, after extensive post processing and refinement of the data also for this flyby an unexpected velocity change became visible. The flyby anomaly has been observed directly for the second time during the Earth flyby of the satellite NEAR on January 23, 1998. During the following flyby of Cassini in August 1999 a navigation control manoeuvre was necessary which complicated the detection of the anomaly. However, it was possible to estimate the increase of the velocity for this flyby too. In March and August 2005 respectively an unexplained increase in velocity has been observed for Rosetta and Messenger after an Earth flyby as well.

The relevant data on the flybys as well as the values of the anomalous velocity jumps have been published in a number of different publications [59, 81, 82, 83]. However, an extensive error analysis which takes into account all conventional disturbances has not yet been conducted. Further publications which sum up the observed effects and analyse the reliability of data have been issued by Lämmerzahl, Preuss and Dittus [13] as well as Anderson and Williams [84]. Due to the unknown origin of the velocity jumps and the lack of accurate trajectory data ESOC decided to track Rosetta during its third and final Earth flyby with a high precision. However for this flyby no anomalous jumps in the velocity of the spacecraft could be detected. Thus the cause of the observed anomalies remains unknown.

8.3 Motivation for thermal investigations of the Rosetta spacecraft

Due to the planned mission profile of Rosetta as well as the total duration of the mission and the geometry of the spacecraft, the influence of SRP on the spacecrafts trajectory is considerably high. This is mainly caused by the fact that the solar arrays are designed to provide approximately 395 W at 5.25 AU which is the largest heliocentric distance Rosetta experiences on its orbit. For the beginning of the mission this implies a huge solar flux on the solar panels as the received solar power is scaled with the inverse square of the spacecrafts heliocentric distance. With a total of about 69 m^2 of exposed area to the Sun (with solar arrays pointing to the Sun at all times) this translates to a radiation pressure at Earths distance in the range of 10^{-7} N (assuming that all of the received energy is converted into thrust), which has to be modelled thoroughly in order to propagate the orbit with adequate precision.

Detailed orbit determination and propagation of the Rosetta orbit has been performed by ESA/ESOC during the course of the mission. However, although qualitative the models fitted quite well with the observations, residuals of up to 10 % of the modelled SRP have been found when comparing the simulation results to the observed orbits [62]. Analytical results have pointed out that these variations may be resolved by accurate modelling of thermal recoils resulting from asymmetric heat radiation of solar panel and bus surfaces. Due to the detected discrepancies and the fact that TRP

effects have not been modelled independently, a detailed investigation aiming at the exact numerical computation of SRP and TRP on Rosetta's orbit is well motivated. This approach also enables the modelling of geometrical details such as the high gain antenna which is difficult to realise using analytical models.

Furthermore the observed anomal velocity jumps during Rosetta's first Gravity assist manoeuvre (and also the fact that the same behaviour could not be detected in the most recent Rosetta flyby event) demands the investigation of the influence of SRP and TRP on the trajectory during the flyby manoeuvre. If thermal effects cause additional momentum during the flyby and the direction matches the direction of flight, these effects may lead to 'jumps' in the spacecrafts velocity, as observed for Rosetta's first Earth flyby and other missions with gravity assist manoeuvres. Therefore an exact analysis of thermal effects during flyby is necessary to resolve if these are the cause of the observed anomalous effect or if they can be excluded from the list of potential explanations.

8.4 Spacecraft design

The main design of the Rosetta satellite is governed by a central box-shaped main bus, which is enclosed by two large solar cell arrays as displayed in figure 8.2[1].

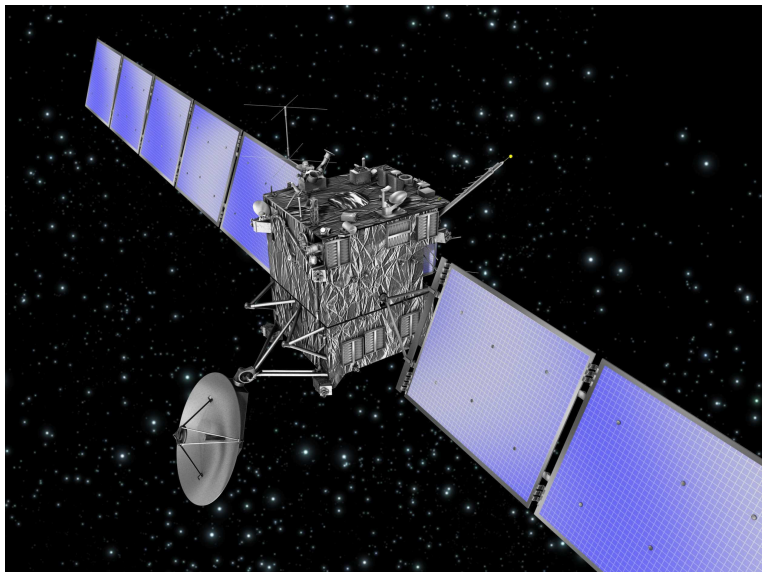

Figure 8.2: Rosetta spacecraft design.

The bus has the dimensions 2.8 m x 2.1 m x 2.0 m while each of the solar arrays mounted at opposite bus panels cover a surface area of approximately 32 m^2. This considerably large solar panel area results from the power requirements at the target body. Here the large heliocentric distance demands a huge solar panel area to generate the needed amount of electrical energy. The resulting high variations of input solar power over the mission is handled by a special power point management [80]. In order to realise a continuous power supply during the deep space phases of the mission, the

[1]Picture: ESA, http://www.esa.int/esa-mmg/mmg.pl, accessed on 08/08/2011.

solar panels are attached to the bus with joints which are rotatable along the long solar panel axis. This enables a constant Sun pointing of the solar panels. In total the Rosetta spacecraft has a launch mass of 2900 kg, where 265 kg can be accounted for the lander Philae and the scientific payloads on board while 1720 kg is the mass of the carried fuel [79].

A 2.2 m diameter high gain antenna is attached to the side panels and can be rotated in two axis after deployment. Due to the design of the joints and the deployed position of the antenna the possible rotations are restricted in terms of elevation (30°/-165°) and azimuth pointing angles (80°/-260°) [85]. This means that in order to keep contact with the ground stations in some phases of the mission the bus had to be rotated to allow for a continuous Earth antenna pointing. Further communication hardware includes a medium gain antenna and two omnidirectional low gain antennas.

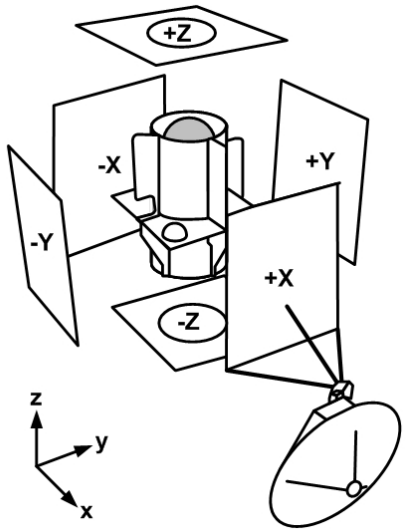

Figure 8.3: Rosetta Panel nomenclature, [79] and internal arrangement.

The main satellite body is divided into a payload support module and a bus support module. The payload support module which is situated in the upper part of the satellite box contains the scientific payloads and two deployment mechanisms for booms. The bus support module contains the satellite infrastructure and is placed in the lower part of the box. The Rosetta side, ground and cover panels (defined with the respective orientation in the coordinate system as displayed in figure 8.3) consist of an aluminium honeycomb core with aluminium face sheets and are covered with black carbon-filled Kapton MLI blankets. The +Z panel (also called science panel) is designed to be facing the comet continuously during the comet orbiting phase. For this reason the optical navigation camera is mounted on this panel. During the cruise phases, +X and +Z panel will be lighted by the Sun while the other panels mostly remain in shadow. Therefore radiators and louvers for thermal control are only mounted on the +Y/-Y and -X faces which are in shadow. The lander payload philae is attached to the -X side to reduce degradation of hardware and surfaces during the transfer to the comet. Once in cometary orbit the lander will detach itself from the box and land on the target body.

The spacecraft is three-axis stabilised and a total of 24 attitude thrusters is distributed on the outer faces of the bus panels. A thrust tube made of corrugated aluminium with strengthen rings is placed in the centre of the craft, aligned with the bus z-axis. The thrust tube can be used for primary attitude and motion manoeuvres (such as delta-v boost for flyby manoeuvres etc.) and contains two 1106 liter propellant tanks, where the upper one stores the propellant (660 kg bipropellant monomethyl hydrazine) and the lower one stores the oxidiser (1060 kg nitrogen tetroxide) providing a total of 2200 m/s delta-v over the course of the mission. Also in the centre of the spacecraft body four smaller pressurant tanks of 35 liters each can be found. For attitude control and determination Rosetta is equipped with four reaction wheels, two star trackers, Sun sensors, navigation cameras and three laser gyro packages. Besides the lander Philae, Rosetta carries 12 different scientific experiments. Details on the respective scientific goals as well as on the design of the payloads can be found in [79].

Chapter 9

Rosetta Finite Element model

This chapter gives an overview on the geometrical modelling, the definition of the material models as well as the boundaries and input data for the Rosetta FE model. The dependence of the component models on the changing pointing and attitude of the spacecraft is highlighted.

9.1 Model overview

For the computation of SRP and TRP acting on Rosetta during cruise phases and flyby a thermal FE model including the spacecraft geometry (which may change by e.g. a rotation of the HGA or a rotation of the solar panels) has been developed. The model is implemented as a set of macros in the ANSYS Parametric Design Language (APDL) comparable to the already discussed Pioneer FE model treated in section 5.1. This approach enables the comfortable performance of subsequent analysis with change of input parameters. By using the corresponding input parameter sets the macro can be used to model different geometric configurations as well as to compute the resulting surface temperature distribution for each point of the mission. Here SRP calculations only demand the geometrical model of the craft while TRP calculations depend on the assessment of the surface temperature distribution. The modelling approach and the different sub models are discussed in the following.

9.2 Coordinate systems

The main included components of the Rosetta FE model are the satellite bus, the solar arrays and the Rosetta high gain antenna. For the modelling of the components different frames have been specified which enable the inclusion of changing orbit and pointing data in the model. All computed resulting forces and geometrical properties are defined in the bus reference frame as displayed in figure 9.1.

The bus frame is positioned in the bus centre with its y-axis aligned with the solar panel hinges and x- and z-axis perpendicular to the other satellite faces. Following the definition of the frame the different bus faces can be specified with +X (in positive bus frame x-direction), +Z (in positive bus frame z-direction), +Y (perpendicular to +X and +Z with right-hand rule), -X, -Y and -Z. Here the +X panel is the panel where

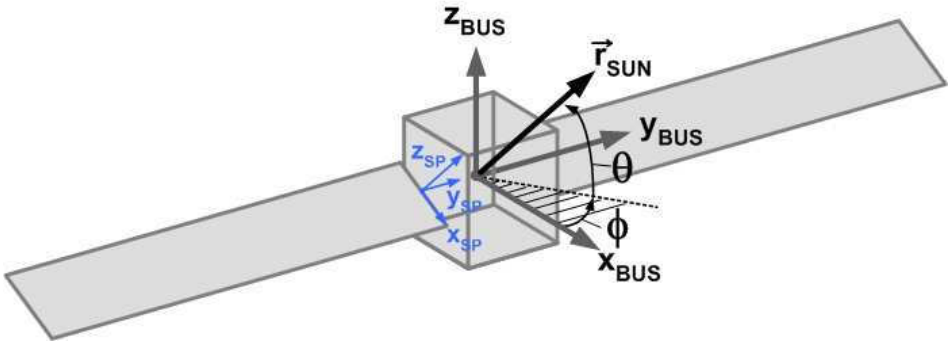

Figure 9.1: Definition of Rosetta bus frame (black) and solar panel frame (blue).

the HGA is mounted. The elevation angle θ is defined as the angle between the solar vector $\vec{r}_{\mathrm{SUN}}$ and the projection of the solar vector on the xy-plane where the elevation is defined as positive for a counterclockwise rotation with respect to y_{BUS}. In other words an increasing elevation leads to an increasing illumination of the +Z face. The azimuth angle ϕ is defined as the angle between the projection of the solar vector on the xy-plane and the x_{BUS}-axis. The angle is positive for counterclockwise rotation with respect to z_{BUS}.

The solar panel frames are placed at the root of each panel. Due to the fact that the surface normal of the Rosetta solar panels always points to the Sun (which is realised by the attitude control system and the actuator which allow for a rotation of the panels), z_{SP} is aligned with the Sun direction. The solar panel y_{SP} axis is aligned with the bus y_{BUS} axis and the x_{BUS} axis is perpendicular to the two other axis. A transformation between bus and solar panel frames may be performed with the transformation matrix:

$$\vec{r}_{\mathrm{BUS}} = \vec{r}_{\mathrm{SP}} \cdot \begin{pmatrix} \cos\theta & 0 & \sin\theta \\ 0 & 1 & 0 \\ -\sin\theta & 0 & \cos\theta \end{pmatrix} + \vec{x_0}\,, \tag{9.1}$$

where $\vec{x_0}$ is the respective offset of the Solar panel frame origin to the bus frame origin in y_{BUS} direction. The definition of the HGA zero position frame is displayed in figure 9.2 left. It results from offsets of the bus frame in bus x,y and z-direction. For non-zero position of the HGA (as displayed in figure 9.2 right) the pointing is characterised by the angles θ_{HGA} and ϕ_{HGA}. Here the configuration $\phi_{\mathrm{HGA}} = 0°$ and $\theta_{\mathrm{HGA}} = 0°$ is defined as the electrical zero position. The azimuth angle ϕ_{HGA} is defined as the angle between HGA x-axis and the projection of the pointing vector $\vec{p}_{\mathrm{HGA}}$ on the HGA xy-plane. Here a counterclockwise rotation with respect to z_0 is defined positive. The elevation angle is defined as the angle between the projection on the xy-plane and the pointing vector itself. Here a clockwise rotation with respect to y_0 is considered positive.

The pointing vector in the HGA frame can be computed with:

$$\vec{p}_{\mathrm{HGA}} = \begin{pmatrix} \cos\theta_{\mathrm{HGA}} \cos\phi_{\mathrm{HGA}} \\ \sin\phi_{\mathrm{HGA}} \\ -\sin\theta_{\mathrm{HGA}} \cos\phi_{\mathrm{HGA}} \end{pmatrix}. \tag{9.2}$$

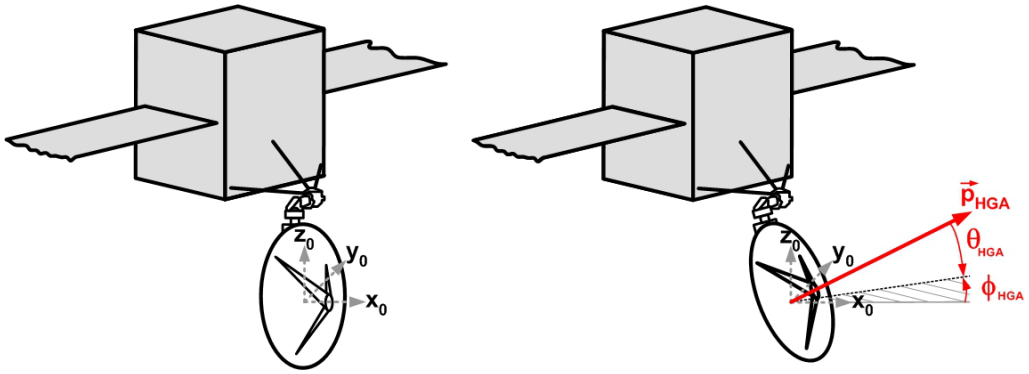

Figure 9.2: Definition of HGA frame and pointing angles.

Note that for the HGA elevation angle the positive direction of rotation is defined opposite to the bus elevation angle rotation direction. Due to the equilibrium of momentum any rotation of the HGA leads to a counteracting rotation of the bus. Resulting from the different definitions of the elevation angles an increase in HGA elevation will lead to an increase of the bus elevation angle.

9.3 Rosetta component models

Geometry

The geometric modelling for the Rosetta FE model has been performed with the same methods as introduced for the Pioneer FE model. Due to the fact that solar illumination is by far the dominant effect for surface heating, only solid volumes have been modelled and the exact internal configuration with different payloads, computers and other bus hardware has been neglected. The resulting FE model is displayed in figure 9.3.

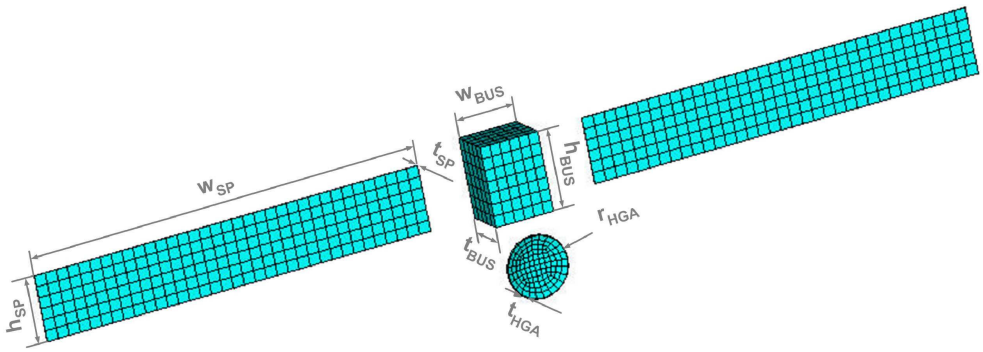

Figure 9.3: Rosetta FE model with bus, solar panels and HGA.

The geometry of the Rosetta spacecraft is modelled from a set of primitive geometry elements provided by ANSYS. Bus and solar panels are implemented by rectangular blocks where the solar panel volumes are mounted on the centres of the +Y/-Y faces. Resulting from the parabolic shape the complexity of the HGA model is much higher and has to be derived from the expansion of its cross-section into a solid volume. Table 9.1 lists the dimensions of the major model components.

Part	Parameter	Name	Value
BUS	Thickness of bus	t_{BUS}	2.000 m
	Width of bus	w_{BUS}	2.100 m
	Height of bus	h_{BUS}	2.800 m
SOLAR PANEL	Thickness of solar panel	t_{SP}	0.022 m
	Width of solar panel	w_{SP}	14.30 m
	Height of solar panel	h_{SP}	2.300 m
HGA	Radius of HGA	R_{HGA}	1.100 m
	Height of HGA	h_{HGA}	0.344 m
	Thickness of HGA	t_{HGA}	0.050 m
HGA FRAME	X-offset w.r.t. bus frame	x_0	1.000 m
	Y-offset w.r.t. bus frame	y_0	0.000 m
	Z-offset w.r.t. bus frame	z_0	-3.00 m

Table 9.1: Geometrical constants of Rosetta FE model.

The general parabolic shape of the HGA can be expressed in HGA coordinates for the height x at a given radius r as:

$$x(r) = a\, r^2 + b\,. \tag{9.3}$$

The offset of the HGA frame to the bus frame at $r = 0$ leads to $b = x_0$. On the outer diameter of the HGA ($r = R$) the height is:

$$x(r = R) = a\, R^2 + x_0 = h + x_0\,. \tag{9.4}$$

This leads to $a = \frac{h}{R^2}$, thus the HGA shape is characterised by:

$$x(r) = h \left(\frac{r}{R}\right)^2 + x_0\,. \tag{9.5}$$

Now the parabolic shape function can be used to generate a spline representing the HGA cross-sectional shape. The resulting spline is rotated by 2π along HGA x-axis to create the full HGA +X face. Using the Euler rotation matrix:

$$\mathbf{A} = \begin{pmatrix} \cos\theta_{\mathrm{HGA}} \cos\phi_{\mathrm{HGA}} & -\cos\theta_{\mathrm{HGA}} \sin\phi_{\mathrm{HGA}} & \sin\theta_{\mathrm{HGA}} \\ \sin\phi_{\mathrm{HGA}} & \cos\phi_{\mathrm{HGA}} & 0 \\ -\sin\theta_{\mathrm{HGA}} \cos\phi_{\mathrm{HGA}} & \sin\theta_{\mathrm{HGA}} \sin\phi_{\mathrm{HGA}} & \cos\theta_{\mathrm{HGA}} \end{pmatrix}, \tag{9.6}$$

the resulting surfaces are oriented corresponding to the HGA pointing characterised by elevation θ_{HGA} and azimuth ϕ_{HGA} angles. Table 9.2 shows the spline vertexes characterising the cross-sectional shape of the HGA in HGA frame. A matlab file has been used to check the validity of the spline data.

Node No.	1	2	3	4	5	6	7	8	9	10	11
r/R	0.0	0.1	0.2	0.3	0.4	0.5	0.6	0.7	0.8	0.9	1.0
x	0.300	0.303	0.314	0.331	0.355	0.386	0.424	0.469	0.520	0.579	0.644

Table 9.2: Set of nodal coordinates for Rosetta HGA spline model.

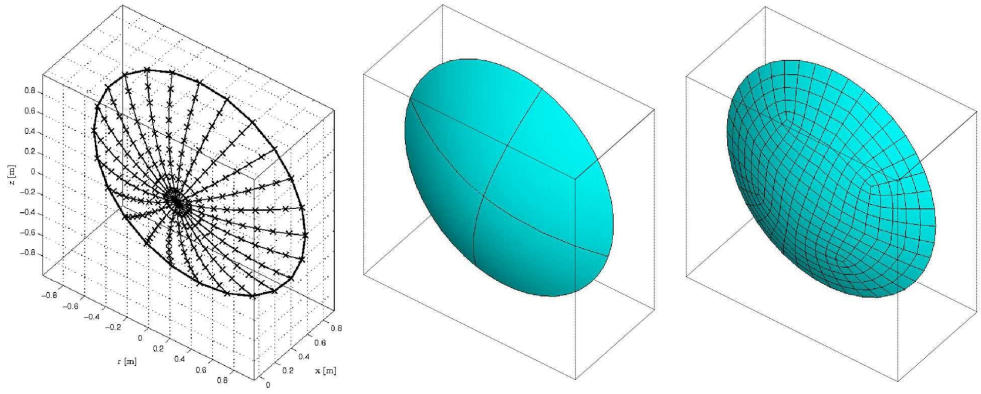

Figure 9.4: Antenna spline (left), surface (centre) and FE model.

Figure 9.4 left shows the resulting matlab plot based on the computed spline data (Using 11 discrete nodal coordinates to build up the spline). The spline is rotated in the APDL macro to generate a set of four 90° surface sections representing the HGA (as seen in figure 9.4 centre). Hexaedral four-node finite surface elements are used for the meshing of each of the surfaces thus creating a discretized HGA surface model as displayed in figure 9.4 right. By extruding the HGA surface in $+x_{HGA}$-direction by the antenna thickness t_{HGA} the HGA volume is generated. The missing side surfaces are created automatically by the preprocessor. Antenna cross-section and Antenna volume are defined in the HGA frame. By applying elevation and azimuth angle as a rotation of the HGA frame and the solar panel frames with respect to the bus frame different HGA pointings and orientations to the Sun as displayed in figure 9.5 may be modelled.

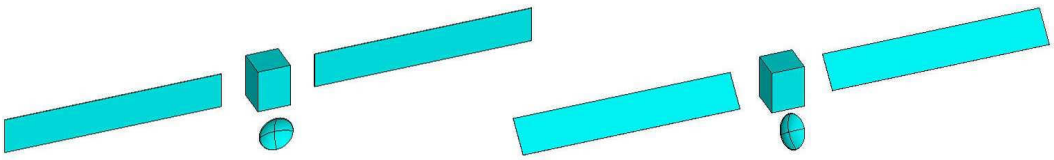

Figure 9.5: Different geometrical configurations of the Rosetta spacecraft, Left: $\theta = \phi = \theta_{HGA} = \phi_{HGA} = 0°$, Right: $\theta = 45°, \phi = 0°, \theta_{HGA} = -30°, \phi_{HGA} = 30°$.

Figure 9.5 left shows the Rosetta configuration for zero elevation and azimuth angles. With this the solar panel z-axes are pointing into positive bus x-direction. For a positive bus elevation angle of 45° (as seen in figure 9.5 right) the solar panels are rotated around the y-axis by an angle of -45° from the zero position. Thus the solar panel normal points to the Sun. Figure 9.5 right furthermore shows the resulting configuration for a HGA elevation angle of -30° and an HGA azimuth angle of 30°. Note that due to the definition of the positive elevation for the rotation of the HGA a negative angle results in a rotation towards the bus.

Material Models

In order to perform a thermal analysis and to compute SRP and TRP acting on the the Rosetta spacecraft optical parameters of the spacecraft surface and the material

conductivity have to be specified. Due to the reduction of the level of modelling complexity by using primitive solid volumes instead of the complex interior composition, representative parameters for the conductivities of solar panels, bus volume and HGA volume have to be determined. Based on the realistic composition of the structural parts these representative values will be computed for each component in the following.

Solar panel properties

The solar panels are composed by two carbon fibre reinforced plastic surface plates with an internal core of aluminium honeycomb cells. Solar cells are mounted to the surface facing the Sun, here denoted as 'front face'. Consequently the surface without solar cells is called 'rear face'. The through-thickness conductivity k_{SP} which governs the heat transport from the front face to the rear face can be computed from the ratio R_{hc} of honeycomb density ρ_{hc} to density of solid aluminium ρ_{Al}:

$$R_{\mathrm{hc}} = \frac{\rho_{\mathrm{hc}}}{\rho_{\mathrm{Al}}}\,, \tag{9.7}$$

and the conductivity of solid aluminium k_{Al} with:

$$k_{\mathrm{SP}} = R_{\mathrm{hc}}\, k_{\mathrm{Al}}\,. \tag{9.8}$$

For the optical properties of the solar panels mean emissivity and absorptivity values can be computed by means of the cell packing factor f_{p} and the properties of solar cells and the surface of the gaps between the individual cells:

$$\alpha_{\mathrm{mean}} = \alpha_{\mathrm{cell}}\, f_{\mathrm{p}} + \alpha_{\mathrm{gap}}(1 - f_{\mathrm{p}}), \qquad \varepsilon_{\mathrm{mean}} = \varepsilon_{\mathrm{cell}}\, f_{\mathrm{p}} + \varepsilon_{\mathrm{gap}}\,. \tag{9.9}$$

The mean surface reflectivity can then be determined by $\gamma_{\mathrm{mean}} = 1 - \alpha_{\mathrm{mean}}$, if the panel is non-transmissive. Note that for solar cells which produce power also the cell conversion efficiency influences the heat balance equation because part of the incoming energy is not converted to heat but to electrical energy. In this case the energy balance can be rewritten to:

$$E_{\mathrm{inc}} = E_{\mathrm{Heat}} + E_{\mathrm{Volt}}\,, \tag{9.10}$$

where $E_{\mathrm{inc}}, E_{\mathrm{Heat}}, E_{\mathrm{Volt}}$, are the incoming energy, the energy converted to heat and the energy converted to electrical energy, respectively. Consequently effective optical constants which convert the incoming solar energy to a change of momentum can be computed with:

$$\alpha_{\mathrm{eff}} = (1 - \eta_{\mathrm{cell}})\, \alpha_{\mathrm{mean}} \quad \text{and} \quad \varepsilon_{\mathrm{eff}} = (1 - \eta_{\mathrm{cell}})\varepsilon_{\mathrm{mean}}\,, \tag{9.11}$$

where η_{cell} is the conversion efficiency (solar energy to electrical energy) of the solar cells. Note that the influence of the conversion factor is disregarded in the SRP/TRP computation performed in this work. This is justified by the fact that for the cruise phase and flyby computations performed in this thesis the heliocentric distances are in the region of 1 AU - 2.5 AU. The solar panels are scaled for full functionality at approximately 5.25 AU which is the approximate heliocentric distance of the target comet. Consequently only at this distance a considerable percentage in the range of 15 % [62] of the incoming solar flux is converted to electrical energy. For a closer Sun proximity the percentage of converted energy scales with the square root of the distance. Thus at a distance of for example 1 AU, the influence of the conversion reduces to 0.5 % and can be neglected for the computations. The calculated and given solar panel properties are listed in table 9.3.

Bus properties

For the bus model an effective conductivity has to be identified to characterise the conductive heat transport. The bus is covered in MLI sheets with an approximate one-dimensional heat transport rate of $q_{\mathrm{MLI}} = 5\ \mathrm{W/m^2}$ assuming the insulation of a 20°C interior against the space environment [62]. In order to compute an isotropic conductivity, it is assumed that the heat flux originating at the fully illuminated +X face is distributed to the other bus faces with the ratio of the respective surface to the sum of all five receiving faces $\sum A_{\mathrm{rec}}$. With this the conductivity in -X direction $k_{\mathrm{BUS,x}}$ can be calculated as:

$$k_{\mathrm{BUS,x}} = \frac{Q_{\mathrm{BUS}} \Delta x}{\Delta T} \frac{A_{\text{-x}}}{\sum A_{\mathrm{rec}}} . \tag{9.12}$$

The resulting calculated conductivity and the given optical properties of the bus surfaces are listed in table 9.3.

HGA properties

The HGA is modelled as a single volume representing the complex composition of antenna dish and the web pattern rear structure. Thus an effective conductivity has to be computed from the available material data. Using Fourier's law of heat conduction the through-thickness HGA conductivity k_{HGA} can be expressed as:

$$k_{\mathrm{HGA}} = \frac{Q_{\mathrm{HGA}} t_{\mathrm{HGA}}}{A_{\mathrm{HGA}}\, \Delta T} , \tag{9.13}$$

where ΔT is the temperature difference between HGA front and rear. Assuming full illumination of the front side, the heat flux radiated by the antenna rear (index r) has to equal the heat flux conducted through the HGA volume:

$$Q_{\mathrm{HGA}} = Q_{\mathrm{HGA,r}} = A_{\mathrm{HGA}}\, \sigma\, \varepsilon_{\mathrm{HGA,r}}\, T^4_{\mathrm{HGA,r}} , \tag{9.14}$$

thus

$$k_{\mathrm{HGA}} = \frac{\sigma\, \varepsilon_{\mathrm{HGA,r}}\, t_{\mathrm{HGA}}\, T^4{}_{\mathrm{HGA,r}}}{\Delta T} . \tag{9.15}$$

By using experimental data provided in [86], the resulting effective conductivity can be computed for the representative HGA volume with thickness t_{HGA}. The resulting value and the optical properties of the HGA are listed in table 9.3.

Component	Material	α_{eff}	$\varepsilon_{\mathrm{eff}}$	$\gamma_{\mathrm{spec,eff}}$	$\gamma_{\mathrm{dif,eff}}$	k_{iso} [W/(mK)]
Bus	Black Kapton	0.93	0.86	~ 0.0	0.07	0.15708
Solar array	CFRP/cells	0.843	0.783	0.141	0.016	$0.63 + 0.142 \cdot 10^{-3}$ $\cdot(T - 273.15)$
HGA front	CFRP	0.93	0.80	0.01	0.06	0.0943
HGA rear	back structure	0.93	0.86	0.01	0.06	0.0943

Table 9.3: Material parameters for Rosetta FE model, Optical properties and data for computation of effective values taken from van der Ha et. al 2010[61] and Stramaccioni 2008[86]. Note that the specified solar array properties are valid for both front and rear panel. In a more realistic case the rear panel emissivity is a function of the panel surface temperature and different from the front emissivity. In the expected temperature range this difference is negligible.

Meshing

Three different types of FEs are implemented in the Rosetta model. For the modelling of heat conduction between the different parts of the satellite all volumes are meshed with the 8-node SOLID70 element. The 4-node thermal element SURF152 is used to implement a simple radiation approach and for the export of surface information for TRP and SRP calculations. Finally the super element AUX12 [70] is used to implement the radiation exchange between different surfaces of the model. Here all radiation boundaries are defined within a global radiation matrix. The mesh resolution (number and size of surface FEs) can be chosen by the user. In general a finer grid will deliver more accurate results but also increases the needed computation time considerably.

For TRP and SRP calculations it is mandatory that all surface normals on the external FE faces have to point outwards of the satellite. Different APDL actions may lead to erroneous inward pointing of surface normals. Thus the orientation of all surface normals has to be validated (as displayed in figure 9.6) before the model may be used safely for SRP or TRP calculations.

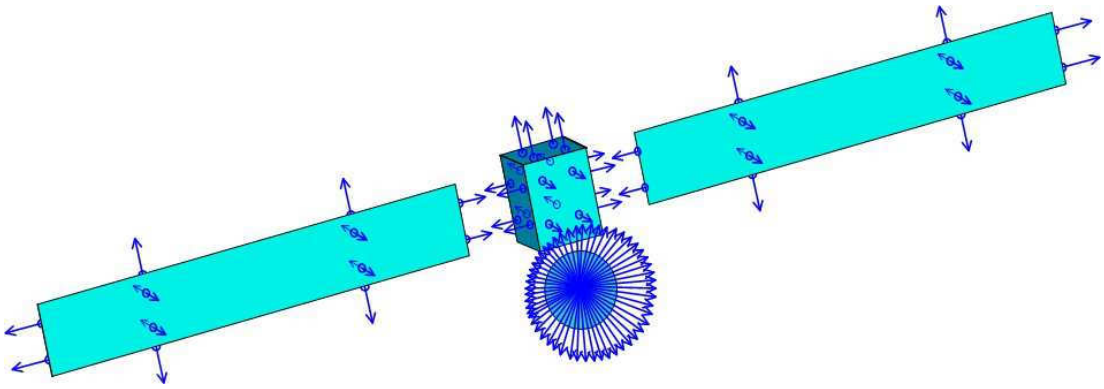

Figure 9.6: FE surface normal check.

After the meshing all information needed for the calculation of SRP is available. For the assessment of TRP also the surface temperature distribution of the spacecraft surface has to be determined. For this the environmental conditions, heat loads and boundaries have to be specified and the FE system of equations has to be solved.

Boundary conditions

The loads and boundaries of the Rosetta thermal FE model are determined by the solar illumination on the satellite surfaces as well as the environmental conditions of deep space surrounding the spacecraft. Solar illumination can be specified as an equally distributed surface specific load on the respective model faces, where the magnitude of the effect depends on the surface orientation (with respect to the Sun), the optical surface properties and the heliocentric distance. Thus different surface loads for solar panels, bus and HGA faces can be specified. The solar panel load P_{SP} can be computed by:

$$P_{\mathrm{SP}} = \alpha_{\mathrm{SP,eff}}\, P_{\odot}(r)\, \cos\phi\,, \tag{9.16}$$

where $P_{\odot}(r)$ is the mean solar flux at the current spacecraft position. Here the load is independent from the elevation angle θ because the solar panels are pointing the Sun at all times by changing the orientation of the panels relative to the bus. The solar flux can be calculated with the distance of the Rosetta spacecraft to the Sun r (in AU) and the mean solar flux at Earths distance $P_{\odot,1\mathrm{AU}}/r^2$ with $P_{\odot}(r) = P_{\odot,1\mathrm{AU}}/r^2$. The heat loads on the bus faces can be formulated with:

$$P_{\mathrm{BUS}}(i) = \alpha_{\mathrm{BUS,eff}}\, P_{\odot}(r)\, \cos\kappa(i)\,, \tag{9.17}$$

where the orientation angle $\kappa(i)$ is specified by the orientation of the respective bus surface normal $\vec{n}(i)$ to the Sun direction $\vec{x}_{\mathrm{SUN}}$ in the satellite frame:

$$\kappa(i) = \arccos \frac{\vec{n}\,\vec{x}_{\mathrm{SUN}}}{|\vec{n}(i)||\vec{x}_{\mathrm{SUN}}|}\,. \tag{9.18}$$

The orientation angle directly follows from elevation and azimuth angle by:

$$\kappa(i) = \arctan\Big(\sqrt{\frac{\sin^2\theta(i) + \tan^2\phi(i)}{\cos^2\theta(i)}}\Big) \tag{9.19}$$

where $\theta(i)$, $\phi(i)$ are the elevation and azimuth angles of the respective panel i. Details on the derivation of this equation from basic trigonometric functions are given in the annex in section V. If the angle ϕ is negative the respective bus face is not illuminated and no heat load will be specified on the surface. Thus only the +X and +Z faces have applied surface heat loads in the analysed cruise phases.

Resulting from the parabolic shape of the HGA the modelling of the heat load on the HGA surfaces is more complex than bus and solar panel heat load modelling. For every individual element surface on the HGA volume the heat load is calculated independently based on the specific normal direction of this element and its surface area as displayed in figure 9.7.

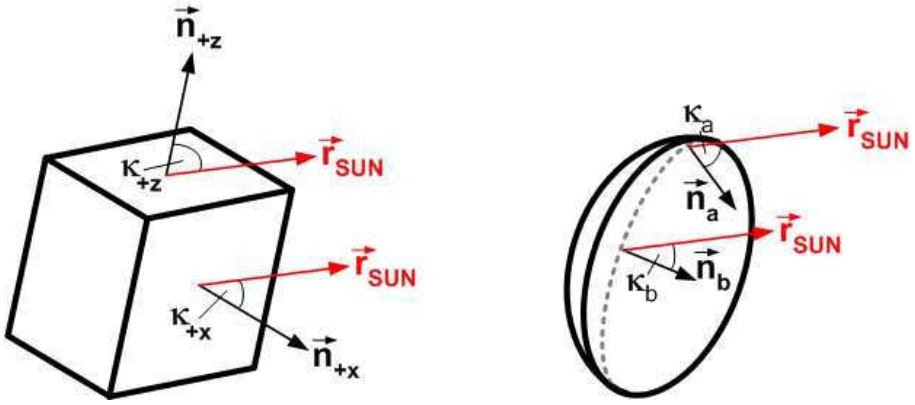

Figure 9.7: Angles for heat load computation on bus and HGA surfaces.

Thus the HGA heat load can be described by:

$$P_{\mathrm{HGA}}(i) = P_{\odot}(r)\alpha_{\mathrm{HGA}}(i)\, \cos\kappa(i)\,, \tag{9.20}$$

where the orientation angle $\kappa(i)$ of the specific surface element i is obtained by using equation (9.18) on each individual HGA element surface i. With this the heat loads on the HGA (and also the heat loads on the bus) strongly depend on the trajectory and the orientation of the craft with respect to the Sun.

In the current approach, SRP and TRP are evaluated during the mission as well as for the first Rosetta Earth flyby. For the analysis of SRP and TRP effects other disturbing effects acting on the satellite have to be well known. Therefore mission phases without orbit or attitude manoeuvres such as thruster firings are best suited for the analysis of thermal perturbations. For this purpose five so called cruise phases can be identified from the Rosetta mission calender [87].

Mission phase	Start [dd/mm/yyyy]	End [dd/mm/yyyy]	Duration [d]
Cruise 1	05/06/2004	05/09/2004	91
Cruise 2	05/04/2005	28/07/2005	480
Cruise 3	29/05/2007	12/09/2007	107
Cruise 4	28/01/2008	03/08/2008	189
Cruise 5	10/06/2008	13/09/2009	343

Table 9.4: Definition of Rosetta cruise phases.

The attitude and trajectory data needed for the evaluation of thermal forces during the specified cruise phases has been acquired from The ESA TASC website[1] which provides all necessary information (state vector, attitude quaternions, angles etc.) needed for the computation of SRP and TRP bit the pointing history of the HGA. Here the position as well as the quaternions are given in J2000 inertial frame centred in the solar system barycentre. HGA Pointing data has been provided by ESA/ESOC. Due to the fact that HGA and spacecraft data come from different sources the time resolution of the data is different. In order to create a unified time step size for the input data HGA data has been interpolated to a higher resolution. The resulting input data for each cruise phase is summarised in figure 9.8. Here the pointing angles are given in radians. For better comparison, HGA elevation and azimuth are expressed with respect to bus frame elevation/azimuth convention (what effectively means that the sign of the the HGA elevation angle has been changed). Note that the course of the bus azimuth is not displayed since it stays close to zero during the analysed cruise phases.

Various attitude and pointing changes are visible for both the bus and the HGA. The geometrical configuration for SRP and TRP computation is extracted from the measured data. However, due to the fact that for each new configuration a complete FE simulation has to be performed a simulation time resolution defining the duration between two simulated points in time has to be specified. For Rosetta this time resolution has been chosen to 8 hours, whereas the data displayed in figure 9.8 has a resolution in the region of 8 minutes. Thus spike signals which are visible mainly in the HGA pointing data may not be considered in the SRP/TRP calculations due to the fact that their duration is too short for the chosen simulation resolution.

[1] http://tasc.esa.int, accessed on 08/08/2011

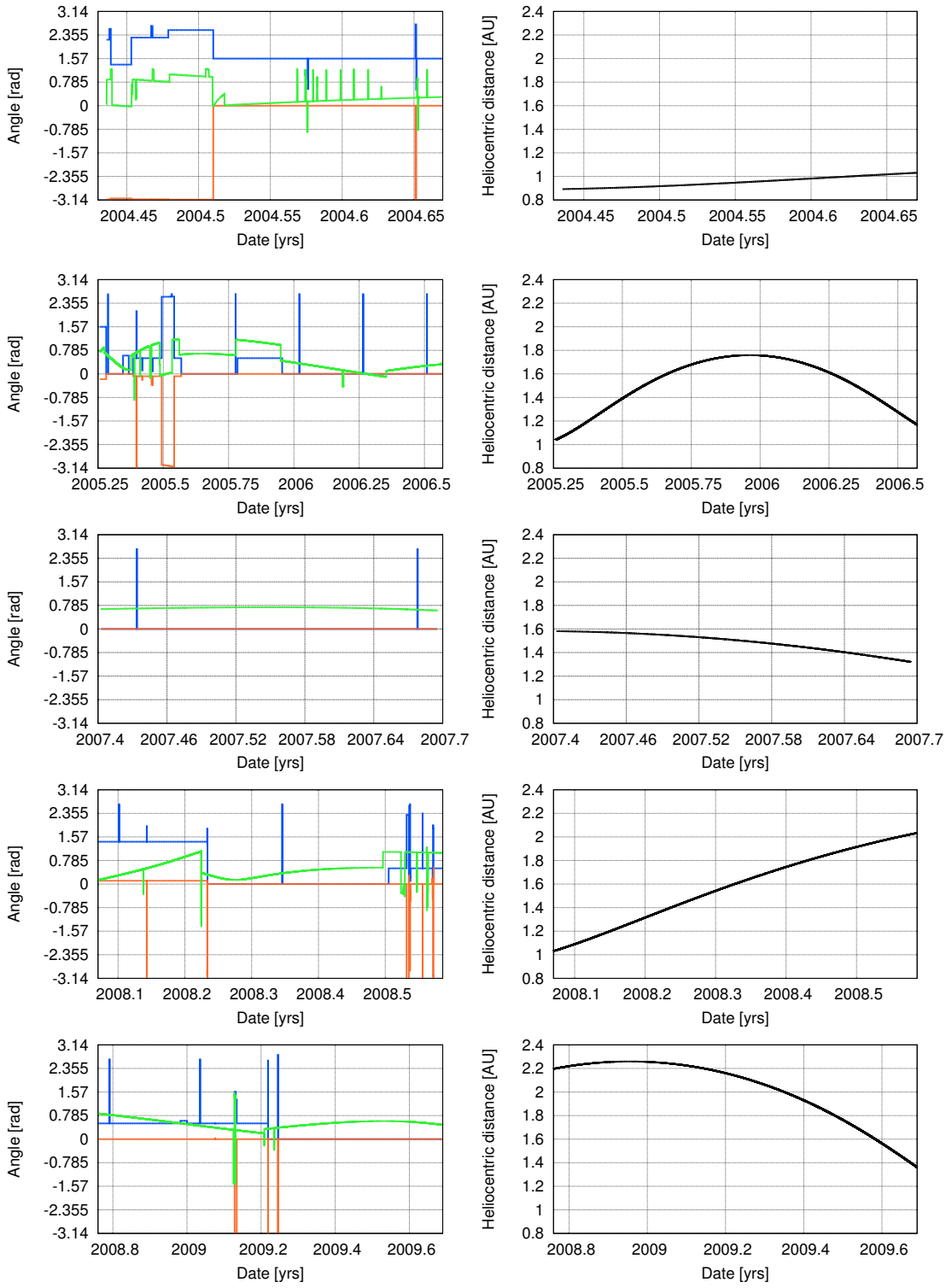

Figure 9.8: From top to bottom: Cruise phases 1- 5 pointing data. Left column: HGA azimuth (red), HGA elevation (blue), bus elevation (green), right column: heliocentric distance.

Besides the heat loads on the external surfaces which introduce heat energy into the model, all outer faces may also emit energy into the space environment. The emission of heat radiation into the environment and the radiation exchange between the different model surfaces is implemented by means of two subsequent steps. In a first step the external element surfaces of the model volumes (Element type SURF152) are applied with an RDSF surface load and a spacenode modelling the environment with a fixed temperature of 3K. Details on this approach can be found in the Pioneer FE model section 5.1 as well as in [70]. Effectively unblocked emission on each outer model surface is modelled using the ANSYS radiosity method [70]. By solving the model a first estimation of the surface temperature distribution is obtained. Now a set of areas with no or only minor influence of radiative coupling to other model parts is selected for each of the components. For this the -X bus face, the outer Y-faces of the solar panels and the HGA front face centre have been chosen. The temperatures obtained in the first estimate are stored and applied as boundary conditions in a subsequent simulation step.

In this second simulation step the SURF152 surface mesh is deleted (and with this also the RDSF boundary conditions) and a super element is initialised on the free bus surfaces using the AUX12-method [70]. With this a view factor matrix implementing radiation exchange between the individual model faces is generated which is already constrained by the surface temperatures obtained in the first computation step. By solving the FE model again, the resulting temperature distribution now includes surface to surface radiation effects. This twofold approach for the solution of the FE model greatly increases computation time compared to a direct approach without fixed temperature boundaries applied to the super element.

In contradiction to the Pioneer FE model, the Rosetta FE model does not use directly measured temperature sensor data as thermal boundaries. However, a comparison with the available temperature sensor data for the Rosetta solar panels shows good agreement of observed and simulated equilibrium temperatures [62].

Chapter 10

Rosetta SRP and TRP Analysis

This chapter summarises the steps needed to perform SRP and TRP analysis for the Rosetta spacecraft. SRP and TRP acting on the craft are evaluated during heliocentric cruise phases as well as during the first Earth flyby trajectory. The results are discussed with respect to observed residual accelerations during cruise phases and the flyby anomaly.

10.1 Procedure for Rosetta SRP and TRP determination

In order to compute the magnitude of SRP and TRP on the orbit of Rosetta, a geometrical model of the satellite, information about material properties as well as the distribution of surface temperatures at the corresponding simulated mission time has to be given. The needed inputs have to be acquired by means of steady-state thermal FE analyses using the Rosetta FE model with updated parameter configurations for each simulated point in time. For SRP calculations the geometry of the surface and the optical parameters can directly be exported from an FE mesh of the satellite. For TRP calculations a complete thermal analysis with inclusion of environmental conditions and the physics of heat transfer has to be performed to calculate also a thermal map of the spacecraft surface. Thus TRP calculations are generally more complex and demanding than SRP calculations.

For each change in geometric parameters (such as a rotation of the HGA or the solar panels) or environmental conditions (e.g. a different orientation to the sun or a different heliocentric distance) within the simulated time frame a new thermal FE analysis needs to be performed for the calculation of the corresponding force. As SRP analysis does not require information about the surface temperatures the calculation speed is highly accelerated (with respect to to TRP calculations) because the FE system of equations does not have to be solved for the generation of the input model. The general procedure for the calculation of SRP and TRP for a given time frame of the Rosetta mission is displayed in figure 10.1.

For each simulated point in time the bus elevation θ_{BUS}, bus azimuth ϕ_{BUS}, HGA elevation θ_{HGA}, HGA azimuth ϕ_{HGA}, and the distance to the Sun have to be specified. In case of Rosetta this information can be imported from the available orbit and HGA pointing data. Based on the specified parameters the surface input model and the

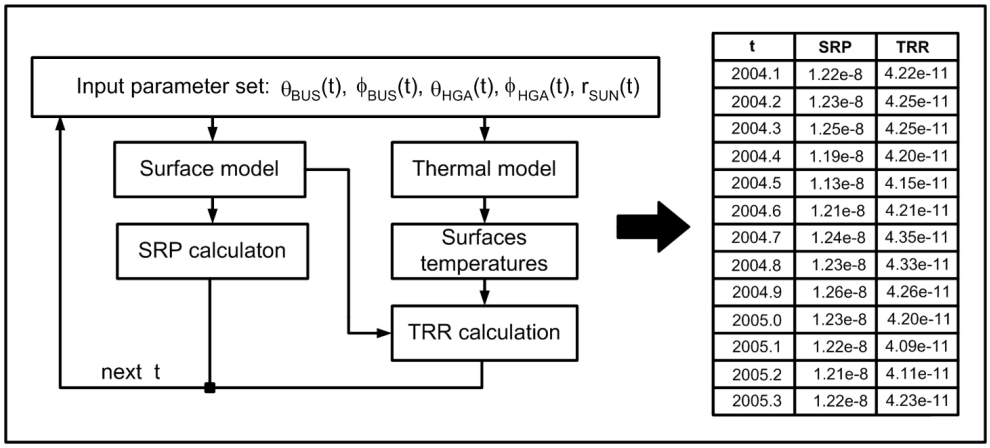

t	SRP	TRR
2004.1	1.22e-8	4.22e-11
2004.2	1.23e-8	4.25e-11
2004.3	1.25e-8	4.25e-11
2004.4	1.19e-8	4.20e-11
2004.5	1.13e-8	4.15e-11
2004.6	1.21e-8	4.21e-11
2004.7	1.24e-8	4.35e-11
2004.8	1.23e-8	4.33e-11
2004.9	1.26e-8	4.26e-11
2005.0	1.23e-8	4.20e-11
2005.1	1.22e-8	4.09e-11
2005.2	1.21e-8	4.11e-11
2005.3	1.22e-8	4.23e-11

Figure 10.1: Procedure for Rosetta SRP and TRP calculation.

thermal surface map are generated. This implies a new FE thermal analysis as well as a new force computation for each simulated point of time. With the resulting models TRP and SRP can be calculated for the specified time. After saving the results the input parameters are updated to the conditions of the next simulated time step and the process is repeated. Thus SRP and TRP evolution can be calculated for chosen time frames of the Rosetta mission with a specified time resolution and the inclusion of measured orbit and pointing data.

10.2 Rosetta Thermal analysis

In order to compute TRP for the Rosetta spacecraft, subsequent thermal analysis have to be performed. The results of these analyses are exported and are the input for the TRP computation algorithm. Since the geometry of the spacecraft (Due to the pointing of HGA and solar panels) as well as external boundaries (distance and orientation to the Sun) are changing during the mission, TRP has to be computed for a huge number of subsequent points on the orbit to account for the changing boundary conditions. In order to realise a high modelling accuracy and to keep the needed computation times at a manageable level a time resolution of eight hours between the simulated data points has been chosen. For each simulated point the actual spacecraft state vector (HGA pointing, spacecraft attitude and distance to the Sun) is imported from the available attitude and orbit data. Thus the resulting model geometry and heat loads on the model surfaces change for each simulation time step.

Figure 10.2 shows the simulated heat distribution on the Rosetta solar panel surface for the front side (left) and the rear side (right). As can be seen the rear temperatures are lower than the front temperatures which directly results from the fact that the panel fronts are always facing the Sun while the panel rears are facing the dark space environment. The temperature gradient between front and rear is determined by the thermal conductivity of the panel material as well as the interior panel design. Here a lower effective conductivity results in a high temperature gradient while a high conductivity reduces the resulting temperature difference.

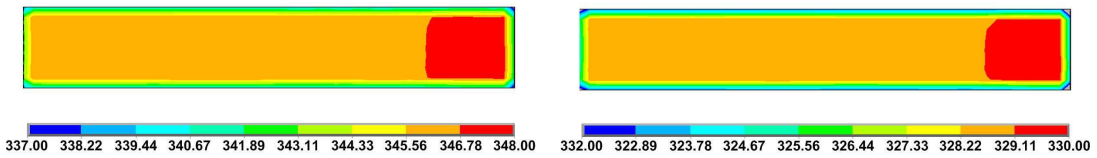

Figure 10.2: Temperature distribution on Rosetta solar panel. Left: front side, right: rear side. Note that the temperatures are given in Kelvin but in different scales.

For both rear and front panel faces higher temperatures generally arise in the regions close the the main bus. This is caused by heat radiation exchange of solar panel and bus surfaces which reduces the effective emitted heat flux for panel faces close to the bus. Here emitted radiation is reflected from the bus and absorbed again by the solar panel surfaces thus causing a local heating of the panel. The same behaviour can be seen in the available data of temperature sensors placed at different places on the solar panels. In general, the simulated and measured temperature match well for the analysed cruise phases [62]. Results for the temperature distribution on the Rosetta bus are displayed in figures 10.3 and 10.4 for different bus elevation angles.

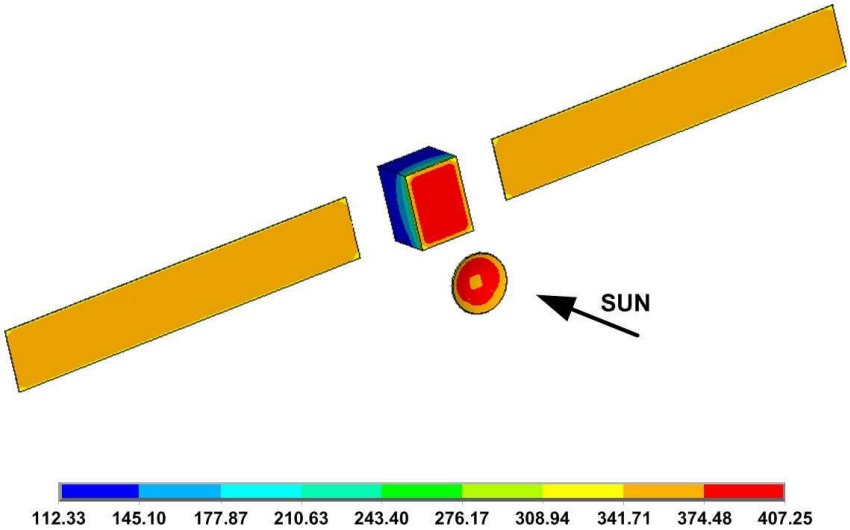

Figure 10.3: Temperature distribution on Rosetta bus for elevation angle $\theta = 0°$, temperatures are given in Kelvin.

Here the bus azimuth angle is kept at zero which resembles the realistic Rosetta attitude during the heliocentric cruise phases for which the observed bus azimuth changes are negligible. As can be seen the highest temperatures are reached in the regions facing the Sun. Maximum and minimum computed temperatures for the different bus panels are listed in table 10.1 and compared to the analytical results provided in [62]. The simulated mean temperatures show a good agreement to the results obtained analytically. This demonstrates the validity of the general approach as well as the thermal FE model of the Rosetta spacecraft.

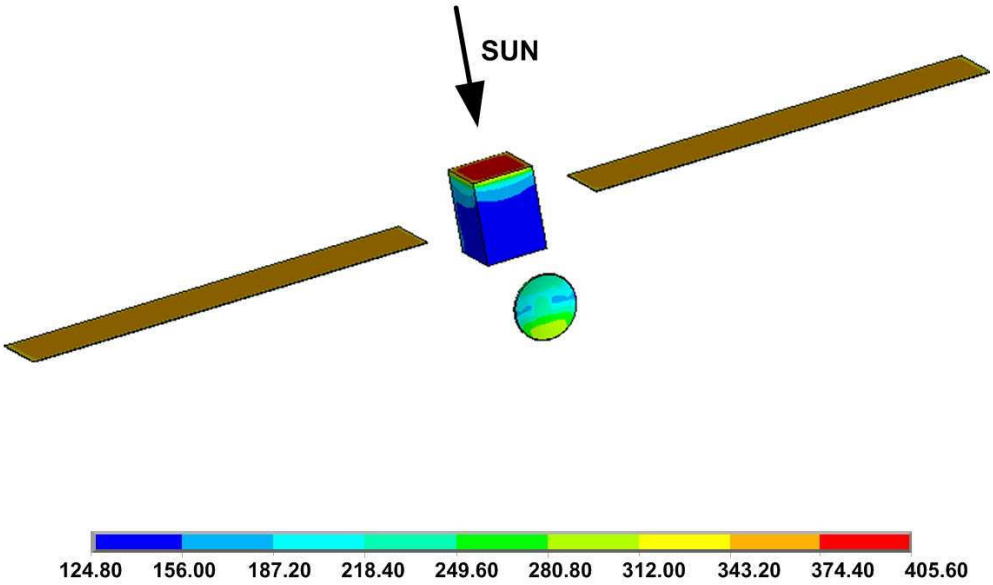

Figure 10.4: Temperature distribution on Rosetta bus for elevation angle $\theta = 90°$.

Component	T_{MAX} [°C]	T_{MIN} [° C]	T_{MEAN} [° C]	T_{ANA} [°C]
Solar panel front	73.1	65.0	70.5	70.2
Solar panel rear	55.6	53.1	54.7	54.8
Bus_{+x} at $\theta = 0°$	129.3	45.3	127.5.5	128.7
Bus_{-x} at $\theta = 0°$	-149.6	-150.8	-150.5	-150.0

Table 10.1: Simulated and analytical temperature results for $\theta = \phi = 0°$ at 1 AU.

The simulated temperature distribution on the HGA is displayed for electrical zero position at 1 AU in figure 10.5. Note that for the HGA temperature distribution no analytical results are available for comparison which is caused by the fact that complex three-dimensional geometric shapes like the HGA are difficult to model. In this respect numerical approaches are more powerful as they are not subject to limitations in geometrical complexity. In general higher temperatures are obtained on the HGA front which is caused by the fact that the HGA front is fully illumination in electrical zero position while the HGA rear is in full shadow. A tendency to higher temperatures in the proximity of the bus is visible both on the front and the rear surface. This effect which resembles the interaction of solar arrays and bus is caused by an exchange of heat radiation between bus -Z face and HGA rear.

10.3 SRP and TRP analysis for Rosetta Cruise phases

SRP and TRP are evaluated with the Rosetta FE model and the SRP/TRP computation methods discussed in sections 3.4 and 7.1. The analysis is performed for the cruise phases on Rosetta's Orbit as specified by table 9.4. The boundary conditions which are considered in the FE thermal analysis (HGA pointing, bus orientation and heliocentric distance) for each part of the considered trajectory range are summarised in figure 9.8.

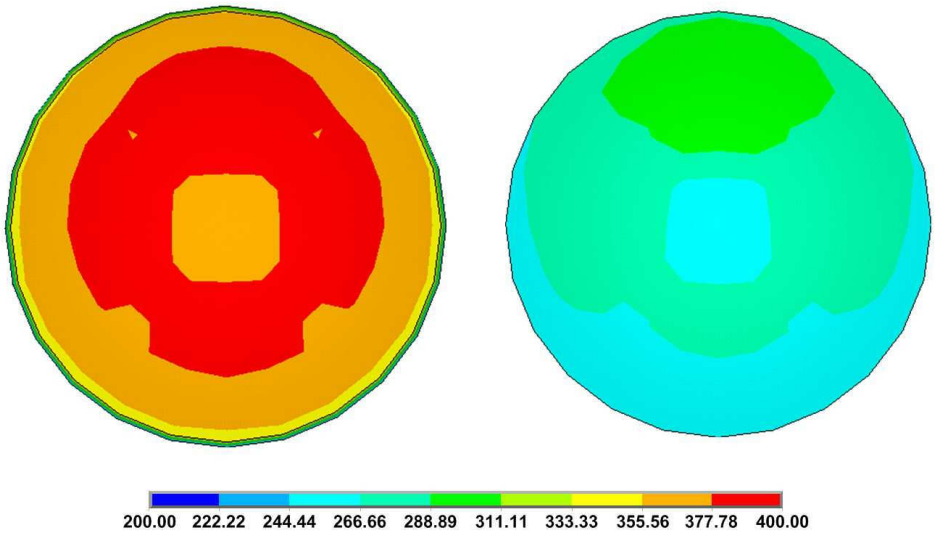

Figure 10.5: Temperature distribution on Rosetta HGA, temperature values are given in Kelvin.

The model is composed by approximately 10000 individual surface FEs and includes both solar panels, the spacecraft bus as well as the HGA. For the SRP calculation a solar pixel resolution of 10^6 has been chosen. For TRP calculations a ray tracing resolution of 150 x 150 rays per FE and a maximum of three subsequent reflections per ray is considered. For the calculation of the resulting pressures a total Rosetta reference mass of 3000 kg has been assumed. The time resolution has been chosen to eight hours between the individual simulated points in the mission. For a better overview of the resulting alignment of SRP and TRP, results are expressed with respect to the Sun vector. This is sensible because the resulting SRP and TRP will be closely aligned to the Sun vector as the solar panels are Sun pointing and the azimuth angle of the bus stays close to zero for the analysed mission parts. Thus variations from Sun vector alignment are mainly caused by a change in HGA pointing. Therefore the resulting accelerations are expressed as a component parallel to the Sun vector a_s and a component a_p perpendicular to the Sun vector which enables the distinction of elevation and azimuth influences.

Figure 10.6 shows the computed evolution of SRP acting on the Rosetta spacecraft during the heliocentric cruise phases. In all cruise phases the acceleration components perpendicular to the Sun direction are almost 3 magnitudes smaller than the components aligned with the Sun direction. Therefore all perpendicular components of the SRP are negligible with respect to the parallel component, which is not surprising, since the solar panels are pointing towards the Sun and the bus shows only small azimuth angles. Furthermore, as SRP is governed by the surface area exposed to the Sun and the sum of bus and solar panel surface make up more than 95 % of the total illuminated surface, it is clear that any change in HGA azimuth cannot change the magnitude of the SRP drastically. By comparing the computed SRP results to the pointing and trajectory input data one finds an anti proportional relation between a_s and the course of the heliocentric distance. This results from the fact, that the heliocentric distance determines the solar flux at the spacecraft's position and thus the magnitude of the SRP.

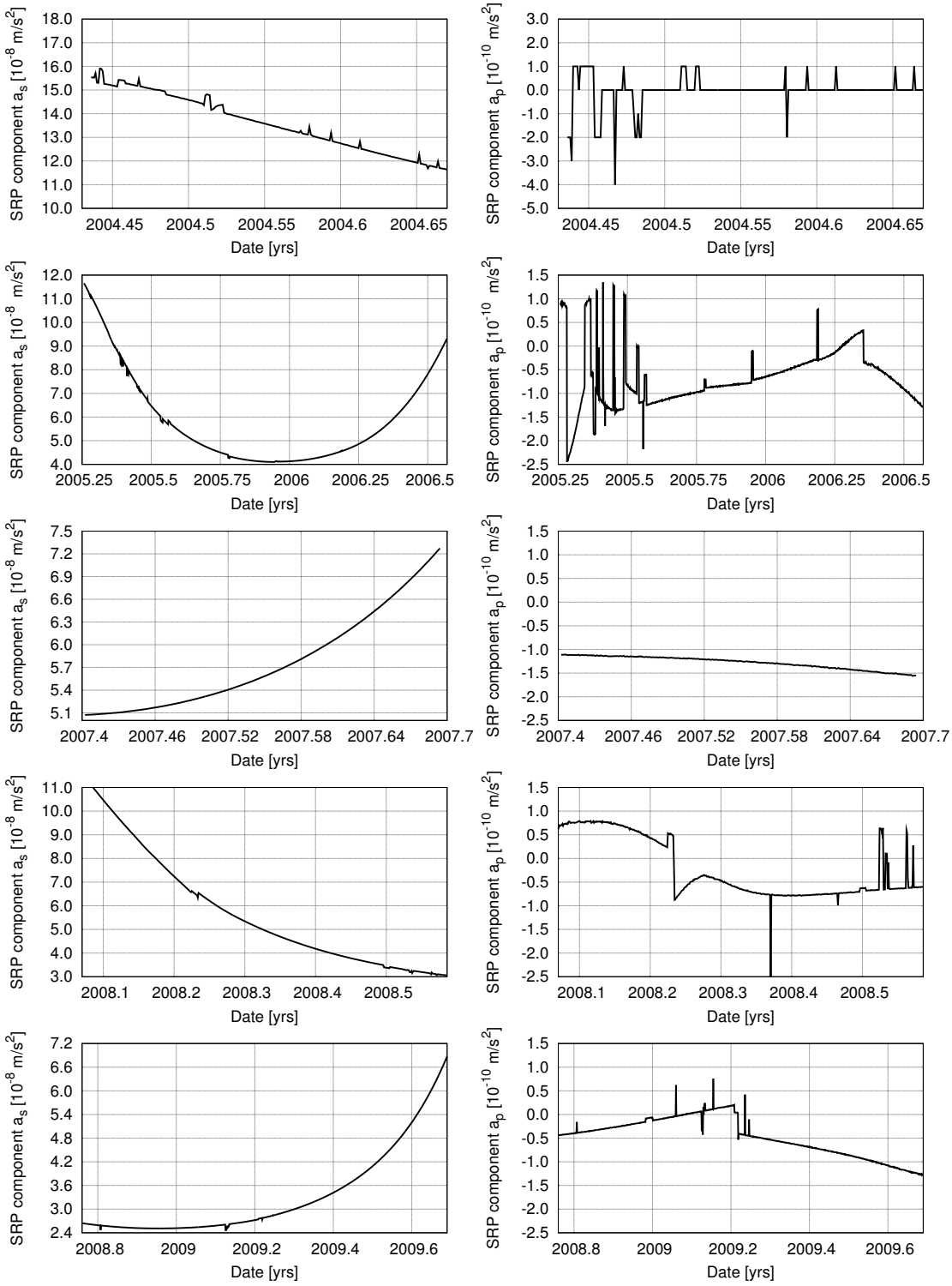

Figure 10.6: From top to bottom: Cruise phases 1- 5 computed SRP acting on the Rosetta spacecraft. Left column: SRP component aligned with the Sun direction, right column: SRP component perpendicular to the Sun direction.

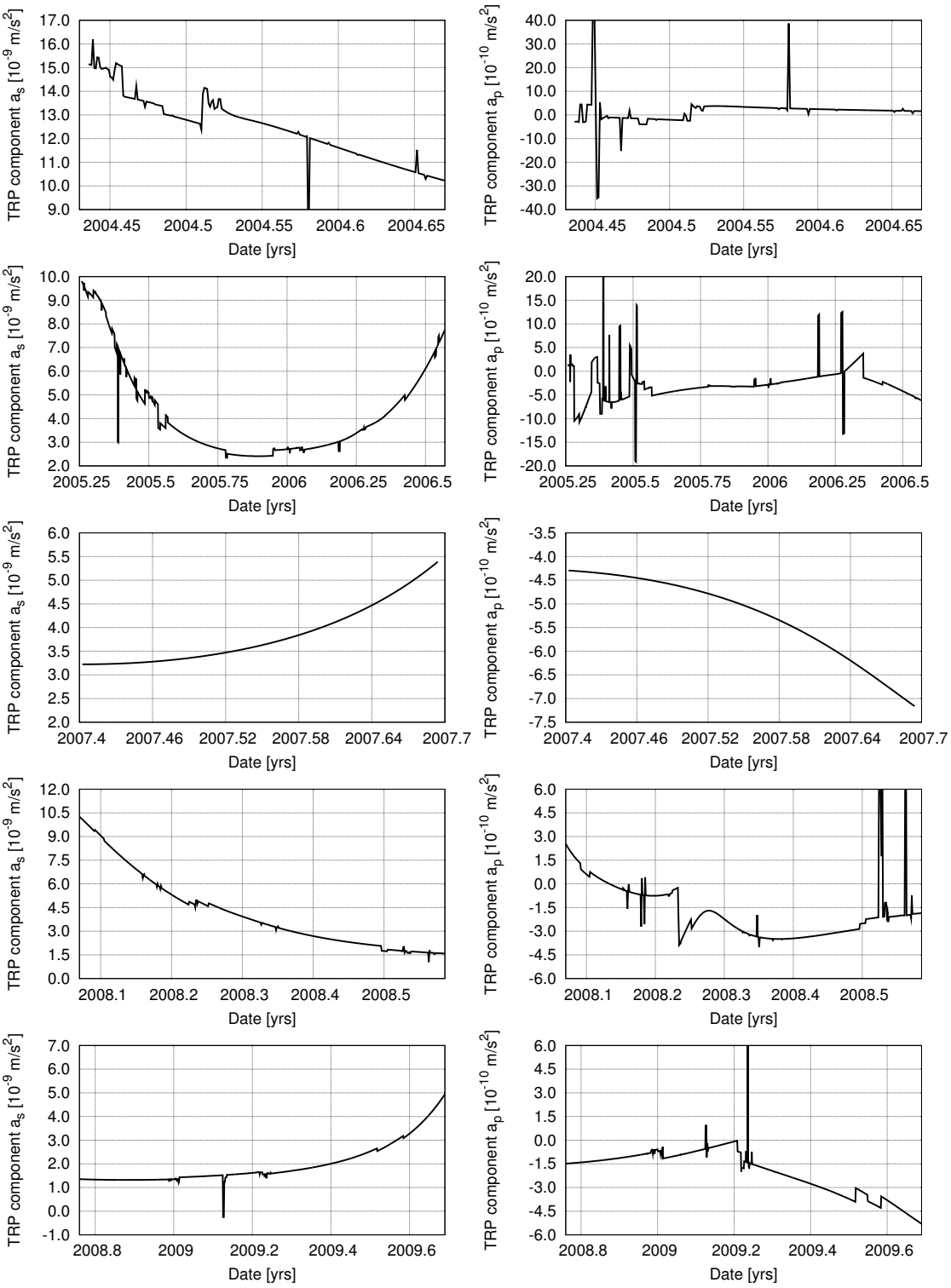

Figure 10.7: From top to bottom: Cruise phases 1- 5 computed TRP acting on the Rosetta spacecraft. Left column: TRP component aligned with the Sun direction, right column: TRP component perpendicular to the Sun direction.

The changes in bus elevation are clearly visible in a_s as sudden drops or increases of the SRP magnitude. These SRP changes reflect the change of the bus cross-sectional surface area exposed to the Sun as well, in some specific cases, the casting of a HGA shadow on the bus. The changes of HGA azimuth are clearly visible as spikes in the computed perpendicular acceleration components while HGA manoeuvres possess only minor influence on the parallel component. Note that some of the HGA spike signals in figure 9.8 may not show up as spikes in the computed acceleration if their duration is considerably shorter than the chosen time resolution of eight hours.

In conclusion one may say, that due to their large surface area the solar panels are the components, which dominate the resulting SRP magnitude as well as its orientation. The changes in the bus attitude appear as spikes and changes in a limited range of about 10 % of the resulting SRP. The HGA contribution to SRP is almost negligible and mostly shows up only in the perpendicular component, when the HGA azimuth angle is different form zero.

The computed TRP is displayed in figure 10.7 for all defined cruise phases. Like the SRP the evolution of the TRP magnitude follows the change of the heliocentric distance which is to be expected as the total solar flux received by the spacecraft surfaces determines the total heat energy to be dissipated and thus the magnitude of TRP acting on the spacecraft. In comparison to the course of the SRP, both TRP components are much more sensitive to changes in bus and HGA orientation. The solution to the understanding of this behaviour is connected to the dependence of TRP on the surface temperatures. While SRP only acts on the surfaces exposed to the Sun, all spacecraft surfaces may contribute to TRP. Therefore the thermal gradients on the spacecraft components in x and z direction are the dominant parameters which determine the magnitude of TRP. While the gradient on the solar panels is comparatively low, the bus and the HGA show a high thermal gradient resulting from the lower conductive properties of the component materials. As thus the bus and HGA are the dominant components for TRP, any change in the orientation will influence the TRP magnitude considerably as the direction of the individual TRP contributions change. As a result of this behaviour, any changes in bus and HGA orientation (as displayed in figure 9.8) cause a change in both parallel and perpendicular TRP components. Note that spike signals do not show up as a change of TRP if the duration of the signal is considerably below 8 hours.

In general the TRP component perpendicular to the Sun vector is about one magnitude smaller than the parallel component. With this the resulting TRP vector is roughly aligned with the Sun vector. The higher magnitude of the perpendicular component (compared to the perpendicular component of SRP) follows from the much higher dependence of the resulting TRP direction on the orientation of the HGA. Effectively if HGA elevation increases, a higher ratio of the total TRP evolves into the perpendicular component. In comparison, the solar panels, which are the dominant component for SRP, do not change elevation which directly results in a much lower perpendicular SRP components as only the HGA, which possesses only a small influence on the total SRP, may contribute significantly to the perpendicular SRP component.

In direct comparison, the computed TRP magnitude stays within the range of about 10 % of the total SRP magnitude in all analysed cruise phases. The results for both SRP and TRP have been compared to analytical ones given in [88]. For SRP the results obtained numerically with the method described in this thesis match the analytical results qualitatively as well as quantitatively. In case of TRP the numerical results also match qualitatively but show additional offsets and jumps in the signal. These differences to the analytical approach are caused by the fact that the HGA is not included in the analytical model. With a closer look on the characteristics of the TRP in both cases one finds that the course of the offset is correlated with the HGA pointing history which indicates that both numerical and analytical model deliver comparable results for bus and solar panels.

10.4 SRP and TRP analysis for Rosetta flyby

In order to determine SRP and TRP acting on the Rosetta spacecraft during its first Earth flyby on fourth of March, 2005, the Rosetta FE model introduced in the last section is modified by specifying the measured trajectory data and spacecraft attitude quaternions during the flyby as boundary conditions for the FE analysis. For this the quaternions are converted into bus pointing data and the HGA is set to electrical zero position for the duration of the flyby. All trajectory and attitude data has been acquired from the ESA TASC website[1] with a time resolution of one minute. This means that the surface temperatures are computed for updated parameter sets with a discrete one-minute time step between the individual simulations. The resulting surface temperature distributions are exported into the ray tracing algorithms to compute the resulting accelerations for each step. Like for the cruise phases analysis a reference mass of 3000 kg is considered.

The trajectory of the first Rosetta Earth flyby and the computed TRP component aligned with the current flight direction is displayed in figure 10.8. The analysed time interval is 6000 minutes long, starting at 2005/03/02, 00:00:00 TDB. This interval corresponds to the time where the spacecraft is inside the gravitational sphere of influence of the Earth. For the incoming branch of the trajectory the computed TRP acts decelerating with a nearly constant magnitude of about $-11 \cdot 10^{-9}\mathrm{m/s^2}$. The resulting direction of the effective TRP is easy to understand because the TRP in general shows only small variations from Sun direction as described for the cruise phase analysis. Just before the closest encounter with the Earth two spikes in the computed TRP are visible. These spikes correlate to changes in the bus attitude data which may indicate an antenna pointing manoeuvre for communication or another pointing test. During the flyby the course of the TRP flight direction component drastically changes due to the quickly changing flight direction.

Looking at the Sun-Earth-spacecraft configuration it can be seen that before the flyby the Sun vector is aligned with flight direction while during the flyby the Sun vector is perpendicular to the flight direction. After the flyby the Sun vector still obtains a steep angle to the flight direction. If one now assumes that the TRP vector is aligned

[1] http://tasc.esa.int, accessed on 08/08/2011

to the Sun vector, it is clear that the net contribution of TRP during the flyby is a deceleration of the craft because the accelerating TRP component after the flyby is negligible to the decelerating effect on the incoming branch. For the analysed time interval this leads to a total deceleration of the craft in the range of $2.510^{-3}\mathrm{m/s}^2$ which rules out TRP as source of the flyby anomaly as the observed anomalous velocity jump was positive. This result is confirmed by analytical models given in [89] and [90], which lead to a comparable evolution and effect of the Rosetta TRP during flyby.

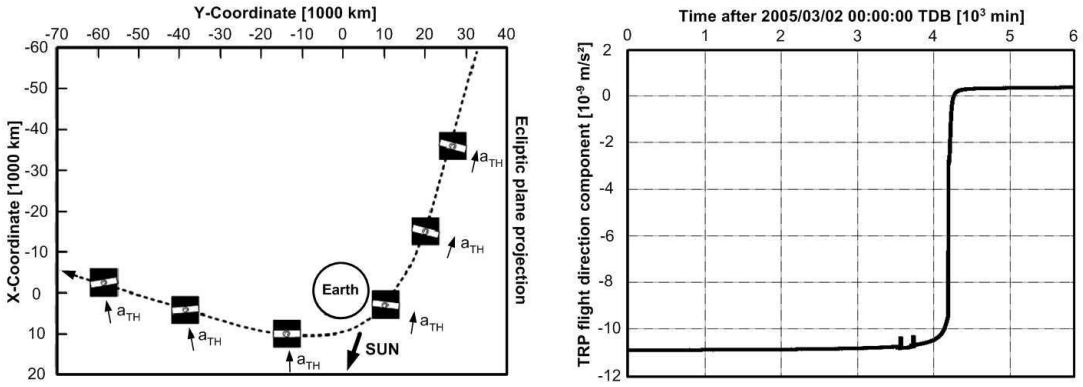

Figure 10.8: Rosetta trajectory for first Earth flyby on fourth of March, 2005 (left) and computed course of the TRP during flyby, aligned with flight direction (right).

For SRP during the first Rosetta flyby the same directional behaviour as shown for the TRP evolution is visible as also for SRP the resulting direction of the acceleration is aligned to the Sun vector. Therefore figure 10.8 also shows the qualitative course of the SRP. In general the magnitude of the SRP aligned to flight direction is about 10 times higher than the corresponding TRP. Thus also the SRP cannot explain the observed anomalous velocity jump. Therefore the origin of the FA remains unknown and has to be analysed further. However, the analysis of TRP and SRP suggests that the magnitude of the resulting velocity jump during flyby is actually higher than the published value, if SRP and TRP are determined precisely.

Part IV

Conclusion

Chapter 11

Summary and outlook

This section summarises the work performed in this thesis and highlights the main scientific results. An outlook on suitable expansions of this work and possible applications is given.

11.1 Summary

This thesis treats the development and utilisation of high precision numerical models for the evaluation of TRP and SRP acting on spacecraft with complex geometrical shape. The work was motivated by the general need for an improved perturbation analysis and the existence of yet unresolved anomalous behaviour of spacecraft which have become known as the Pioneer anomaly and the flyby anomaly. As application for our developed perturbation analysis methods, the deep space probes Pioneer 10 and Rosetta have been chosen as evaluation cases. The work which has been performed in this respect aims at a precise computation of TRP (for Pioneer and Rosetta) and SRP (only for Rosetta) as well as an evaluation of the obtained results with respect to the observed anomalies.

An introduction to the basics of TRP modelling has been given and an analytical model for TRP has been expanded to a numerical approach for the calculation of TRP on complex bodies. The elaborated method consists of two subsequent modelling steps. First a complete thermal FE analysis has to be performed in order to calculate the temperature distribution along the spacecraft surface. For this detailed material models and the complex geometrical shape of the spacecraft have to be specified as a detailed FE model of the craft. Housekeeping and trajectory data can be added as boundary conditions to enable the determination of the steady state surface temperatures. In a second computation step the obtained temperature distribution as well as a geometrical surface model are processed with a newly developed ray tracing method which computes the resulting TRP based on radiation exchange, reflection and shadowing.

After a short description of the Pioneer 10 spacecraft and its main mission characteristics, the numerical TRP analysis method has been used for the determination of the magnitude of the TRP acting on the spacecraft during its 30 years mission. For this a detailed FE model of the craft has been developed which allows for the simulation of exterior as well as interior temperatures for the complete Pioneer 10 mission.

Conductive and radiative heat transfer between all model components have been implemented. Here measured temperature sensor data as well as the measured Pioneer 10 trajectory have been taken into account as boundary conditions. Based on the calculated temperatures for each mission time, the resulting TRP has been determined with the ray tracing approach. Here a high precision computation of radiation exchange (by means of numerical integration of radiation view factors) has been implemented. The computed TRP results have been compared to the Pioneer 10 residual accelerations published in [9]. It was found that the course of the TRP matches in characteristics as well as in magnitude nearly perfectly with the residual acceleration. Thus it can be stated that the Pioneer anomaly can fully be explained by an unmodeled TRP. The performance of this solution has been evaluated by means of parameter sensitivity analyses. It has been shown that within realistic parameter sets (which include errors in sensor data, degradation of surface properties etc.) the resulting TRP may vary by a maximum of $\pm$ 11.5 %. This result proofs that a very robust solution to the Pioneer anomaly has been found.

The thermal recoil acting on the spacecraft is caused by two major sources. The major contribution results from RTG radiation reflected at the back of the HGA, a smaller fraction of the TRP can be credited to heat radiation emitted by the louver system and parts of the MLI on the compartment rear surface. Both effects together lead to a recoil acting against flight direction with the magnitude of the PA. An interesting aspect is that for the first time the complete characteristics of the evolution of the residuals could be explained in this thesis. Within the first part of the mission the heliocentric distance is quite small which leads to a high thermal load (resulting from solar illumination) on the HGA. Owing to the fact that the HGA always points towards the Earth, the main direction of emission is directed against flight direction and the resulting TRP leads to an acceleration of the craft. While the distance to the Sun increases, the thermal load on the HGA and its TRP contribution decrease until at a distance of about 5 AU the HGA contribution and the RTG/compartment contributions become competitive and cancel each other. With larger heliocentric distance, the RTG and compartment contribution become dominating and the resulting TRP acts against flight direction, leading to a decelerating the craft. At about 15 AU the contribution of the HGA becomes negligible with respect to the RTG and compartment contribution leading to a maximum of deceleration. From there on the TRP decreases with a slow rate corresponding to the decreasing available electrical and thermal energy in the course of the mission. As the JPL assumes now that the constancy is only credited to the short evaluated time and that the recently finished evaluation of the longer Doppler interval shows a decrease of the residual acceleration over mission time, the computed evolution of the TRP also fits with the update of the observed anomaly [74].

Based on the principles of TRP determination a corresponding modelling method for SRP has been developed. A short review of the Rosetta mission profile and the main geometrical aspects has been given. TRP and SRP have been evaluated for the heliocentric cruise phases by means of a detailed Rosetta FE model. It has been found that the TRP reaches about 10 % of the SRP magnitude within the analysed mission periods. The coincidence of this result with the discrepancies of the modelled and

measured accelerations acting on Rosetta as observed by ESA/ESOC suggests that unmodeled TRP is responsible for the experienced offsets. This assumption is supported by the fact that the TRP is not treated in current ESA/ESOC orbit determination codes and that an independent evaluation of this effect by means of analytical methods came to a comparable conclusion [62, 88]. In addition, SRP and TRP have been evaluated for the first Rosetta Earth flyby on March 4, 2005. The results have ruled out both effects as sources of the flyby anomaly since the observed anomalous velocity jump manifests itself as an acceleration of the spacecraft while both TRP and SRP are effectively decelerating the craft during the flyby manoeuvre.

11.2 Main scientific results

The work that has been performed in this thesis has lead to the precise evaluation of an unmodeled thermal recoil acting on the Pioneer 10 spacecraft which is caused by anisotropic heat radiation. The elaborated model explains the observed anomalous behaviour of the spacecraft in both magnitude and characteristics with a very high consistency. Furthermore the computed slow decrease of the TRP with mission time is in good agreement with the recent evaluation of the longer Doppler data set for Pioneer 10 which states that such a decreasing effect is visible in the residuals [74]. Recently, an independent analysis with a simpler model approach has confirmed this result for the later stage of the Pioneer 10 mission [91]. This clearly suggests that the origin of the Pioneer anomaly can be found in the anisotropic heat radiation pattern and that the controversial debate on a solution of the PA can now be finally closed.

Furthermore, it has been found that the flyby anomaly is neither caused by SRP nor TRP. Nevertheless, the results computed in this work will contribute to future flyby anomaly investigations as these two effects can now be excluded from the list of possible sources. The analysis of SRP and TRP during the heliocentric cruise phases of Rosetta has shown that inconsistencies of simulated and measured Rosetta trajectory, as detected by ESOC, can be credited to unmodeled TRP.

The numerical models and methods developed in this thesis are of generic character and can be applied to all spacecraft missions which depend on accurate modelling of disturbances influences on the spacecraft motion or attitude as, e.g. LISA. Therefore the orbit determination for existing spacecraft missions as well as the design of new spacecraft will benefit from the results of this work.

11.3 Outlook

The developed models for the high precision determination of TRP and SRP can be used for any spacecraft geometry. In particular the currently planned fundamental physics missions LISA, LISA pathfinder and MICROSCOPE require a precise knowledge of external disturbances and can benefit considerably from the methods developed in this thesis. In addition to this, all missions which operate close to the Sun (e.g. solar orbiter, MEX and VEX) are subject to a high SRP and need improved modelling techniques to compute the disturbances imposed by attitude changes or changing orbits.

In the same scope, the techniques may be used for the evaluation and the development of solar sail missions which effectively use SRP to navigate the spacecraft. With the developed models it is possible to compute the forces and torques resulting from SRP with a very high precision. Based on this, attitude control concepts can be evaluated and the general design of solar sail missions can be optimised.

Due to the generic character of the numerical methods developed in this thesis, the main principles of the approach can be adapted to other disturbance effects which interact with the spacecraft surface. This has been demonstrated by expanding the numerical approach for TRP modelling to a technique for the evaluation of SRP. The most suitable effects for such an expanded model would be atmospheric drag, space debris and micro meteoroid impacts as well as albedo pressure. As all these effects interact with the spacecraft surface, the ray tracing approach developed in this thesis can directly be applied. For albedo pressure, even the same force and radiation models may be used, since the source of the resulting pressure is heat radiation (which is also the case for SRP and TRP). For atmospheric drag and space debris impact new force models would be needed as the disturbances result from interaction with matter instead of radiation. For the definition of the satellite geometry the same input model can be used for all disturbance models. With this it would be possible to compile a universal numerical tool for the computation of all external perturbations acting on spacecraft surfaces. Since FE modelling is already part of modern spacecraft development procedures, the FE tools developed in this thesis would contribute well to an optimisation of the spacecraft design process.

The applications of the methods for numerical perturbation analysis are not restricted to spacecraft, but may also be used for the analysis of single experimental components. One example for this are high precision accelerometers, where the dynamics of the test masses may be influenced by radiation effects. High precision thermal modelling in general can also be applied to a wide range of topics. Here the design and evaluation of optical cavities is of particular interest. Due to recent improvements in the determination of the length-stability of optical resonators [92] (which significantly influence the achievable measurement accuracy), new improved modelling methods, which allow for a comparable modelling accuracy in the range of 10^{-20} will have to be developed. The development of high precision algorithms capable of achieving this goal will include the detailed FE modelling, the precise determination of radiation view factors as well as an accurate implementation of the coupling of thermo-mechanical effects. Therefore the models and methods invented in this thesis can contribute significantly to the future development of high precision hardware design and verification.

11.4 Zusammenfassung in Deutscher Sprache

Diese Doktorarbeit behandelt die Entwicklung und Verwendung von hochpräzisen numerischen Modellen zur Bestimmung von TRP und SRP auf Satelliten mit komplexen geometrischen Formen. Die Arbeiten sind durch die generelle Notwendigkeit von verbesserter Störanalyse sowie durch durch das Auftreten von bislang ungeklärtem Störugen der Trajektorien einzelner Satelliten, die als Pioneer und Flyby Anomalien bekannt geworden sind, motiviert. Zur Anwendung der entwickelten Analysemethoden wurden die Raum-

fahrzeuge Pioneer 10 und Rosetta als Testfälle ausgewählt. Die Arbeiten in dieser Hinsicht zielen auf eine präzise Berechnung von TRP (für Pioneer und Rosetta) und SRP (nur für Rosetta), sowie eine Bewertung der Ergebnisse hinsichtlich der beobachteten Anomalien.

Die Grundlagen der TRP Modellierung wurden eingeführt und das analytische Modell für TRP wurde in ein numerisches Verfahren für die Berechnung von TRP auf komplexen Geometrien weiterentwickelt. Die ausgearbeitetet Methode besteht aus zwei aufeinander folgenden Modellierungsschritten. Zunächst wird eine vollständige thermale FE analyse durchgeführt, um die Temperaturverteilung entlang der Oberfläche des Satelliten zu ermitteln. Hierfür werden detaillierte Materialmodelle sowie die Geometrie des Satelliten als detailliertes FE Modell umgesetzt. Sensordaten sowie die Trajektorie können als Randbedingungen spezifiziert werden, was die Ermittlung der Gleichgewichtstemperaturen für jeden Zeitpunkt der Mission ermöglicht. In einem zweiten Modellierungsschritt werden dann die Temperaturlösungen sowie ein mathematisches Modell der Satellitenoberfläche mittels Raytracing prozessiert, was die Berechnung des resultierenden TRP unter Berücksichtigung von Strahlungsaustausch zwishcen den verschiedenen Modelloberflächen, Abschattung und Mehrfachreflexion ermöglicht.

Nach einer kurzen Beschreibung des Pioneer 10 Satelliten und der wichtigsten Missionsziele, wurde die numerische Methode zur Analyse des TRPs verwendet, um die Größenordung des aus der asymmetrichen Wärmeabstrahlung resultierenden TRPs für Pioneer 10 während der 30-jährigen Mission zu bestimmen. Hierfür wurde ein detailliertes FE model des Satelliten erstellt, mit dem die inneren und äußeren Temperaturen für die komplette Mission bestimmt werden können. Der Wärmetransport über Wärmeleitung und -strahlung wurde zwischen allen Komponenten des Modells implementiert. Hierbei wurden sowohl die verfügbaren Temperatursensordaten, als auch die gemessene Trajektorie als Randbedingungen in das Modell aufgeprägt. Basierend auf den so berechneten Temperaturen, wurde der TRP für die gesamte Mission mit Hilfe der entwickelten Raytracing Methode berechnet. Hierbei wurde der Austausch von Wärmestrahlung über die numerische Integration der geometrischen Sichtfaktoren hochgenau implementiert. Die berechneten TRP Ergebnisse wurden mit den für Pioneer 10 ermittelten residualen Beschleunigungen [9] verglichen. Hierbei wurde festgestellt, dass der Verlauf des berechneten TRPs sowohl qualitativ als auch quantitativ nahezu perfekt mit der beobachteten anomalen Beschleunigung übereinstimmt. Demnach lässt sich sagen, dass die so genannte Pioneer Anomalie mit einem nicht modellierten TRP vollständig erklärt werden kann. Die Güte dieser Lösung wurde mittels Parameteranalyse überprüft. Hierbei konnte gezeigt werden, dass der resultierende TRP innerhalb von realistischen Parameterkonfigurationen (welche mögliche Fehler in den Sensordaten, Variationen in den optischen Eigenschaften etc. beinhalten) um maximal 11.5 % variiert. Diese Ergebnis zeigt, dass somit eine sehr robuste Erklärung für die Ursache Pioneer Anomalie gefunden wurde.

Der thermale Rückstoss, der auf den Satelliten wirkt, wird hierbei von zwei dominierenden Effekten erzeugt. Der größere Beitrag resultiert aus von den Kernbatterien abgegebener Zerfallswärmestrahlung, die an der Rückseite der Hochgewinnantenne (HGA) reflektiert in Flugrichtung wird. Ein weiterer, kleinerer Teil des Gesamtef-

fekts resultiert aus Wärmestrahlung, die über das passive Louversystem sowie Teile der rückwärtigen Mehrschichtisolationsfolie abgegeben wird. In Kombination ergeben beide Effekte einen Rückstoßeffekt in der Größenordnung der Pioneer Anomalie, welcher aufgrund der geometrischen Anordnung der Komponenten entgegen der Flugrichtung wirkt. Hierbei konnte in der vorliegenden Arbeit zum ersten Mal der komplette charakteristische Verlauf der beobachteten Residuen als Störeffekt rekonstruiert werden. Im frühen Teil der Mission ist der Abstand des Satelliten zur Sonne klein, was zu einer hohen Wärmelast auf der Vorderseite der HGA führt. Da die Antenne zu jedem Zeitpunkt auf die Erde ausgerichtet ist, wird die Wärme zur Erde hin emittiert, was zunächst zu einem TRP führt, der den Satelliten beschleunigt. Während der Abstand zur Sonne mit zunehmender Missionsdauer immer größer wird, fällt die Wärmelast auf der HGA ab, bis sich die Beiträge von HGA, RTG und Compartment bei ca. 5 AU ausgleichen. Für höhere Entfernungen von der Sonne werden RTG und Compartment Beitrag dominant und es ergibt sich ein TRP, der entgegen der Flugrichtung wirkt und somit zu einer Abbremsung des Satelliten führt. Ab ca. 15 AU ist der Beitrag der HGA schließlich vernachlässigbar klein, wodurch sich ein Abbremsungsmaximum einstellt. Von hier an nimmt der TRP mit einer schwachen Rate stetig ab, was der abnehmenden zur Verfügung stehenden elektrischen und thermischen Energien während der Mission entspricht. Da das JPL mittlerweile davon ausgeht, dass die Konstanz der beobachteten Pioneer Anomalie auf die kürze des ausgewerteten Misisionsintervals zurückzuführen ist, und die kürzlich abgeschlossene Auswertung eines längeren Dopplerdaten Sets eine Abnahme der beobachteten Beschleunigung zeigt, stimmt der berechnete Verlauf auch qualitativ mit den neusten Auswertungen der Beobachtungen überein [74].

Basierend auf den Prinzipien der TRP Bestimmung wurde desweiteren eine Modellierungsmethode zur Auswertung von SRP enwickelt. Ein kurzer Überblick über die Rosetta Mission sowie die Geometrie des Satellien wurde gegeben. TRP and SRP wurden für ausgewählte Freiflugphasen mit Hilfe eines detaiilierten FE Modells des Satelliten untersucht. Hierbei konnte ermittelt werden, dass der TRP während der untersuchten Missionsabschnitte in etwa 10 % der Größenordung des SRPs erreicht. Die Übereinstimmung dieses Ergebnisses mit den von ESA/ESOC beobachteten Abweichungen von modellierter und gemessener Beschleunigung legt nahe, dass ein nicht modellierter TRP die Ursache dieser Diskrepanzen ist. Dies wird zum einen dadurch untertützt, dass TRP Modeliierungen nicht Teil gegenwärtiger ESA/ESOC Programmme zur Orbitbestimmung sind und zum anderen dadurch, dass eine unabhängige Untersuchung basierend auf analytischen Methoden zu einem ähnlichen Ergebnis gekommen ist [62, 88]. Neben der Berechnung für die Freiflugphasen wurden SRP und TRP für den ersten Rosetta Erd-Flyby am 4. März 2005 untersucht. Hierbei konnten beide Effekte als mögliche Ursachen für die beobachtete Flyby Anomalie ausgeschlossen werden, da sowohl TRP als auch SRP dem beobachteten Geschwindigkeitszuwachs entgegen wirken.

Bibliography

[1] K. Danzmann. LISA – An ESA cornerstone mission for the detection and observation of gravitational waves. *Adv. Space Res.*, 32:1233–1242, 2003.

[2] G. D. Racca and P. W. McNamara. The LISA pathfinder mission - Tracing Einstein's Geodesics in Space. *Space Sci. Rev.*, 151:159–181, 2010.

[3] B. Touboul. The Microscope Mission and Its Uncertainty Analysis. *Space Sci. Rev.*, 148:455–474, 2009.

[4] D. M. Lucchesi and V. Iafolla. The Non-Gravitational Perturbations impact on the Bepi Colombo Radio Science Experiment and the key role of the ISA accelerometer: direct solar radiation and albedo effects. *Celestial Mech. Dyn. Astr.*, 96:99–127, 2006.

[5] B. L. Schumaker. Disturbance reduction requirements for LISA. *Class. Quantum Grav.*, 20:239, 2003.

[6] H. Peabody and S. Merkowitz. LISA Thermal Design. *Class. Quantum Grav.*, 22:403, 2005.

[7] S. Merkowitz, S. Conkey, W. B. Haile, W. R. Kelly III, H. Peabody, and Dumont P. J. Structural, thermal, optical and gravitational modelling for LISA. *Class. Quantum Grav.*, 21:603–610, 2004.

[8] D. Lucchesi. Reassessment of the error modelling of non-gravitational perturbations on LAGEOS ii and their impact in the lense-thirring determination. *Planetary and Space Science*, 49:447–463, 2001.

[9] J. D. Anderson, P. A. Laing, E. L. Lau, A. S. Liu, M. M. Nieto, and S. G. Turyshev. Indication, from Pioneer 10/11, Galileo, and Ulysses Data, of an Apparent Anomalous, Weak, Long–Range Acceleration. *Phys. Rev. Lett.*, 81:2858–2861, 1998.

[10] E. Hackmann and C. Lämmerzahl. Geodesic equation in Schwarzschild-(anti-)de Sitter space-times: Analytical solutions and applications. *Phys. Rev.*, D 78:024035, 2008.

[11] M. Carrera and D. Giulini. On Doppler tracking in cosmological spacetimes. *Class. Quantum Grav.*, 23:7483, 2006.

[12] M. Milgrom. The MOND paradigm, 2008. arXiv, astro-ph: 0801.3133.

[13] C. Lämmerzahl, O. Preuss, and H. Dittus. Is the Physics Within the Solar System Really Understood? In Hansjorg Dittus, Claus Lämmerzahl, and Slava G. Turyshev, editors, *Lasers, Clocks and Drag-Free Control*, volume 349 of *Astrophysics and Space Science Library*, pages 75–101. Springer Berlin Heidelberg, 2008.

[14] J. W. Moffat and V. T. Toth. Modified Gravity: Cosmology without dark matter or Einstein's cosmological constant, 2007. arXiv, astro-ph: 0710.0364.

[15] J. R. Brownstein and J. W. Moffat. Gravitational solution to the Pioneer 10/11 anomaly. *Class. Quant. Grav.*, 23:3427–3436, 2006.

[16] S. G. Turyshev and V. T. Toth. The Pioneer anomaly. *Living Reviews in Relativity*, 13, 2010. http://www.livingreviews.org/lrr-2010-4.pdf, accessed on 08/08/2011.

[17] M. E. McCulloch. Modelling the Pioneer anomaly as modified inertia. *Mon. Not. Roy. Astron. Soc.*, 376:338–342, 2007.

[18] J. D. Anderson, P. A. Laing, E. L. Lau, A. S. Liu, M. M. Nieto, and S. G. Turyshev. Study of the anomalous acceleration of Pioneer 10 and 11. *Phys.Rev. D*, 65:082004, 2002.

[19] O. Bertolami and P. Vieira. Pioneer anomaly and the Kuiper Belt mass distribution. *Class. Quant. Grav.*, 23:4625–4635, 2006.

[20] L. K. Scheffer. A Conventional Physics Explanation for the Anomalous Acceleration of Pioneer 10/11, 2001. arXiv, gr-qc: 0108054v1.

[21] C. Berner, L. Bourillet, J. van Casteren, J. Ellwood, M. Kasper, P. Kletzkine, R. Schulz, G. Schwehm, M. Warhaut, and P. Bond. Rosetta: ESA's Comet Chaser. Technical report, ESA Bulletin 112, 2002. http://www.esa.int/esapub/bulletin/bullet112/chapter1_bul112.pdf, accessed on 08/08/2011.

[22] J. D. Anderson, J. K. Campbell, J. E. Ekelund, J. Ellis, and J. F. Jordan. Anomalous Orbital-Energy Changes Observed during Spacecraft Flybys of Earth. *Phys. Rev. Lett.*, 100:091102, 2008.

[23] M. B. Gerrard and T. J. Sumner. Earth Flyby and Pioneer Anomalies, 2008. arXiv, gr-qc: 0807.315.

[24] D. P. Rubincam. Asteroid orbit evolution due to thermal drag. *Journal of Geophysical Research*, 100(E1):1585–1594, 1995.

[25] D. P. Rubincam. Radiative spin-up and spin-down of small asteroids. *Icarus*, 148:2–11, 2000.

[26] S. C. Lowry. Direct detection of the asteroidal yorp effect. *Science*, 316:272–274, 2007.

[27] D. P. Rubincam. LAGEOS Orbit Decay Due to Infrared Radiation from Earth. *Journal of Geophysical research*, 92:1287–1294, 1987.

[28] D. P. Rubincam. Yarkovsky thermal drag on LAGEOS. *Journal of Geophysical Research*, 93:13805–13810, 1988.

[29] V. J. Slabinski. LAGEOS Acceleration Due to Intermittent Solar Heating During Eclipse Periods. *Bulletin of the American Astronomical Society*, 20:902, 1988.

[30] R. A. Cook. The Effects of Thermal Imbalance Forces on Simple Spacecraft. *University of Texas, Centre for Space Research, Austin*, Technical Memorandum 89-02, 1989.

[31] P. Farinella, A. M. Nobili, F. Barlier, and F. Mignard. Effects of thermal thrust on the node and inclination of LAGEOS. *Astron. Astrophys.*, 234:546–554, 1989.

[32] F. Mignard, G. Afonso, F. Barlier, M. Carpino, P. Farinella, A. Milani, and A. M. Nobili. LAGEOS: Ten years of quest for the non-gravitational forces. *Adv. Space Res.*, 10:221–227, 1990.

[33] H. Klinkrad, Ch. Koeck, and P. Renard. Key Features of a Satellite Skin Force Modelling Technique by Means of Monte-Carlo Ray Tracing. *Adv. Space Res.*, 11:147–150, 1991.

[34] H. F. Fliegel, T. E. Gallini, and E. R. Swift. Global Positioning System Radiation Force Model for Geodetic Applications. *Journal of Geophysical Research*, 97, No. B1:559–568, 1992.

[35] Y. Vigue, B. E. Schutz, and P. A. Abusali. Thermal Force Modelling for Global Positioning System Satellites Using the Finite Element Method. *Journal of Spacecraft and Rockets*, 31, No.5:855–859, 1994.

[36] Y. Vigue, M. Lichten, R. Muellerschoen, G. Blewitt, and M. B. Heflin. Improved GPS Solar Radiation Pressure Modelling for Precise Orbit Determination. *Journal of Spacecraft and Rockets*, 31, No.5:830–833, 1994.

[37] A. Sengoku, M. K. Cheng, and B. E. Schutz. Anisotropic reflection effect on satellite, Ajisai. *Journal of Geodesy*, 70:140–145, 1995.

[38] G. Metris and D. Voukrouhlicky. Thermal force perturbations of the LAGEOS Orbit: The albedo radiation part. *Planet. Space Sci.*, 44, No. 6:611–617, 1996.

[39] J. Duha, B. A. Germano, and D. D. F. Luiz. Thermal re-emission effects on the LAGEOS I satellite versus spin axis orientation. *Brazilian Journal of Geophysics*, 19 (2):185–198, 2001.

[40] M. Ziebart and P. Dare. Analytical Solar Radiation Pressure Modelling for GLONASS Using a Pixel Array. *Journal of Geodesy*, 75:587–599, 2001.

[41] M. Ziebart. Generalized Analytical Solar Radiation Pressure Modeling Algorithm for Spacecraft of Complex Shape. *Journal of Spacecraft and Rockets*, 41, No. 5:840–848, 2004.

[42] S. Adhia, M. Ziebart, A. Sibthorpe, P. Arrowsmith, and P. Cross. Thermal Re-Radiation Modeling for the Precise Prediction and Determination of Spacecraft Orbits. *Navigation*, 52, No. 3:131–144, 2005.

[43] M. Ziebart, S. Adhya, A. Sibthorpe, S. Edwards, and P. Cross. Combined radiation pressure and thermal modelling of complex satellites: Algorithms and on-orbit tests. *Adv. Space Res.*, 36:24–430, 2005.

[44] J. McMahon. *An analytical theory for the Perturbative Effect of Solar Radiation Pressure on Natural and and Artificial Satellites*. PhD thesis, Department of Aerospace Engineering Sciences, University of Colorado, 2011.

[45] C. Markwardt. Independent Confirmation of the Pioneer 10 Anomalous Acceleration, 2002.

[46] O. Olsen. The constancy of the Pioneer anomalous acceleration. *Astronomy and Astrophysics*, 463:393–397, 2007.

[47] A. Levy, B. Christophe, P. Berio, G. Metris, J-M. Courty, and S. Reynaud. Pioneer 10 Doppler data analysis: disentangling periodic and secular anomalies. *Adv. Space Res.*, 43:1538–1544, 2009.

[48] V. T. Toth. Independent analysis of the orbits of Pioneer 10 and 11. *Int. . MOd. Phys. D.*, 5:717–741, 2009.

[49] E. M. Murphy. A prosaic explanation for the Anomalous Accelerations seen in distant spacecraft. *Phys. Rev. Lett.*, 83:1890, 1999.

[50] J. Katz. Comment on : A prosaic explanation for the Anomalous Accelerations seen in distant spacecraft. *Phys. Rev. Lett.*, 83:1890, 1999.

[51] L. K. Scheffer. Conventional Forces can explain the anomalous acceleration of Pioneer 10. *Phys.Rev. D*, 67:084021, 2003.

[52] S. G. Turyshev, N. N. Nieto, and J. D. Anderson. Study of the Pioneer anomaly: A problem set. *American Journal of Physics*, 73, Issue 11:1033–1044, 2005.

[53] B. Rievers, C. Lämmerzahl, S. Bremer, M. List, and H. Dittus. New powerful thermal modelling for high-precision gravity missions with application to Pioneer 10/11. *New Journal of Physics*, 11:113032, 2009.

[54] B. Rievers, S. Bremer, M. List, C. Lämmerzahl, and H. Dittus. Thermal dissipation force modeling with preliminary results for Pioneer 10/11. *Acta Astronautica*, 66, No. 3-4:467–476, 2010.

[55] B. Rievers and C. Lämmerzahl. High precision thermal modeling of complex systems with application to the flyby and Pioneer anomaly. *Ann. Phys.*, 523:439–449, 2011.

[56] O. Bertolami, F. Francisco, P. J. S. Gil, and J. Páramos. Thermal analysis of the Pioneer anomaly: A method to estimate radiative momentum transfer. *Phys. Rev. D*, 78:103001, 2008.

[57] S. G. Turyshev and V. T. Toth. The Pioneer anomaly in the Light of New Data. *Space Science Reviews*, 148:149–167, 2009.

[58] V. T. Toth and S. G. Turyshev. Thermal recoil force, telemetry, and the Pioneer anomaly. *Phys. Rev. D*, 79:043011, 2009.

[59] P. G. Antreasian and J. R. Guinn. *Investigations into the unexpected Delta–v increase during the Earth Gravity Assist of GALILEO and NEAR.* American Institute of Aeronautics and Astronautics, astrodynamics specialist conf. and exhibition edition, 1998.

[60] P. R. Weissman and E. D. Rosenberg. Thermal Modeling of Rosetta Flyby Asteroid 21 Lutetia. *American Geophysical Union, Fall Meeting 2010*, 2010.

[61] J. C. Van der Ha and D. Stramaccioni. Thermal Radiation Effects on Deep-Space Trajectories. In *AAS/AIAA 10-226 Spaceflight Mechanics Meeting*, 2010.

[62] J. C. Van der Ha. Development of a Model for Thermal Radiation Forces with Applications to Interplanetary Spacecraft, Final Report, 2010. ESA/ESOC ITT/RFP Reference: RFP 14-FD.

[63] C. Misner, W. H. Freeman, and J. A. Wheeler. *Gravitation.* W. H. Freeman and Company, New York, USA, 1973.

[64] S. Kabelac. *Thermodynamik der Strahlung.* Verlag Vieweg, Braunschweig/ Wiesbaden, 1993.

[65] J. R. Wertz. *Spacecraft Attitude Determination and Control.* Kluwer Academic Publishers, The Netherlands, 1978.

[66] H. Coxeter. *Introduction to Geometry.* John Wiley and Sons, Inc., USA, 1961.

[67] F. Hell. *Grundlagen der Waermeuebertragung.* VDI-Verlag, Düsseldorf, 1982.

[68] W. Dahmen and A. Resuken. *Numerik für Ingenieure und Naturwissenschaftler.* Springer, Berlin, 2008.

[69] K. Meyberg and P. Vachenhauer. *Höhere Mathematik I.* Springer, Berlin, 1999.

[70] Ansys Inc. *ANSYS Theory Manual*, Ansys Release 11.0 edition, 2007. http://www.kxcad.net/ansys/ANSYS/ansyshelp/theory_toc.html, accessed on 08/08/2011.

[71] Ansys Inc. *ANSYS Thermal Analysis Guide*, Ansys Release 11.0 edition. http://www1.ansys.com/customer/content/documentation/121/ans_the.pdf, accessed on 08/08/2011.

[72] C. P. Ferreira. A heuristic solution for the Pioneer anomaly employing an ELA metric with dark matter in the outskirts of the Solar system, 2011. arXiv, gr-qc: 1102.2061.

[73] F. I. Cooperstock, V. Faraoni, and D. N. Vollick. The Influence of the Cosmological Expansion on Local Systems. *Astrophys. J.*, 503:61, 1998.

[74] S. G. Turyshev, V. T. Toth, J. Ellis, and C. B. Markwardt. Support for temporally varying behavior of the Pioneer anomaly from the extended Pioneer 10 and 11 Doppler data sets, 2011. arXiv, gr-qc: 1107.2886.

[75] S. G. Turyshev and V. T. Toth. Physics Engineering in the Study of the Pioneer anomaly, 2007. arXiv, physics.space-ph: 0710.0191.

[76] C. F. Hall. *Pioneer F/G Project: Spacecraft Operational Characteristics*. NASA/ARC Moffet Field, California, 1970.

[77] V. T. Toth and S. G. Turyshev. The Pioneer anomaly: seeking an explanation in newly recovered data. *Can. J. Phys.*, 84:1063–1087, 2006.

[78] M. Verdant and G.H. Schwehm. The international Rosetta Mission. *ESA bulletin*, 93, 1998.

[79] K. Glassmeier, H. Boehnhardt, D. Koschny, E. Kurht, and I. Richter. The Rosetta Mission: Flying towards the origin of the Solar System. *Space Science Reviews*, 128:1–21, 2007.

[80] M. Hechler. Rosetta Mission Design. *Adv. Space Res.*, 19, No. 1:127–136, 1997.

[81] C. Edwards, J. Anderson, P. Beyer, S. Bhaskaran, J. Border, S. DiNardo, W. Folkner, R. Haw, S. Nandi, F. Nicholson, T. Ottenhoff, and S. Stevens. Tracking Galileo at Earth-2 Perigee using the Tracking and Delay Relay Satellite System. *Adv. Astron. Sci.*, 85:1609, 1994.

[82] T. Morley and F. Budnik. Rosetta Navigation at its First Earth-Swingby. In *paper ISTS 2006-d-52, 19th Int. Smyp. on Space Flight Dynamics*, 2006.

[83] M. D. Guman, D. C. Ionasescu, R. Goodson, A. H. Taylor, and J. B. Jones. Cassini Orbit Determination from First Venus Flyby to Earth Flyby. *Advances in the Astronautical Sciences*, 105:1053, 2002.

[84] J. D. Anderson and J.G. Williams. Long-range tests of the equivalence principle. *Class. Quantum Grav.*, 18:2447, 2001.

[85] EADS Astrium GmbH. *Rosetta Users manual Vol. 1*, ro-dss-ma-1001 edition, 2003. ftp://ftp.irit.fr/IRIT/CSC/3548.pdf, accessed on 08/08/2011.

[86] D. Stramaccioni, R. Kerner, and S. Tuttle. The New Mission of Rosetta Comet Chaser and In-Orbit First Temperature Results. *SAE*, 2004-01-2356, 2004.

[87] ESA/ESOC. Rosetta Mission Calendar, 2009. RO-ESC-PL-5026, Issue 2.1, online available at ftp://naif.jpl.nasa.gov/pub/naif/pds/data/ros-e_m_a_c-spice-6-v1.0/rossp_1000/DOCUMENT/RO_ESC_PL_5026.pdf, accessed on 08/08/2011.

[88] T. Kato. *Development and Validation of Precise Models for Non-Conservative Forces on Spacecraft*. PhD thesis, Department of Aeronautics and Astronautics, Kyushu Universiy, Japan, 2010.

[89] M. Terauchi, I. Kim, T. Hanada, and J.C. van der Ha. Effect of Thermal Radiation Force for Trajectory during Swing-by. In *Proceedings of the Symposium on Space Technology and Science*, 2008.

[90] M. Terauchi. Radiation Effects on Trajectory during Earth Gravity Assist. Master's thesis, Space System Dynamics Laboratory, Department of Aeronautics and Astronautics, Graduate School of Engineering, Kyushu University, 2008.

[91] F. Francisco, O. Bertolami, P. Gil, and J. Páramos. Modelling the reflective thermal contribution to the acceleration of the pioneer spacecraft, 2011. arXiv, physics.space-ph: 1103.5222v.

[92] Ch. Eisele, Nevsky A. Yu., and S. Schiller. Laboratory Test of the Isotropy of Light Propagation at the 10^{-17} Level. *Phys. Rev. Letters*, 103:090401, 2009.

Part V

Appendix

V.1 Measured payload temperatures

During development of the Pioneer 10 spacecraft different spacecraft states have been simulated using an engineering hardware model. These temperatures, as specified in table V.1 deliver a realistic set of temperatures to be expected during the mission and can be used for first sanity checks of the calculated steady state temperatures for thermal FE analysis.

Component	I	II	III	IV	V
1	10.00	-2.22	8.89	12.78	22.22
2	24.44	13.33	14.44	22.78	38.89
3	15.56	3.89	2.78	11.67	25.00
4	46.67	29.44	15	32.78	52.78
5	25.56	21.67	20.00	21.67	41.11
6	33.89	18.89	21.67	30.56	45
7	11.67	2.78	9.44	13.33	21.67
8	-15.56	-28.89	-2.78	-0.56	9.44
9	7.22	-3.89	10.56	13.33	18.89
10	7.22	-3.89	10.56	13.33	18.89
11	11.67	-15.00	18.33	20.56	28.89
12	10.00	-14.44	14.44	17.22	25.00
13	12.78	-1.11	10.56	14.44	22.22
14	14.44	3.33	10.00	15.56	24.44
15	14.44	2.78	10.00	15.56	24.44
16	14.44	2.78	10.00	15.56	24.44
17	33.89	18.89	21.67	30.56	45
20	5.56	-10	10	18.33	22.22
21	5.56	-10	10	13.33	22.22
23	10.00	-14.44	14.44	17.22	25.00
24	10.00	-14.44	14.44	17.22	25.00
35	5.56	-17.78	14.44	18.89	25.56
36	-3.89	-22.78	8.89	11.11	16.11
37	-7.22	-24.44	6.67	8.33	14.44
38	-5.00	-23.33	8.89	11.67	17.22
39	-6.67	-26.67	3.89	6.11	11.67
40	3.89	-6.11	5.56	8.89	15.56
41	-2.78	-27.78	1.11	3.33	7.78
42	3.33	-14.44	10.56	15	22.22
43	12.78	0.56	10	15	25

Table V.1: Estimated payload temperatures for different satellite states, values in °C. Component IDs as specified by table 4.1.

V.2 Computation of fuel half-time from telemetry

An accurate value for the half-time of the RTG fuel material can be extracted from the available temperature sensor readings. As a best fit in the measured RTG temperature data, the fin root temperature data can be computed by:

$$T^4 = {T_0}^4 \cdot 2^{-(t-t_0)/t_{\text{half}}} \quad , \tag{11.1}$$

following the model proposed by JPL [77]. The reference temperatures T_0, valid for the reference date 01/01/1973, midnight and T_{2002}, valid for $t = 31/12/2002$ are given in table V.2.

RTG No.	1	2	3	4
T_0 [K]	422.59	416.92	422.59	415.96
T_{2002} [K]	398.66	392.87	398.66	392.87

Table V.2: RTG reference temperatures.

Equation 11.1 can be used to compute the half-time t_{half}:

$$t_{\text{half}} = -\frac{t - t_0}{\log_2(\frac{T^4}{{T_0}^4})} \, . \tag{11.2}$$

Using RTG 2 as reference case, the half-time can be determined to $t_{\text{half}} = 87.77$ yrs, which is very close to the value delivered by JPL (87.73 yrs) [77]. The maximum error in this value can be determined by assuming the telemetry quantisation error for both the reference value and the temperature at end of 2002. With this assumption (both values vary by 0.7 K, directly resulting from the 6-bit resolution of the data files) the resulting error can be obtained by equation 11.2 to $\pm$ 5.37 yrs which again is in good agreement with the JPL result (5.45 yrs) [77].

V.3 Computation of illumination angle

Solar illumination acting on any surface can either be specified by the elevation angle θ and the azimuth angle ϕ or the orientation angle κ which denotes the direct angle between the surface normal and the Sun direction. Figure V.1 shows the geometric configuration for a flat surface illuminated with arbritrary orientation.

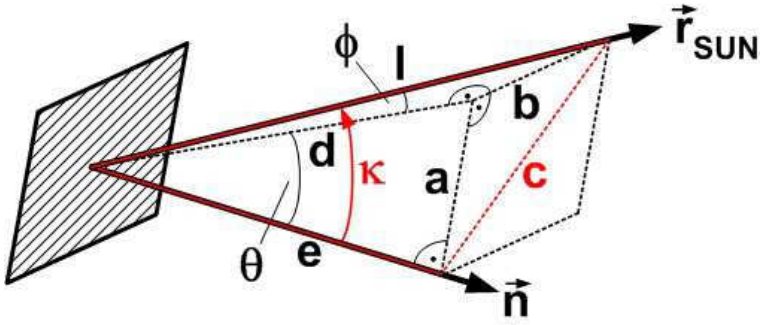

Figure V.1: Geometric configuration for flat plate, illuminated with orientation angle κ.

The connection between the elevation/azimuth angles and the orientation angle can now be derived by simple trigonometry. With the normalized vector $\vec{n}$, the lenghts a and b are given as

$$a = \tan\theta \quad ; \quad b = \tan\phi \cdot d = \frac{\tan\phi}{\cos\theta}\,. \tag{11.3}$$

As the resulting triangle mounted by normal vector and Sun direction is a perpendicular triangle ($c^2 = a^2 + b^2$), the orientation angle κ can be expressed as

$$\kappa = \arctan c = \arctan\sqrt{\frac{\sin^2\theta + \tan^2\phi}{\cos^2\theta}}\,. \tag{11.4}$$

Another geometric relation between the three angles can be found by using the cosine equation

$$c^2 = 1 + l^2 - 2l\cos\phi\,, \tag{11.5}$$

with

$$d^2 = a^2 + 1 \quad ; \quad l^2 = a^2 + b^2 + 1 \quad ; \quad b = \tan\phi\sqrt{\tan^2\theta + 1}\,. \tag{11.6}$$

Thus κ evolves to

$$\kappa = \arccos\left(\sqrt{\frac{1}{\tan^2\theta + \tan^2\phi\sqrt{\tan^2\theta + 1} + 1}}\right)\,. \tag{11.7}$$

Note that the orientation angle can also be computed simply from the scalar product of normal and Sun direction, if both are known. This is the standard case during the numerical application of heat loads in all FE models discussed in this thesis.

V.4 Handling of SRP and TRP algorithm

The codes for SRP and TRP analysis developed in this thesis are available on request by mail (Benny.Rievers@zarm.uni-bremen.de). All functions are available in standard c-code and have been tested for Linux as well as windows. The handling of the code, the compilation procedure as well as the configuration of an analysis will be described in the following for the TRP algorithm. As the SRP algorithm has been developed as a modification of the TRP algorithm the handling is nearly identical. Differences will be highlighted.

Folder structure

The folder structure of the TRP algorithm is displayed in figure V.2. The SRP algorithm structure is nearly identical but lacks the *Datafiles* folder due t a slightly different approach of the treatment of radiation exchange between the model surfaces. The functions and files are ordered in eight sub folders which store different parts of the algorithm. Two classes of folders can be identified:

1. Code and compiling folders.

2. User interface folders.

The code and compiling folders include all functions, the makefiles and the executable binary. After the initial compiling the user should not change the contents of these folders. The user interface folders store all files which have to be provided by the user or can be edited to change simulation options or to compile subsequent TRP/SRP analysis with a loop control method. The contents of the different folders are described shortly in the following.

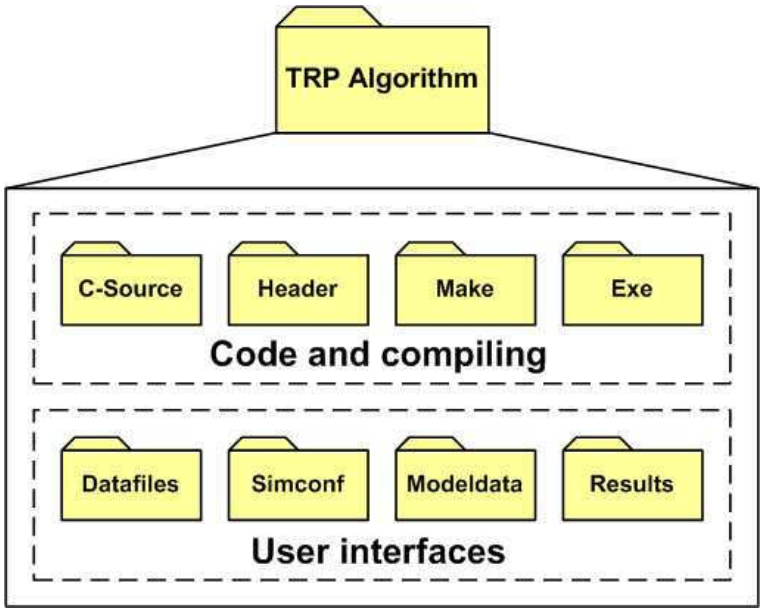

Figure V.2: Folder structure of the TRP algorithm.

C-Source: Includes all c-routines used by the algorithms A detailed description of each routine is given in the next section.

Header: Stores the header files as well as the included packages for the c-routines.

Make: Stores the makefile for compiling and linking of the C-routines and the corresponding header files.

Exe: The executable binary is saved in this folder after the code has been compiled. The algorithm should be started within this directory as all relative paths are defined with respect to the *Exe* level.

Datafiles: Includes the *hit.txt* and the *view.txt* text files. These files are used to provide hit- and view factor information for the TRP calculations to be performed. If those files are provided, the ray tracer will not re-calculate view factor and hit information which considerably speeds up the computation process. Note that the files have to match the specified geometry models. If hit and view factor information are not provided, they will be calculated automatically in the first simulation run and then reused for all later runs. This is only sensible if the geometry of the model does not change for during the different simulation runs. If. e.g a model part is rotated, *hit.txt* and *view.txt* have to be calculated for each simulation run separately. For this the automatic re-use of the files has to be deactivated within the *viewfactors.c* and *check_hit.c* files and a recompiling of the code is necessary.

Sim_conf: Include the simulation configuration files for the definition of subsequent simulation runs (*loop_info.txt*) as well as the ray tracing options chosen for the analysis (*sim_conf.txt*). Furthermore debug output options can be activated with the file *data_opts.txt*.

Modelfiles: Stores all model files (*et.txt*,*nt.txt*, *tmp.txt*,*ct.txt*) for the different simulation runs. The actual names of the text files are specified within the loop_info.txt) file and can be chosen freely by the user.

Results: The computed TRP (with reference mass of 1 kg) is stored in this folder. For a mass different from the reference mass the result has to be scaled correspondingly. All individual simulation results are stored with the names specified in the loop_info.txt) file. A summarising table which includes the TRP computed for all subsequent simulation runs is provided as well.

List of functions

Table V.3 lists the different sub functions included in the TRP algorithm and describes the tasks performed by the respective function shortly. Additional functions defined for the SRP algorithm are listed in table V.4. For each of the described c-functions a corresponding header file is included in the *Header* folder.

Function	Description
alloc_arrays_char.c	Allocates memory for an array with type char.
alloc_arrays_double.c	Allocates memory for an array with type double.
alloc_arrays_int.c	Allocates memory for an array with type int.
check_hit.c	Checks if a ray emitted from an active element hits a receiving element.
check_visibility.c	Computes the element visibility matrix.
close_arrays_char.c	Frees memory for an array with type char.
close_arrays_double.c	Frees memory for an array with type double.
close_arrays_int.c	Frees memory for an array with type int.
condition.c	Computes the condition of an input matrix.
compute_absrefl.c	Initialises and coordinates the computation of absorption and reflection.
compute_emis.c	Computes the total emission force component without losses
compute_emis.c	Calculates the resulting recoil force by the sum of all emission, absorption and reflection components.
compute_time.c	Computes the total simulation duration.
compute_vis_angles.c	Computes the visibility angles between the surfaces of the input model.
create_dm.c	Composes the a global data matrix based on the input data. The information stored in the data matrix is available for all sub functions.
eNormal.c	Computes the normal vector based on element node coordinates.
gauss_4d.c	Computes the Gauss function value for actual mantises and weights.
gen_ray_pattern.c	Initialises the local pattern of emitted ray vectors.
get_angle.c	Computes the angle between two input vectors and the rotation axis to translate the first input vector into the second vector direction.
init_sim.c	Main function, calls initialisation and computation functions.
inside.c	Checks whether the intersection points of emitted rays and receiving elements lies within the surface element boundaries.
inverse.c	Calculates the inverse of an input matrix.
loop_control.c	Reads in text file names for subsequent simulation runs and defines the total number of performed simulations.
normalize.c	Computes the normal vector of an input vector.
output.c	Assembles the output files and sets up the result files.
process_rays.c	Processes selected ray, initialises new reflected rays and computes cumulative absorption and reflection corrections.
quicksort.c	Quick sorting of Array values.
read_in_sim_conf.c	Reads in simulation configuration from text files.
read_modelfiles.c	Reads in text input file data stored in *nt.txt*,*et.txt*,*tmp.txt*,*ct.txt.c*.
raytrace.c	Controls the ray initialisation and the tracing of the reflected rays.
rotate_ray_pattern.c	Rotates ray pattern for elements corresponding to the normal vector.
rotate_vec.c	Rotates a vector by angle ϕ around input rotation axis using quaternions.
sort_by_distance.c	Sorts receiving surface elements by distance from an active element.
startupscreen.c	Provides a user interface and progress information during simulation.
time_output.c	Computes the current system time.
viewfactors.c	Computes the view factors between all elements of the input model.

Table V.3: List of functions included in the TRP algorithm.

Function	Description
check_sun_visibility.c	Checks if the model surface elements are visible to the Sun.
compute_SRP.c	Steers the solar radiation pressure computing process.
read_in_cruisedata.c	Reads in the cruise data file information.

Table V.4: List of additional functions included in the SRP algorithm.

Compiling procedure

The compiling procedure needed to make the code run on different systems may differ from the steps described at this place. The method described here is valid for SUSE Linux 13.1 using the GNU-gcc compiler, version 4.1.2. Adjustments may be necessary to make the code run on other systems.

A makefile which takes over all linking and compiling options for the TRP as well as the SRP algorithm is delivered in the folder *./MAKE*. In order to compile the code and create an executable binary change into the folder *./MAKE* and issue the command *make realclean* to delete any unneeded object files which may have been created in previous compilation attempts. After the database has been cleaned the code can be compiled by the command *make all*. The binary will then be automatically created in the folder *./EXE*. The calculation can be started with *start.trp* and *start.srp* respectively.

Instruction for TRP/SRP evaluation

The performing of SRP and TRP analysis with the numerical methods involves a number of different steps as listed below:

1. Creation of a detailed hexaedral/quadrilateral FE mesh of the respective spacecraft.

2. Conduction of an FE analysis with varying input parameters corresponding to the mission profile (For TRP).

3. Export of surface information (quadrilateral surface mesh, optical surface parameters, steady state temperatures from the FE analysis.

4. Configuration of TRP/SRP analysis and loop control.

The input model for both SRP and TRP analysis consisting of four different data files (element, node, coefficient and temperature data file) has been defined by table 3.1. For TRP evaluation all four data files are required while the temperature table is not required for SRP calculations. A step-by-step instruction for the calculation of TRP and SRP as well as an overview on the internal structure of both algorithms is given in the following.

Creating the input models

In order to create the input models, the geometry of the respective satellite has to be modelled in a FE preprocessor resulting in a GMM of the spacecraft. The basic geometry has to be assembled by means of primitives where details can be added subsequently by Boolean operations (such as cutting, extruding etc.). For the conducting of a thermal FE analysis, thermal conductivity as well as the radiative properties of the outer surfaces have to be specified for each model component. By specifying boundary conditions and solving the systems of equations with an FE solver a temperature map of the spacecraft surface can be determined. The results are exported to generate the input text files for the ray tracer. The format for both SRP and TRP input files is defined by table 3.1. Note that the actual names of the text files may be chosen freely as they are specified in the *loop_info.txt* file. A suitable way to name models for different simulation runs is the attachment of a simulation ID counter to the name of the text file (e.g. resulting into text file names such as *et1.txt*, *et2.txt*,*et3.txt*...). This reduces the effort needed to compose the *loop_info.txt* file considerably.

For each change in boundary conditions (such as a rotation of model parts, different heat loads/sensor data etc.) a new analysis has to be performed. By doing this e.g. the dynamic change of TRP/SRP on a spacecraft trajectory or the dependence of the disturbances on chosen parameters may be resolved. Consequently a new set of input files results for each new boundary set. For all Pioneer 10 and Rosetta simulations performed in this thesis an APDL macro which automatically updates boundary conditions, starts new analysis and exports the results marked with a run ID has been used. An exemplary APDL macro for the export procedure is presented for the Pioneer 10 model in Annex section V.5. Due to the huge size of the code ($>$ 10000 lines) all other APDL macros which have been developed for the thermal modelling of Pioneer 10 and Rosetta are not printed in the annex but can be requested by mail (Benny.Rievers@zarm.uni-bremen.de).

Configuring the analysis

As a first step all input models included in the TRP/SRP analysis have to be put into the *./Modelfiles* folder. The actual names of the text files can be chosen freely as they will be specified later in the loop control configuration. The simulation has to be configured in the *./Sim_conf* folder. Here three text files are available.

1. The file *data_opts.txt* contains output options for debugging purposes and should remain unchanged.

2. The file *sim_conf.txt* contains information about the ray tracing options chosen for the analysis.

3. The file *loop_info.txt* contains information about the subsequent simulation runs.

The structure of *sim_conf.txt* for the TRP algorithm is displayed in table V.5. The numbers have to be separated by simple blanks.

For the utilisation of the SRP algorithm, *sim_conf.txt* is defined differently as in this case the rays which are traced originate from a solar pixel array and not from the

$n_{\mathrm{rays},\phi}$	$n_{\mathrm{rays},\theta}$	n_{refl}

Table V.5: Composition of *sim_conf.txt* for the TRP algorithm with number of rays in ϕ-direction $n_{\mathrm{rays},\phi}$, number of rays in θ-direction $n_{\mathrm{rays},\theta}$ and number of considered reflections n_{refl}.

spacecraft itself. The structure of *./sim_conf.txt* for the SRP algorithm is displayed in table V.6. Note that the actual name for the file *./sim_conf.txt* can be chosen freely

x_{tot}	y_{tot}	n_{x}	n_{y}	$r_{\mathrm{SUN,x}}$	$r_{\mathrm{SUN,y}}$	$r_{\mathrm{SUN,z}}$

Table V.6: Composition of *sim_conf.txt* for the SRP algorithm with total x-size of the array x_{tot}, total y-size of the array y_{tot}, number of rays in x-direction n_{x}, number of rays in y-direction n_{y} and Sun direction ($r_{\mathrm{SUN,x}}$/ $r_{\mathrm{SUN,y}}$/$r_{\mathrm{SUN,z}}$).

as it is specified by the user in the loop control file. Thus it is possible to perform subsequent analysis with changing ray tracing options. For this a new *./sim_conf.txt* file has to be saved with a different name for each change in ray tracing options.

Lastly the configuration of subsequent simulation runs has to be chosen by editing the file *loop_info.txt*. Here the names of the input models, the names of the simulation configuration files as well as the names for the output files in which the simulation results are stored have to be chosen. Table shows an exemplary configuration of *loop_info.txt* with 5 subsequent simulation runs. Additional runs can be defined by adding new lines to the text file.

et1.txt	nt1.txt	tmp1.txt	ct1.txt	sim_conf1.txt	out1.txt	end
et2.txt	nt2.txt	tmp2.txt	ct2.txt	sim_conf2.txt	out2.txt	end
et3.txt	nt3.txt	tmp3.txt	ct3.txt	sim_conf3.txt	out3.txt	end
et4.txt	nt4.txt	tmp4.txt	ct4.txt	sim_conf4.txt	out4.txt	end
et5.txt	nt5.txt	tmp5.txt	ct5.txt	sim_conf5.txt	out5.txt	end

Table V.7: Structure of the file *loop_info.txt* for TRP calculations. The example results in the calculation of 5 subsequent TRP analyses where the input model may vary. TRP results will be saved in the output files *out1.txt* - *out5.txt*. The structure of *loop_info.txt* for SRP calculations is as displayed without the tmp-column.

Performing the analysis

After configuring the analysis and providing the input files TRP and SRP analysis can be started by executing the compiled binary in the *./Exe* folder. If all specified files exist a start up screen as displayed in figure V.3 will appear. The simulation counter is updated for each new analysis. Furthermore a the percental progress of each analysis is displayed for convenience. TRP and SRP results based on a reference mass of 1 kg are saved in the *./Results* folder with the names specified in the *loop_info.txt* file. An overview file which stores the results of all subsequently performed analysis in a list with the respective computation times is automatically generated with the name *loop_results.txt*.

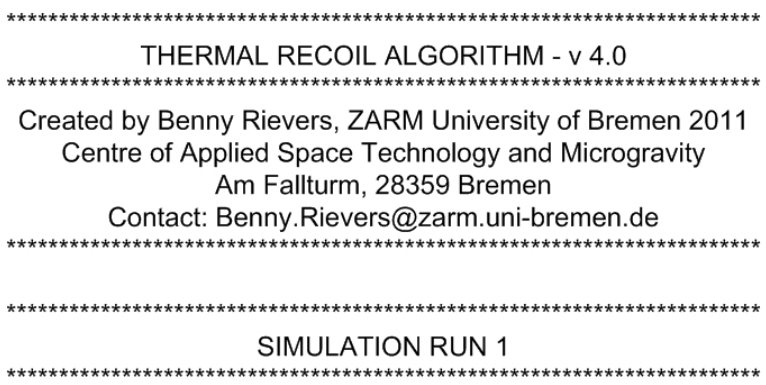

Figure V.3: Start up screen of TRP algorithm.

V.5 Exemplary APDL model export macro

This section presents the APDL macro code for the automatic extraction of the surface model geometry and the thermal analysis results for the Pioneer 10 ANSYS FE model. Note that all FE modeling performed in this thesis has been performed with APDL, the individual macros are available by request (Benny.Rievers@zarm.uni-bremen.de) and not included in the anney due to size limitations. In order to use the export macro for other models the meshing section has to be adjusted to the respective model geometry. For the extraction of subsequnet models the export macro has to be included into a loop where the modelling of each step is performed. The loop variable can be defined as an input parameter which enables the automatic numbering of teh different output models. Note that in this case the text file creation macro definitions (initialised by *CREATE) have to be placed outside the simulation loop.

APDL Code:

```
1:  ! *************************************************************************
2:  ! * MACRO 'EXPORT_MODEL.MAC'
3:  ! *************************************************************************
4:  ! * created by Benny Rievers, ZARM University of Bremen 2010
5:  ! * Center of Applied Space Technology and Microgravity
6:  ! * Am Fallturm, 28359 Bremen
7:  ! * Contact: rievers@zarm.uni-bremen.de
8:  ! *************************************************************************
9:  ! * Exports GMM, Material and nodal temperatures of surface
10: ! *************************************************************************
11: ! * INPUTS
12: ! * ARG1 : Model ID
13: ! * ARG2 : Export option 0 = all, 1 = ant, 2 = comp, 3 = RTGs
14: ! * 4 = all w/o outer pl
15: ! *************************************************************************
16: ! * Macro start
17: ! *************************************************************************
18:     exportid = ARG1
19:     exp_opt = ARG2
20:     name_et = '../export/et%exportid'
21:     name_nt = '../export/nt%exportid'
```

```
22:         name_ct = '../export/ct%exportid'
23:         name_tmp = '../export/tmp%exportid'
24:    ! ------------------------------
25:    ! Set up Output
26:    ! ------------------------------
27:         FINISH
28:         CSYS,0
29:         WPCSYS,1,0
30:         /page,100000,,100000
31:         /title, Postprocessing
32:         /units,si ! use SI units
33:         /prep7
34:         csys,0
35:    ! Select only outer surfaces
36:         ALLSEL
37:         ASEL,R,EXT
38:    ! Create new element type for superimposing on volume faces
39:         ET,10,SURF152
40:         TYPE,10
41:         MSHKEY,1 ! 0 = free meshing, 1 = mapped meshing, 2 = mapped dominant meshing
42:         MSHAPE,0
43    ! Mesh model surfaces with 2D Fes
44:         CMSEL,S,HGA_front
45:         MAT,mat_HGA_front
46:         AMESH,ALL
47:         CMSEL,S,HGA_rear
48:         MAT,mat_HGA_rear
49:         AMESH,ALL
50:         CMSEL,S,HGA_meteoroid
51:         MAT,mat_HGA_meteoroid
52:         AMESH,ALL
53:         CMSEL,S,RTG
54:         MAT,mat_RTG
55:         AMESH,ALL
56:         CMSEL,S,MLI_1
57:         MAT,mat_MLI_1
58:         AMESH,ALL
59:         CMSEL,S,MLI_2
60:         MAT,mat_MLI_2
61:         AMESH,ALL
62:         CMSEL,S,MLI_3
63:         MAT,mat_MLI_3
64:         AMESH,ALL
65:         CMSEL,S,LOUVER
66:         MAT,mat_LOUVER
67:         AMESH,ALL
68:    ! Delete link and volume elements
69:         ALLSEL
70:         VCLEAR,ALL
71:         LCLEAR,ALL
72:         NUMCMP,ALL
73:         ALLSEL
74:         CSYS,0
75:    ! - - - - - - - - - - - - - - - - - - - - - - - - - - - - - - - - - - - - - - - - - - - -
76:    ! Retrieve model information
77:    ! - - - - - - - - - - - - - - - - - - - - - - - - - - - - - - - - - - - - - - - - - - - -
78:      *GET,en,ELEM,,COUNT,,,, ! en = number of elements
79:      *get,nn,NODE,,COUNT,,,, ! nn = number of nodes
```

```
80:     *GET,mn,MAT,,COUNT ! mn = number of materials
81:  ! - - - - - - - - - - - - - - - - - - - - - - - - - - - - - - - - - - - - - - - - - - - - - - -
82:  ! Node table initialisation
83:  ! - - - - - - - - - - - - - - - - - - - - - - - - - - - - - - - - - - - - - - - - - - - - - - -
84:      *DIM,nt,array,nn,3 ! nt = nodes table
85:      *VGET,nt(1,1),NODE,,LOC,X ! write x LOCation to NODEs table - 1. column
86:      *VGET,nt(1,2),NODE,,LOC,Y ! write y LOCation to NODEs table - 2. column
87:      *VGET,nt(1,3),NODE,,LOC,Z ! write z LOCation to NODEs table - 3. column
88:  ! - - - - - - - - - - - - - - - - - - - - - - - - - - - - - - - - - - - - - - - - - - - - - - -
89:  ! Element table initialisation
90:  ! - - - - - - - - - - - - - - - - - - - - - - - - - - - - - - - - - - - - - - - - - - - - - - -
91:      *dim,et,array,en,12 ! et = Element table
92:      *VGET,et(1,1),ELEM,,geom ! fill array with geometry info on el
93:      *VGET,et(1,2),ELEM,,cent,X ! fill array with el center-x
94:      *VGET,et(1,3),ELEM,,cent,Y ! fill array with el center-y
95:      *VGET,et(1,4),ELEM,,cent,Z ! fill array with el center-z
96:      *VGET,et(1,5),ELEM,,NODE,1 ! fill array with el NODE 1
97:      *VGET,et(1,6),ELEM,,NODE,2 ! fill array with el NODE 2
98:      *VGET,et(1,7),ELEM,,NODE,3 ! fill array with el NODE 3
99:      *VGET,et(1,8),ELEM,,NODE,4 ! fill array with el NODE 4
100:     *VGET,et(1,9),ELEM,,ATTR,mat ! fill array with el material nummer
101:     *VGET,et(1,10),ELEM,,ATTR,real ! fill array with el real konstant
102:     *VGET,et(1,11),ELEM,,ATTR,esys ! fill array with el esys
103:     *VGET,et(1,12),ELEM,,ATTR,type ! fill array with el type
104: ! - - - - - - - - - - - - - - - - - - - - - - - - - - - - - - - - - - - - - - - - - - - - - - -
105: ! Coefficient table initialisation
106: ! - - - - - - - - - - - - - - - - - - - - - - - - - - - - - - - - - - - - - - - - - - - - - - -
107:     *DIM,matcoeffs,ARRAY,mn,4 ! Table for material coefficients
108:     *DIM,ct,ARRAY,en,4 ! Element coefficient table
109:     *DO,i,1,en,1
110:         *IF,et(i,9),EQ,1,THEN ! Antenna front, 1:abs, 2:emis, 3:refl_spec, 4: refl_dif
111:             ct(i,1) = alpha_HGA
112:             ct(i,2) = emis_HGA_front
113:             ct(i,3) = 1 - emis_HGA_front
114:             ct(i,4) = 0.0
115:         *ENDIF
116:             *IF,et(i,9),EQ,2,THEN ! Antenna met detectors, 1:abs, 2:emis, 3:refl_spec, 4:refl_dif
117:             ct(i,1) = 0.0
118:             ct(i,2) = emis_HGA_mets
119:             ct(i,3) = 1 - emis_HGA_mets
120:             ct(i,4) = 0
121:         *ENDIF
122:         *IF,et(i,9),EQ,3,THEN ! Antenna rear faces, 1:abs, 2:emis, 3:refl_spec, 4: refl_dif
123:             ct(i,1) = 0.0
124:             ct(i,2) = emis_HGA_rear
125:             ct(i,3) = 1 - emis_HGA_rear
126:             ct(i,4) = 0
127:         *ENDIF
128:         *IF,et(i,9),EQ,4,THEN ! Equip panels, 1:abs, 2:emis, 3:refl_spec, 4: refl_dif
129:             ct(i,1) = 0.0
130:             ct(i,2) = emis_int
131:             ct(i,3) = 1 - emis_int
132:             ct(i,4) = 0
133:         *ENDIF
134:         *IF,et(i,9),EQ,5,THEN ! SS Mirrors, 1:abs, 2:emis, 3:refl_spec, 4: refl_dif
135:             ct(i,1) = 0.0
136:             ct(i,2) = emis_louver
137:             ct(i,3) = 1 - emis_louver
```

```
138:              ct(i,4) = 0
139:          *ENDIF
140:          *IF,et(i,9),EQ,6,THEN ! SS Louver, 1:abs, 2:emis, 3:refl_spec, 4: refl_dif
141:              ct(i,1) = 0.0 ! ss emis is set to louver emis (louver baldes closed)
142:              ct(i,2) = emis_louver
143:              ct(i,3) = 1 - emis_louver
144:              ct(i,4) = 0
145:          *ENDIF
146:          *IF,et(i,9),EQ,7,THEN ! Alu Kapton , 1:abs, 2:emis, 3:refl_spec, 4: refl_dif
147:              ct(i,1) = 0.0
148:              ct(i,2) = emis_MLI
149:              ct(i,3) = 1 - emis_MLI
150:              ct(i,4) = 0
151:          *ENDIF
152:          *IF,et(i,9),EQ,8,THEN ! Kapton , 1:abs, 2:emis, 3:refl_spec, 4: refl_dif
153:              ct(i,1) = 0.0
154:              ct(i,2) = emis_MLI
155:              ct(i,3) = 1 - emis_MLI
156:              ct(i,4) = 0
157:          *ENDIF
158:          *IF,et(i,9),EQ,9,THEN ! Mylar , 1:abs, 2:emis, 3:refl_spec, 4: refl_dif
159:              ct(i,1) = 0.0
160:              ct(i,2) = emis_MLI
161:              ct(i,3) = 1 - emis_MLI
162:              ct(i,4) = 0
163:          *ENDIF
164:          *IF,et(i,9),EQ,10,THEN ! Bearings , 1:abs, 2:emis, 3:refl_spec, 4: refl_dif
165:              ct(i,1) = 0.0
166:              ct(i,2) = 0.0
167:              ct(i,3) = 0.0
168:              ct(i,4) = 0.0
169:          *ENDIF
170:          *IF,et(i,9),EQ,11,THEN ! AlHC , 1:abs, 2:emis, 3:refl_spec, 4: refl_dif
171:              ct(i,1) = 0.0
172:              ct(i,2) = 0.0
173:              ct(i,3) = 0.0
174:              ct(i,4) = 0.0
175:          *ENDIF
176:          *IF,et(i,9),EQ,12,THEN ! RTG Housing , 1:abs, 2:emis, 3:refl_spec, 4: refl_dif
177:              ct(i,1) = 0.0
178:              ct(i,2) = 0.82
179:              ct(i,3) = 0.18
180:              ct(i,4) = 0.0
181:          *ENDIF
182:          *IF,et(i,9),EQ,13,THEN ! RTG heat shield , 1:abs, 2:emis, 3:refl_spec, 4: refl_dif
183:              ct(i,1) = 0.0
184:              ct(i,2) = 0.0
185:              ct(i,3) = 0.0
186:              ct(i,4) = 0.0
187:          *ENDIF
188:          *IF,et(i,9),EQ,14,THEN ! RTG fuel , 1:abs, 2:emis, 3:refl_spec, 4: refl_dif
189:              ct(i,1) = 0.0
190:              ct(i,2) = 0.0
191:              ct(i,3) = 0.0
192:              ct(i,4) = 0.0
193:          *ENDIF
194:      *ENDDO
195:  ! - - - - - - - - - - - - - - - - - - - - - - - - - - - - - - - - - - - - - - - - - - - - - - - - - - - - - - - - -
```

```
196: ! Nodal temperature table initialisation
197: ! - - - - - - - - - - - - - - - - - - - - - - - - - - - - - - - - - - - - - - - - - - - - - - - - - - - - - - - - - - - - -
198:       *dim,tmp,array,nn,1 ! tmp = temperature array
199:       FINISH
200:       /POST1
201:       ESEL,S,MAT,,7
202:       ESEL,A,MAT,,8
203:       ESEL,A,MAT,,9
204:       NSLE,S,1
205:       *GET,nn_mli,NODE,,COUNT
206:       *IF,nn_mli,NE,0,THEN
207:           *DO,i,1,nn_mli,1
208:               *GET,n_min,NODE, ,NUM,MIN
209:               *GET,tmp(n_min,1),NODE,n_min,TTOP
210:               NSEL,U,NODE,,n_min
211:           *ENDDO
212:       *ENDIF
213:       ESEL,INVE
214:       NSLE,S,1
215:       *GET,nn_rest,NODE,,COUNT
216:       *DO,i,1,nn_rest,1
217:           *GET,n_min,NODE, ,NUM,MIN
218:           *GET,tmp(n_min,1),NODE,n_min,TEMP
219:           NSEL,U,NODE,,n_min
220:       *ENDDO
221:       etable,ex,cent,x
222:       etable,ey,cent,y
223:       etable,ez,cent,z
224: - - - - - - - - - - - - - - - - - - - - - - - - - - - - - - - - - - - - - - - - - - - - - - - - - - - - - - - - - - - - -
225: ! Create ELEMent temp table
226: - - - - - - - - - - - - - - - - - - - - - - - - - - - - - - - - - - - - - - - - - - - - - - - - - - - - - - - - - - - - -
227:       *dim,tmp_E,array,en,1,1
228:       *DO,i,1,en,1
229:           N_1 = et(i,5)
230:           N_2 = et(i,6)
231:           N_3 = et(i,7)
232:           N_4 = et(i,8)
233:           tmp_E(i,1,1) = (tmp(N_1,1) + tmp(N_2,1)+ tmp(N_3,1)+ tmp(N_4,1))/4
234:       *ENDDO
235: - - - - - - - - - - - - - - - - - - - - - - - - - - - - - - - - - - - - - - - - - - - - - - - - - - - - - - - - - - - - -
236: ! Save data arrays in textfiles
237: - - - - - - - - - - - - - - - - - - - - - - - - - - - - - - - - - - - - - - - - - - - - - - - - - - - - - - - - - - - - -
238:       *CREATE,ansuitmp_1
239:           *cfopen,name_nt,'txt' ! write NODEs table as txt-file
240:           *vwrite,nt(1,1,1),nt(1,2,1),nt(1,3,1)
241: (F12.4,F12.4,F12.4)
242:           *cfclos
243:       *END
244:       /INPUT,ansuitmp_1
245: - - - - - - - - - - - - - - - - - - - - - - - - - - - - - - - - - - - - - - - - - - - - - - - - - - - - - - - - - - - - -
246:       *CREATE,ansuitmp_2
247:           *cfopen,name_et,'txt' ! write ELEMent table as txt-file
248:           *vwrite,sequ,et(1,1,1),et(1,2,1),et(1,3,1),et(1,4,1),et(1,5,1),et(1,6,1),et(1,7,1),et(1,8,1)
249: (f12.0,F10.6,F12.4,F12.4,f12.4,f12.0,f12.0,f12.0,f12.0)
251:           *cfclos
252:       *END
253:       /INPUT,ansuitmp_2
254: - - - - - - - - - - - - - - - - - - - - - - - - - - - - - - - - - - - - - - - - - - - - - - - - - - - - - - - - - - - - -
```

```
255:        *CREATE,ansuitmp_3
256:            *cfopen,name_tmp,'txt' ! write temperature table as txt-file
257:            *vwrite,tmp_E(1,1,1)
258:   (F12.4)
259:            *cfclos
260:        *END
261:        /INPUT,ansuitmp_3
262:   - - - - - - - - - - - - - - - - - - - - - - - - - - - - - - - - - - - - - - - - - - - - - - - - - - - - -
263:        *CREATE,ansuitmp_4
264:            *cfopen,name_ct,'txt' ! write temperature table as txt-file
265:            *vwrite,ct(1,1,1),ct(1,2,1),ct(1,3,1),ct(1,4,1)
266:   (F12.4,F12.4,F12.4,F12.4,)
267:            *cfclos
268:        *END
269:        /INPUT,ansuitmp_4
```